STRONG MOTION SIMULATION BY EMPIRICAL GREEN'S FUNCTION METHOD FOR BURSA ARMUTLU PENINSULA

by

Neval Savaş

B.S., Civil Engineering, Yıldız Technical University, 2000

Submitted to the Kandilli Observatory and
Earthquake Research Institute in partial fulfillment of
the requirements for the degree of
Master of Science

Graduate Program in Earthquake Engineering
Boğaziçi University
2008

ACKNOWLEDGEMENTS

I would like to express my sincere gratefulness to my thesis supervisor, Assistant Prof. Gülüm Tanırcan, for her patience and her invaluable guidance and also for not begrudging her efficacious help despite her health issues. I would also like to thank her for effectively conveying me her vast knowledge on Empirical Green's Function Simulation, which I utilized in my thesis and which she had directly learnt from the Japanese Professor, Kojiro Irikura, the inventor of the method.

ABSTRACT

STRONG MOTION SIMULATION BY EMPIRICAL GREEN'S FUNCTION METHOD FOR BURSA ARMUTLU PENINSULA

According to results of time dependent probabilistic hazard assessments, The fault segment extending between Gemlik-Bandirma and segment passing through the southern part of Iznik Lake have potentials of producing a magnitude 7.2+ event with 1000 year recurrence time and second highest hazard rate in Marmara Region. For future risk mitigation strategies, it necessitates preparing scenario earthquakes.

Near-field generation of scenario events from mentioned fault segments was performed at nine BYTNET stations. Horizontal components of records with frequency range of 0.5-10 Hertz were used. Simulations were performed by using Empirical Green's Function Method which essentially uses small events as Green's function and sums them up to follow the omega-squared scaling law. Gemlik Earthquake was utilized as Green's Function throughout analysis. As an initial calculation focal mechanism of Gemlik Earthquake was confirmed by simulating it with Mw= 3.3 event.

For scenario case, assumption is that scenarios occur at the same location of Mw= 4.8 event with same focal mechanism. A single asperity model was adopted. Size of asperities was determined according to stress drop ratio equality between target and element event. Scenarios were defined by changing rupture initiation points. Near field effects at each scenario simulation were investigated via observing components perpendicular and parallel to fault plane. Various empirical attenuation relationships were compared with simulated peak ground accelerations and velocities. Simulated acceleration spectra pertaining to fault parallel and normal components were compared with Turkish Seismic Design Code. Finally, It was observed whether peak values were in harmony with attenuation curves or not.

ÖZET

BURSA ARMUTLU YARIMADASI İÇİN AMPİRİK GREEN FONKSİYONU YÖNTEMİYLE KUVVETLİ YER HAREKETİ BENZEŞİMİ

Probabilistik deprem tehlike analizlerinin sonuçlarına göre, Gemlik'den Bandirma'ya kadar uzanan fay kısmı ve Iznik Gölünün güneyinden gecen fay segmenti 1000 yıllık tekrarlama süreciyle 7.2 değerinden daha büyük depremleri ve Marmara Bölgesinde ikinci en yüksek deprem tehlikesi üretme potansiyeline sahiptir. Gelecekte risk azaltma stratejileri bakımından, bu durum senaryo depremler hazırlamayı gerektirir

Bahsedilen fay segmentlerinden senaryo depremlerinin yakın saha üretimi dokuz BYT-NET istasyonunda gerçekleştirildi. Kayıtlarının yatay bileşenleri 0.5-10 Hz ferkans aralığında kullanıldı. Benzeşimler ampirik Green fonksiyon metodu kullanılarak gerçekleştirildi, ki bu metod esasen küçük depremleri Green fonksiyonları olarak kullanır ve omega-kare ölçeklendirme kuralını takiben onları toplamak suretiyle bir araya getirir. Gemlik depremi analiz boyunca Green fonksiyonu olarak kullanıldı. Hesaplarda ilk olarak, Gemlik depreminin odak mekanizması moment büyüklüğü 3.3 olan depremle benzeştirilerek teyit edildi.

Senaryo durumu için, senaryo depremlerinin Mw= 4.8 depremiyle aynı yerde ve aynı odak mekanizmasıyla oldukları kabulü yapıldı.Yalnız bir asperity kullanıldı. Esas ve hedef deprem arasındaki eşit gerilme düşüşü oranına gore asperitilerin büyüklüğü belirlendi. Senaryolar kırılma başlangıç noktasının değiştirilmesi yoluyla tanımlandı. Fay düzlemine parallel ve dik yöndeki bileşenleri gözlemleme yoluyla her bir senaryo benzeşimi için yakın saha yer hareketi etkileri incelendi. Çeşitli ampirik azalım ilişkileriyle benzeşim sonucu elde edilen maksimum yer ivmeleri ve hızları karşılaştırıldı. Fay düzlemine paralel ve dik bileşenlere ait benzeştirilmiş ivme spektrumu Türk Deprem

Yönetmeliğiyle karşılaştırıldı. Sonuçta, maksimum değerlerin azalım eğrileriyle uyum içinde olup olmadığı gözlemlendi.

TABLE OF CONTENTS

LIST OF FIGURES

LIST OF TABLES

LIST OF SYMBOLS / ABBREVIATIONS

AD	Average fault displacement
$A(f)$	Ground-motion amplitude spectrum
AP	Parameter of filter
AS	Parameter of filter
$A(t)$	Seismogram for the target event
A(T)	Spectral acceleration coefficient
$a(t)$	Seismogram for the subevent
A_0	Constant level of amplitude of the acceleration spectra for the large event
A_o	Effective ground acceleration coefficient
a_o	Constant level of amplitude of the acceleration spectra for the small event
A_{1100}	Value of peak ground acceleration on rock with 1100 m/sec shear wave velocity
a_{1b} and a_{2b}	Period-independent site-amplification coefficients
b_{lin}	Linear period-dependent site-amplification coefficient
b_{nl}	Nonlinear slope term for Boore and Atkinson (2007) NGA relation
b_V	Coefficient for Boore *et al.,* 1997 attenuation relationship
Bαβ	Instrument in building
b_i, i= 1, 2, 3 and 5	Coefficients for Boore *et al.,* 1997 attenuation relationship
b_{1ALL}	Coefficient for different slip earthquakes in Boore *et al.,* 1997 attenuation relationship
b_{1b} and b_{2b}	Period-dependent site-amplification coefficients
b_{1SS}, b_{1RS}	Coefficients for different slip earthquakes in Boore *et al.,* 1997 attenuation relationship
C	Stress drop ratio between large and small event

$\bar{c}$	Coefficient for Boore and Atkinson (2007) NGA relation
$\overline{cc}$	Period-independent, theoretically constrained model coefficient
CMP	Angle, measured clockwise from the north, indicating the component of the data
cmp	Number of components
c_i , i= 1,..., 17	Coefficients for Campbell and Bozorgnia (2003) attenuation relationship
c_{1b}, c_{2b}, and c_{3b}	Distance-scaling coefficients for Boore and Atkinson (2007) NGA relation
c_{ic} , i= 0, 1,…, 12	Empirically derived model coefficients for Campbell and Bozorgnia (2006) NGA relation
D	Fault slip for large event
d	Fault slip for small event
$\overline{d}$	Coefficient for Boore and Atkinson (2007) NGA relation
DIP	Dip angle of the target event
DIPA	Dip angle of the element event
DW	Length of the fault along the dip direction
DW0	Multiple shock parameter
DX	Length of the fault along the strike direction
DX0	Multiple shock parameter
$E(f)$	Earthquake source effect
E_S	Vertical ratio of Rayleigh waves
e_{ib} i= 1, 2,..., 7	Magnitude scaling coefficients in Boore and Atkinson (2007) NGA relation
f	Frequency
f_c	Corner frequency
f_{ca}	Corner frequency of the small event
f_{cm}	Corner frequency of the large event
F_D	Distance function parameter for Boore and Atkinson (2007) NGA relation

f_{dis}	Modeling parameter dependence on source-to-site distance
f_{flt}	Modeling parameter dependence on style of faulting
FH	Parameter of filter
f_{hng}	Modeling parameter dependence on hanging-wall effects
FL	Parameter of filter
F_{LIN}	Linear term in site amplification equation
F_M	Magnitude scaling parameter for Boore and Atkinson (2007) NGA relation
f_{mag}	Modeling parameter dependence on magnitude
$f_{\max}$	Cut-off frequency
F_{NL}	Nonlinear term in site amplification equation
F_{NM}	Indicator variable representing normal and normal-oblique faulting
F_{RV}	Indicator variable representing reverse and reverse-oblique faulting
F_S	Site amplification parameter for Boore and Atkinson (2007) NGA relation
FS	Parameter of filter
f_{sed}	Modeling parameter dependence on shallow sediment effects and 3-D basin effects
f_{site}	Modeling parameter dependence on linear and nonlinear shallow site conditions
$F(t)$	Filtering function or correction function
F_{TH}	Thrust faulting system parameter
$f_3(F)$	Faulting mechanism parameter for Campbell and Bozorgnia (2003) attenuation relationship
$f_5(HW, F, \mathrm{M_W}, r_{seis})$	Hanging wall parameter for Campbell and Bozorgnia (2003) attenuation relationship

$f_1(\mathrm{M_W})$	Magnitude scaling parameter for Campbell and Bozorgnia (2003) attenuation relationship
$f_2(\mathrm{M_W}, r_{seis}, S)$	Distance scaling parameter for Campbell and Bozorgnia (2003) attenuation relationship
$f_4(S)$	Far-source effect parameter of local site conditions for Campbell and Bozorgnia (2003) attenuation relationship
$g(S)$	Near-source effect parameter of local site conditions for Campbell and Bozorgnia (2003) attenuation relationship
h	Distance scaling coefficient to be changed by different attenuation relationships
$\overline{\mathrm{h}}$	Thickness of soil
h_i	Each soil column height in 30 m
HW	Hanging wall
I	Building importance factor
IE	Ending data point for the spectra
$I(f)$	Recording instrument effect
IFILT	Filter option
IMDL	Shape of slip time function
IS	Starting data point for the spectra
IWIND	Window length for the calculating the spectra
KEA	Ending data point for the target event
KEM	Ending data point for the element event
KSA	Starting data point for the target event
KSM	Starting data point for the target event
k_1, k_2, and k_3	Period-dependent, theoretically constrained model coefficients for Campbell and Bozorgnia (2006) NGA relation
L	Fault length for large event
l	Fault length for small event
M	Magnitude
MD	Maximum fault displacement
Md	Duration magnitude

M_h	Hinge magnitude
MI	Local magnitude
M_{ref}	Reference magnitude for Boore and Atkinson (2007) NGA relation
Ms	Magnitude based on surface waves
M_w	Moment Magnitude
M_0	Seismic moment for large event
m_0	Seismic moment for small event
N	Fault dimension ratio between large and small event
$\overline{N}$	Blow count
n'	Integer to shift the artificial periodicity into a higher frequency range of interest
NCMPT	Number of the components
$\overline{nn}$	Period-independent, theoretically constrained model coefficient
NS	Dummy variable used to denote normal-slip fault type for Boore and Atkinson (2007) NGA relation
NSX and NSW	Location of the rupture starting point
NT	Number of the element event summed up at each subfault
NW	Number of the subfaults along the dip direction
NX	Number of the subfaults along the strike direction
O_i	Displacement of the observed motion
PA	Azimuth of the element event
$P(f)$	Propagation effect
pga_low	Period-independent site-amplification coefficient for Boore and Atkinson (2007) NGA relation
$pga4nl$	Initial estimate value of predicted peak ground acceleration for 760 m/s reference shear wave velocity
PM	Azimuth of the target event
p_i, i= 1,..., 10	Regression coefficients for Akkar and Bommer (2007) peak ground velocity attenuation relationship

r	Distance from the hypocenter of the small event to the site
RA	Epicentral distance of the element event
r_a	Radius of asperity
RAK	Rake angle of the target event
RAKA	Rake angle of the element event
R_f	Radius of circular fault
r_{ij}	Distance from (i,j) element to the site
r_{jb}	Closest horizontal distance from the station to a point (Joyner-Boore distance)
RM	Epicentral distance of the target event
r_{ref}	Reference distance for Boore and Atkinson (2007) NGA relation
r_{rs}	Closest distance from rupture to the station
r_{rup}	Closest distance to coseismic rupture
RS	Dummy variable used to denote reverse-slip fault type for Boore and Atkinson (2007) NGA relation
r_{seis}	Closest distance to seismogenic rupture
r_0	Distance from the hypocenter of the large event to the site
S_A	Dummy variable representing the influence of site class for Akkar and Bommer (2007) peak ground velocity attenuation relationship
S_a	Total asperity area
$S(f)$	Site response effect
S_f	Total fault area
S_{FR}	Local site condition parameter for Campbell and Bozorgnia (2003) attenuation relationship
S_{HB}	Horizontal microtremor on the substratum
S_{HS}	Horizontal microtremor spectrum at the surface
S_i, i= 1, 2, 3, ..., N	Displacement of the synthesized motion

SS	Dummy variable used to denote strike-slip fault type for Boore and Atkinson (2007) NGA relation
S_S	Dummy variable representing the influence of site class for Akkar and Bommer (2007) peak ground velocity attenuation relationship
S_{SR}	Local site condition parameter for Campbell and Bozorgnia (2003) attenuation relationship
S(T)	Spectrum coefficient
st	Number of stations
STR	Strike angle of the target event
STRA	Strike angle of the element event
Su	Average undrained shear strength
S_{VB}	Vertical spectrum at the base ground
S_{VFS}	Local site condition parameter for Campbell and Bozorgnia (2003) attenuation relationship
S_{VS}	Vertical spectrum at the surface
Si , i= 1, 2, 3, ...	Fault names
T	Slip duration time for large event
T	Period
T_A and T_B	Spectrum characteristic periods
T_d	Source duration
T_F	Transfer function of surface layers
T_{ij}	Sum of the delay from the rupture starting point to the (i,j) element
T_P	Period of the pulse
T_R	Rise time of slip
TRA	Rise of the element event
TR0	Multiple shock parameter
U	Dummy variable used to denote unspecified fault type for Boore and Atkinson (2007) NGA relation
$U(t)$	Simulated waveform for the large event

$u(t)$	Observed waveform for the small event
U_0	Constant level of amplitude of the displacement spectra for the large event
u_0	Constant level of amplitude of the displacement spectra for the small event
V_A	Coefficient for Boore *et al.,* 1997 attenuation relationship
V_{h_i}	Shear wave velocity at each soil column height
V_r	Rupture velocity
V_{ref}	Specified reference velocity taken as 760 m/s
V_{S30} or V_S	Average shear-wave velocity to the depth of 30 m
V_1	Period-independent site-amplification coefficient as 180 m/s shear wave velocity
V_2	Period-independent site-amplification coefficient as 300 m/s shear wave velocity
W	Fault width for large event
w	Fault width for small event
X	Fraction of the fault rupture surface lying between the hypocenter and the site for strike-slip faults
Δx	Coefficient for Boore and Atkinson (2007) NGA relation
Y	Fraction of the fault rupture surface lying between the hypocenter and the site for dip-slip faults
$\overline{Y}$	Peak values for acceleration or velocity or five per cent damped response spectral acceleration
Δy	Coefficient for Boore and Atkinson (2007) NGA relation
Z	Number of soil columns for 30 m
Z_{TOR}	Depth to the top of coseismic rupture
$Z_{2.5}$	Depth to the 2.5 km/s shear-wave velocity horizon (sediment depth)

σ	Intra-event aleatory uncertainty coefficient
$\sigma_{\ln \overline{Y}}$	Standard deviation
σ_T	Total aleatory standard deviation
$\sigma_{T\overline{M}}$	Combined uncertainty coefficient for specified fault type
$\sigma_{T\overline{U}}$	Combined uncertainty coefficient for unspecified fault type
σ_1	Magnitude dependent intra-event standard deviation
σ_2	Magnitude dependent inter-event standard deviation
$\Delta\sigma_{ave}$	Average stress drop
$\Delta\sigma_L$	Stress drop for large events
$\Delta\sigma_S$	Stress drop for small events
δ	Dip angle
τ	Inter-event aleatory uncertainty coefficient
$\tau_{\overline{M}}$	Inter-event uncertainty coefficient for specified fault type
τ_s	Slip duration time for small event
$\tau_{\overline{U}}$	Inter-event uncertainty coefficient for unspecified fault type
ϕ	Angle between the directions of rupture propagation and waves traveling from the fault to the site for dip-slip faults
ξ_i	Distance from the rupture nucleation point to the i-th subfault
*	Convolution
ε	Random error term
λ	Rake angle
ρ_0	Radius of circular crack
Ø	Strike angle measured clockwise from North
θ	Angle between the directions of rupture propagation and waves traveling from the fault to the site for strike-slip faults
α	Total number of stories of the buildings (including ground floor)
β	Floor where the instrument is installed

Acc	Acceleration
ADU	Automatic dial-up
Amp Max	Maximum value of amplitude
BYTNet	Bursa-Yalova Turkey Accelograph Network
CT	Continuous, real time transmission
DCF	Distributed coordination function
Disp	Displacement
EGF	Empirical Green's function
EMSC	European-Mediterranean Seismological Centre
EQ	Earthquake
ETHZ	Swiss Seismological Service Institute of Geophysics (Eidgenössische Technische Hochschule Zürich)
ETNA	Electronic transactions on numerical analysis
EW	East-West component of record
FAS	Fourier amplitude spectra
FEMA	Federal Emergency Management Agency
FF	Free field
FFT	Fast fourier transform
GMPE	Ground motion prediction equation
GPS	Global positioning system
H	Horizontal component of record
Hs	Hard soil
HVSR	Horizontal to vertical spectral ratio
H/V	Horizontal-to-vertical component ratio
Hz	Hertz
Iline	Internet leased line
INGV	Istituto Nazionale di Geofisica e Vulcanologia
Int	Internal
KOERI	Kandilli Observatory and Eartquke Research Institute
LAAS	Logarithmic acceleration amplitude spectra
Lat	Latitude
LDAS	Logarithmic displacement amplitude spectra

Loc	Local communication system
Long	Longitude
MDU	Manual dial-up
METU	Middle East Technical University
MSK	Medvedev-Sponheur-Karnik (earthquake intensity scale)
MTA	General Directorate of Mineral Research and Exploration
N	North component of record
NAFZ	North Anatolian Fault Zone
NCEER	National Center for Earthquake Engineering Research
NEHRP	National earthquake hazard reduction program
NGA	Next generation attenuation
NOA	National Observatory of Athens Institute of Geodynamics
NS	North-South component of record
PCMCIA	Personel computer memory card international association
PGA	Peak ground acceleration
PGD	Peak ground displacement
PGV	Peak ground velocity
PI	Plasticity index
PSA	Peak spectral acceleration
Rc	Rock
RSP	Rupture starting point
S	South component of record
SA	Spectral acceleration
SEAOC	Structural Engineers Association of California
SH	Horizontal S wave
SN	Strike normal
S/N	Signal to noise ratio
SP	Strike parallel
Ss	Soft soil
Stl	Satellite
TCG	Geocentric coordinate time
TCU	Tai-chung station

Tlf	Telephone
TSDC	Turkish Seismic Design Code
UD	Up-Down component of record
V	Vertical component of record
Ve	Velocity

1. INTRODUCTION

1.1. Near Fault Ground Motion and Its Characteristics

Ground motions close to a ruptured fault can be significantly different than those further away from the seismic source. The near-fault zone is typically assumed to be within a distance of about 20-60 km from a ruptured fault (Stewart *et al*., 2001). Near-fault ground motions are different from ordinary ground motions in that they often contain strong coherent dynamic long period pulses (near-field motions exhibit distinct lower-frequency pulses) and permanent ground displacements. The dynamic motions are dominated by a large long period pulse of motion that occurs on the horizontal component perpendicular to the strike of the fault, caused by rupture directivity effects. These pulses can place very high demand on certain types of buildings and other structures. Within near-fault zone, ground motions are significantly influenced by the rupture mechanism, the direction of rupture propagation relative to the site, and possible permanent ground displacements resulting from the fault slip. These factors result in effects termed herein as "rupture-directivity" and "fling step." The estimation of ground motions close to an active fault should account for these characteristics of near-fault ground motions. Near-field effects include "directivity pulse" (wave field buildup in the direction of rupture propagation), "fling step" (motions very near the fault trace associated with permanent offset of the ground surface), and the polarization (radiation pattern) of energy release that causes different motions to occur in the strike-parallel and strike-normal directions. In earthquake engineering, the terms "directivity" and "fling" have been used interchangeably. Both effects result in large velocity pulses in the near fault ground motion, but they have very different causes. Directivity effects result from constructive interference of ground motions generated from different patches of slip located down strike for strike-slip faults or down dip for dip-slip faults (Somerville *et al.*, 1997). Fling effects result from tectonic deformation at the site and are related to the slip on the fault near the site. Fling can lead to very large velocities and displacements.

Near-field ground motions include large pulses that may greatly amplify the dynamic response of long period structures, particularly if structures are called upon to respond inelastically to earthquake ground motion. Pulses will amplify the maximum interstory drift for elastic structures, and more so for inelastic structures. The amplified interstory drifts may impose excessive deformation demands on elements, which in turn may lead to incremental (P-delta) collapse.

1.2. Near Fault Effects

1.2.1. Rupture Directivity Effects

The effects of rupture directivity on near-fault ground motions have been recognized by strong-motion seismologists for several decades. An earthquake is a shear dislocation that begins at a point on a fault and spreads at a velocity that is almost as large as the shear wave velocity. The propagation of fault rupture toward a site at a velocity close to the shear wave velocity causes most of the seismic energy from the rupture to arrive in a single large pulse of motion that occurs at the beginning of the record (Archuleta and Hartzell, 1981; Somerville *et al.*, 1997). This pulse of motion represents the cumulative effect of almost all of the seismic radiation from the fault. The radiation pattern of the shear dislocation on the fault causes this large pulse of motion to be oriented in the direction perpendicular to the fault, as illustrated schematically in Figure 1.1 for strike-slip faulting. This causes the strike-normal ground motions to be larger than the strike-parallel ground motions at periods longer than about 0.5 seconds. To accurately characterize near fault ground motions, it is therefore necessary to specify separate response spectra and time histories for the fault normal and fault parallel components of ground motion.

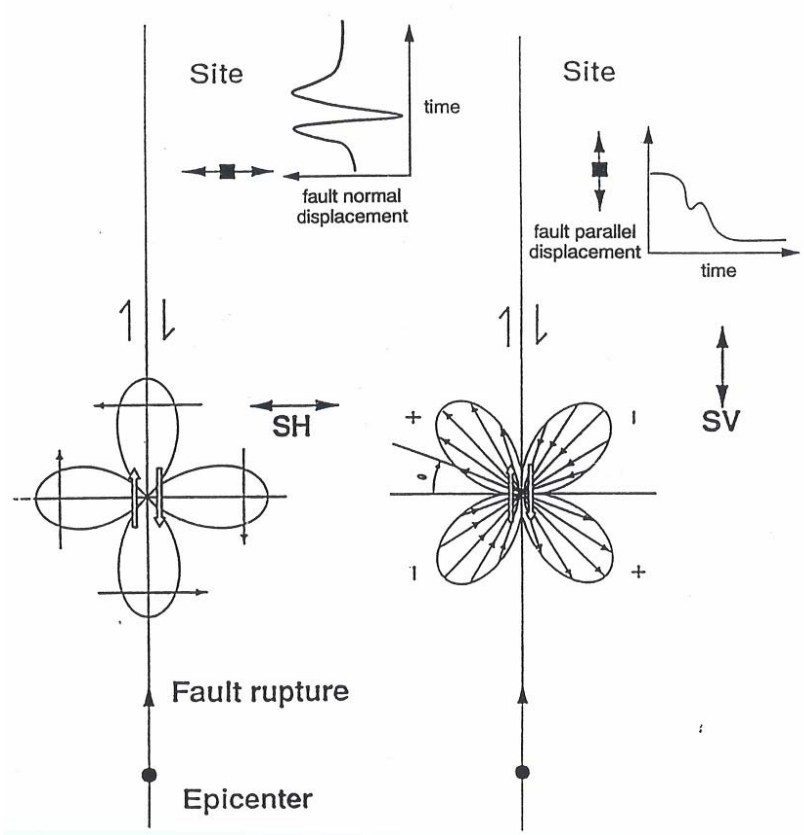

Figure 1.1. Schematic map view of the radiation pattern for a vertical strike-slip fault and its effect on near-fault ground displacements (Somerville *et al.*, 1995)

Forward rupture directivity effects occur when two conditions are met: the rupture front propagates toward the site, and the direction of slip on the fault is aligned with the site. The conditions for generating forward rupture directivity effects are readily met in strike-slip faulting, where the rupture propagates horizontally along strike either unilaterally or bilaterally, and the fault slip direction is oriented horizontally in the direction along the strike of the fault. However, not all near-fault locations experience forward rupture directivity effects in a given event. Backward directivity effects, which occur when the rupture propagates away from the site, give rise to the opposite effect: long duration motions having low amplitudes at long periods, as shown in Figure 1.2.

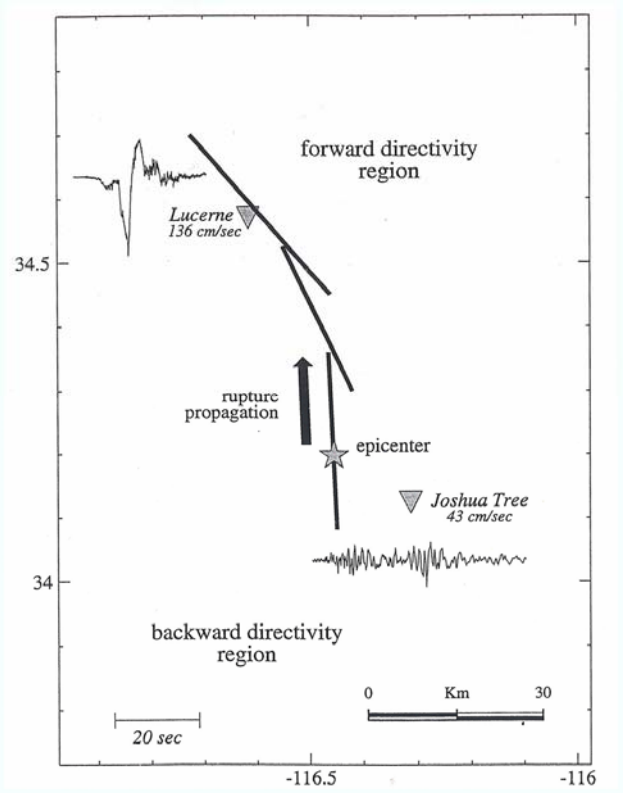

Figure 1.2. Map of the Landers region showing the location of the the rupture (Wald and Heaton, 1994)

The conditions required for forward directivity are also met in dip slip faulting. The alignment of both the rupture direction and the slip direction updip on the fault plane produces rupture directivity effects at sites located around the surface exposure of the fault (or its updip projection if it does not break the surface). Unlike the case for strike-slip faulting, where forward rupture directivity effects occur at all locations along the fault away from the hypocenter, dip slip faulting produces directivity effects on the ground surface that are most concentrated in a limited region updip from the hypocenter. For this reason, rupture directivity effects in the 1999 Chi-Chi earthquake were confined to stations such as Tsaotun (TCU075) and Mingchien (TCU129), which are located updip from the hypocenter along the southern part of the fault rupture.

For moderate magnitude earthquakes, near-field ground accelerations, velocities, and displacements, can be quite high especially toward the direction of propagation of fault rupture. Peak accelerations can exceed 1g, while peak velocities may exceed 1.5 m/sec, and peak displacements can exceed one meter.

1.2.2. Fling Step Effects

The effects of fling step ground motions on the structural performance of buildings have received less attention than the effects of rupture-directivity. Recent earthquakes in Turkey and Taiwan have highlighted the importance of permanent ground deformation associated with surface rupture on the performance of buildings and lifelines that cross, or are situated close to, active fault traces. The effects of surface fault rupture are commonly evaluated as pseudo-static ground deformations that are decoupled from the ground shaking hazard. Distinct offsets across ruptures, differential settlement, ground warping, ground cracking, and extensional and compressional horizontal ground strains are the focus of these evaluations, as differential ground movements and ground strains are most damaging to overlying structures. As pointed out by numerous researchers (e.g., Byerly and DeNoyer, 1958; Bray *et al.,* 1994 and Lazarte *et al.,* 1994), significant ground deformation can occur away from the primary trace of the ruptured fault, so tectonic deformation associated with surface fault rupture can affect structures located some distance from the fault (although there are also many cases where relative ground displacements are restricted to a fairly narrow zone along the main fault trace).

Fling step, being a result of a static ground displacement, is generally characterized by a unidirectional velocity pulse and a monotonic step in the displacement time history. The discrete step in the displacement time history occurs parallel to the direction of fault slip (i.e., along strike for strike-slip events and along dip for dip-slip events). To gain a sense of the magnitude of the fling step displacement that may be present in near-fault records, the compilation of empirical data by Wells and Coppersmith (1994) provides a useful starting point. For all fault types, the maximum fault displacement (*MD*) in meters can be related to the moment magnitude (M) of the event through the regression equation

$$\log_{10}(MD) = -5.46 + 0.82\,M \qquad (1.1)$$

where the standard deviation for this estimate is 0.42 (in $\log_{10}$ units). The magnitude range over which Equation 1.1 applies is M= 5.2-8.1, and the range of *MD* is 0.01 m to 14.6 m. The estimate of fault displacement is somewhat dependent on fault type, and regression coefficients are given for strike-slip and normal faults separately in Wells and

Coppersmith (1994). Regressions on reverse fault data set were not statistically significant. The maximum fault displacement occurs at one point along the fault with the amount of fault displacement varying along the fault trace.

The average fault displacement (*AD*) for all fault types is

$$\log_{10}(AD) = -4.80 + 0.69\ M \qquad (1.2)$$

where the standard deviation for this estimate is 0.36 (in $\log_{10}$ units). The magnitude range for these events is M= 5.6-8.1. In general, the average displacement along the surface fault rupture is about half of the maximum displacement, although this ratio varies significantly.

Strong fling effects were observed in the near fault ground motions from the 1999 Turkey and Taiwan earthquakes. For example, the very large velocities (300 cm/s) recorded at the northern end of the Chilungpu fault during the Chi-Chi earthquake were due to fling effects. If the fling effect is separated out from these recordings, the peak velocity of the remaining ground motion due to transient displacement is reduced to about 90 cm/s.

A preliminary model of the fling is developed based on a single sine-wave cycle to model the fling in acceleration. There are three parameters for this model: the amplitude of the sine-wave, the period of the sine-wave, and the arrival time of the fling. The amplitude is determined using empirical models of tectonic deformation based on geodetic data. The period is based on empirical observations of fling from the 1992 Landers, 1999 Chi-Chi and 1999 Kocaeli earthquakes. The arrival time of the fling pulse is just before the S-wave arrival.

Existing ground motion attenuation relations do not include fling effects. A separate ground motion model needs to be developed for the fling. The total ground motion is then computed by combining the ground motion from attenuation relations with the ground motion from the fling.

An important outstanding question is does the fling have a significant effect on the response of structures. Incorporating the fling into the ground motion adds complexity to the development of the ground motion. It has not yet been determined which classes of structures are affected by the fling that would justify the additional complexity in the development of the design ground motions.

1.3. Orientation of Dynamic and Static Near Fault Ground Motions

Figure 1.3 schematically illustrates the orientations of dynamic and static near fault ground motions. The strike-slip case is shown in map view, where the fault defines the strike direction. The rupture directivity pulse is oriented in the strike-normal direction and the static ground displacement ("fling step") is oriented parallel to the fault strike. The dip-slip case is shown in vertical cross section, where the fault defines the dip direction; the strike direction is orthogonal to the page. The rupture directivity pulse is oriented in the direction normal to the fault dip, and has components in both the vertical direction and the horizontal strike normal directions. The static ground displacement is oriented in the direction parallel to the fault dip, and has components in both the vertical direction and the horizontal strike normal direction.

Figure 1.4 schematically illustrates the partition of near fault ground motions into the dynamic ground motion, which is dominated by the rupture directivity pulse, and the static ground displacement. For a strike-slip earthquake, the rupture directivity pulse is partitioned mainly on the strike-normal component, and the static ground displacement is partitioned on the strike-parallel component. If the static ground displacement is removed from the strike-parallel component, very little dynamic motion remains. For a dip-slip earthquake, the dynamic and static displacements occur together on the strike-normal component, and there is little of either motion on the strike-parallel component. If the static ground displacement is removed from the strike-normal component, a large directivity pulse remains.

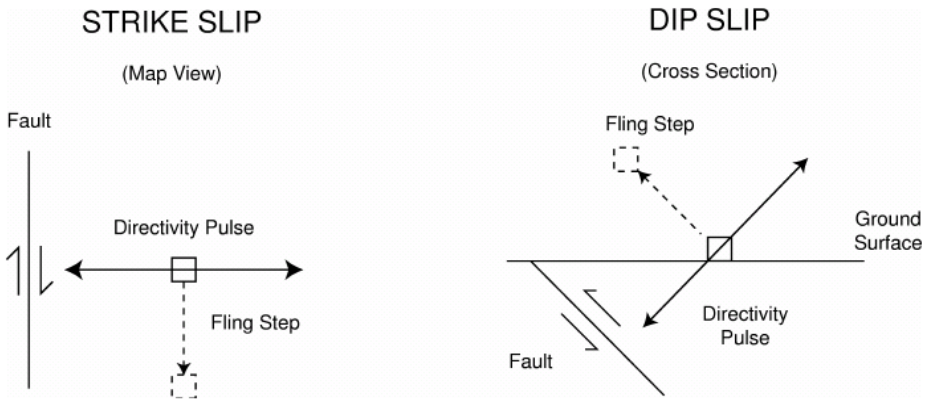

Figure 1.3. Schematic diagram showing the orientations of fling step and directivity pulse for strike-slip and dip-slip faulting (Somerville, 2002)

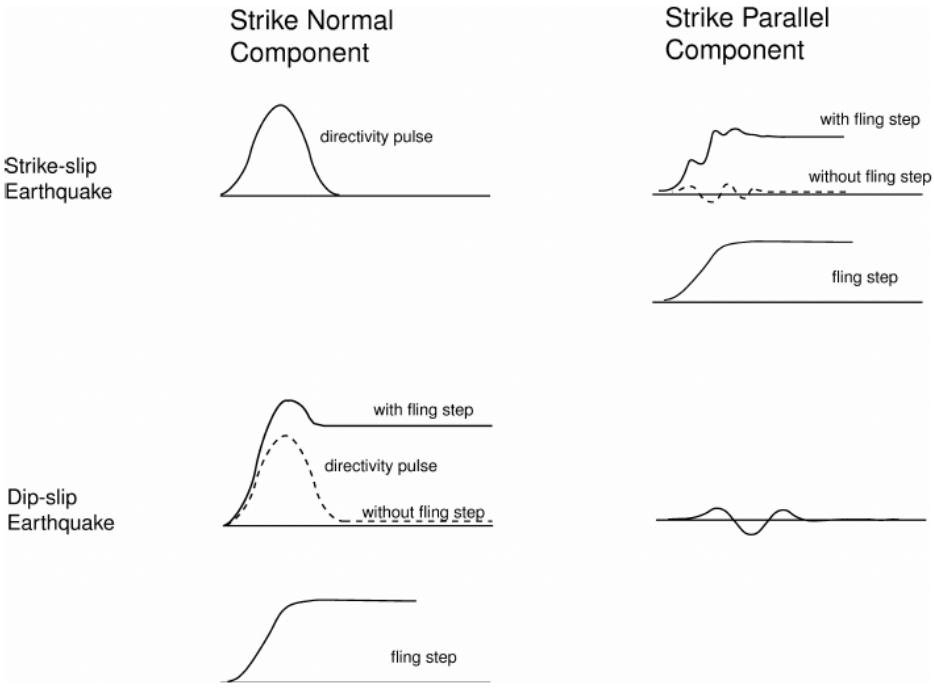

Figure 1.4. Schematic diagram of time histories for strike-slip and dip-slip faulting in which the fling step and directivity pulse are shown together and separately (Somerville, 2002)

1.4. Parameterization of Near-Fault Ground Motion

Somerville *et al.* (1997) parameterized the conditions that lead to forward and backward-directivity. As shown in Figure 1.5, the spatial variation of directivity effects depends on the angle between the direction of rupture propagation and the direction of waves traveling from the fault to the site (θ for strike-slip faults, and ϕ for dip-slip faults), and on the fraction of the fault rupture surface that lies between the hypocenter and the site (X for strike-slip faults and Y for dip-slip faults). More significant forward-directivity results from smaller angles between the site and fault and for larger fractions of ruptured fault between the site and hypocenter. It should be noted that even when the geometric conditions for forward directivity are satisfied, the effects of forward directivity may not occur. This could happen if a station is at the end of a fault and rupture occurs toward the station but slip is concentrated near the end of the fault where the station is located.

To account for directivity effects, Somerville *et al*. (1997) correlated the residuals of response spectral ordinates (at five per cent damping) to the geometric parameters defined in Figure 1.5, with the results shown in Figure 1.6. The ground motion parameters that are modified are the average horizontal response spectra and the ratios of fault-normal to fault-parallel response spectra (Stewart *et al.*, 2001).

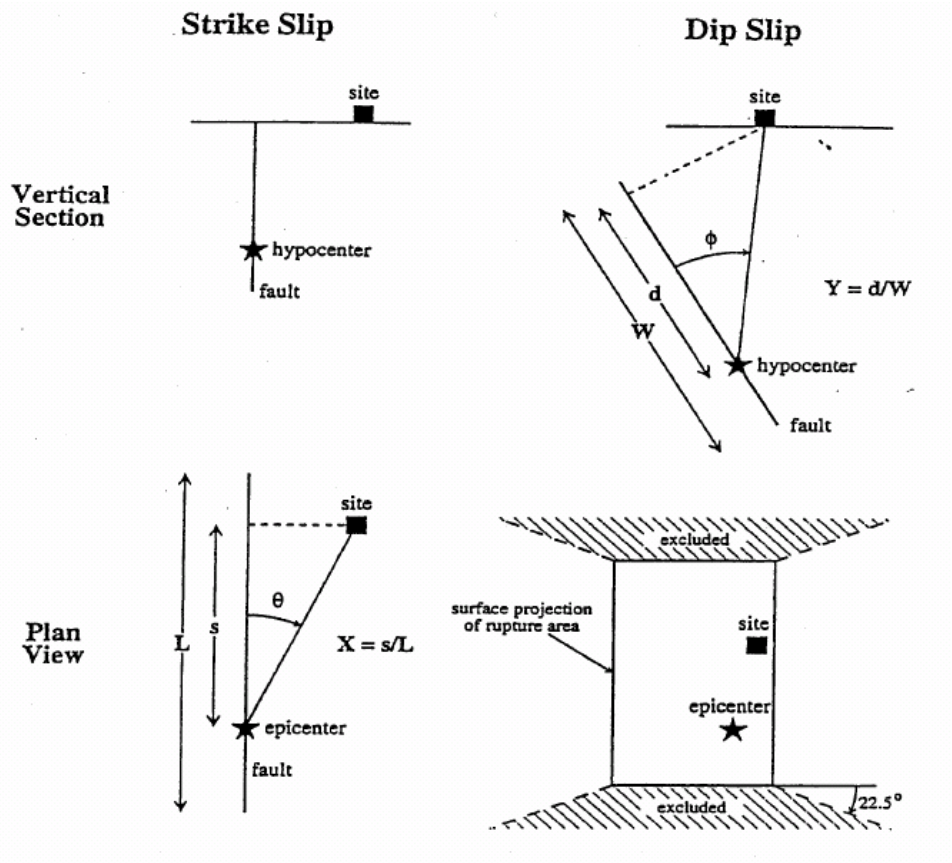

Figure 1.5. Parameters used to define rupture-directivity conditions (adapted from Somerville *et al*., 1997)

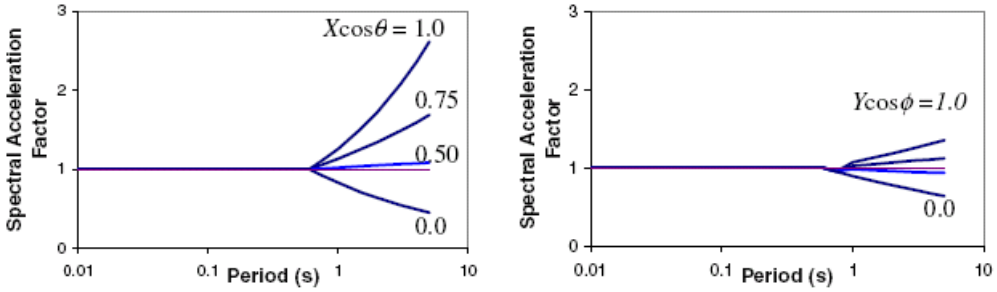

(a) Average response spectra ratio, showing dependence on period and on directivity parameters

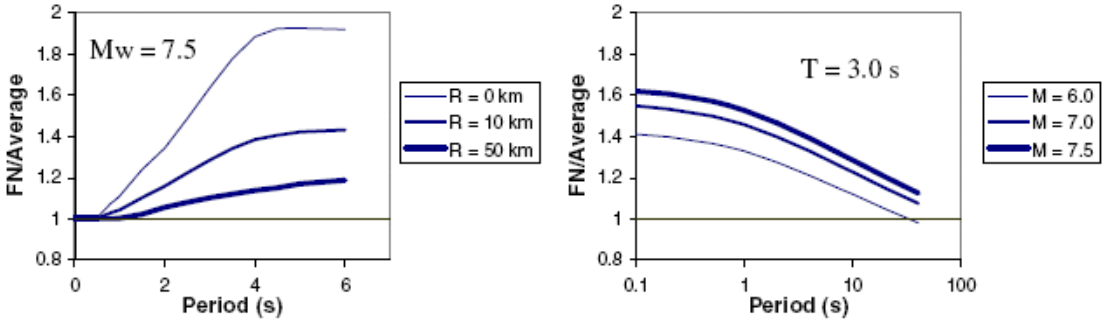

(b) Strike-normal to average horizontal response spectral ratio for maximum forward directivity conditions $(X\cos\theta = 1)$

Figure 1.6. Predictions from the Somerville *et al*. (1997) relationship for varying directivity conditions

1.5. Development of an Improved Representation of Near-Fault Ground Motions

An improved representation of near-fault ground motions for use in building codes is developed by Somerville (1998). Currently, all seismic design guidelines and codes specify design ground motions using the response spectrum. The effect of forward rupture directivity on the response spectrum is to increase the level of the response spectrum of the horizontal component normal to the fault strike at periods longer than 0.5 seconds (Somerville, 1996; Somerville *et al*., 1997). This causes the peak response spectral acceleration of the strike-normal component to shift to longer periods, for example from 0.25 seconds to as much as 0.75 seconds (Somerville, 1998). Near fault effects cannot be adequately described by uniform scaling of a fixed response spectral shape; instead the

shape of the spectrum becomes richer in long periods as the level of the spectrum increase.

Although the response spectrum provides the basis for the specification of design ground motions in all current design guidelines and code provisions, there is a growing recognition that the response spectrum alone does not provide an adequate characterization of near-fault ground motions. For example, a broad consensus was reached at the NCEER Workshop on National Representation of Seismic Ground Motion for New and Existing Highway Facilities, held in San Francisco on May 29-30, 1997, that the response spectrum alone does not provide an appropriate characterization of near-fault ground motions for the design of bridges. This is because near fault ground motions are characterized by a relatively simple long period pulse of strong motion having relatively brief duration, rather than by a stochastic process having relatively long duration the characterizes more distant ground motion. Unlike the case for more distant ground motion, the resonance phenomenon that the response spectrum is designed to represent has insufficient time to build up when the input is a near-fault pulse. The response spectrum is thus not capable of adequately describing the seismic demands presented by a near-fault pulse.

Current trends in the development of future building codes have all embraced the concept of performance based design, and conceptual frameworks of that approach have been developed by SEAOC Vision 2000 and FEMA-273. Since the goal of performance based design depends heavily on realistic specification of ground motion inputs and realistic models of building response, it is clear that some alternative approach needs to be developed for specifying near-fault ground motions for seismic design. The new approach that has been developed has the goal of supplementing the response spectrum with time domain parameters such as the period and amplitude of the near-fault pulse. These ground motion parameters have been identified as being important for predicting damage to structures.

1.6. Various Relations in Near-Field Ground Motion

1.6.1. Relationship between Pulse Period and Rise Time

It is expected that the period of the pulse is most strongly influenced by the rise time T_R of slip on the fault, which measures the duration of slip at a single point on the fault. Somerville *et al*. (1999) found a self-similar relation between rise time and magnitude from an empirical analysis of 15 crustal earthquakes:

$$\log_{10} T_R = -3.34 + 0.5 M_w \tag{1.3}$$

The self-similar relation between pulse period and magnitude obtained above is:

$$\log_{10} T_P = -3 + 0.5 M_w \tag{1.4}$$

Eliminating M_w from these two equations, the period T_P of the pulse is related to the rise time T_R that is found by the relation:

$$T_P = 2.2\ T_R \tag{1.5}$$

The period of the pulse is thus equal to about twice the rise time of slip on the fault. This is consistent with the fact that the rise time is a lower bound on the period of the pulse. If the fault were a point source, then the only source parameter that would contribute to the period of the pulse would be the rise time, and the period of the pulse would equal the rise time if wave propagation effects ignored. Since the fault is actually finite, and the rupture velocity is less than the shear wave velocity, the finite apparent duration of the rupture also contributes to the widening of the pulse.

1.6.2. Dependence of Rise Time (and pulse period) on Style of Faulting

Analyses performed by Professor Krawinkler (Krawinkler and Alavi, 1998) demonstrate that the period of the near-fault pulse has a strong influence on the demands

on the structure. The period of the pulse is directly related to the rise time. It is found that a correlation between rise time and faulting mechanism may explain the style-of-faulting factor. For a given seismic moment, the rise times for reverse earthquakes are on average about half as long as those for strike-slip earthquakes. Strong ground motion simulations show that halving the rise time causes an increase in ground motion amplitudes. This increase is consistent with the style of faulting factor in empirical strong motion attenuation relations, in which ground motions for reverse earthquakes typically exceed those for strike-slip earthquakes. Thus the larger ground motion levels in thrust faulting may be due to a shorter rise time. The shorter rise times of the reverse faulting events are manifested in the velocity response spectrum by a peak or plateau occurring at a shorter period than for strike-slip faults (Somerville, 1998).

1.6.3. Importance of Multiple Pulses

Structural response analyses by Professor Krawinkler (Krawinkler and Alavi, 1998) using simple input pulses show that the response grows rapidly with the number of half-cycles of input motion. The presence of multiple pulses in the velocity time history can thus dramatically increase the damage potential of the ground motions. For example, the destructiveness of the ground motions from the 1995 Kobe earthquake was accentuated by the presence of two consecutive pulses in the recorded velocity waveforms. Some recordings of the 1994 Northridge and 1989 Loma Prieta earthquakes also contained velocity pulses having more than the 1 to $1^{1/2}$ cycles that characterize the simplest pulses recorded in other earthquakes. This indicates the need to identify the conditions that give rise to multiple pulses in near-fault ground motions. A preliminary review indicates that they may be due to multiple asperities on the fault rupture plane, and that their occurrence depends on the relative location of the hypocenter, of asperities on the fault, and of the recording site.

1.7. Magnitude Scaling of Response Spectra of Near Fault Ground Motions

Strong motion recordings of the recent large earthquakes in Turkey and Taiwan confirm that the near fault pulse is a narrow band pulse whose period increases with magnitude. The period of the near fault pulse is related to source parameters such as the

rise time (duration of slip at a point on the fault) and the fault dimensions, which generally increase with magnitude. These recent earthquakes also have surprisingly weak ground motions at short and intermediate periods (0.1 to 3.0 seconds), weaker than those of smaller (magnitude 6 ¾ - 7.0) earthquakes. Near fault ground motions containing forward rupture directivity may be simple enough to be represented by simple time domain pulses. The narrow band nature of these pulses causes their elastic response spectra to have peaks whose period increases with magnitude. The elastic spectra of near-fault recordings of earthquakes with magnitudes 6.75 to 7.0 are much stronger than those of the larger earthquakes (magnitudes 7.25 to 7.5) in the intermediate period range of 0.5-2.5 sec, but are weaker at longer periods. These observations require reevaluation of the magnitude scaling in current models of near fault ground motions and in current source scaling relations (Somerville *et al*., 1999).

1.8. Ground Motions from Surface and Subsurface Faulting

The recent Turkey and Taiwan earthquakes have surprisingly weak ground motions at short and intermediate periods (0.1 to 3.0 seconds), about 40 per cent weaker than those of current empirical ground motion models. The recent large earthquakes in Turkey and Taiwan, which caused large surface ruptures, have surprisingly weak ground motions at short and intermediate periods. These new observations are consistent with previous earthquakes that the strong ground motions of earthquakes that produce surface faulting are weaker than the ground motions of events whose rupture is confined to the subsurface. The rupture of the 1989 Loma Prieta and 1994 Northridge earthquakes stopped at depths of several km below the surface. Although there was some surface faulting on Awaji Island during the 1995 Kobe earthquake, the strong motion recordings of the Kobe event were dominated by subsurface faulting on the Suwa and Sumayama faults. Thus the earthquakes in the magnitude range of 6.7 – 7.0 characterized by subsurface faulting, while all of the earthquakes in the magnitude range of 7.2 to 7.6 are characterized by large amounts of surface faulting (Somerville, 2003). Consequently, some of the differences may be attributable not only to magnitude effects, but to the effects of buried faulting. Indeed, at short and intermediate periods, the ground motions from earthquakes that produce large surface rupture appear to be systematically weaker than those whose

rupture is confined to the subsurface, although current empirical ground motion models do not distinguish between these different categories of earthquakes.

Information about near fault effects can be summurized as follows:

Near Fault Effects

- Directivity
  – Related to the direction of the rupture front
- Forward directivity: rupture toward the site (site away from the epicenter)
- Backward directivity: rupture away from the site (site near the epicenter)
- Fling
  – Related to the permanent tectonic deformation at the site

Velocity Pulses

- Forward Directivity
  – Two-sided velocity pulse due to constructive interference of SH waves from generated from parts of the rupture located between the site and epicenter
- Constructive interference occurs if slip direction is aligned with the rupture direction
- Occurs at sites located close to the fault but away from the epicenter for strike-slip
- Fling
  – One-sided velocity pulse due to tectonic deformation
  – Occurs at sites located near the fault rupture independent of the epicenter location

Table 1.1. Observations of directivity and fling

Sense of Slip	Directivity	Fling
Strike-Slip	Fault Normal	Fault Parallel
Dip-Slip	Fault Normal	Fault Normal

1.9. Scope, Objective and Goals

The major goal of this study was to investigate the methodology, applicability scope of empirical Green's function method in near field ground motion simulation by handling

the Gemlik Bay earthquake, the area of Armutlu Peninsula and field-test the methodology for this task. In addition, it was to observe that how graphs that were drawn according to simulated values obtained by changing some source parameters were influenced by the near-field strong ground motion effects. In order to fulfill this general goal, the following objectives are aimed:

- To do a literature review about near-field ground motion, its characteristics, effects and simulation methods
- To gather and review the available information about concerned area, Gemlik earthquake and recording stations
- To investigate the site by using H/V method
- To confirm focal mechanism of Gemlik earthquake via performing test simulation
- To get information about up-to-date empirical attenuation relationships (next generation attenuation)

2. GENERAL INFORMATION ABOUT GROUND MOTION SIMULATION

2.1. Ground Motion Simulation

If strong motion recordings are unavailable for a particular earthquake engineering application, simulated earthquake motions are utilized. Strong motion recordings may not be available for some geographical regions where recordings are meager or for particular magnitude and distance ranges that may be within the scope of a project. In both cases, simulated earthquake motions stand for synthetic data which can supplement recorded motions. Earthquake ground motion results from a complex physical system which involves three processes: The strain energy released due to the rupture of an active geologic fault (earthquake source process) generate seismic waves; the subsequent propagation of the seismic waves through the earth's crust (wave propagation) and the approach of the seismic waves to the surface of the earth, where they are further modified during their propagation through shallow soils (shallow soil response). These three processes give rise to complex earthquake ground motions, with basically different characteristics in the short-period and long-period ranges.

Generally, it is recognized that long-period motions are deterministic since their waveforms and spectral contents can be reasonably predicted with the use of seismological models that do not include any stochastic element either in the input or the theoretical formulation. It is relatively difficult to achieve matches to the high frequency waveforms of earthquake motions with the use of a deterministic approach since source radiation and wave propagation become progressively more incoherent at short periods on account of some diminutive heterogeneities in the earthquake source process and crustal properties. In short, the behavior of the observed high-frequency motions is stochastic.

2.1.1. Earthquake Source Processes

The basic framework for modernized seismic source modeling of tectonic earthquakes is provided by the elastic rebound theory proposed by Reid (1911). According to Reid's (1911) theory, rupture takes place when stress accumulation on a fault reaches the point which exceeds the shear strength of the rock, resulting in rapid rupture across the fault. The point where the rupture begins is called hypocenter. The rupture then propagates across the fault surface. The propagation speed is typically less than or close to shear wave velocity of the rock. Slip at a particular point on the fault takes place when the rupture front passes that point, and the duration of the slip's reaching its final value and stopping is a finite amount of time. The rise time is defined as the time between the initiation and termination of the slip. A kinematic source model is typically utilized in a simulation procedure in order to describe such a fault slip process. Rupture geometry (rupture area, fault strike, and fault dip), rupture nucleation point, rupture velocity, slip direction (rake angle), and a slip-time function form the key parameters of a kinematic source model.

2.1.2. Point Source or Finite Source

The fault slip process is finite in both time and space. A finite source is necessary when a site is located a few fault lengths from the source of a strong earthquake. However, a point source in space may be assumed rather than a finite source at considerable distances from the fault, and/or for small-magnitude earthquakes. The assumption of a point source model is advantageous over using a finite source model in that it is computationally less demanding (Stewart *et al.*, 2001)

2.2. Simulation Methods

Three different approaches can be used to simulate ground motion generated by an earthquake. A fourth approach which is a combination of the three approaches is also available. Stochastic simulation is the first approach which is used to simulate high frequency ground motion while deterministic approach is the second one for simulating

low frequency motion. Third one is Empirical Green's function method. Hybrid method is a combination of these three methods, taking the advantage of them.

2.2.1. Stochastic Method

As mentioned before, high frequency accelerations are very incoherent, and they result from rupture irregularities, heterogeneous co-seismic slip distribution and irregularity of the fault geometry, propagation transfer, and abrupt changes in rupture velocity and slip amplitude. It is not possible to know and predict these irregularities and hence, which is why it is difficult to model them by deterministic method. Thus, the use of stochastic models account for the incoherence of ground accelerations in strong ground motion simulations. The work of Hanks and McGuire (1981) forms the basis of the stochastic method. Hanks and McGuire (1981) combined seismological models of the spectral amplitude of ground motion with the engineering approach that high-frequency motions are intrinsically random (Hanks and McGuire, 1981). Filtering and windowing the white-noise time series in accordance with seismologically determined average spectra and duration is traditionally accomplished in stochastic simulation (Boore, 1983). This is a common and practical method for simulating higher-frequency motions; nevertheless, it lacks low frequency information.

2.2.2. Deterministic Method

A variety of methods have been used to achieve deterministic simulation of strong ground motion. Virtually, in all of these deterministic methods, the source function is convolved with synthetic Green's functions in order to produce the motion at ground surface. Discrete wave-number method, three-dimensional finite difference method, indirect boundary element method, modal summation method, ray theory, 2.5-D discrete wave number-boundary integral equation method, 2.5-D pseudo spectral method, and 2.5-D finite difference method are some of the deterministic methods.

2.2.3. Empirical Green's Function Method

The general concept of the empirical Green's function method (Hartzell, 1978) is to account for realistic path and site effects by using observed records of so-called subevent small earthquakes originating within the rupture area of the simulated large earthquake, which can individually represent heterogeneities, asperities, etc. For the validity of this approach, all subevents must have focal mechanisms similar to that of the simulated main event. That is, empirical Green's function methods use micro earthquakes as point dislocation Green's functions, assuming that the focal mechanisms and propagation paths of the small and large earthquakes are identical. The method is valid up to the corner frequency of small earthquakes used in the simulation of large earthquakes, and depends on the availability of micro earthquake data.

Since the method utilizes real recordings associated with a subsection of a fault, small event data already contain all the information about the physical processes involved in the problem, such as source effects, seismic energy radiation, anelastic wave propagation, scattering by random heterogeneities, the effect of the Earth's surface, and local site effects. The main shock or a future large event expected on the fault is found by moment scaling of small events, correction for radiation pattern, introducing a lag time for modeling of rupture propagation along the fault, and possibly a correction for site conditions if the original data are from sites with different site conditions (Erdik and Durukal, 2002).

2.2.4. Hybrid Method

It is not possible to extend deterministic predictions into the frequency regions above 3- 4 Hz, because the heterogeneities in the fault rupture, which are impossible to be accounted through a deterministic manner, control high frequency ground motions. Thus, either the stochastic source models or the stochastic treatment of the high frequency component of the ground motion is necessary for this. Hence, in order to simulate strong ground motion, hybrid methods are developed. Thereby, ground motions are computed separately in the short and long period ranges, and they are combined into a single time history using matched filters. It is thought that the transition from the deterministic to

stochastic behavior is associated with source radiation and wave propagation conditions, which are coherent at long periods and incoherent at short periods. There are several hybrid techniques proposed. The finite fault methodology of Hartzell and Heaton (1983) was combined by Wald *et al*. (1997) for long period deterministic simulation of ground motion with actual acceleration recordings. The low frequency part was simulated by Papageorgio *et al*. (1997) with the use of the discrete wave number method of Bouchon (1979). Besides, Papageorgio *et al*. (1997) used an empirical Green's function method in order to simulate intermediate and high frequencies, and superposed the two. Moreover, low frequency motions for point sources are calculated numerically by Irikura and Kamae (1996), who found corresponding high frequency motions following Boore (1983). Irikura and Kamae (1996) combined the two and determined ground motions caused by a large earthquake by summing these hybrid Green's functions with regard to the empirical Green's function method. A similar study was made by Pitarka *et al*. (2000) who added the effect of radiation pattern to the stochastic Green's function. Hutchings *et al*. (1997) combined synthetic Green's functions computed by Kennett's (Kennett, 1983) reflectivity code through empirical Green's functions in order to synthesize strong ground motion along the Sanyi-Tungshih-Puli seismic zone. The hybrid broadband simulation procedure adopted by Pitarka *et al*. (2000) involves the source as an empirical source time function. A theoretical representation of radiation pattern, rupture directivity and wave propagation effects are included in Green's function computations to achieve low frequency simulation. Stochastic techniques are used for higher frequency simulations.

3. INFORMATION ABOUT GEMLIK EARTHQUAKE, MARMARA REGION, STATIONS AND SITE INVESTIGATION

3.1. Information about Gemlik Earthquake

Gulf of Gemlik Earthquake occurred at the west of Iznik Lake and south of the Armutlu Peninsula on October 24, 2006 had a moment magnitude of 4.8 with 20 km depth (according to determination of KOERI). Gemlik Earthquake was recorded by nine BYTNet stations (BYT01, BYT02, BYT04, BYT05, BYT06, BYT07, BYT08, BYT11 and BYT12).

Moment tensor solutions for Gemlik Earthquake were obtained from web page http://www.emsc-csem.org/index.php?page=current&sub=rawmt&id= GASU9 via European-Mediterranean Seismological Centre (EMSC). EMSC moment tensor solutions are provided by ETHZ (Swiss Seismological Service Institute of Geophysics, ETH-Zurich), KOERI (Kandilli Observatory and Earthquake Research Institute), NOA (National Observatory of Athens Institute of Geodynamics), and INGV-MEDNET (Istituto Nazionale di Geofisica e Vulcanologia) as presented in Table 3.1 and depicted in Figure 3.1. Figure 3.1 was downloaded from web page of EMSC (http://www.emsc-csem.org/index.php?page=current&sub=indepth&id=OF512;INFO).

Table 3.1. Moment tensor solutions provided by ETHZ, KOERI, NOA and INGV-MEDNET

EMSC Moment Tensor Solutions		ETHZ	KOERI	NOA	INGV-MEDNET
GULF OF GEMLIK EARTHQUAKE Date (10/24/2006)		14:00:20.8	14:00:21	14:00:21	14:00:37
Coordinates of the epicenter	Latitude	40.40N	40.421N	40.52N	40.32N
	Longitude	29.00E	28.996E	29.24E	28.25E
Depth(km)		25	20	5	12
Moment Magnitude		$M_w = 5.15$	$M_w = 4.78$	$M_w = 5.10$	$M_w = 4.9$
Plane	Strike	250	316.83	125	226
	Dip	32	86.55	40	69
	Rake	-144	156.91	-30	-179

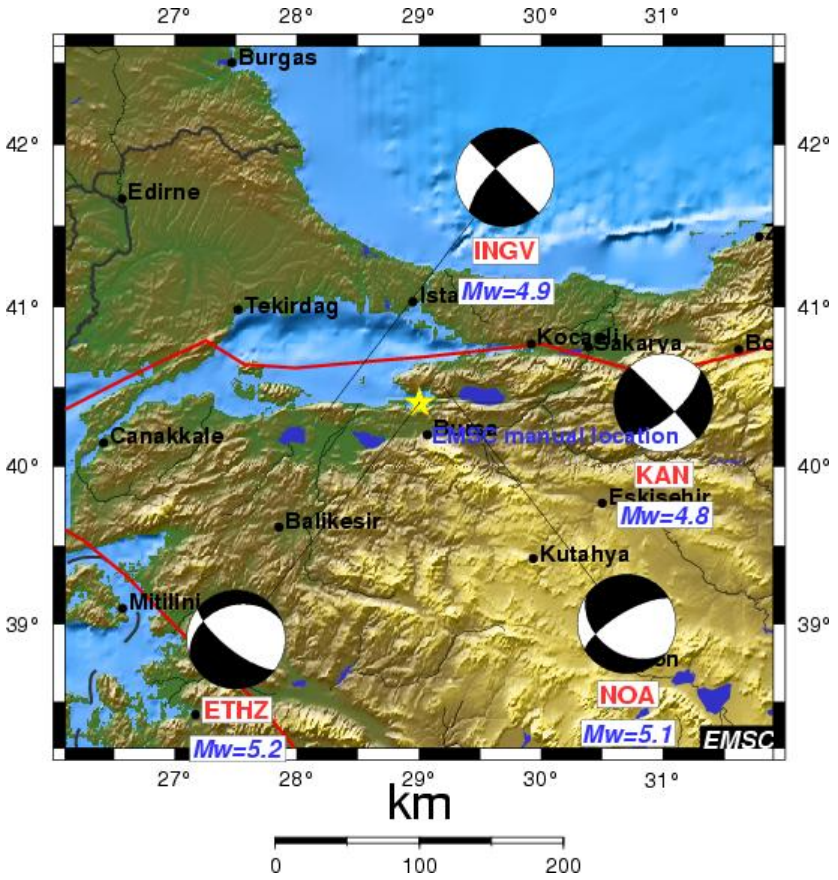

Figure 3.1. EMSC moment tensor solutions

In a study by some geophysicists of Kocaeli University (Irmak *et al*., 2007) focal mechanism was given as strike-slip, strike 14, dip 71 and rake -12. As it is going to be described in the next section test simulations were performed by using the focal mechanisms determined by KOERI and Kocaeli University geophysicists (Irmak *et al*., 2007) and real record figures and synthetic figures drawn after simulations were compared. As a result of this comparison scenario simulations were started taking the focal mechanism proposed by KOERI as basis.

For Gemlik Earthquake recorded by nine BYTNet stations, Band-pass filtering was applied to the records for the frequency intervals [0.5-2] Hz and [1-5] Hz. Instantaneous and sharp peaks were investigated in a short time interval of the records through the plots produced with these frequency intervals. As it is known, in short time interval hard grounds give instantaneous and sharp peaks. It is wanted to obtain information by looking at the general trends of the plots. Instantaneous and sharp peaks in short time intervals cannot be observed for soft grounds. Given in Appendix A are the figures generated with

the data of Gemlik Earthquake which were band-pass filtered for [0.5-2] and [1-5] Hz. intervals. In these figures, X and Y axes show the time (sec) and numerical values belonging to acceleration in cm/s^2, velocity in cm/s and displacement in cm, respectively.

3.2. Information about Marmara Region

Since there is not information in the literature about the tectonic properties, seismicity and hazard assessment for the region of Armutlu Peninsula, information about the Marmara Region is going to be given. In the prospect of the studies performed in the Marmara Region, it has been tried to obtain a general knowledge about the region where Gemlik Earthquake occurred.

3.2.1. Tectonic Properties of the Marmara Region

Western portion of the North Anatolian Fault Zone (NAFZ) controls the tectonic regime in the Marmara region. West of 31.58E toward the Marmara Sea region (Mudurnu/ Akyazı) the NAFZ begins to loose its single fault line character and splays into a complex fault system. Based on low-resolution bathymetric data and earthquake occurrences, several researchers have developed different tectonic models for Marmara Sea (Pinar, 1943; Barka and Kadinsky-Cade, 1988; Crampin and Evans, 1986).

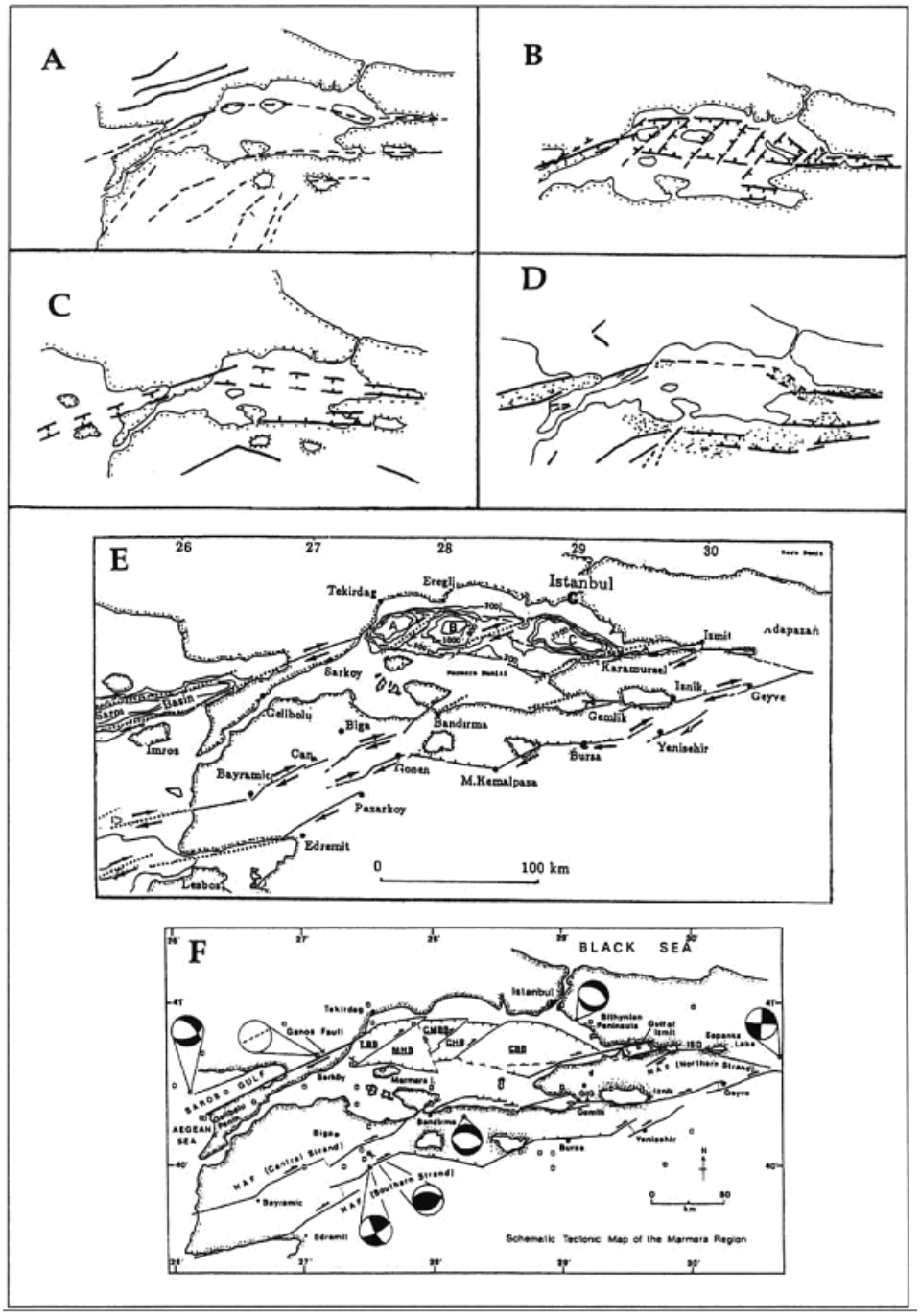

Figure 3.2. Comparison of the structural models suggested for the Marmara Region (Erdik *et al*., 2004)

The active tectonic map of the region prepared by the General Directorate of Mineral Research and Exploration (MTA) Turkey is given in Figure 3.3. Le Pichon *et al*. (1999) developed a fault model based on the data collected in 1997 by the ship 'MTA Sismik-1'. Data obtained during the recent high-resolution bathymetric survey of the Ifremer RV Le Suroit vessel indicates that a single, thoroughgoing strike-slip fault system

(Main Marmara Fault) cuts the Marmara Sea from east to west joining the 17.8.1999 Kocaeli earthquake fault with the 9.8.1912 Şarkoy-Mürefte earthquake fault (Le Pichon *et al*., 2001) as in Figure 3.4.

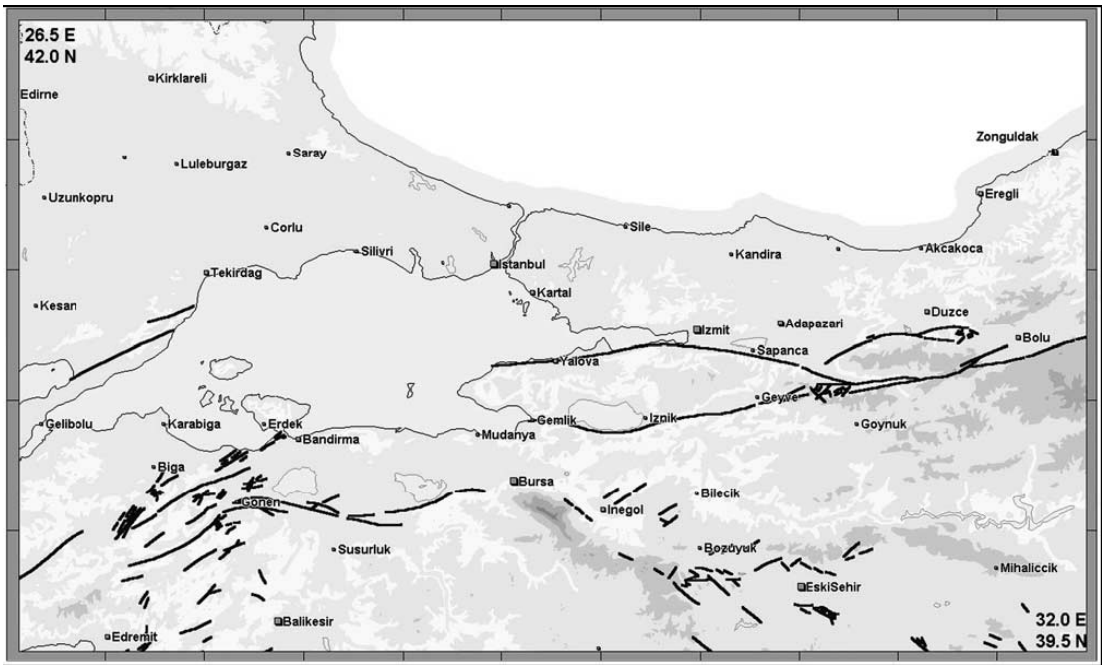

Figure 3.3. Active fault map of the region (Erdik *et al*., 2004)

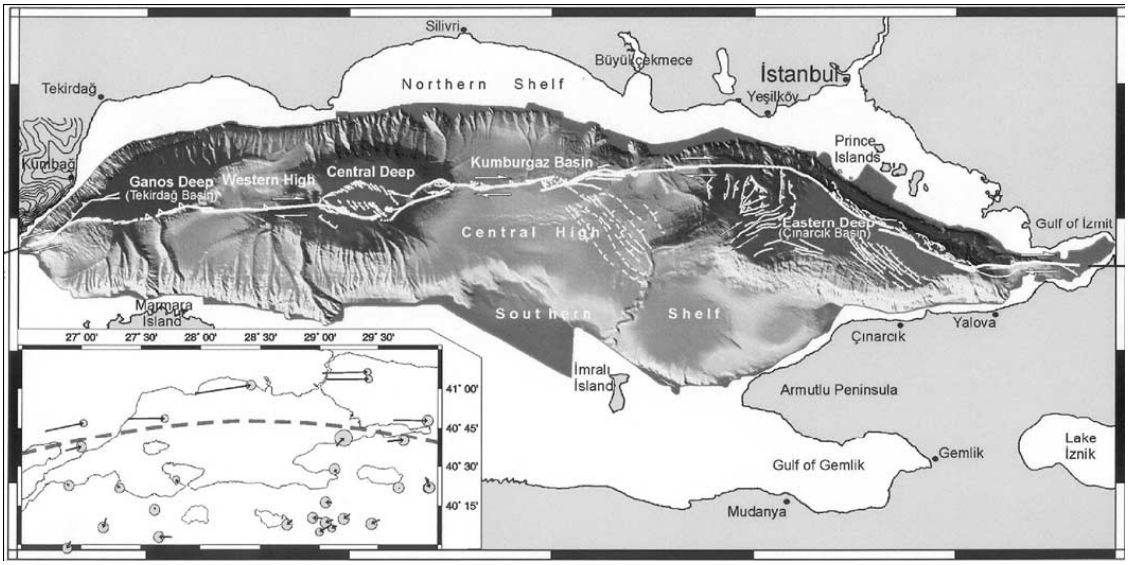

Figure 3.4. High-resolution bathymetric map obtained from the survey of the Ifremer RV Le Suroit vessel that indicates a single, thoroughgoing strike-slip fault system (Le Pichon *et al*., 2001)

Building upon and reinterpreting the extensive studies conducted, the tectonic evolution of the Marmara Sea region is defined as the superposition of two different aged fault systems. These are the early Miocene–early Pliocene Thrace–Eskişehir Fault Zone and its branches and the late Pliocene–recent NAF and its branches. The northwest–southeast trending Thrace–Eskişehir fault is a major dextral strike-slip system, which was active during the early Miocene–early Pliocene. It has been divided into four parts by the NAF at the end of the late- Pliocene. This event marked the initiation of the late neotectonic period. During that period the NAF extended westward as a number of splays by joining the Ganos, Bandırma–Behramkale and Manyas–Edremit Fault Zones. The connection of the northern branch of the NAF to the Ganos Fault Zone in the west caused the development of a single buried fault in the Marmara Sea and the formation of the troughs and ridges, superimposed onto the negative flower structure formed by the Ganos fault in the early neotectonic period. The middle strand extends East–West from Iznik Lake to Bandırma and connects to the N608E-trending Bandırma–Behramkale zone and turns southward near Bandırma. The southern branch of the NAF connects to the Manyas–Edremit Fault zone, forming three pull-apart basins along Yenişehir, Bursa and Manyas segments. The branches of the NAF cut the Thrace-Eskişehir fault at three places: the East Marmara Sea region, in Gemlik Bay and to the East of Bursa. The lateral offsets at those locations which amount to 58–59, 7–8 and 10–11 km respectively give a clear idea about the relative displacements and slip rates along each of the three branches of the NAF in the Marmara Sea region. Based on recent findings it has been developed a fault segmentation model for the Marmara Sea region. This model is based on the tectonic model of the Marmara Sea, defining the Main Marmara fault, a thoroughgoing dextral strike-slip fault system, as the most significant tectonic element in the region.

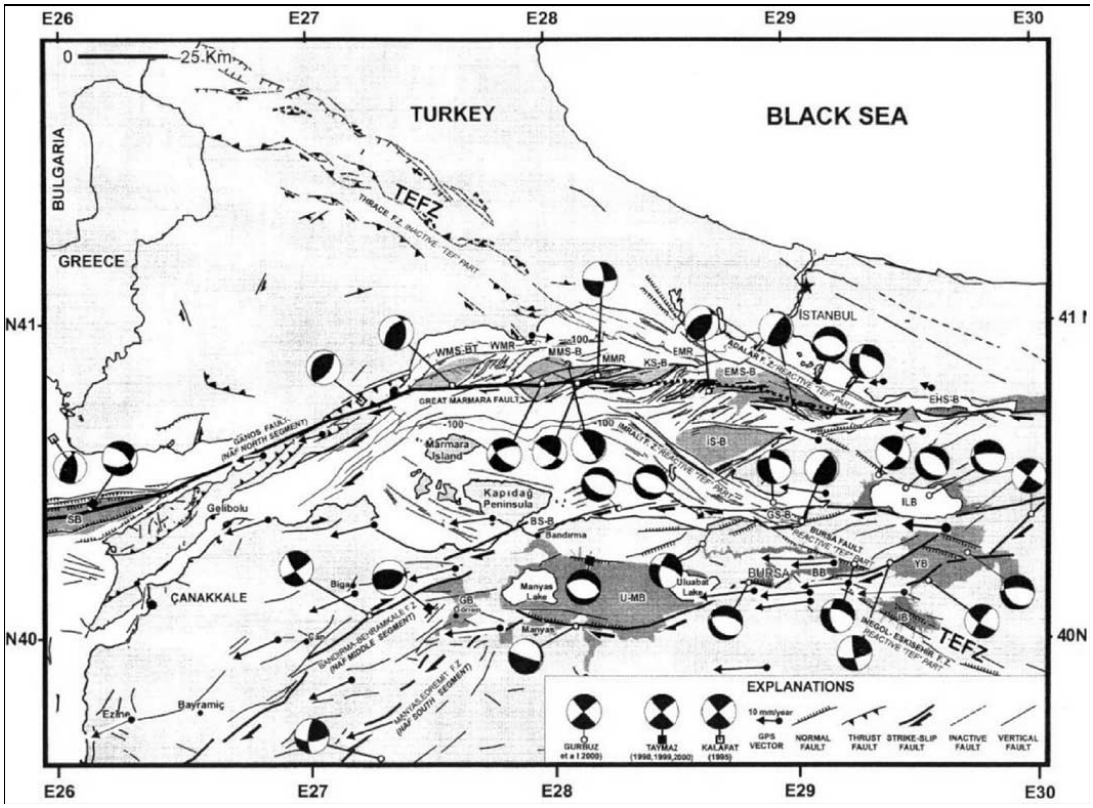

Figure 3.5. Tectonic map of Marmara region compiled from various studies (Yaltırak, 2002)

The segmentation provided relies on (Le Pichon *et al*., 2001) discussion of several portions of the Main Marmara Fault based on bathymetric, sparker and deeptowed seismic reflection data and interprets it in terms of fault segments identifiable for different structural, tectonic and geometrical features. From east to west the Main Marmara fault cuts through Çınarcık, Central and Tekirdağ basins, which are connected by higher lying elements. The fault follows the northern margin of the basin when going through the Çınarcık trough in the northwesterly sense, makes a sharp bend towards west to the south of Yeşilkoy, entering central highs, cuts through the Central basin and alternates in this manner until it reaches the 1912 Mürefte–Şarköy rupture.

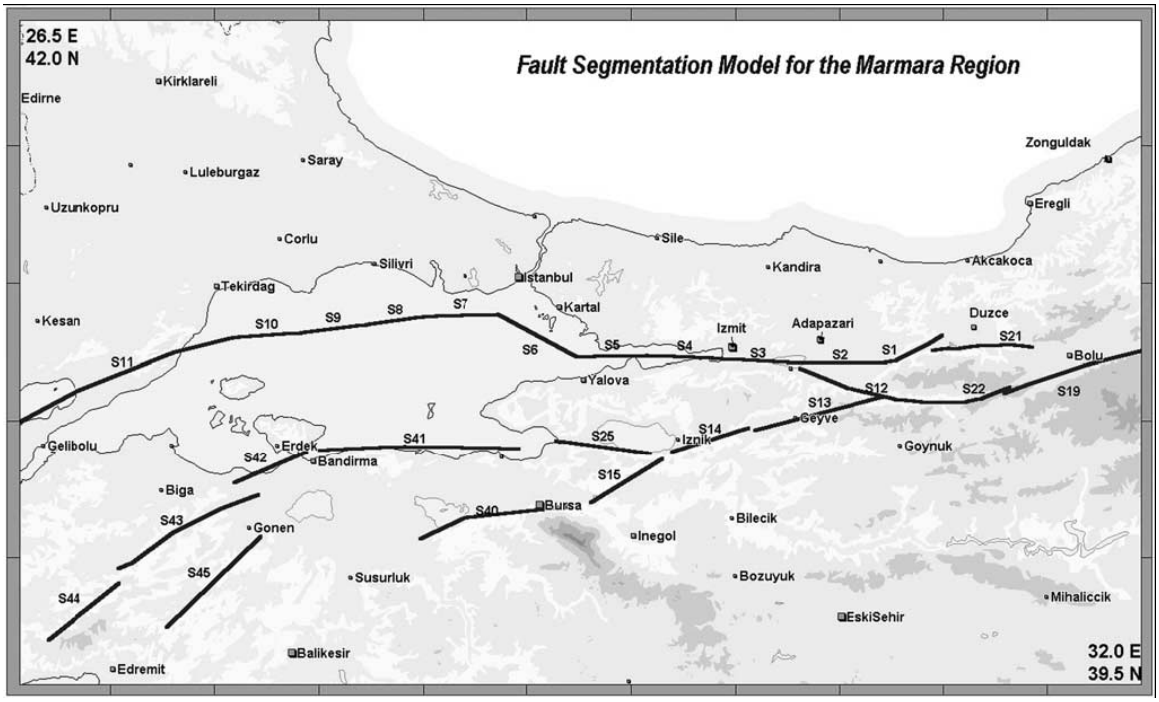

Figure 3.6. Fault segmentation model proposed for the Marmara region (Erdik *et al*., 2004)

3.2.2. Seismicity of the Marmara Region

For more than two millennia the Marmara region has been the crossroads between east and west. Being a continuously populated region and having as its center Istanbul, the capital of both Byzantine and Ottoman empires, the historical seismic records are continuous and assumed to be complete (Erdik *et al*., 2004). The long-term seismicity of the Marmara region is illustrated in Figure 3.7. Earthquake records spanning two millennia indicate that, on average, at least one medium intensity (I_0= VII–VIII) earthquake has affected Istanbul in every 50 years. The average return period for high intensity (I_0=VIII–IX) events has been 300 years. Ambraseys (2002) states that: there has not been any earthquake that ruptured the entire length of the Main Marmara Fault from Gulf of İzmit to Gulf of Saros; the seismicty accounts for all of the expected 2.2 cm/year slip and; there is a time dependence of seismic activity that should be accounted in earthquake hazard assessments.

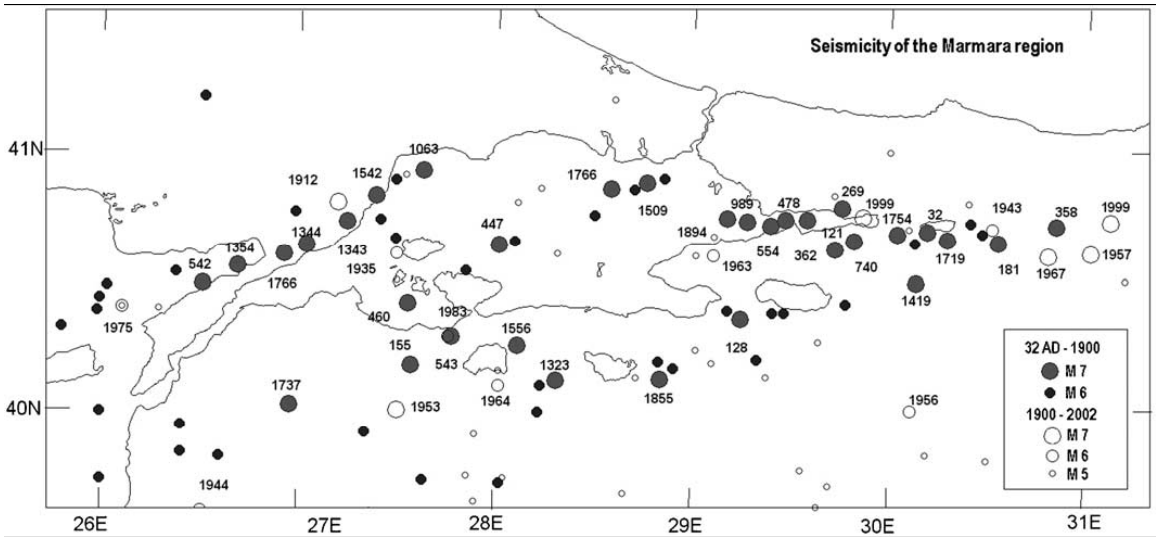

Figure 3.7. The long-term seismicity of the Marmara region (Erdik *et al*., 2004)

Recent studies conducted after the 1999 Kocaeli (M_w = 7.4) and Düzce (M_w = 7.2) earthquakes indicate (assuming that the stress regime in the Marmara Sea remains unchanged) about 65 per cent probability for the occurrence of an $M_w \geq 7$ magnitude earthquake affecting Istanbul which is the most critical region. The earthquake damage experienced by regional cities as well as by the historical structures in Istanbul has been well documented. It is known that the 1470-year old Hagia Sophia Museum was strongly and repeatedly affected by the earthquakes that took place in the region and was subsequently repaired after every damaging earthquake. Compared to seismic activity in the Marmara region during the past two millennia, the 20th century has been relatively active with five earthquakes of Ms ≥ 7.0 (9.8.1912 Ms = 7.3, 18.3.1953 Ms = 7.1, 26.5.1957 Ms = 7.2, 22.7.1967 Ms = 7.2 and 17.8.1999 Ms = 7.4) (Erdik *et al*., 2004). The association of earthquakes between 1500 to present with the segmentation proposed for the North Anatolian Fault in the Marmara Region is given in Table 3.2.

Table 3.2. Association of earthquakes between 1500-present with the segmentation proposed for the North Anatolian fault in the Marmara region (Erdik *et al*., 2004)

Earthquake	Fault Segment
10.9.1509 (Ms= 7.2)	7, 8
10.5.1556 (Ms= 7.2)	9
25.5.1719 (Ms= 7.4)	2, 3, 4, 5
6.3.1737 (Ms= 7.2)	43
2.9.1754 (Ms= 6.8)	6
22.5.1766 (Ms= 7.1)	7, 8
5.8.1766 (Ms= 7.4)	11
28.2.1855 (Ms= 7.1)	40
10.7.1894 (Ms= 7.3)	3, 4, 5
9.8.1912 (Ms= 7.3)	11
1.2.1944 (Ms= 7.3)	19
18.3.1953 (Ms= 7.2)	45
26.5.1957 (Ms= 7.0)	22
22.7.1967 (Ms= 6.8)	12
17.8.1999 (Mw= 7.4)	1, 2, 3, 4
12.11.1999 (Mw= 7.2)	21

In the Marmara region, there exist some potential seismic gaps. For example, along the middle strand from the Mudurnu Valley region to the Aegean Sea there has not been any significant earthquake for the last 400 years, except the 1737 earthquake in the Biga peninsula (Erdik *et al*., 2004). The most western portion of the southern strand has not ruptured since 1855. Maps of recent seismicity indicate a potential seismic gap in the central part of the Marmara Sea. Ambraseys and Jackson (2000), based on the absence of large, damaging earthquakes along the northern shore of the Marmara Sea, define this area as seismically quiet. The rupture associated with the Kocaeli earthquake leaves the only remaining gap across the Marmara Sea, to the south of Istanbul. This gap is well defined and corresponds to the location of the 1766 earthquake. This implies increased probabilities for a strong earthquake similar to the 1766 event. Recent paleoseismological studies indicate that the surface rupture of this event extended towards Düzce, thus having a similar geometry with the August 17, 1999 event (Erdik *et al*., 2004).

The 1995 microseismic experiment conducted in the Marmara region (Polat *et al*., 2002) has shown a lineament in coincidence with the location of the main Marmara fault. The alignment of the Marmara Fault is also clearly evident in Figure 3.8, where respectively the epicentral distribution of earthquakes with M > 3 from 17.08.1999 to

present is illustrated. There exists a seismic gap associated with segments S6, S7 and S8 (Figure 3.6) that correspond to ruptures associated with 1754 and 1766 earthquakes. The existence of these seismic gaps was also confirmed by the results of the microseismic experiment carried out in the Marmara region by Gurbuz *et al*. (2000).

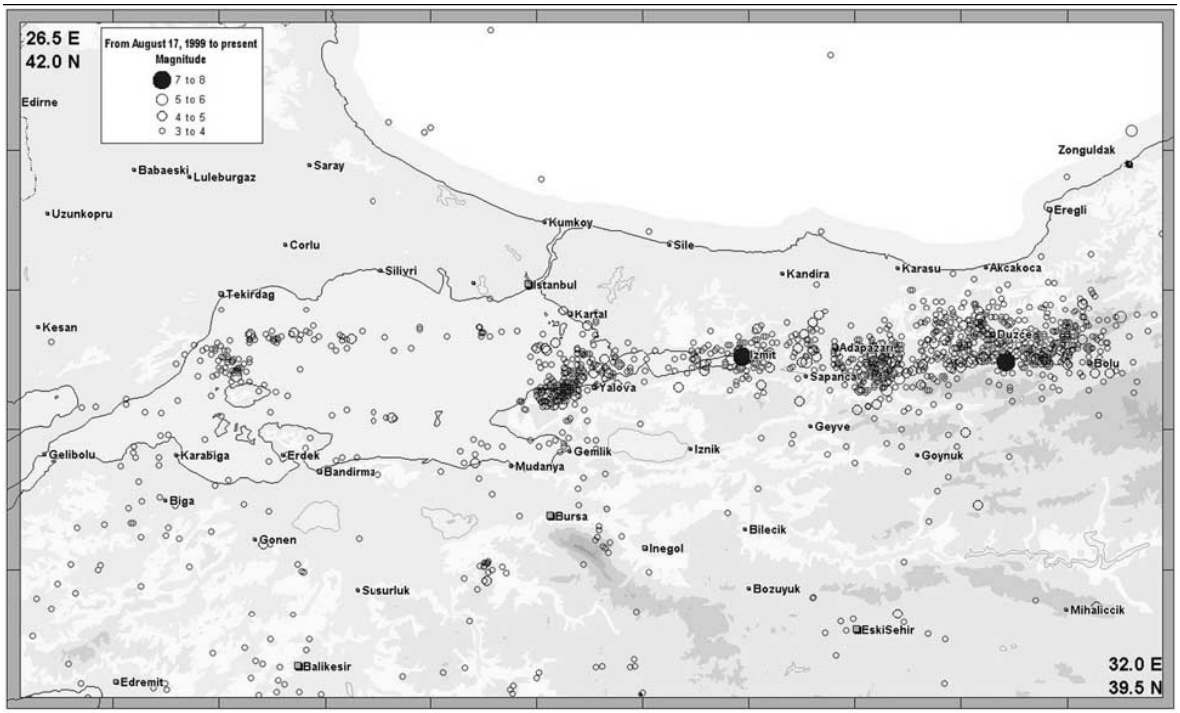

Figure 3.8. The seismic activity of the Marmara region with M > 3 events from August 17, 1999 to present (Erdik *et al*., 2004)

In Figure 3.9, epicenters of all events with M ≥ 1 are plotted for the last 10 years. Most of the small events on the Thrace peninsula seen in Figure 3.9 to the north of the main Marmara Fault are associated with rock blasts (Erdik *et al*., 2004). Clusters of seismic activity in Yalova and Gulf of Izmit are mainly the aftershocks of 1999 earthquake. The activity in the Marmara Sea stops at the west of Gazikoy in the Gelibolu Peninsula forming a seismic gap at the location of the 1912 earthquake.

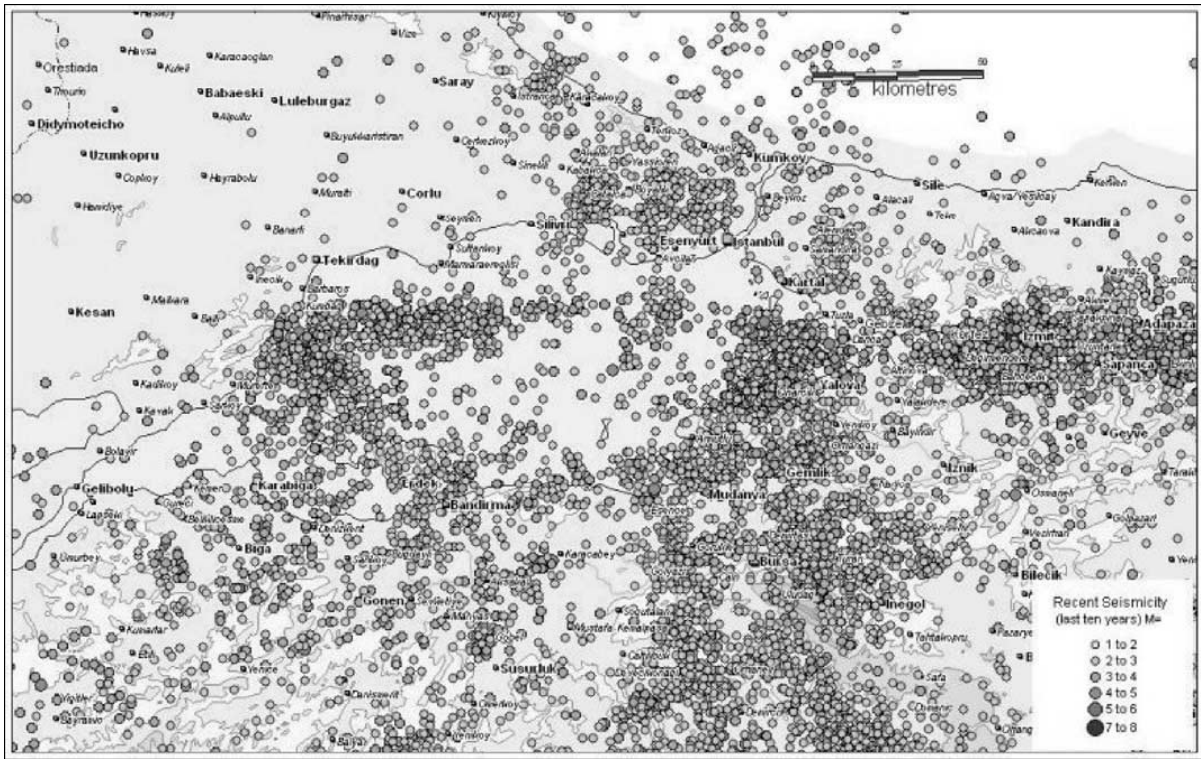

Figure 3.9. The seismic activity of the Marmara region with M ≥ 1 events between 1994 and 2004 (Erdik *et al*., 2004)

Some cluster of seismic activity exists to the south of the Iznik Lake on the middle branch of the North Anatolian Fault. The southern branch of the North Anatolian Fault shows a rather diffuse activity in the vicinity of Bursa.

An earthquake of magnitude M_w 7.4 occurred on the NAFZ with a macroseismic epicenter near the town of Golcuk (40.702 N, 29.987 E) in the western part of Turkey on 17 August 1999. The total observable length of the rupture was about 100 km. The lateral offset varied between 1.5 and 5 m. Most of the aftershock activity is confined to the region bounded by 40.5–40.8N and 29.8–30.0E, which covers the area between Izmit and Adapazari to the east of the epicenter. Seismic imaging of the Kocaeli earthquake rupture indicates almost pure lateral strike-slip rupture that runs west at a velocity of about 3 km/s and towards east at a very high velocity of 4.7 km/s for a distance of about 40 km before dropping to about 3.1 km/s at the easternmost segment (Erdik *et al*., 2004). The largest slip, 7 m, occurred between 25 and 45 km east of the epicenter. At west of the epicenter the slip is large between distances of 10–30 km. The rise time is generally between 2–4 s.

The damage caused by the earthquake covered a very large region extending from Tekirdağ to Eskişehir, cities mostly affected being Sakarya, Yalova, Kocaeli, Bolu and Istanbul. The intensively damaged area follows a zone of about 20 km in width (10 km to the north and south of the fault) along the fault rupture. The numbers of condemned buildings after the earthquakes are declared as 23,400. 18,373 persons were killed and 48,901 injuries occurred. 120,000 families were left in need of homes after the earthquake. The maximum MSK intensity of the Kocaeli earthquake was X, essentially assigned on the basis of fault rupture and excessive ground deformations.

This earthquake is associated with fault segments 1, 2, 3 and 4 (Erdik *et al*., 2004). Location of these segments is shown in Figure 3.6. That earthquake generated six motions within 20 km of the fault (Sakarya, Yarımca, İzmit, Düzce, Arçelik, and Gebze), adding significantly to the near-field database of ground motions for $M_w \geq 7.0$ strike-slip earthquakes. According to Polat *et al*. (2002) the rupture propagation to the west was relatively homogenous with a rupture velocity of about 3.5 km/s. To the east, however, the fault within the first 7.5 s of the process ruptured slower than it did on the west, afterwards accelerating to velocity levels of 3.5 km/s and thus contributing to the high amplitude motion observed at Sakarya station. According to Delouis *et al*. (2002) the rupture reached the speed of about 4.8 m/s at this portion of the fault. As indicated in the source rupture models developed for the earthquake, the directivity effects may have contributed to damage in Yalova and Çınarcık. 'Fling' type pulses due to directivity effects are evident in the strong motion data of the Kocaeli earthquake with fling durations in the order of 2–3 s (Erdik *et al*., 2004). The Ambarli region to the west of Istanbul recorded unusually large accelerations.

3.2.3. Earthquake hazard in Marmara Region

Earthquake hazard in the Marmara Region has been investigated using time-independent probabilistic (simple Poissonian) and time-dependent probabilistic (renewal) models (Erdik *et al*., 2004).

In this study, it is acted in thought of dealing with fault segments which go along from Gemlik to Bandırma and go along the south of Iznik Lake to Gemlik (S41 and S25). As it can be seen in the Figure 3.6, S25 fault directs to the north-west. It can be shown

that strike is 316.83 if the focal mechanism of Gemlik Earthquake (M_w=4.8) determined by KOERI is checked. This gives the indications that S25 fault and believed to be its continuation S41 fault conform to the focal mechanisms determined by KOERI. Strike angle corresponds to 316.83 north-west direction measured from north in clockwise direction.

According to the results of time dependent probabilistic hazard assessments for Turkey, the middle strand of the North Anatolian Fault (NAF) which passes through Iznik Lake to Bandirma has been found to be capable of producing the second highest hazard rate (PGA: 0.4-0.6g for bedrock) in the Marmara Region as compared to the Northern strands in Marmara Sea with the highest rate. As clarified in Table 3.3, the fault segment corresponding to S41 fault extending between Gemlik-Bandirma and the segment corresponding to S25 fault passing through the southern part of Iznik Lake have potentials of producing a magnitude 7.2+ event with 1000 year recurrence time (Erdik *et al*., 2004). For future risk mitigation strategies it is necessary to prepare scenario earthquakes so as to understand the complexity of the ground shaking to be expected in a future earthquake, since the concerned area accommodates dense urban and industrial areas.

Table 3.3. Poisson and renewal model characteristic earthquake parameters associated with the segments (Erdik *et al*., 2004)

Segment	Last characteristic earthquakes	'cov'	Mean recurrence time	Char. magnitude	Time since last char. eq.	Time dependent (renewal)		Poissonian
						50 year prob.	Annual rate	Annual rate
1	1999	0. 5	140	7. 2	3	0. 0344	0. 0007	0. 0071
2	1999	0. 5	140	7. 2	3	0. 0344	0. 0007	0. 0071
3	1999	0. 5	140	7. 2	3	0. 0344	0. 0007	0. 0071
4	1999	0. 5	140	7. 2	3	0. 0344	0. 0007	0. 0071
5	1894	0. 5	175	7. 2	108	0. 3723	0. 0093	0. 0057
6	1754	0. 5	210	7. 2	248	0. 4095	0. 0105	0. 0048
7	1766	0. 5	250	7. 2	236	0. 3374	0. 0082	0. 0040
8	1766	0. 5	250	7. 2	236	0. 3374	0. 0082	0. 0040
9	1556	0. 5	200	7. 2	446	0. 4191	0. 0109	0. 0050
10	Unavailable	0. 5	200	7. 2	1000	0. 3340	0. 0081	0. 0050
11	1912	0. 5	150	7. 5	90	0. 4206	0. 0109	0. 0067
12	1967	0. 5	250	7. 2	35	0. 0203	0. 0004	0. 0040
13	Unavailable	0. 5	600	7. 2	1000	0. 1771	0. 0039	0. 0017
14	Unavailable	0. 5	600	7. 2	1000	0. 1771	0. 0039	0. 0017
15	Unavailable	0. 5	1000	7. 2	1000	0. 0974	0. 0020	0. 0010
19	1944	0. 5	250	7. 5	58	0. 0597	0. 0012	0. 0040
21	1999	0. 5	250	7. 2	3	0. 0012	0. 0000	0. 0040
22	1957	0. 5	250	7. 2	45	0. 0347	0. 0007	0. 0040
25	Unavailable	0. 5	1000	7. 2	1000	0. 0974	0. 0020	0. 0010
40	1855	0. 5	1000	7. 2	147	0. 0006	0. 00001	0. 0010
41	Unavailable	0. 5	1000	7. 2	1000	0. 0974	0. 0020	0. 0010
42	Unavailable	0. 5	1000	7. 2	1000	0. 0974	0. 0020	0. 0010
43	1737	0. 5	1000	7. 2	265	0. 0086	0. 0002	0. 0010
44	Unavailable	0. 5	1000	7. 2	1000	0. 0974	0. 0020	0. 0010
45	1953	0. 5	1000	7. 2	49	Unavailable	Unavailable	0. 0010

3.3. Information about Stations

3.3.1. Strong Motion Network

Occurrence of the major Marmara and Bolu earthquakes in Turkey during 1999 has brought the importance of strong motion seismology into renewed focus. The need for better acceleration records to be used in earthquake engineering applications was realized once again after these destructive earthquakes. Although Turkey is an earthquake country, there is still an inadequate number of seismological and strong earthquake motion recording stations. When the intensity of earthquake activity and the land area of Turkey are considered, it can easily be said that Turkey has a very sparse strong ground motion network (Figure 3.10). Figure 3.10 was obtained from web page of General Directorate of Disaster Affairs Earthquake Research Department (http://angora.deprem.gov.tr/BYTNet/smamap.gif). Some "early warning" networks, which are built in Istanbul, may only give information about ground motion intensity on a local basis. On the other hand, stations installed within or around a probable earthquake nucleating zone in a geometrical pattern will yield valuable information about the mechanism of the rupture, properties of the ground waves produced, attenuation relationships and spectral properties of a probable future earthquake in that area.

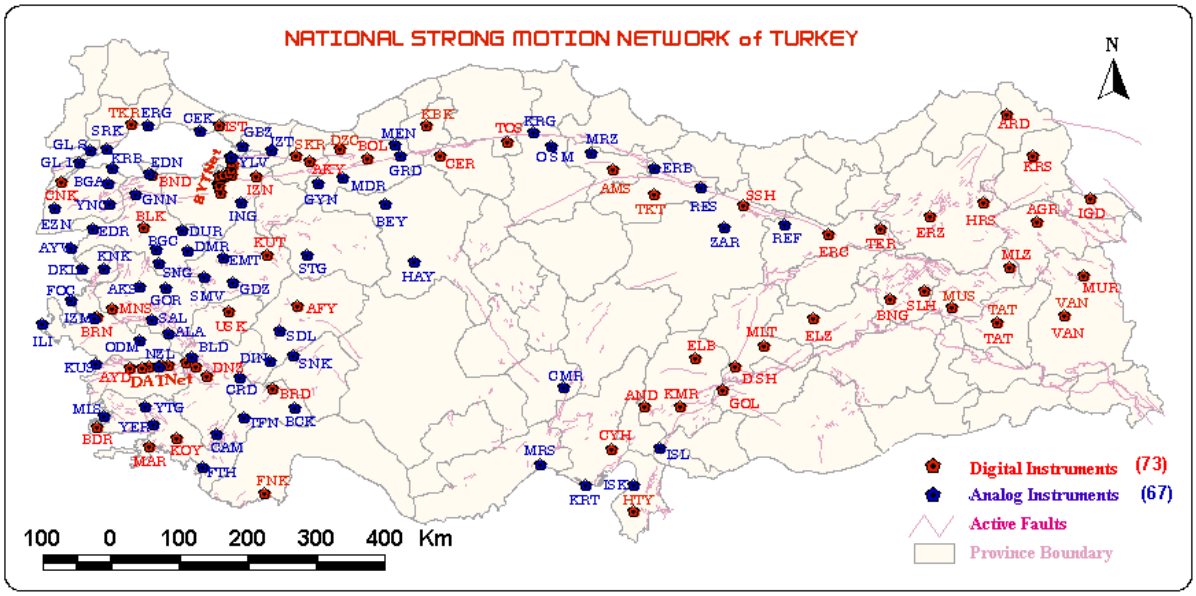

Figure 3.10. National Strong Motion Network of Turkey

Enhancement and modernization of the current Turkish National Ground Motion Network, which consists of about 140 instruments having different technologies, is very helpful for the studies on decreasing the damage of future earthquakes.

3.3.2. Information about BYTNet (Bursa – Yalova Turkey Accelograph Network)

BYTNet, local accelograph network, has been positioned near one of Turkey's active seismic regions in the Bursa – Yalova region. Stations have been positioned on the splitting western part of the North Anatolian Fault and on an axis traversing fault lines near Bursa in North-South direction (Figure 3.11). It consists of 14 Kinemetrics Etna instruments that have been emplaced in small structures specially built for recording free field acceleration within gardens of, or inside, one story public buildings (Figure 3.11). In Figure 3.11, map of BYTNet strong motion stations was obtained from web page of General Directorate of Disaster Affairs Earthquake Research Department (http://angora.deprem.gov.tr/BYTNet/BYTNetharita.htm). Names and coordinates of the stations are given in Table 3.4 downloaded from the web page of General Directorate of Disaster Affairs (http://angora.deprem.gov.tr/BYTNet/BYTNetistyer.htm).

Table 3.4. Names and coordinates of BYTNet stations

Station Code	Latitude, N	Longitude, E	Description of Station Location
BYT01	40,18249	29,12966	General Directorate of Rural Services 17th Regional Office
BYT02	40,22606	29,07522	Bursa Emergency Management Center
BYT03	40,27360	29,09611	Demirtas Town, Kirantepe
BYT04	40,36322	29,12221	Kurtul Village, Garden of the Mosque
BYT05	40,39431	29,09811	Gemlik Military Veterinary Training Command
BYT06	40,41039	29,17993	Umurbey Town, Celal Bayar Medical High School
BYT07	40,42510	29,16659	Gemlik Industrial Crafts Vocational School
BYT08	40,42223	29,29090	Cargill Agricultural Industries Factory
BYT09	40,44975	29,25869	Gedelek Medical Services Building
BYT10	40,49440	29,29976	Orhangazi Basic Education School
BYT11	40,56413	29,30600	Dogus Meat and Milk Company
BYT12	40,59648	29,27140	Sogucak Post Office
BYT13	40,65069	29,27900	Yalova Nursing Home for the Aged
BYT14	40,65753	29,24722	Yalova Atatürk Agriculture Works Directorate

Figure 3.11. BYTNet strong motion stations

Stations are located near residential areas for the ease of obtaining electricity and telephone lines. All of the stations are connected to METU and General Directorate of Disaster Affairs Earthquake Research Department's monitoring centers. Recordings made on all of the planned arrays are available to the world research community on the Internet.

Local ground conditions, wave velocities and geological profiles of most stations in Turkey are unknown. Further, a major part of those stations are placed inside buildings, and as a result they record the modified earthquake motion, affected by the motion of the building, rather than the true free field motion. Stations for the subject arrays are purposely placed on sites with different lithological properties. Some geological, geophysical and borehole tests (down to 30 meters) were performed on all sites by staff of the General Directorate and the ground profiles have been obtained. Also detailed investigations were made in order to obtain the ground profiles of the stations located in small huts. Both the records obtained and other information, which may be helpful for the researchers, are available.

The location of all BYTNet stations, S41 and S25 faults were placed on the map shown in Figure 3.12.

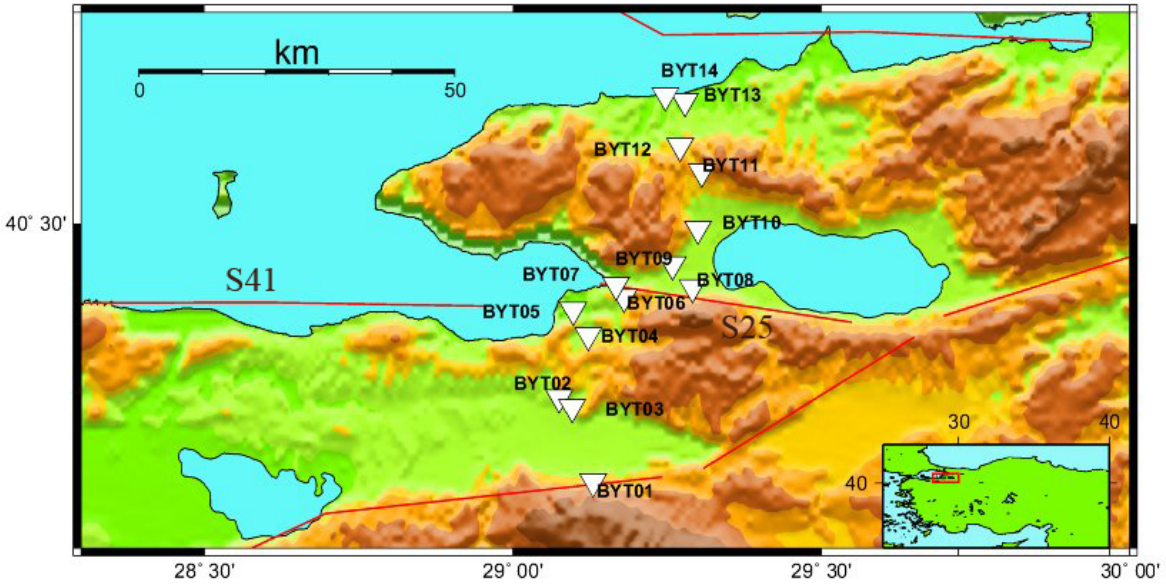

Figure 3.12. Location of BYTNet stations, fault S41 and S25

In NEHRP-2000 (http://www.bssconline.org/NEHRP2000/comments/provisions/), sites are classified as follows:

A- Hard rock with measured shear wave velocity $V_S \geq 1500$ m/s

B- Rock with (760 m/s < V_S < 1500 m/s)

C- Very dense soil and soft rock with (360 m/s < V_S < 760 m/s) or with either Standard Penetration $\overline{N} > 50$ or Average undrained shear strength at top 30 m Su ≥ 100 kPa

D- Stiff soil with (180 m/s < V_S < 360 m/s) or with either 15 < $\overline{N}$ < 50 or (50 kPa < Su < 100 kPa)

E- A soil profile with V_S < 180 m/s or with either $\overline{N}$ < 15, Su < 50 kPa or any profile with more than 3 m of soft clay defined as soil with PI > 20 and Su < 25 kPa

F- Soils requiring site-specific evaluations:

- Soils vulnerable to potential failure or collapse under seismic loading such as liquefiable soils, quick and highly sensitive clays, collapsible weakly cemented soils.
- Peats and/or highly organic clays with thickness $\bar{h}$ > 3 m of peat and /or highly organic clay
- Very high plasticity clays ($\bar{h}$ > 8 m with PI > 75)
- Very thick soft/medium stiff clays ($\bar{h}$ > 36 m)

Information about bore hole data and soil column of each BYTNet stations for 30 m is obtained from BYTNet web page. Soil columns belonging to each BYTNet stations for 30 m are indicated through Figure 3.13. Under this circumstance, average V_{S30} value for each BYTNet station can be calculated with the assistance of Equation 3.1. and sites pertaining to each station can be classified according to NEHRP-2000 as illustrated in Table 3.5.

$$V_{S30} = \frac{30}{\sum_{i}^{z} \frac{h_i}{V_{h_i}}} \tag{3.1}$$

where ;

V_{S30} : Average shear wave velocity for 30 m

h_i : Each soil column height

V_{h_i} : Shear wave velocity at each soil column height

Z : Number of soil columns

Table 3.5. Soil conditions and S-wave velocities of medium belonging to BYTNet stations

Stations	BYTNet web page Soil Condition	Calculation result Average V_{S30} (m/s)	Estimation Soil Condition(NEHRP)
BYT1	Rock	369	C
BYT2	Soft Soil	No information	–
BYT3	Hard Soil	570	C
BYT4	Soft Soil	338	D
BYT5	Soft Soil	279	D
BYT6	Soft Soil	299	D
BYT7	Soft Soil	274	D
BYT8	Soft Soil	462	C
BYT9	Hard Soil	503	C
BYT10	Rock	No information	–
BYT11	Hard Soil	No information	–
BYT12	Soft Soil	678	C
BYT13	Soft Soil	260	D

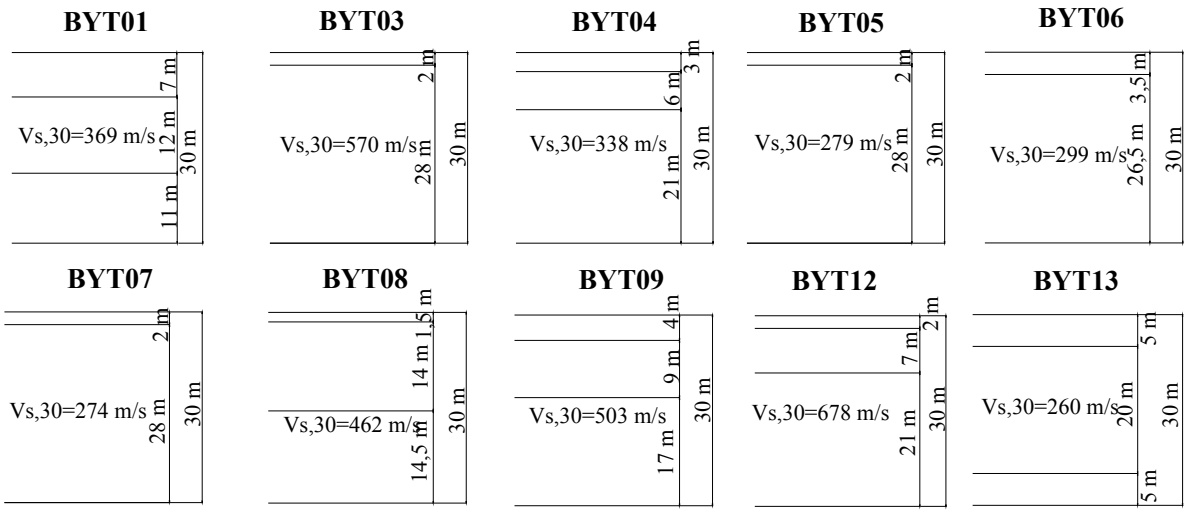

Figure 3.13. Soil columns pertaining to BYTNet stations for 30 m

Table 3.6. BYTNet station information of National Strong-Motion Network of Turkey (Part1)

No	City	Station Name	Station Code	Lat. (North)	Long. (East)	Altitude (m)	Opening Date	Number of bits	Amp. Max. (cm/s^2)	Timing System (Internal/GPS /DCF/TCG)	Acc. triggering level (cm/s^2)	Com. System
45	Bursa	Cargil	BYT08	40,422	29,291	20	2001	18	2500	GPS	1.25	Tlf
46	Bursa	Demirtaş	BYT03	40,274	29,096	180	2001	18	2500	GPS	1.25	Tlf
47	Bursa	Engürücük Köyü	BYT05	40,394	29,098	66	2001	18	2500	GPS	1.25	Tlf
48	Bursa	Gedelek Köyü	BYT09	40,450	29,259	211	2001	18	2500	GPS	1.25	Tlf
49	Bursa	Gemlik	BYT07	40,425	29,167	65	2001	18	2500	GPS	Threshold	Tlf
53	Bursa	Kurtul Köyü	BYT04	40,363	29,122	109	2001	18	2500	GPS	1.25	Tlf
54	Bursa	Merkez	BYT01	40,182	29,130		2001	18	2500	GPS	1.25	Tlf
55	Bursa	Merkez	BYT02	40,286	29,075	50	2001	18	2500	GPS	1.25	Tlf
57	Bursa	Orhangazi	BYT10	40,494	29,300	897	2006	11	1000	Int	1.25	Tlf
58	Bursa	Umurbey	BYT06	40,410	29,180	252	2001	18	2500	GPS	1.25	Tlf
167	Yalova	Merkez	BYT13	40,651	29,279	106	2001	18	2500	GPS	1.25	Tlf
168	Yalova	Merkez	BYT14	40,658	29,247	33	2001	18	2500	GPS	1.25	Tlf
169	Yalova	Soğucak Köyü	BYT12	40,596	29,271	181	2001	18	2500	GPS	1.25	Tlf
170	Yalova	Su Gören Köyü	BYT11	40,564	29,306	904	2001	18	2500	GPS	1.25	Tlf

Table 3.7.BYTNet station information of National Strong-Motion Network of Turkey (Part 2)

No	City	Station Name	Station Code	Lat. (North)	Long. (East	Interr. System	Sensor	Recording system	Samp. rate (bits)	Soil qualitative description	Instrument site
45	Bursa	Cargil	BYT08	40,422	29,291	MDU	Kinemetrics Episensor	Kinemetrics ETNA/PCMCIA	100	Ss	B10
46	Bursa	Demirtaş	BYT03	40,274	29,096	MDU	Kinemetrics Episensor	Kinemetrics ETNA/PCMCIA	100	Hs	FF
47	Bursa	Engürücük Köyü	BYT05	40,394	29,098	MDU	Kinemetrics Episensor	Kinemetrics ETNA/PCMCIA	100	Ss	FF
48	Bursa	Gedelek Köyü	BYT09	40,450	29,259	MDU	Kinemetrics Episensor	Kinemetrics ETNA/PCMCIA	100	Hs	B10
49	Bursa	Gemlik	BYT07	40,425	29,167	MDU	Kinemetrics Episensor	Kinemetrics ETNA/PCMCIA	100	Ss	FF
53	Bursa	Kurtul Köyü	BYT04	40,363	29,122	MDU	Kinemetrics Episensor	Kinemetrics ETNA/PCMCIA	100	Ss	FF
54	Bursa	Merkez	BYT01	40,182	29,130	MDU	Kinemetrics Episensor	Kinemetrics ETNA/PCMCIA	100	Rc	B10
55	Bursa	Merkez	BYT02	40,286	29,075	MDU	Kinemetrics Episensor	Kinemetrics ETNA/PCMCIA	100	Ss	FF
57	Bursa	Orhangazi	BYT10	40,494	29,300	MDU	Kinemetrics Episensor	Kinemetrics ETNA/PCMCIA	100	Rc	B20
58	Bursa	Umurbey	BYT06	40,410	29,180	MDU	Kinemetrics Episensor	Kinemetrics ETNA/PCMCIA	100	Ss	FF
167	Yalova	Merkez	BYT13	40,651	29,279	MDU	Kinemetrics Episensor	Kinemetrics ETNA/PCMCIA	100	Ss	FF
168	Yalova	Merkez	BYT14	40,658	29,247	MDU	Kinemetrics Episensor	Kinemetrics ETNA/PCMCIA	100	Ss	FF
169	Yalova	Soğucak Köyü	BYT12	40,596	29,271	MDU	Kinemetrics Episensor	Kinemetrics ETNA/PCMCIA	100	Ss	B50
170	Yalova	Su Gören Köyü	BYT11	40,564	29,306	MDU	Kinemetrics Episensor	Kinemetrics ETNA/PCMCIA	100	Hs	FF

Some abbreviations given in Table 3.7 and 3.8 were explained as follows:

(1)- ANALOG / DİGİTAL

Loc : Local (no communication system available)

Tlf : Telephone

Iline : Internet leased line

Stl : Satellite

(2)- MDU : Manual dial-up

ADU : Automatic dial-up

CT : Continuous, real time transmission

(3)- Ss : Soft soil

Hs : Hard soil

Rc : Rock

(4)- FF : Free Field

B αβ : Instrument in building

α : Total number of stories of the buildings (including ground floor)

β : Floor where the instrument is installed

3.4. Site Investigation

3.4.1. Introduction to method of Spectral Ratio between Horizontal and Vertical Components (H/V Ratio)

A technique using horizontal-to-vertical spectral ratios (H/V ratios) of the microtremors, which was first applied by Nogoshi and Igarashi (1970, 1971) and popularized by Nakamura (1989), has sometimes been used to estimate the site effects (Near-surface sedimentary deposits significantly amplify earthquake ground motion, which is often referred to as site effects). Several recent applications of this technique have proved to be effective in estimating fundamental periods (e.g., Field and Jacob, 1993; Ohmachi *et al*., 1994) as well as relative amplification factors (e.g., Lermo and Chavez-Garcia, 1994; Konno and Ohmachi, 1995). However, in the authors' opinion, the technique lacks a rigorous theoretical background still now (Konno and Ohmachi, 1998).

Several recent studies of microtremor recordings have been made to investigate the spectral ratio between the horizontal and vertical components (H/V ratio) (e.g., Nakamura, 1989). Nakamura (1989) suggest that this ratio is a good technique for site effect evaluation since it shows a peak which corresponds to the predominant frequency of the soil. It has also been shown that the predominant frequency of microtremors is dependent on the type of soil considered (rock, alluvium, etc.) (Bouckovalas and Krikeli, 1991; Finn, 1991). This clearly points to the fact that microtremors for microzonation studies could be used. Moreover, knowledge of the resonance frequency of the soil could be used in predicting the kinds of buildings which are likely to suffer the greatest damage (Ohmachi *et al*., 1991). This method seems to be very suitable for site effect evaluation in urban areas. In addition, the amplitude of the H/V peak is reliable enough to be used in amplification studies.

The technique developed by Nakamura (1989) is based on an estimation of the transfer function using microtremors. Usually, the transfer function of surface layers is given by

$$T_F = S_{HS} / S_{HB} \tag{3.2}$$

where ;

S_{HS} : The horizontal microtremor spectrum at the surface

S_{HB} : The horizontal microtremor on the substratum

Considering that artificial noise is not only propagated as body waves, but comprises an important part of Rayleigh waves, it is necessary to make a correction to remove the effect of surface waves. Nakamura (1989) assumes that the effect of Rayleigh waves is included in the vertical spectrum at the surface (S_{VS}) and not at the base ground (S_{VB}), then it could be defined as

$$E_S = S_{VS} / S_{VB} \tag{3.3}$$

Assuming also that the effect of Rayleigh waves is equal for the vertical and horizontal components, Nakamura (1989) gives the new transfer function as

$$T_{FF} = (S_{HS} / S_{VS}) / (S_{HB} / S_{VB}) \tag{3.4}$$

Some recordings gave results where the ratio S_{HB} / S_{VB} is nearly one for a relatively wide frequency range. Thus, Nakamura (1989) considers the horizontal to vertical spectral ratio for microtremors as an estimation of the transfer function for body waves. In addition, Nakamura (1989) suggests that the location of H/V ratio peaks does not depend on the source characteristics (Lachet and Bard, 1994).

3.4.2. Estimating Site Response by Spectral Ratio

The ground-motion amplitude spectrum (A) is considered to be the product of the earthquake source effect (E), propagation effects from the source to the recording site (P), the recording instrument effect (I), and the site response (S):

$$A(f) = E(f).P(f).I(f).S(f) \tag{3.5}$$

The source effect depends on the size and nature of the rupture. In general, increasing the magnitude of an earthquake increases the amplitudes at all frequencies, with the greatest increase at low frequencies (Molnar *et al*., 2004). The path effect preferentially attenuates the amplitude at high frequencies. The site response includes the effect of the uppermost several hundred meters of rock and soil and the surface topography at the recording site. The soil column acts like a filter with strain-dependent properties that can increase the duration and amplitude of shaking in a narrow frequency band related to the soil thickness, physical properties, and geometry at the site (Hays, 1986).

The greatest challenge in estimating the site response involves removing the source and path effects. Several methods have been proposed [for a review see Bard (1994)]. Two different methods in determining predominant frequencies and estimating site

response are presented. These methods are standard spectral ratios and horizontal-to-vertical (H/V) spectral ratios.

3.4.2.1. Standard Spectral Ratios

The most common technique for estimating site response is the standard spectral ratio method (Borcherdt, 1970; Borcherdt and Gibbs, 1976). In this method, the amplitude spectrum of a soil site (A_s) is divided by that of a nearby bedrock site (A_b):

$$\frac{A_s(f)}{A_b(f)} = \frac{E_s(f)P_s(f)I_s(f)S_s(f)}{E_b(f)P_b(f)I_b(f)S_b(f)} \cong \frac{S_s(f)}{S_b(f)} \cong S_s(f) \tag{3.6}$$

The result is that the response characteristics of the soil column are preserved, whereas the effects of the source, travel path, and the recording instruments are removed because they are assumed to be the same as for the bedrock reference site. The source-amplitude spectra are similar for the two sites provided they are at approximately the same azimuth with respect to the source. Travel-path effects are similar provided the bedrock reference site is close to the soil site compared with the distance to the earthquake source. Finally, the bedrock site is assumed to be free from amplification (i.e., $S_b(f) = 1$), thereby isolating the amplitude spectrum of the soil column.

The ratios are computed by dividing the site spectra by the reference bedrock spectra. Especially, the method is applicable when the distances between sites are small (Molnar *et al.*, 2004).

3.4.2.2. Horizontal-to-Vertical Spectral Ratios

The H/V spectral ratio method requires only a single station earthquake recording and uses the vertical component as reference. Lermo and Chavez-Garcia (1993) first applied the H/V ratio technique using spectra produced by earthquake S waves. This method is a combination of the receiver-function technique used by Langston (1979) to determine the velocity structure of the crust from teleseismic P waves and the proposal by Nakamura (1989) to use this ratio to analyze Rayleigh surface waves from recorded urban

noise (microtremors). Site response can be determined with the receiver-function method of Langston (1979) because the horizontal components contain P-to-S wave conversions due to local geological layering at the site, which are not contained in the vertical component. Similarly, Nakamura (1989) defined site response as the ratio of the horizontal and vertical motion at the surface of a soil layer by assuming that the vertical component is not amplified by the surface layers and the procedure removes the effect of the Rayleigh wave.

In general, the standard spectral ratio method is the preferred spectral ratio method if a bedrock recording is available, because the H/V ratio method has not provided consistent results (Lachet and Bard, 1994; Bonilla *et al*., 1997; Triantafyllidis *et al*., 1999). It is generally agreed that the H/V ratio method recovers the fundamental amplification frequency, but that the amplitude is usually lower than that from the standard spectral ratio method (Field and Jacob, 1995; Field, 1996; Lachet *et al*., 1996).

From mentioned methods of standard spectral ratios and horizontal-to-vertical (H/V) spectral ratios, the method of horizontal-to-vertical (H/V) spectral ratio is carried out due to the fact that there is no available bedrock recording.

3.4.3. Calculation Procedure of H/V

Earthquake data recorded by BYTNet were downloaded from the website of BYTNet. These data correspond to 39 earthquake events and this number was reduced to 27 after placing all of the events on a map according to the longitude and latitude data and determining the stations that are far away from the corresponding earthquakes. As shown in Table 3.8 and 3.9, these 27 earthquakes are listed and depicted in Figure 3.14. Some of the earthquake events lack the information about their properties and necessary information was obtained from people in KOERI who are studying on the topic. The reason of eliminating some of the far events is that the possibility of determining and catching the S and P onset values is low. For this study H/V (Horizontal-to-Vertical Spectral Ratio) computations was made for a total of 27 events (95 records).

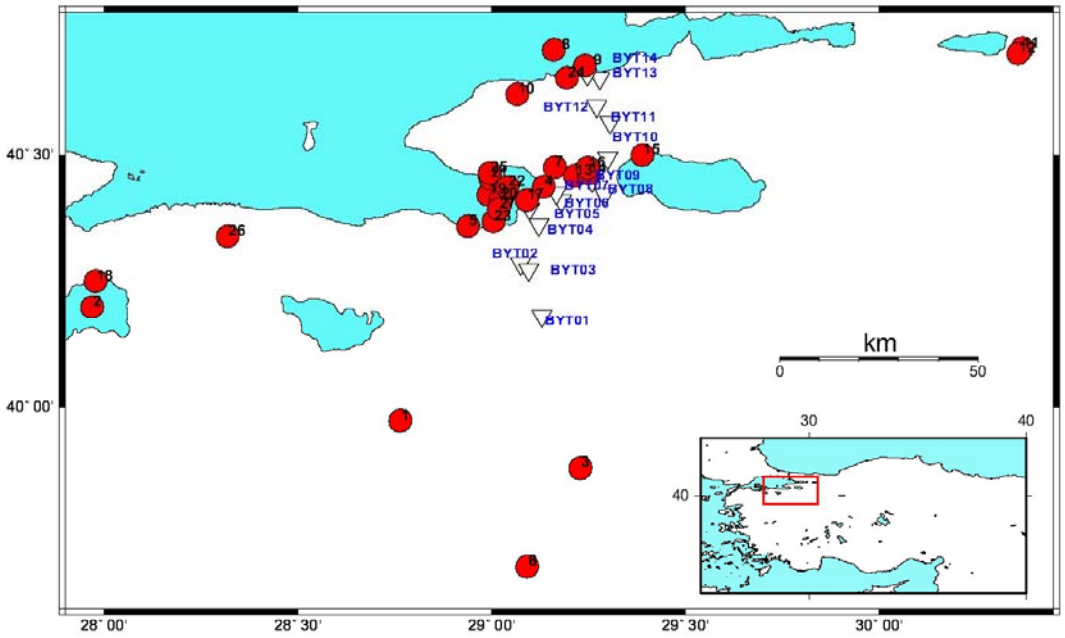

Figure 3.14. Location of 27 earthquake events and BYTNet stations

3.4.3.1. Description of Computations

In order not to miss S-onsets starting from one second before the S-onset and three seconds after the data were extracted for tapering purpose. FFT (Fast Fourier Transform) of each NS (North-South), EW (East-West), and UD (Up-Down) component was taken. H/V ratio is found in the form of

$$H=\sqrt{FFTNS^2 + FFTEW^2} \tag{3.7}$$

In Equation 3.7, it is valid for horizontal component (not the FFT transform of the square sum of the records). For vertical component, Equation can be given as;

$$V=FFTUD \tag{3.8}$$

After these procedures, low-pass filter was applied with two Hz. Upon failure of determining peaks clearly by looking at plotted H/V figures, zero-padding application was resorted to. In zero-padding five seconds interval was extracted starting from the S-onset and these data were appended to zero valued data for two seconds. After following

the steps previously stated, low pass-filter was applied with two Hz. Since clear peaks cannot be observed after these processes, logarithmic smoothing application was used. For the records saved in the Matlab program, with the help of the Fortran program, 20 per cent smoothing was applied.

General shape of the H/V ratio graphs presenting a clear peak at a frequency corresponding to predominant frequency is expected like in Figure 3.15. It didn't obtain the shape like Figure 3.15 for all BYTNet stations, so the predominant frequency belonging to each BYTNet stations can not be determined.

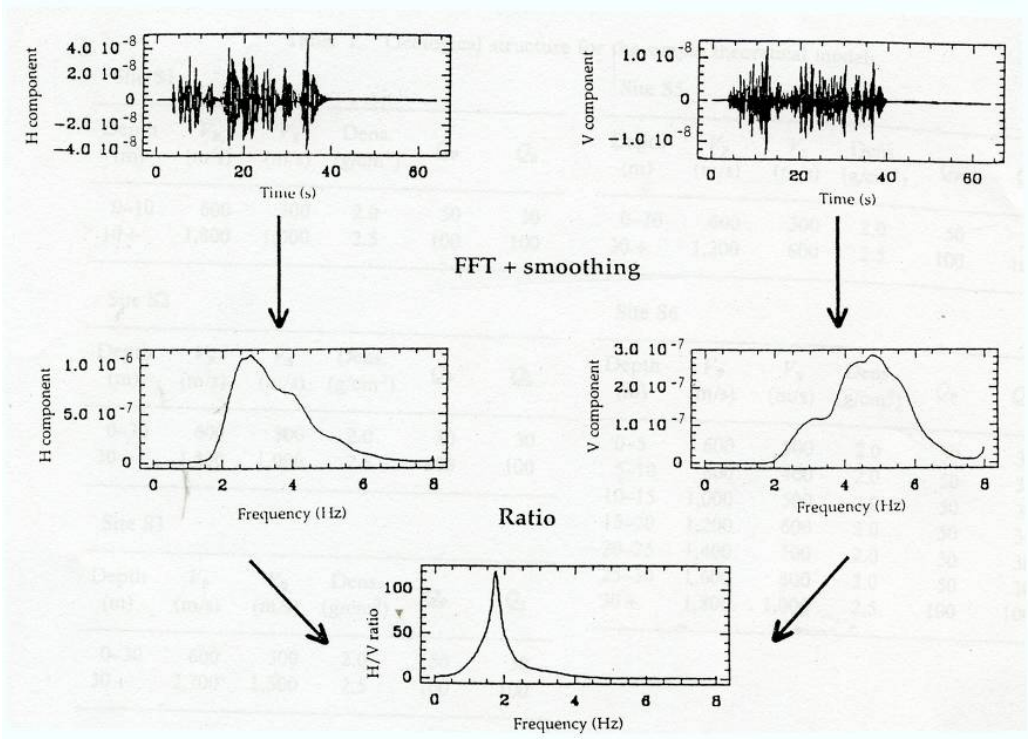

Figure 3.15. An example for typical shape showing predominant frequency in H/V ratio graph (Lachet and Bard, 1994)

Black lines in the resulting H/V figures (Figure 3.16 and 3.17) show mean values. In conclusion figures drawn after the application of logarithmic smoothing, clear peaks necessary to determine the predominant frequency were not observed. In general relatively small peaks were observed in the interval 0.8-2 Hz.

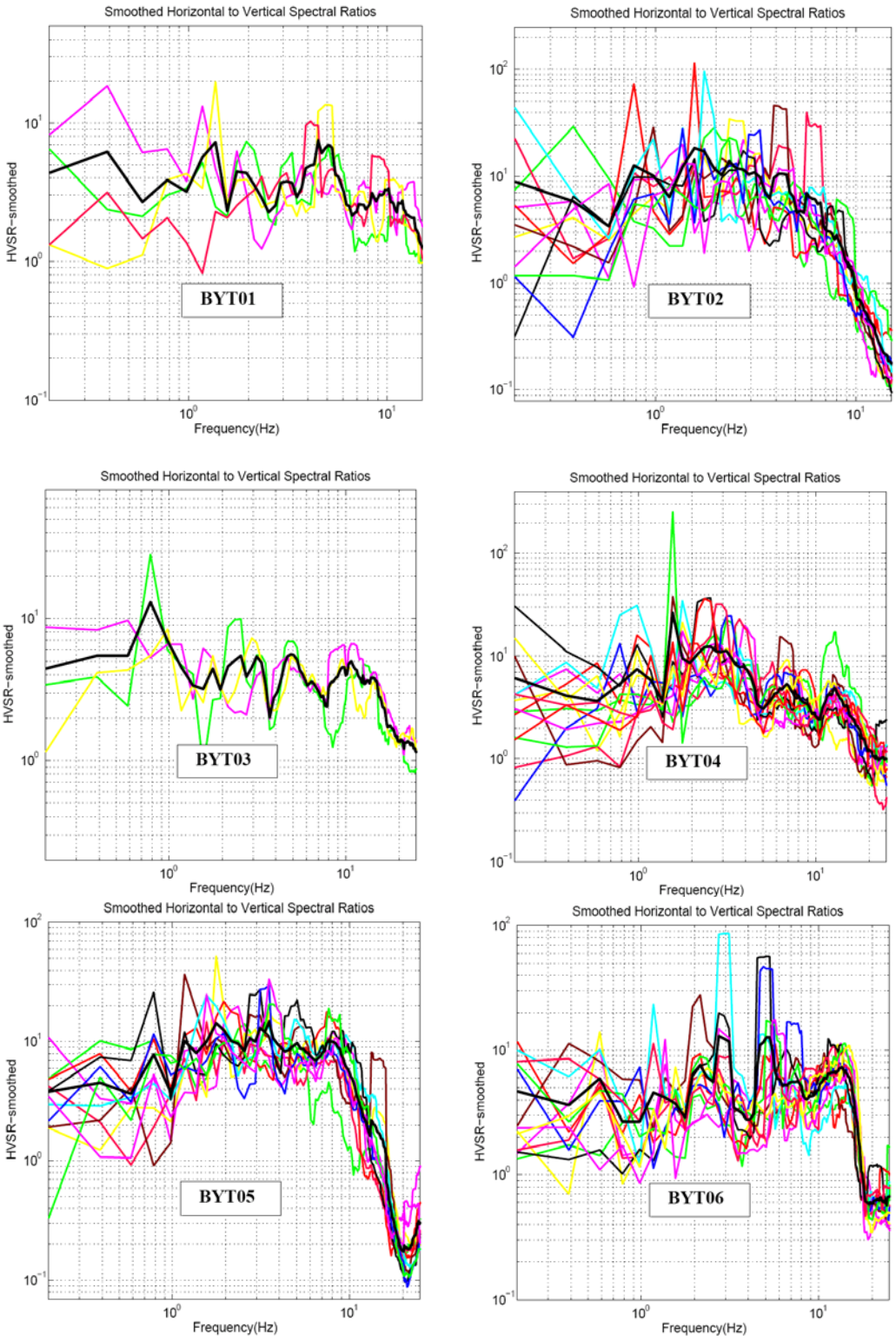

Figure 3.16. H/V Ratios vs. Frequency for BYT01, BYT02, BYT03, BYT04 BYT05 and BYT06 stations

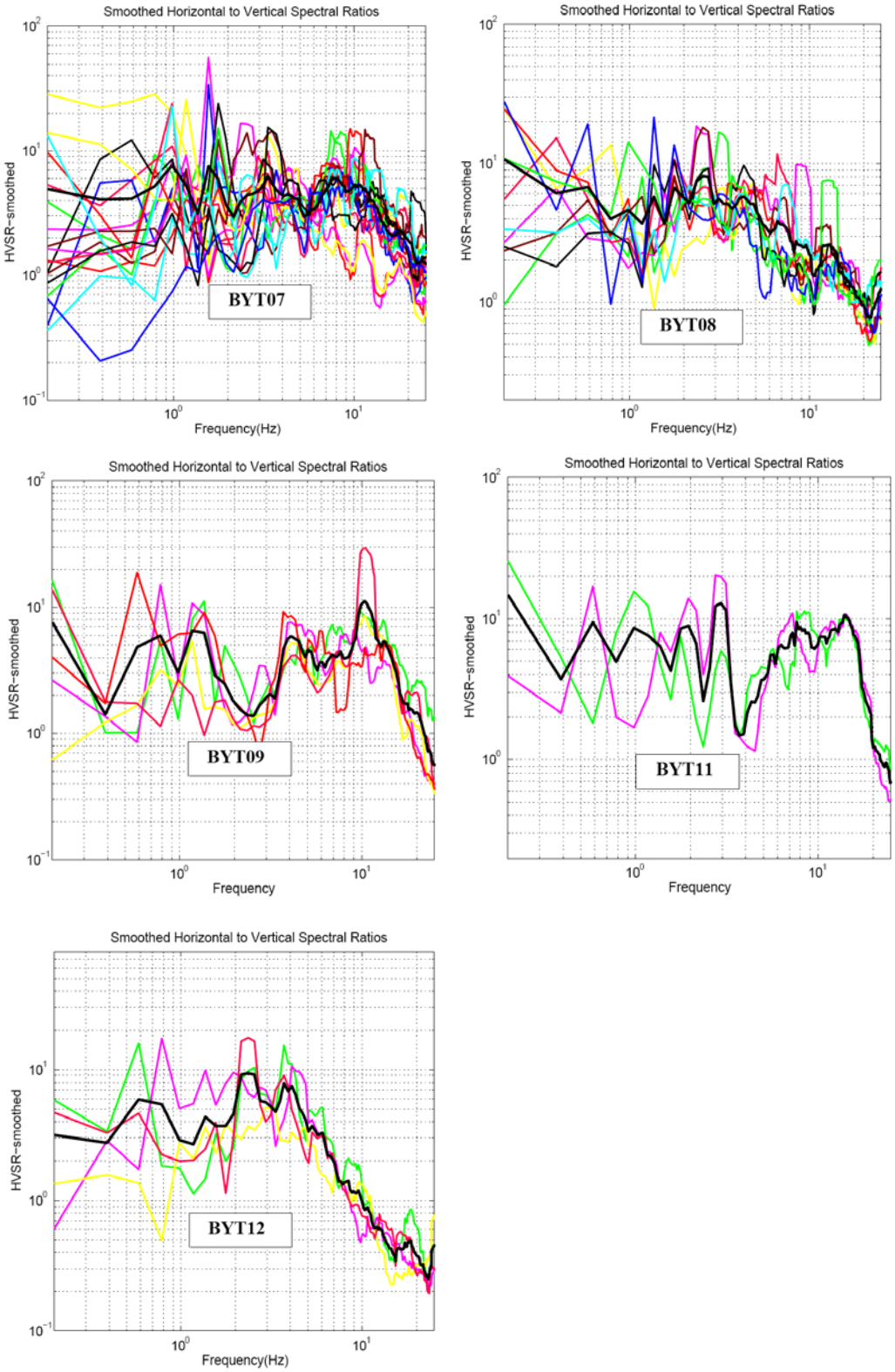

Figure 3.17. H/V Ratios vs. Frequency for BYT07, BYT08, BYT09, BYT11 and BYT12 stations

Table 3.8. All earthquake events recorded by BYT01, BYT02, BYT03, BYT04, BYT05 and BYT06 stations

EARTHQUAKE NO	DATE	EQ EPICENTER COORD.	EQ MAGNITUDE	TIME	BYT01	BYT02	BYT03	BYT04	BYT05	BYT06
1	03-20-2003	39.974N - 28.765E	4. 5Md				X	X	X	X
2	06-09-2003	40.20N – 27. 97E	5. 1Md			X	X	X		
3	12-23-2003	39.88N - 29. 23E	4. 8Ml			X		X		
4	05-25-2004	40.438N - 29.135E	3.7Md			X		X		
5	10-11-2004	40.36N - 28. 94E	3.5Md			X		X		X
6	06-20-2005	39.6844N - 29. 0928E	4. 2Md							
7	06-22-2005	40.4761N - 29.1639E	2. 8Md							
8	09-07-2005	40.7068N - 29.1613E	3. 5Md	09.07. 2005(13.22)						X
9	09-07-2005	40.6760N - 29. 2416E	3. 4Md	09.07. 2005(13.50)						X
10	11-26-2005	40.620N - 29.067E	3. 3Md							X
11	02-08-2006	N/A(40.71N-30. 37E)	N/A(4. 5Md)	02.08. 2006(04.08)		X		X	X	X
12	02-08-2006	N/A(40.70N-30. 36E)	N/A(3. 6Md)	02.08. 2006(05.25)				X		
13	02-23-2006	40.4596N - 29. 2161E	3.1Md							
14	03-20-2006	40.4642N – 29.2516E	2. 8Md							
15	04-12-2006	N/A(40.50N-29. 39E)	N/A(2. 5Md)							
16	04-15-2006	40.4752N - 29. 2485E	3. 2Md							
17	05-04-2006	40.4114N - 29. 0921E	2. 5Md						X	
18	10-20-2006	40.2519N - 27. 9792E	5. 2Md	10.20. 2006(18.15)	X	X		X	X	X
19	10-24-2006	40.422N - 28. 993E	4. 8Mw		X	X		X	X	X
20	10-25-2006	40.4130N - 29. 0238E	3. 3Mw	10.25. 2006(00.57)		X		X	X	X
21	10-25-2006	40.4549N - 28.9970E	3. 0Md	10.25. 2006(03.42)					X	
22	10-25-2006	40.4376N - 29. 0420E	3. 1Md	10.25. 2006(11.12)					X	
23	10-25-2006	40.3698N - 29. 0059E	3. 6Md	10.25. 2006(11.55)	X	X		X	X	X
24	10-28-2006	40.6523N - 29.1950E	3. 3Md							X
25	11-03-2006	40.4652N - 28. 9963E	3. 0Md	11.03. 2006(00.20)		X		X	X	X
26	12-19-2006	40.34N - 28. 32E	4. 2Md		X	X	X	X	X	X
27	01-15-2007	40.3942N - 29. 0193E	3. 1Md					X		
				TOTAL=	4	11	3	14	11	13

Table 3.9. All earthquake events recorded by BYT07, BYT08, BYT09, BYT10, BYT11, BYT12, BYT13 and BYT14 Stations

EARTHQUAKE NO	DATE	EQ EPICENTER COORD.	EQ MAGNITUDE	TIME	BYT07	BYT08	BYT09	BYT10	BYT11	BYT12	BYT13	BYT14
1	03-20-2003	39.974N - 28.765E	4. 5Md			X						
2	06-09-2003	40.20N – 27. 97E	5. 1Md		X	X						
3	12-23-2003	39.88N - 29. 23E	4. 8Ml			X						
4	05-25-2004	40.438N - 29.135E	3.7Md		X	X	X					
5	10-11-2004	40.36N - 28. 94E	3.5Md		X	X				X		
6	06-20-2005	39.6844N - 29. 0928E	4. 2Md		X							
7	06-22-2005	40.4761N - 29.1639E	2. 8Md		X							
8	09-07-2005	40.7068N - 29.1613E	3. 5Md	09.07. 2005(13.22)	X					X		
9	09-07-2005	40.6760N - 29. 2416E	3. 4Md	09.07. 2005(13.50)	X							
10	11-26-2005	40.620N - 29.067E	3. 3Md		X							
11	02-08-2006	N/A(40.71N-30. 37E)	N/A(4. 5Md)	02.08. 2006(04.08)	X	X				X		
12	02-08-2006	N/A(40.70N-30. 36E)	N/A(3. 6Md)	02.08. 2006(05.25)	X							
13	02-23-2006	40.4596N - 29. 2161E	3.1Md		X		X					
14	03-20-2006	40.4642N – 29.2516E	2. 8Md				X					
15	04-12-2006	N/A(40.50N-29. 39E)	N/A(2. 5Md)				X					
16	04-15-2006	40.4752N - 29. 2485E	3. 2Md		X		X					
17	05-04-2006	40.4114N - 29. 0921E	2. 5Md									
18	10-20-2006	40.2519N - 27. 9792E	5. 2Md	10.20. 2006(18.15)	X	X			X			
19	10-24-2006	40.422N - 28. 993E	4. 8Mw		X	X			X	X		
20	10-25-2006	40.4130N - 29. 0238E	3. 3Mw	10.25. 2006(00.57)	X							
21	10-25-2006	40.4549N - 28.9970E	3. 0Md	10.25. 2006(03.42)								
22	10-25-2006	40.4376N - 29. 0420E	3. 1Md	10.25. 2006(11.12)								
23	10-25-2006	40.3698N - 29. 0059E	3. 6Md	10.25. 2006(11.55)	X	X						
24	10-28-2006	40.6523N - 29.1950E	3. 3Md		X							
25	11-03-2006	40.4652N - 28. 9963E	3. 0Md	11.03. 2006(00.20)								
26	12-19-2006	40.34N - 28. 32E	4. 2Md		X	X						
27	01-15-2007	40.3942N - 29. 0193E	3. 1Md									
				TOTAL=	18	10	5		2	4		

4. EMPIRICAL GREEN'S FUNCTION SIMULATION

4.1. Empirical Green's Function Technique

4.1.1. Introduction

Accurate estimation of strong ground motion waveform in a broad-frequency band is indispensable to establishing the recent technology of the earthquake-resistant design and response-controlled design of structure to reduce earthquake damage. However, it is still difficult to calculate Green's function theoretically in a broad-frequency band for realistic complex media. The reason is that geophysical and geotechnical information on propagation-paths from source to site exactly enough for the numerical calculation of Green's function cannot be obtained, although the calculation techniques for the 3-D and computer abilities have been developed. A useful approach for this purpose is to estimate strong ground motion for a large earthquake using the records of small earthquakes, considered as empirical Green's function .The technique by which waveforms for large events are synthesized follows the empirical Green's function method proposed by Hartzell (1978). Revisions have been made by Kanamori (1979), Irikura (1983, 1986), and others. This section introduces the empirical Green's function method formulated by Irikura (1986), based on a scaling law of fault parameters for large and small events (Kanamori and Anderson, 1975) and the omega-squared source spectra (Aki, 1967).

One of the most effective methods for simulating broadband strong ground motion that comes from a large earthquake is to use observed records from small earthquakes occurring around the source area of a large earthquake. Actual geological structure from source to site is generally more complex than that assumed in theoretical models. Actual ground motion is complicated not only by refraction and reflection due to layer interfaces and ground surface but also by scattering and attenuation due to lateral heterogeneities and anelastic properties in the propagation path. Complete modeling of the wave field in realistic media would be extremely difficult. The frequency range available for simulations in this method depends on the signal-to-noise ratios of weak motion records from small events.

The original idea of the empirical Green's function method comes from the use of the records of small events instead of the theoretical Green's function. From the above point of view, it is desirable that the small events should be as small as possible to be able to assume a point source solution in fault size. However, most successful simulations with the empirical Green's function method have been made using not so small event as compared to the target events. To simulate strong ground motions from very large earthquakes using the records of a small event, the fault area of the target event is divided into a large number of identical subfaults whose size coincides with the small-event fault area. Then, some deficiencies of synthetic spectra are inevitably produced even if the small event records are accurate enough in broad-frequency band, similar to the procedure of Joyner and Boore (1986). To avoid such spectral deficiencies, a fractal distribution of a set of subfaults with different sizes in the fault area in simulating large earthquake motions is introduced.

4.1.2. Similarity Relationships of Earthquakes

There are considered two similarity relations between large and small earthquakes. One is the scaling relations of source parameters such as fault area, slip and slip duration, and the other is the scaling relations of source spectra.

The scaling of the source parameters studied by Kanamori and Anderson (1975) are given as

$$L/l = W/w = T/\tau_s = (M_0/m_0)^{1/3} = N,\ D/d = N \tag{4.1}$$

where, for large and small events, L and l are fault length, W and w are width, T and τ_s are slip duration time, M_0 and m_0 are seismic moment, and D and d are fault slip respectively. This scaling is based on the idea of size-independent stress drop, as static stress drop is proportional to $M_0/(LW)^{3/2}$ [equal to $m_0/(lw)^{3/2}$]. Under the above conditions, when the fault area of the target event is divided into $N \times N$ subfaults, the area of each subfaults coincide with that of the small event.

The other scaling, so-called the ω^2 spectral scaling model, was studied by Aki (1967) and Brune (1970). This model has been considered a useful reference model even for great earthquakes (Houston and Kanamori, 1986) as well as intermediate-sized earthquakes (Hanks and McGuire, 1981). The shape of the ω^2 source spectrum U, regardless of the earthquake size, is given by

$$U(f) = U_0 / [1 + (f / f_c)^2] \tag{4.2}$$

where spectral corner frequency f_c and the low-frequency ($f < f_c$) level U_0 are proportional to the inverse of the fault dimensions $(LW)^{-1}$ and the seismic moment M_0, respectively. Then, the average stress drop is proportional to $M_0 f_c^3$. If the average stress drop is independent of M_0, self-similarity exists among earthquakes (Aki, 1967). Then the corner frequency is proportional to M_0^{-3} and the high-frequency, ($f > f_c$) acceleration flat-level A_0 is proportional to $M_0^{1/3}$ as shown in Figure 4.1.a, b. Therefore, the spectral relationship between large and small events is as follows:

$$U_0 / u_0 = M_0 / m_0 = N^3, A_0 / a_0 = (M_0 / m_0)^{1/3} = N \tag{4.3}$$

where U_0 and u_0 are the flat level of the displacement spectrum, A_0 and a_0 are that of the acceleration spectrum, for large and small events, respectively.

The failure of self-similarity for very large earthquakes more than M_w=8.25 is indicated by Hartzell and Heaton (1988), because the rupture width for such large earthquakes reaches the uppermost mantle with significant rheological differences. In other words, the ω^2 scaling model is useful up to very large earthquakes with M_w=8.25.

One problem comes from the observational fact that the condition of constant stress drop does not always hold in wide magnitude range. Therefore, introduction of a small flexible condition for the ω^2 model is deemed necessary, having the shape of the ω^2 source spectrum, but not constant stress drop. Then, the spectral relationships between large and small earthquakes (4.3) are changed as follows.

$$U_0 / u_0 = M_0 / m_0 = CN^3, A_0 / a_0 = CN \tag{4.4}$$

where C is the stress drop ratio between both events. The scaling of source parameters (4.1) is also necessarily modified to be

$$L / l = W / w = T / \tau_s = [M_0 / (Cm_0)]^{1/3} = N,\ D / d = CN \tag{4.5}$$

The algorithm simulating strong ground motion from a large earthquake has to be made to satisfy the above two scaling relations (4.1) and (4.3), or (4.5) and (4.4).

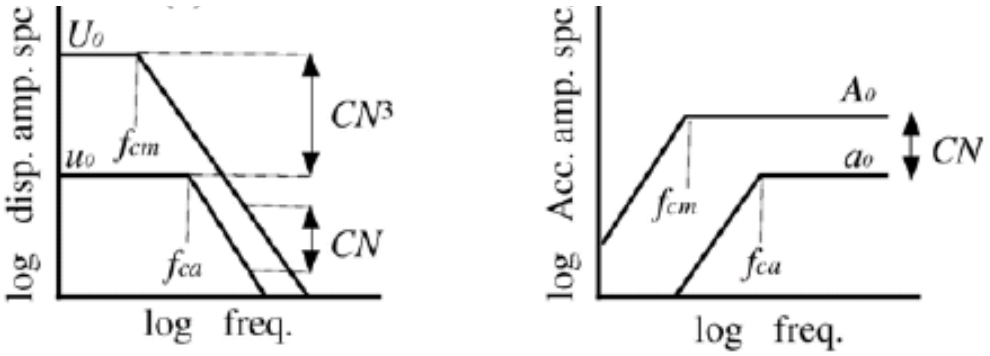

(a) (b)

Figure 4.1. Theoretical displacement (a) and acceleration (b) source spectra for different-sized events predicted by the ω^2 spectral scaling model with constant stress drop. For large and small events, respectively, U_0 and u_0 are the flat level of the displacement spectrum at low frequencies. f_{cm} and f_{ca} are corner frequencies, and A_0 and a_0 are the flat level of the acceleration spectrum at high frequencies between the corner frequency and cut-off frequency (f_{max})
(Irikura and Katsuhiro, 1994)

4.1.3. Simulation Algorithm for the ω^2 Scaling Model

The schematic illustration is shown in Figure 4.2.a for simulating strong motion from a large earthquake using the records of a small event as empirical Green's functions. For simplification, here it is assummed the ω^2 scaling model with constant stress drop

between the target event and small event, i.e. $C = 1$ in (4.4). For the case of not constant stress drop, a modified method for the simulation will be described later.

Let the moment of the target event be N^3 times that of the small events. The fault plane can be divided into $N \times N$ subfaults. Then the subfault size is equivalent to the small event (hence-forth called subevent). The seismogram $A(t)$ for the target event is expressed in terms of the seismogram $a(t)$ of the subevent as follows:

$$A(t) = \sum_{i=1}^{N^2} (r / r_i) F(t - t_i) * a(t) \tag{4.6}$$

$$F(t) = \delta(t) + \frac{1}{n'} \sum_{j=1}^{(N-1)n'} \delta[t - (j-1)T/(N-1)n'] \tag{4.7}$$

and

$$t_i = r_i / V_s + \xi_i / V_r + e_i \tag{4.8}$$

where r is the hypocentral distance from the observation point to the subevent, r_i is the distance from the observation point to the i-th subfault, ξ_i is the distance from the rupture nucleation point to the i-th subfault, V_r is the rupture speed, V_s is the velocity of seismic waves under consideration, T is the rise time of the target event, n' is an appropriate integer to eliminate spurious periodicity (Irikura, 1983), e_i is a random number between $-c_w / V_r$ and $+c_w / V_r (0 < c < 1)$ and $*$ represents the convolution. $F(t)$ is a filtering function to adjust a difference in slip time function between the target event and the subevent shown in Figure 4.2.b.

In operating (4.6), the low frequency motions are summed coherently, the spectral amplitude of the subevent in the low frequency limit being amplified N^3 times and matching the moment of the target event. The high frequency motions, on the other hand, are summed incoherently, the high frequency spectral level of the subevent, being

amplified N times (the square root of the summation number N^2), because $F(t)$ has an asymptotic spectral-level of unity at high-frequencies. Thus, the spectral amplitude ratio between the simulated ground motion and the subevent record in the high frequency limit is proportional to the cube root of that in the low frequency limit, meeting the condition (4.3) for the ω^2 scaling law. The time-domain filter $F(t)$ described in the above equation is equivalent to the frequency-domain filter used by Boatwright (1988) for the same purpose.

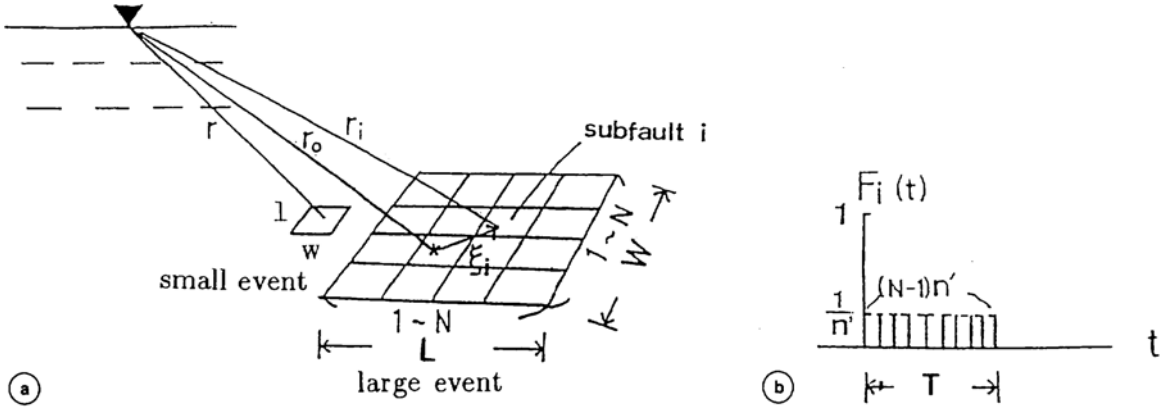

Figure 4.2. a) Schematic illustration of fault parameterization used for computing Green's functions. The fault areas of the large and small events are defined to be $L \times W$ and $l \times w$, respectively. b) $F_i(t)$ is a filtering function to adjust a difference in slip time function between the large and small events (Irikura and Katsuhiro, 1994)

Case of different stress drop between large and small events were given as follows:

$$C = \frac{\Delta\sigma_L}{\Delta\sigma_S} \tag{4.9}$$

where ;

$\Delta\sigma_L$: Stress drop for large events

$\Delta\sigma_S$: Stress drop for small events

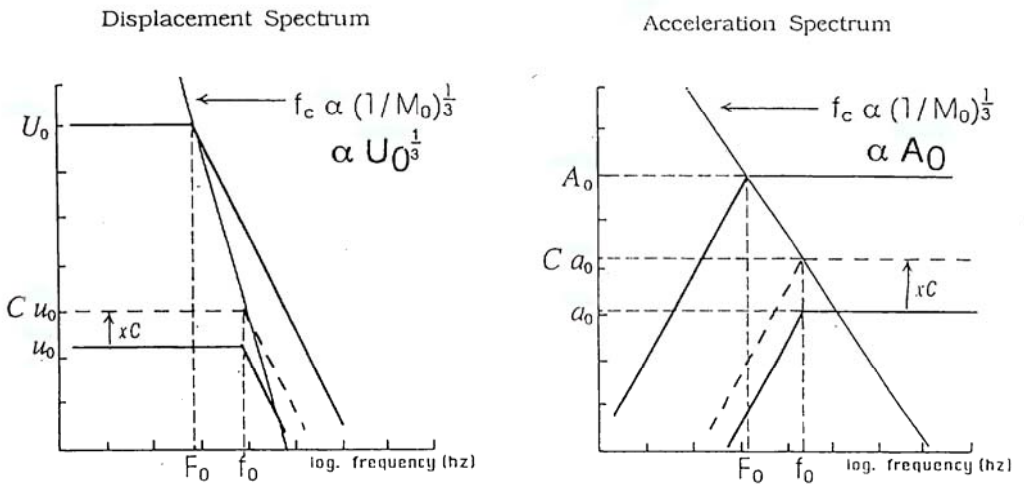

Figure 4.3. Correction for a difference in stress drop between large and small events (Irikura and Katsuhiro, 1994)

The above algorithm is extended to be applicable to more general cases of source modeling, such as heterogeneous faulting models and multiple source models. In Figure 4.3., F_0 and f_0 represent f_{cm} and f_{ca} corner frequencies.

4.1.4. Difference in the Stress Drop between Large and Small Events

Small events occurring in the source area of the target events, do not always have the same quantity of stress drop as the target and small events follow the spectral shapes expected from the ω^2 model even if they have different stress drops.

Then, first the scaling parameter N and the stress drop ratio C between the target and small events are determined by solving simple equations given as (4.4) from the spectral amplitude ratios at the low-frequencies and at the high frequencies. Next, the small event record $u(t)$ is simply amplified by C. After that, the simulations in the same manner as the previous algorithm for constant stress drop are dealt with by using $Cu(t)$ instead of $u(t)$ in eq. (4.3) as illustrated shown in Figure 4.3.

Further, this idea can be extended to an arbitrary distribution of stress drop for subfaults, if parameter C is taken to be varied from subfault to subfault (Irikura, 1988).

4.1.5. Summary of EGF Methodology after Last Revisions

After last revisions, mentioned EGF methodology can be summarized as follows:

The waveform for a large event is synthesized by summing the records of small events with corrections for the difference in the slip velocity time function between the large and small events.

This method does not require knowledge of the explicit shape of the slip velocity time function for the small event.

The synthetic motions for the large event are given using the small event $u(t)$ by the following equation:

$$U(t) = \sum_{i=1}^{N}\sum_{j=1}^{N} \frac{r}{r_{ij}} F(t) * (C \cdot u(t)) \tag{4.10}$$

$$F(t) = \delta(t - t_{ij}) + \frac{1}{n'} \sum_{k=1}^{(N-1)n'} [\delta\{t - t_{ij} - \frac{(k-1)T}{(N-1)n'}\}] \tag{4.11}$$

$$t_{ij} = \frac{r_{ij} - r_0}{V_s} + \frac{\xi_{ij}}{V_r} \tag{4.12}$$

where, $U(t)$ is the simulated waveform for the large event (the synthetic motions for the large event), $u(t)$ the observed waveform for the small event, N and C are the ratios of the fault dimensions (asperity dimensions) and stress drops between the large and small events, respectively, and the * indicates convolution. r and r_{ij} are the distance from the hypocenter of the small event and from (i,j) element to the site (Figure 4.4.). $F(t)$ is the filtering function (correction function) to adjust the difference in the slip velocity time functions between the large and small events. V_s and V_r are the *S*-wave velocity near the source area and the rupture velocity on the fault plane, respectively. T is the rise time for the large event, and defined as duration of the filtering function $F(t)$ (in Figure 4.4.(b)

and (c)). It corresponds the duration of slip velocity time function on subfault from the beginning to the time before the tail starts. n' is an appropriate integer to shift the artificial periodicity into a higher frequency range of interest. T_{ij} is the sum of the delay from the rupture starting point to the (i, j) element. The other parameters are given in Figure 4.4. (a). Regarding the filtering function $F(t)$, Irikura *et al*. (1997) proposed a modification to Equation (4.11) in order to prevent sag at multiples of 1/T (Hz) from appearing in the amplitude spectra. The discretized equation for the modified $F(t)$ is,

$$F(t) = \delta(t - t_{ij}) + \frac{1}{n'(1 - \frac{1}{e})} \sum_{k=1}^{(N-1)n'} [\frac{1}{e^{\frac{(k-1)}{(N-1)n'}}} \delta\{t - t_{ij} - \frac{(k-1)T}{(N-1)n'}\}] \tag{4.13}$$

The shape of Equation (4.13) is shown in Figure 4.4 (c). In Irikura (1986), the scaling parameters needed for this technique, N (integer value) and C, can be derived from the constant levels of the displacement and acceleration amplitude spectra of the large and small events with the equations,

$$\frac{U_0}{u_0} = CN^3 \tag{4.14}$$

$$\frac{A_0}{a_0} = CN \tag{4.15}$$

$$\frac{M_0}{m_0} = CN^3 \tag{4.16}$$

Here, U_0 and u_0 indicate the constant levels of amplitude of the displacement spectra for the large and small events, respectively. M_0 and m_0 correspond to the seismic moments for the large and small events. A_0 and a_0 indicate the constant levels of the amplitude of the acceleration spectra for the large and small events (Figure 4.4.(d), (e)).

N and C are derived from Equations 4.14, 4.15 and 4.16,

$$N = \left(\frac{U_0}{u_0}\right)^{\frac{1}{2}} \left(\frac{a_0}{A_0}\right)^{\frac{1}{2}} \tag{4.17}$$

$$C = \left(\frac{u_0}{U_0}\right)^{\frac{1}{2}} \left(\frac{A_0}{a_0}\right)^{\frac{3}{2}} \tag{4.18}$$

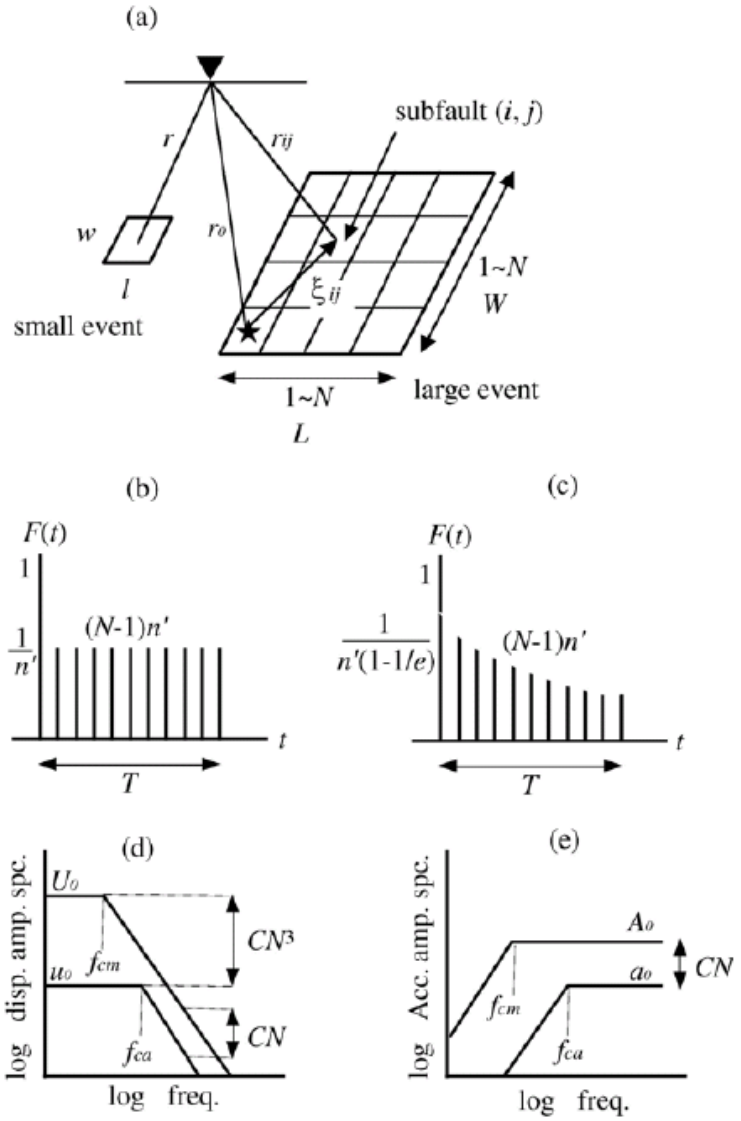

Figure 4.4. Schematic illustrations of the empirical Green's function method. (a) Fault areas of the mainshock and aftershock are defined (b) Filtering function $F(t)$ (after Irikura, 1986) to adjust to the difference in slip velocity function between the large and small events. This function is expressed as the sum of a delta and a boxcar function. (c) Modified filtering function (after Irikura *et al*., 1997) with an exponentially decaying function instead of a boxcar function. T is the rise time for the large event. (d and e) Displacement and acceleration amplitude spectra following ω^2 source scaling model assuming the stress drop ratio C between the mainshock and aftershock (after Miyake *et al*., 1999) (Irikura and Miyake, 2003)

4.1.6. Advantages and Drawbacks of Empirical Green's Function Method

The empirical Green's function (EGF) method takes the advantage of small event records occurring near the source of a large earthquake for empirical earth responses (Irikura, 1986). Simulation of strong ground motion from large earthquakes is performed by summing subevent records which already includes the path and site effects, to follow the omega square law. The original idea of empirical Green's function method comes from the use of small records instead of the theoretical Green's function since it is difficult to calculate the Green's function theoretically in a broad frequency band for realistic complex media, mainly because of the lack of geophysical and geotechnical information about propagation-paths from source to site. Compared with other deterministic techniques, it has the advantage of not requiring computing numerically the propagation path and local site effects (only requiring source parameters). In order to simulate the ground motion at a site, particularly where the geological information is too limited, Irikura (1983) proposed the EGF model in which a mainshock is synthesized from the linear superposition of a small event occurred close to the mainshock. The method is applicable to broad frequency band whereas the frequency band available for simulations depends on the signal to noise ratio of the small earthquake records. The main limitation of the method is that it can be applied only in cases where appropriate records of small events in the source area, which are considered as Green's functions, are available.

4.2. Focal Mechanism Confirmation

As stated previously in Table 3.8 and 3.9, out of the 27 earthquakes recorded by BYTNet stations it is necessary decide on which earthquake data to use as small event in test simulations and to be used in focal mechanism confirmation. The earthquake with a moment magnitude around 3.5 and closest in epicentral distance (approximately found 2.8 km) to the Gemlik Earthquake was selected. This selected earthquake corresponds to the one numbered as 20 in Table 3.8 and 3.9. In order to test whether the focal mechanism provided by KOERI is corrected or not, test simulations are going to be performed. In the test simulation, aftershock is going to be taken as a small event and trying to obtain synthesized data of main shock, the result will be compared to the actual observed

records. If the plots of the synthetic and observed data of the main shock give close fit, it is going to be understood that the selected focal mechanism is correct.

4.2.1. Frequency Range Determination

The frequency range available for simulations in EGF method depends on the signal-to-noise ratios of weak motion records from small events. The first step in the test simulation is the determination of the frequency interval. To achieve this, S/N ratio plots are generated taking S/N as three. As a description of how S/N plots are generated, it can be said that initially FFT of data portion of three seconds starting from S onset was taken and its FAS plot was produced. This part belongs to the signal part on the graphs. Out of the data, three seconds portion ending at P-onset was extracted and its FFT was taken and the results were multiplied by three to form noise portion. The points where signal and noise portions intersect on the S/N ratio graphs correspond to the high and low frequency of the frequency interval being used.

Looking at the graphs produced by taking S/N ratio as three, intersection point of the noise part and signal part plotted for the horizontal components occurs to be before 0.1 Hz and after 10 Hz. As a result of this, frequency interval was selected as 0.1-10 Hz. (broadband). This means that studies will be performed in this interval. In order to obtain a more proper appearance in the displacement time series graph plotted after the test simulation, the frequency interval was changed to [0.5-10] Hz.

.

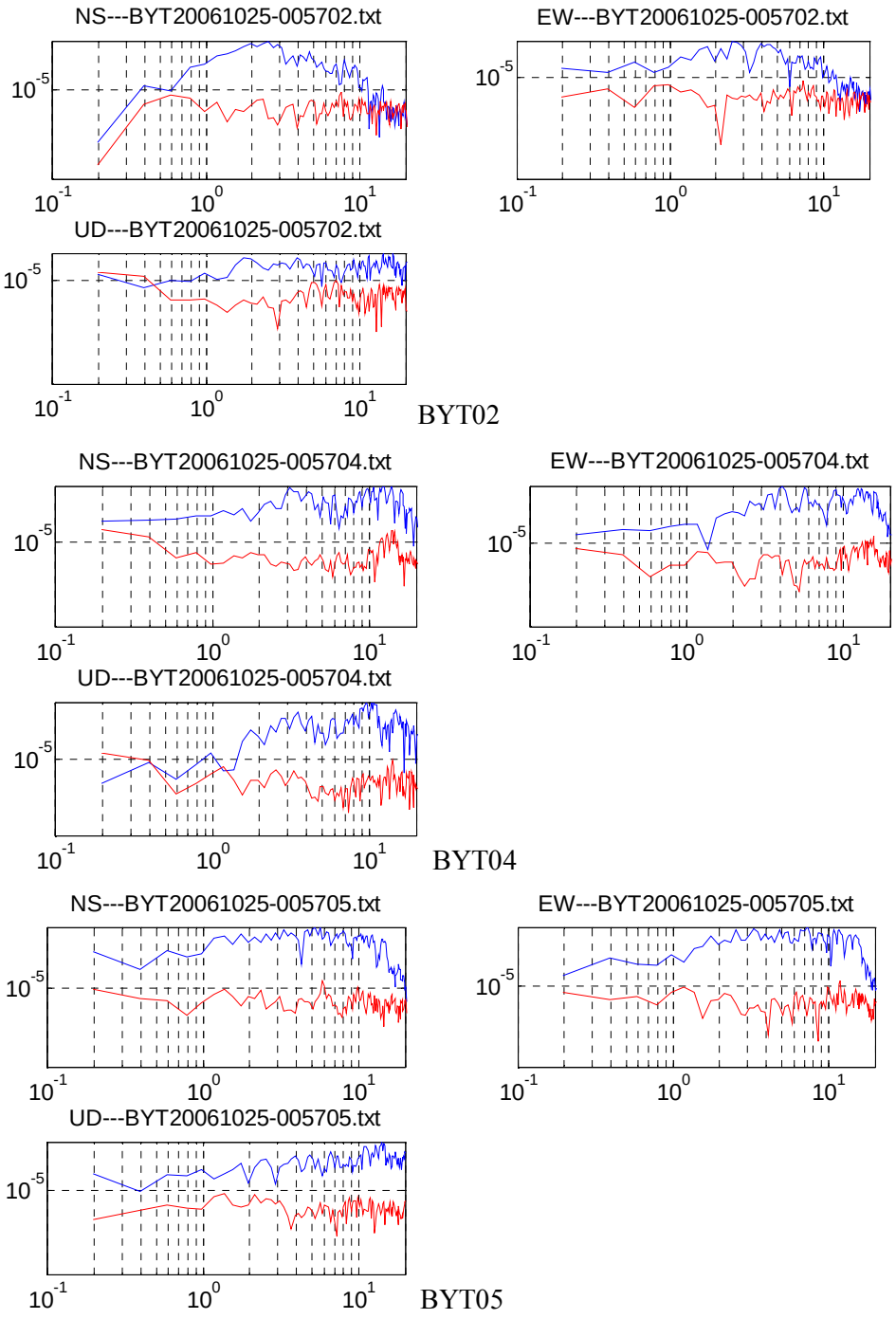

Figure 4.5. Comparison between the FAS of acceleration and noise for aftershock at BYT02, BYT04 and BYT05 stations

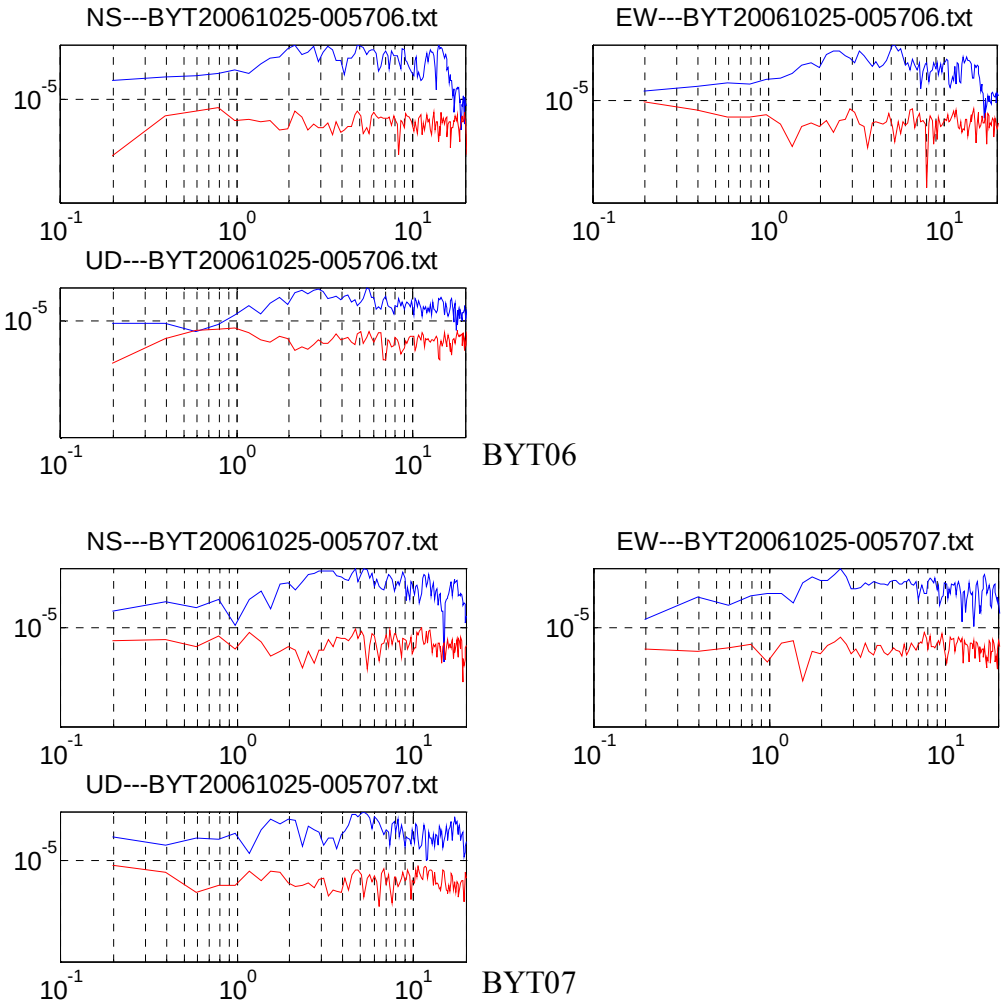

Figure 4.6. Comparison between the FAS of acceleration and noise for aftershock at BYT06 and BYT07 stations

4.2.2. Corner Frequency Determination

For the horizontal components (NS and EW) starting from the S-onset a three seconds portion of the data was extracted. Then, after taking FFT of each of the NS and EW components, total horizontal component is obtained by the Equation 3.7.

As a result of multiplying total horizontal component by the hypocentral distance (indicated in Table 4.1 and Table 4.2 for mainshock and aftershock respectively) that is found for each of the stations with the help of the Fortran program, acceleration spectrum graph was plotted on a logarithmic axis as depicted in Figure 4.7. In this figure, X and Y

axes show the frequency (Hz) and the multiplication of total horizontal component and hypocentral distance respectively.

Table 4.1. Epicentral , hypocentral distance and azimuth values pertaining to mainshock

Station Code	Latitude, N	Longitude, E	Epicentral Distance(km)	Hypocentral Distance(km)	Azimuth (Degree)
BYT01	40.182000	29.129000	29.17904000	35.37537000	156.98350000
BYT02	40.226000	29.075000	23.06805000	30.53089000	162.78980000
BYT04	40.363000	29.122000	12.82490000	23.75875000	122.09500000
BYT05	40.394000	29.098000	9.33148200	22.06981000	110.82330000
BYT06	40.410000	29.179000	15.70723000	25.43063000	95.62546000
BYT07	40.425000	29.166000	14.58951000	24.75589000	89.50502000
BYT08	40.422000	29.290000	25.07762000	32.07627000	90.41183000
BYT11	40.564000	29.306000	30.63484000	36.58543000	59.37318000
BYT12	40.596000	29.271000	30.23748000	36.25335000	50.67816000

Table 4.2. Epicentral , hypocentral distance and azimuth values pertaining to aftershock

Station Code	Latitude, N	Longitude, E	Epicentral Distance(km)	Hypocentral Distance(km)	Azimuth (Degree)
BYT02	40.226000	29.075000	21.21075000	23.44986000	168.14640000
BYT04	40.363000	29.122000	10.07915000	14.19822000	123.62500000
BYT05	40.394000	29.098000	6.59835400	11.98075000	108.49050000
BYT06	40.410000	29.179000	13.19671000	16.55757000	91.39752000
BYT07	40.425000	29.166000	12.04689000	15.65655000	83.65237000

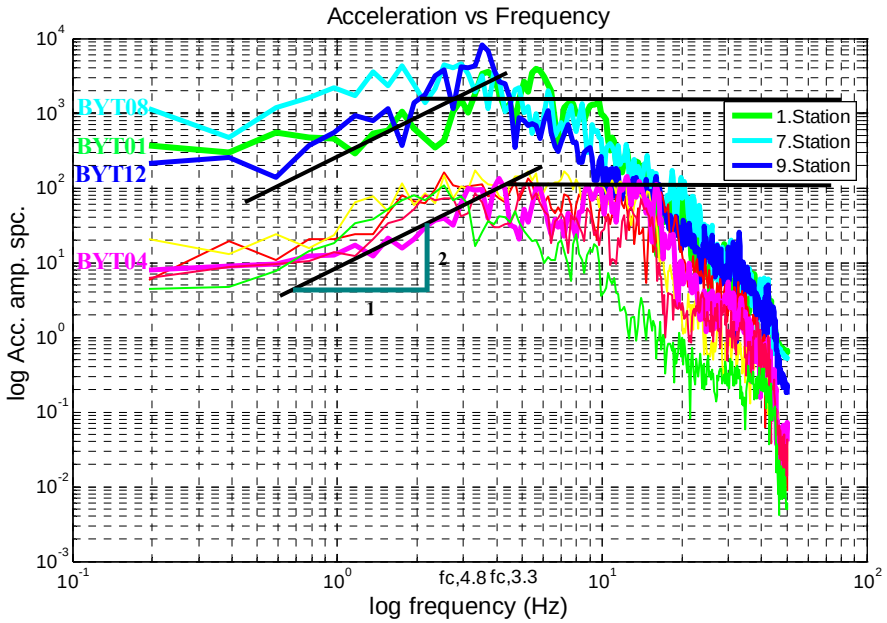

Figure 4.7. Logarithmic acceleration amplitude spectra graphs of mainshock and aftershock

According to the Equation 4.19, spectral graph of the logarithmic displacement amplitude can be plotted by making use of the spectral logarithmic acceleration amplitude graph.

$$LDAS = \frac{LAAS}{(2\pi f)^2} \tag{4.19}$$

where ;

$LDAS$: Logarithmic displacement amplitude spectra

$LAAS$: Logarithmic acceleration amplitude spectra

f : Frequency

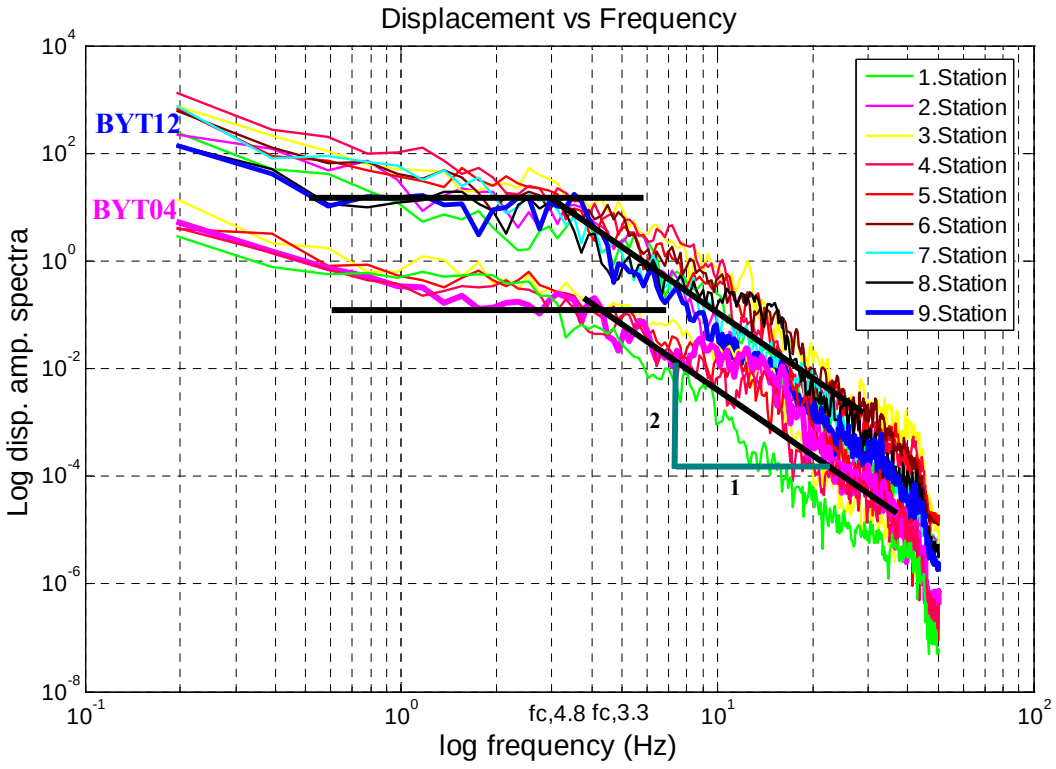

Figure 4.8. Logarithmic displacement amplitude spectra graphs of mainshock and aftershock

Combining LDAS graphs of the aftershock and main shock into one figure, flat level ratio belonging to these two graphs is expressed in Equation 4.14. Again, combining LAAS graphs of after shock and main shock into one figure, the ratio of the flat levels of these two graphs can be given by Equation 4.15.

The stations taken as basis for the determination of flat levels for the earthquakes M_w=4.8 and M_w=3.3 in LDAS and LAAS graphs are BYT12 and BYT04 respectively. The reason for choosing these stations as identifier is the values of V_{S30} which are relatively higher than those of the other stations. Because these stations are on a harder ground they give more reliable and accurate results.

Table 4.3. Rows of mainshock and aftershock according to stations represented by colors

Earthquake	M_w =4.8 Earthquake	M_w =3.3 Earthquake	Colors representing stations
1.Station	BYT01	BYT02	
2.Station	BYT02	BYT04	
3.Station	BYT04	BYT05	
4.Station	BYT05	BYT06	
5.Station	BYT06	BYT07	
6.Station	BYT07		
7.Station	BYT08		
8.Station	BYT11		
9.Station	BYT12		

The location of mainshock, aftershock, BYT02, BYT04, BYT05, BYT06 and BYT07 that are common stations to both mainshock and aftershock on the map was depicted in Figure 4.9.

Figure 4.9. Location of mainshock, aftershock and BYT02, BYT04, BYT05, BYT06 and BYT07 stations

Table 4.4. Mainshock and aftershock used in the EGF simulation

	Date Yr/Mo/Hr:Min(GMT)	Lat (deg)	Long (deg)	Depth (km)	M_w (Moment magnitude)
Mainshock	10/24/2006(14:00)	40.422	28.993	20	4.8
Aftershock	10/25/2006(00:57)	40.413	29.0238	10	3.3

The corner frequency is related to the radius of an equivalent circular crack that is used to model an earthquake source. The relation between radius of circular crack and the corner frequency is given by Brune (1970, 1971) and is as follows:

$$\rho_0 = \frac{2,34V_s}{2\pi f_c} \tag{4.20}$$

where ;

V_s : S-wave velocity of the medium

f_c : Corner frequency

$$log(2\rho_0) = -2.58 + 0.5M_w \quad (4.21)$$

where ;

ρ_0 : Radius of circular crack

M_w : Moment magnitude

With the help of (4.20) and (4.21) Equations, Radius and area of circular crack belonging to mainshock were calculated. The square shaped rupture area corresponding to this circular area was found to be 0.49 km^2. That is to say, one dimension of the square shaped rupture area is equal to 0.7 km. The rupture begins at the hypocenter and spreads circularly at a speed that is about 80 per cent of the shear wave velocity and shear wave velocity is accepted as 3.5 km/sec.

By Hanks and McGuire (1981), source duration is evaluated as follows:

$$T_d = f_c^{-1} \quad (4.22)$$

where ;

T_d : Source duration (rise time)

f_c : Corner frequency

Table 4.5. Some numerical values pertaining to mainshock and aftershock

	Flat level of the disp. spectrum	Flat level of the acc. spectrum	Corner frequency	Rise time	Seismic moment (M_0 *and* m_0) (Dyne*cm)
Mainshock	15.85	1423.4	3.2	0.31	$10^{23.25}$
Aftershock	0.1006	107.97	4.3	0.23	$10^{20.94}$

The empirical relation of Hanks and Kanamori (1979) is used to estimate the seismic moment of mainshock via Equation 4.23.

$$\log(M_0) = (M_w + 10.7) * 3/2 \quad (4.23)$$

Seismic moment of aftershock is found by the empirical relation taken from Catalyurekli (2004) and shown in Equation 4.24.

$$\log(M_0) = -4.3425\log(f_c) + 23.697 \tag{4.24}$$

The ratio between equations (4.14) and (4.15) gives the value of N as 3. And then, C was found to be 7.6 by inserting the computed M_o (according to Equation 4.23) and m_o (according to Equation 4.24) values into Equation (4.16).

The stress drop for the circular source model can be estimated with the help of the equation developed by Brune (1970);

$$\Delta\sigma = \frac{7M_0}{16\rho_0^3} \tag{4.25}$$

Stress drop of the mainshock and aftershock can be found by using the Equation 4.25. According to scaling rule by Irikura (1986) the ratio of the stress drop was given by Equation 4.9. C value was found to be 7.8 via using the Equations 4.25 and 4.9 (done by verification purpose). These values are the computation results when the rupture area of the main shock is divided into 3x3 subfaults.

While simulating M_w=4.8 earthquake with M_w=3.8 earthquake, values of $N = 3(3\times3)$ and $C = 8$ were used. From the synthetic and observed data suitable correlation and shift intervals were determined (As will be stated in later section).

When M_w=4.8 earthquake was simulated by means of using $N = 3(3\times3)$ and $C = 8$ values, it was observed that synthetic graphs have smaller value so that the way of increasing C value was followed. Increasing the C value up to 12, resulting graphs were observed so that the best fit was obtained at $C = 12$. EGF program written in Fortran produces correlation and residual values for each station acceleration, velocity, displacement and spectral values. After determining the suitable correlation and shift

interval, the aim is to find the best simulation that gives correlations closest to 1 and residual closest to 0.

In the simulations taking $N = 3$ all possible division alternatives that are $2\times3,\ 3\times2,\ 3\times3,\ 4\times2,\ 2\times4,\ 2\times5,\ 5\times2,\ 3\times4,\ 4\times3$ were tried. Of these alternatives the first number shows the number of subfaults along the strike direction and the second number shows the number of subfaults along the dip direction. Each subfault alternative was tried for different rupture starting points over 100 trials and displacement residual sum of the displacement residuals that were computed for all of the stations by the EGF program, was obtained. Test simulations were performed according to the division alternatives and rupture starting point alternatives that give the smallest displacement residual sum.

The best division alternative was found to be 4×3 and RSP was 1 to 2. Schematic representation corresponding to the best division alternative is shown in Figure 4.10.

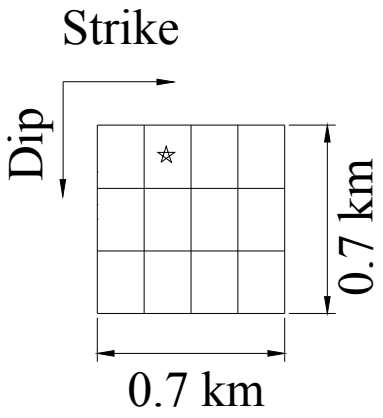

Figure 4.10. Example illustration of best division alternative to subfaults for calculation (4×3 RSP 2×1) and rupture starting point is represented by ☆

After determination of 4×3 to be the best division alternative out of the stations at which simulations were performed (BYT02, BYT04, BYT05, BYT06 and BYT07) minimum residual sum was obtained at RSP 2×1. For 4×3 division alternative at 2×1 RSP displacement residual sum was obtained as 11.2. With contour plot and 3D plot of the 4×3 alternative for different RSP, it was verified that minimum residual sum was at RSP 2×1. This test was performed according to the focal mechanism provided by KOERI.

The goodness of the fitting between the observed and synthesized motion was judged by the displacement residual defined as;

$$residual = \sum_{st}\sum_{cmp}\sum_{i=1}^{N}\left(\frac{\sum_{i=1}^{N}(O_i - S_i)^2}{\sqrt{\sum_{i=1}^{N}O_i^2}\sqrt{\sum_{i=1}^{N}S_i^2}}\right) \tag{4.26}$$

where, st and cmp define the number of stations, and components, respectively. O_i and S_i are the displacements of the observed and synthesized motion, respectively (Birgören and Irikura, 2004).

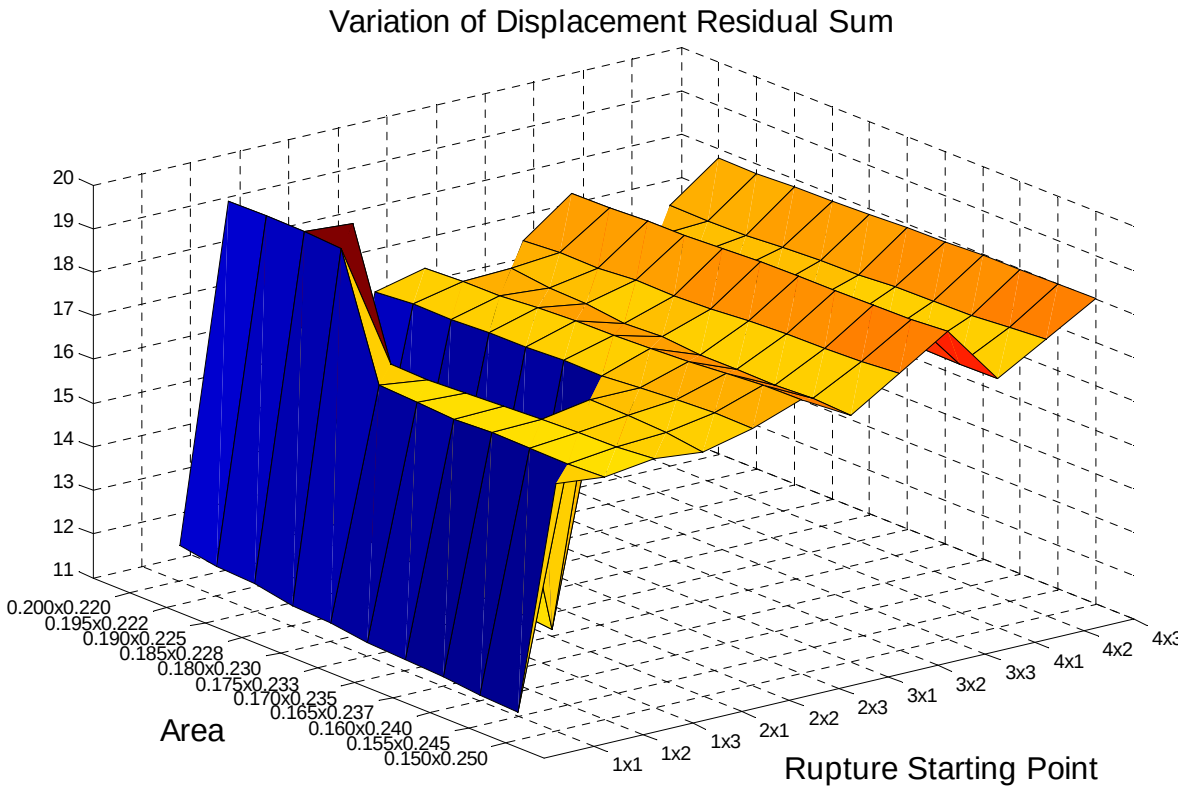

Figure 4.11. 3D plot of the 4x3 division alternative for different RSPs according to focal mechanism determined by KOERI

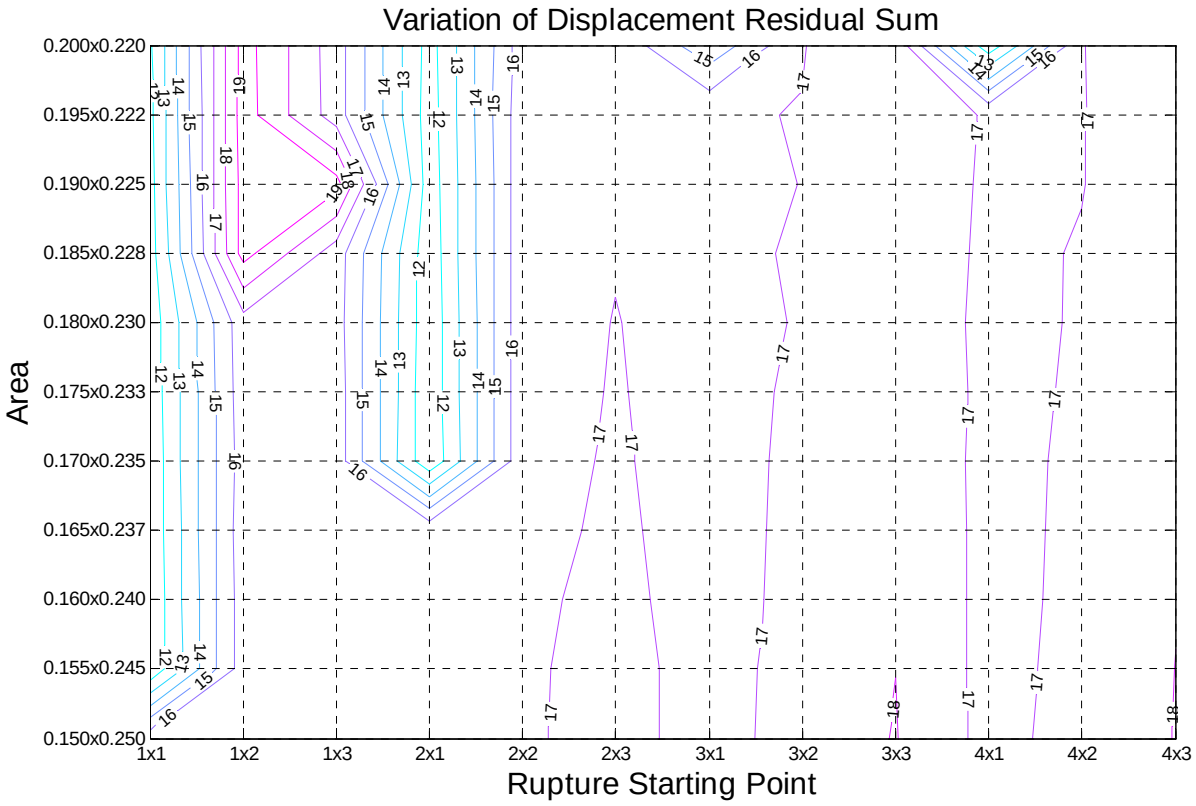

Figure 4.12. Contour plot of the 4x3 division alternative for different RSPs according to focal mechanism determined by KOERI

When the same process applied to the focal mechanism (strike-slip mechanism, strike 14, dip 71, rake -12) determined by Kocaeli University geophysicists (Irmak *et al*., 2007) for the same RSP, displacement residual sum was found to be 16.58. In conclusion it can be said that due to obtaining displacement residual sum lower than 16.58 and obtaining better fits between observed and synthesized motion, focal mechanism determined by KOERI is preferable. This is the mechanism used in the scenario simulations.

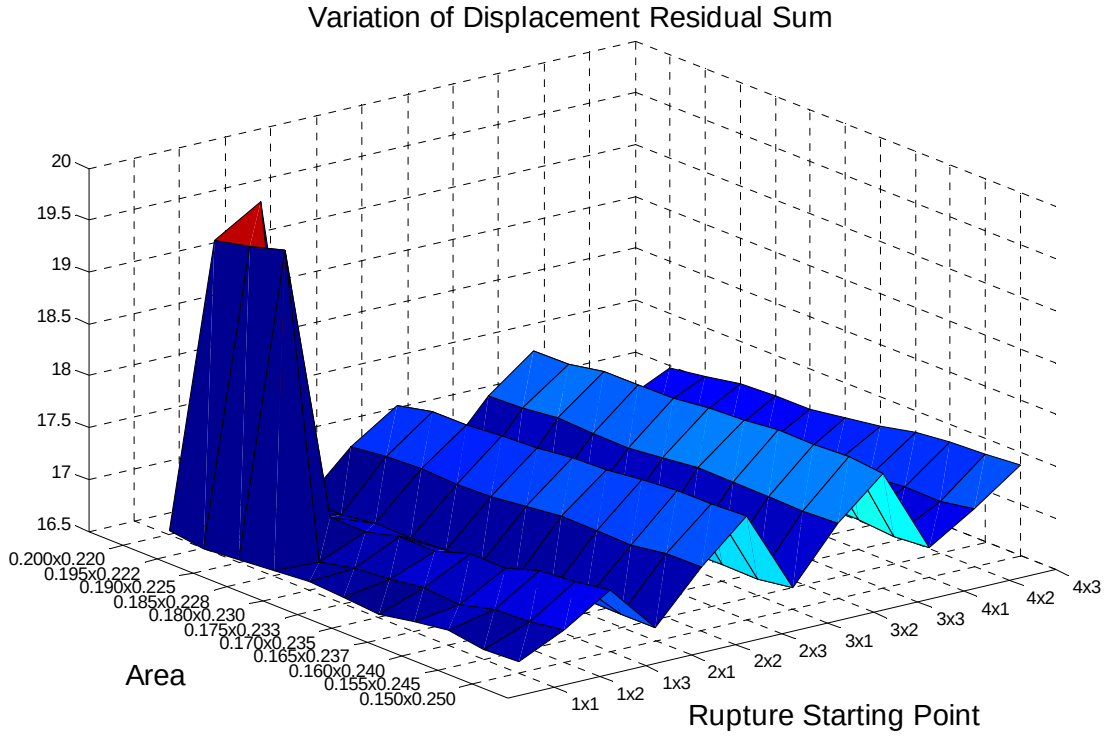

Figure 4.13. 3D plot of the 4x3 division alternative for different RSPs according to focal mechanism determined by Kocaeli University geophysicists

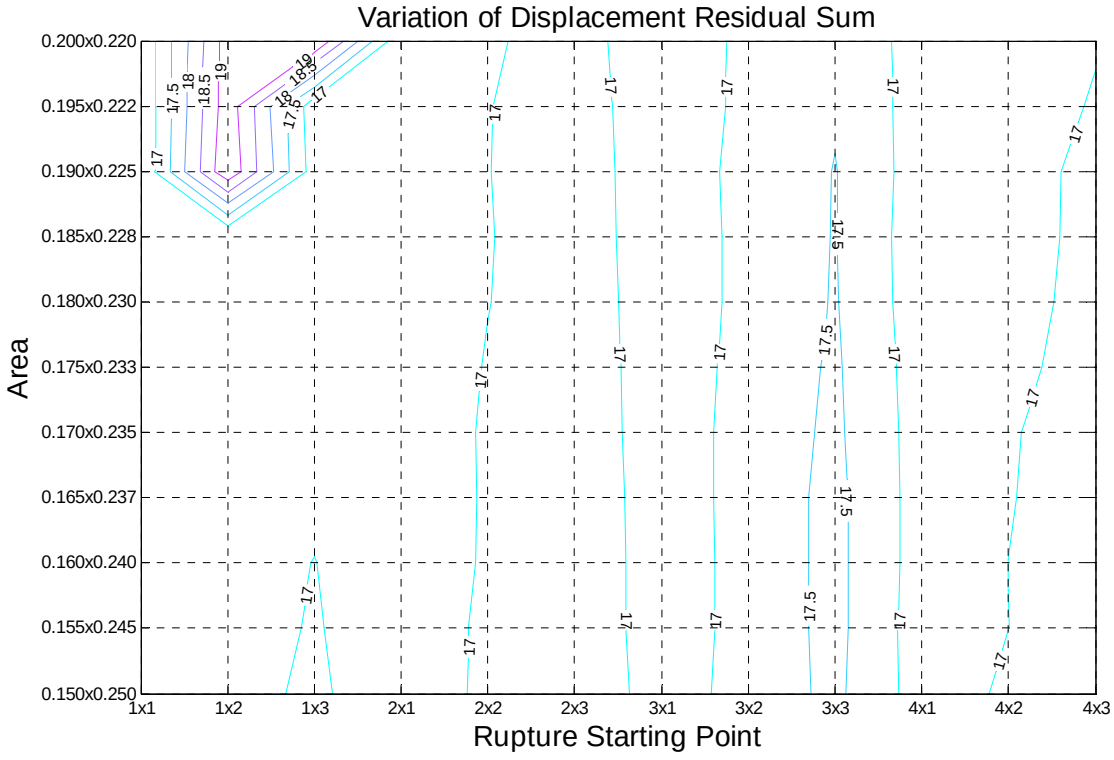

Figure 4.14. Contour plot of the 4x3 division alternative for different RSPs according to focal mechanism determined by Kocaeli University geophysicists

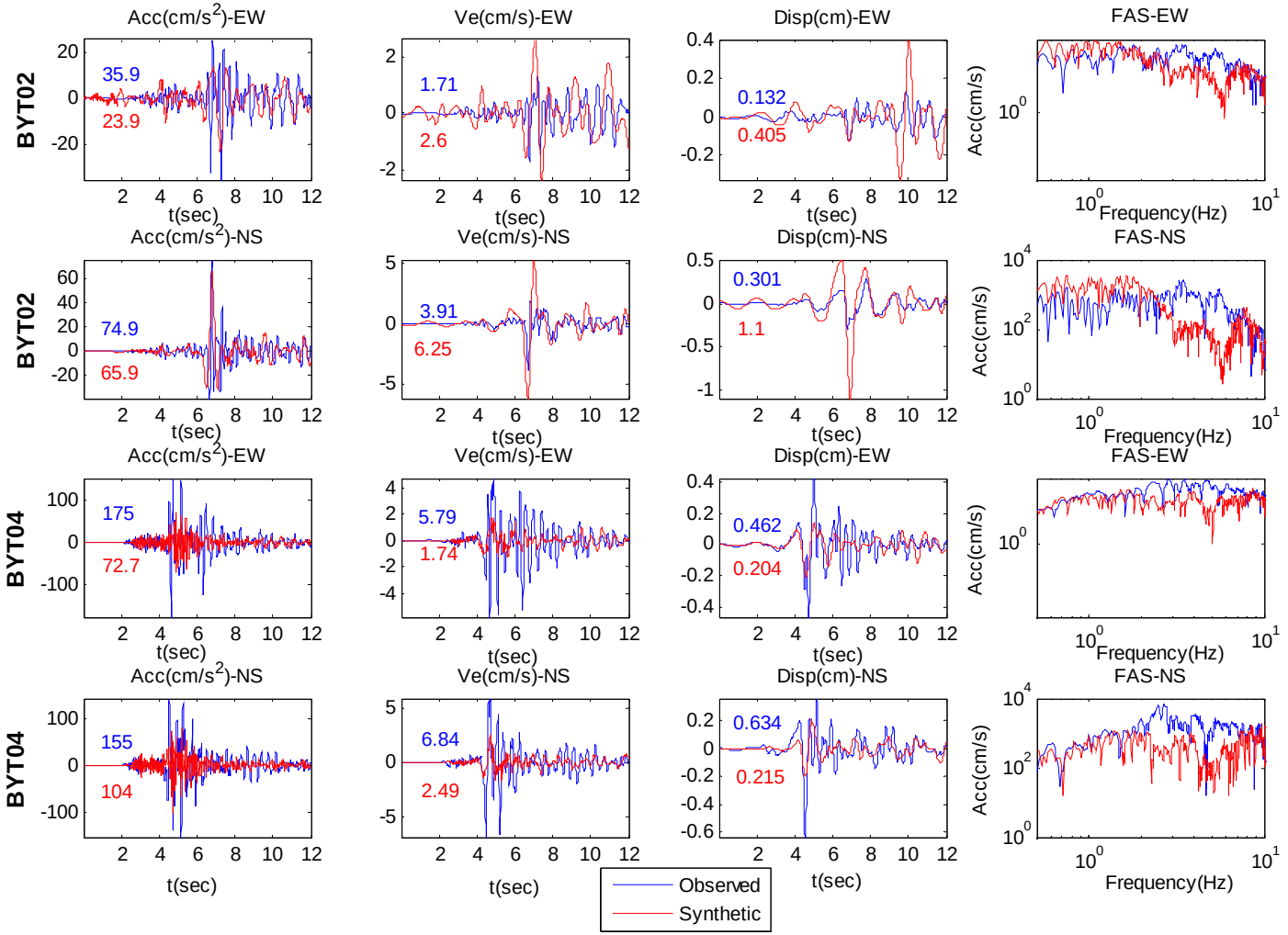

Figure 4.15. Comparison of observed and synthetic waveforms of acceleration, velocity, displacement and acceleration spectra for the 2006 Gemlik earthquake, October, at the BYT02 and BYT04 stations according to the focal mechanism provided by KOERI

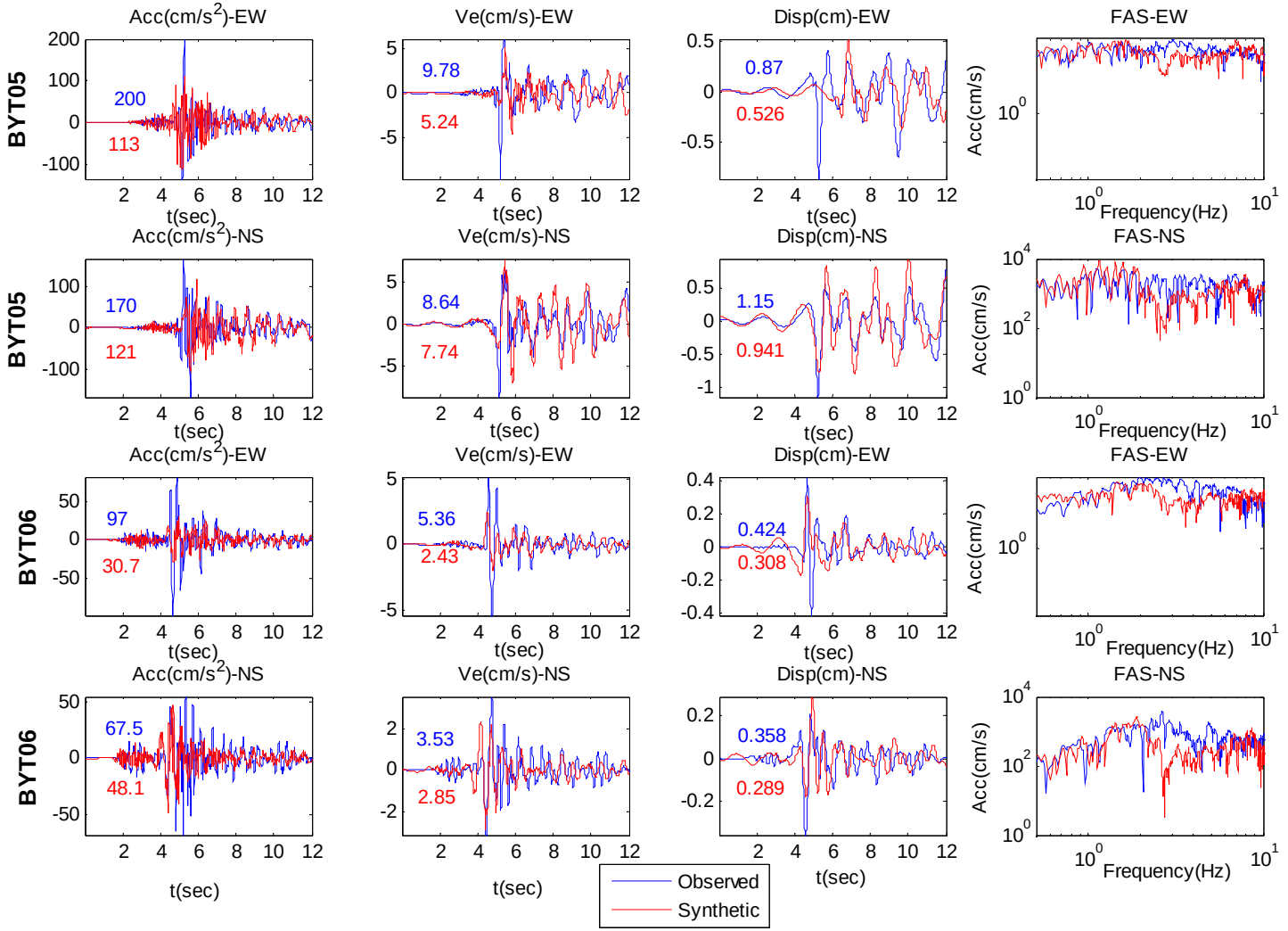

Figure 4.16. Comparison of observed and synthetic waveforms of acceleration, velocity, displacement and acceleration spectra for the 2006 Gemlik earthquake, October, at the BYT05 and BYT06 stations according to the focal mechanism provided by KOERI

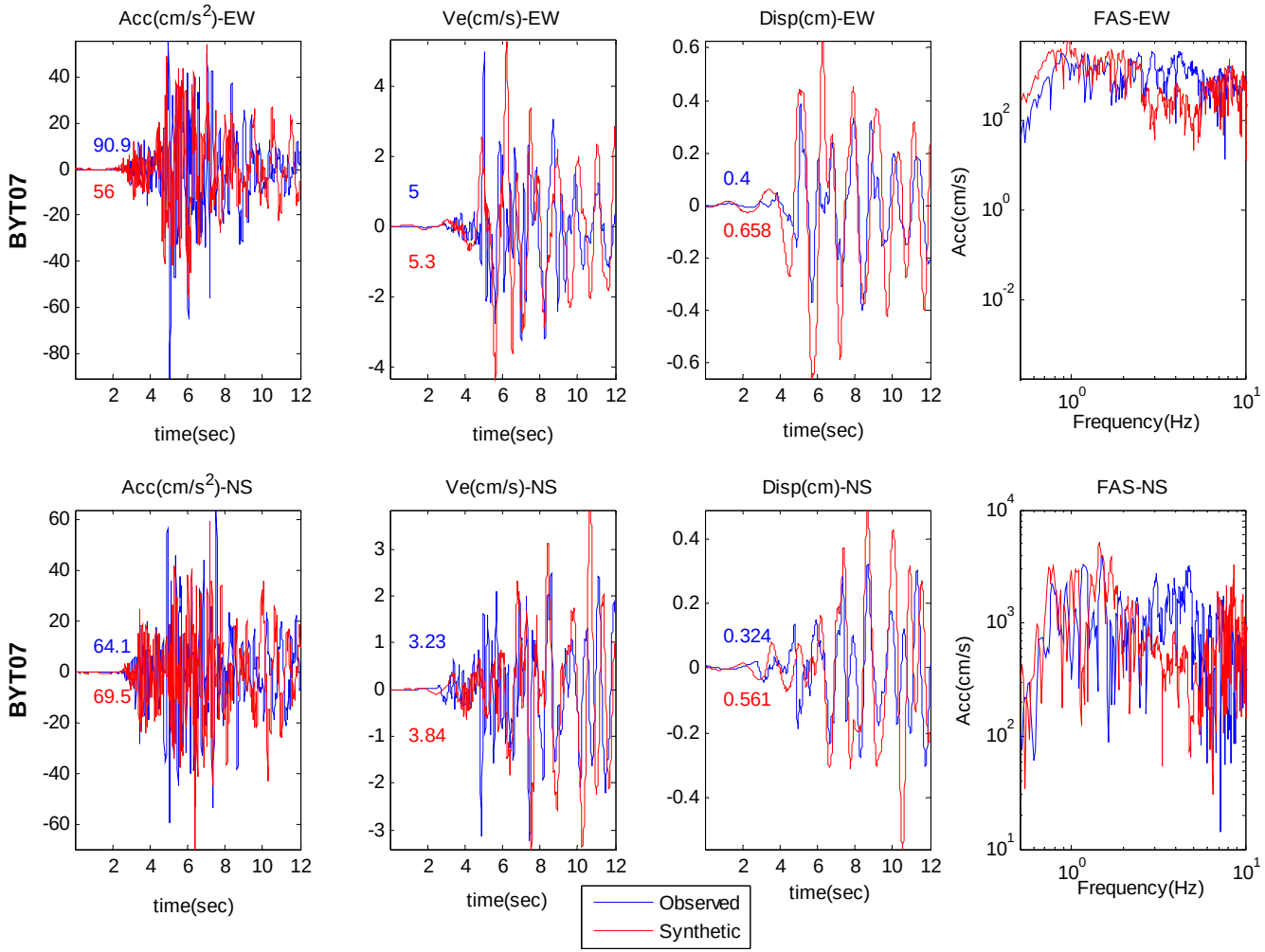

Figure 4.17. Comparison of observed and synthetic waveforms of acceleration, velocity, displacement and acceleration spectra for the 2006 Gemlik earthquake, October, at the BYT07 station according to the focal mechanism provided by KOERI

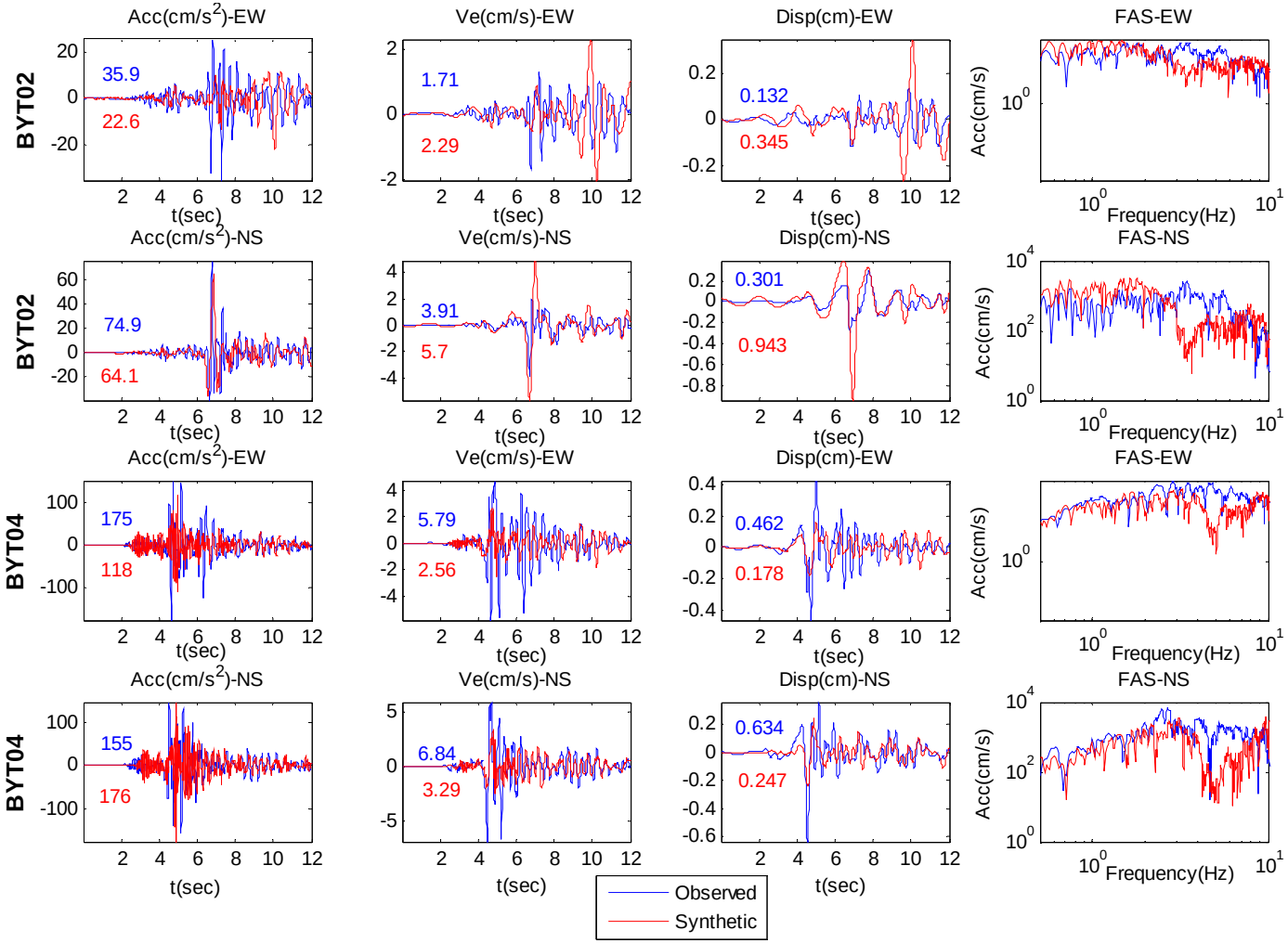

Figure 4.18. Comparison of observed and synthetic waveforms of acceleration, velocity, displacement and acceleration spectra for the 2006 Gemlik earthquake, October, at the BYT02 and BYT04 stations according to the focal mechanism determined by Kocaeli University geophysicists

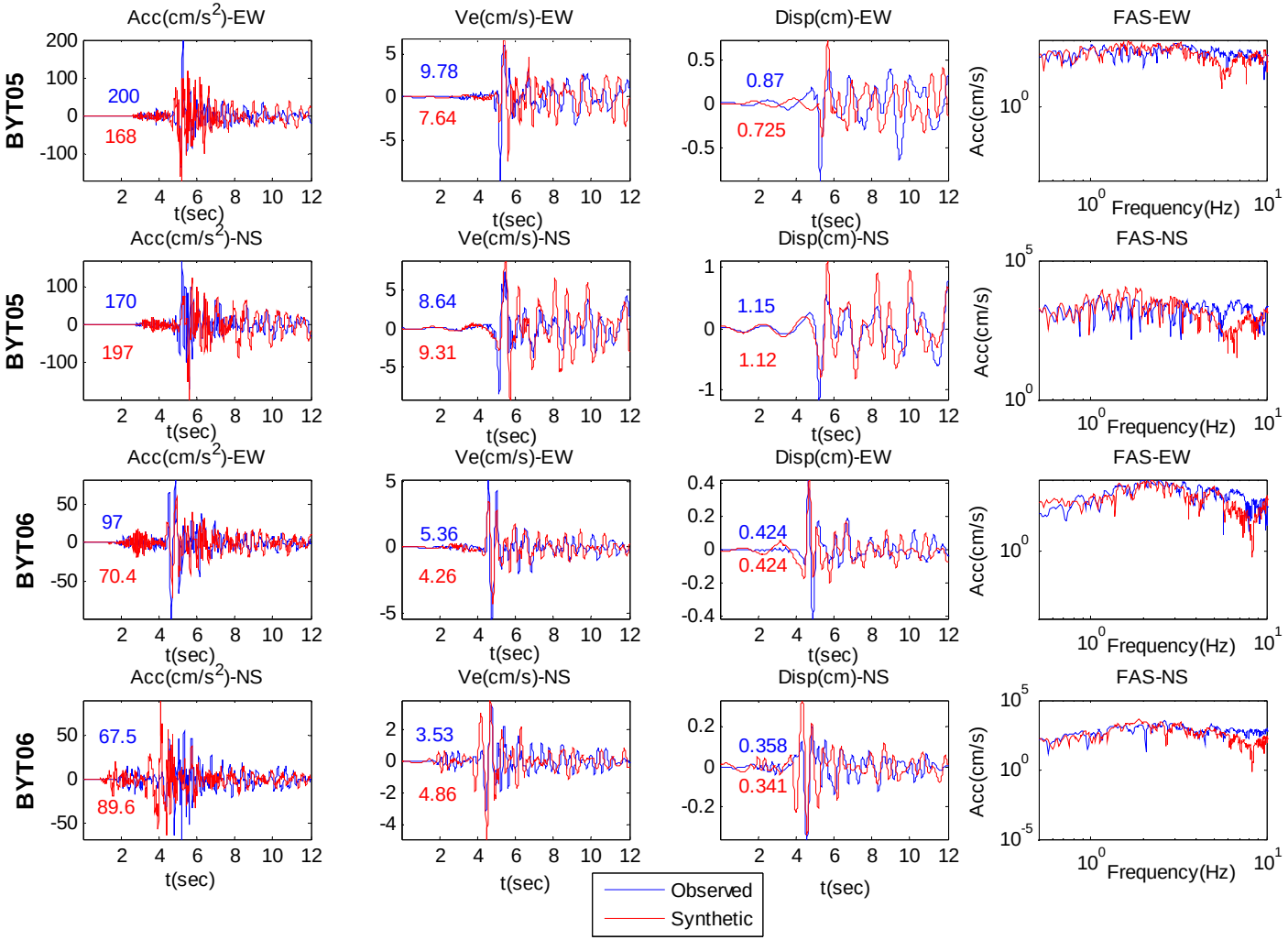

Figure 4.19. Comparison of observed and synthetic waveforms of acceleration, velocity, displacement and acceleration spectra for the 2006 Gemlik earthquake, October, at the BYT05 and BYT06 stations according to the focal mechanism determined by Kocaeli University geophysicists

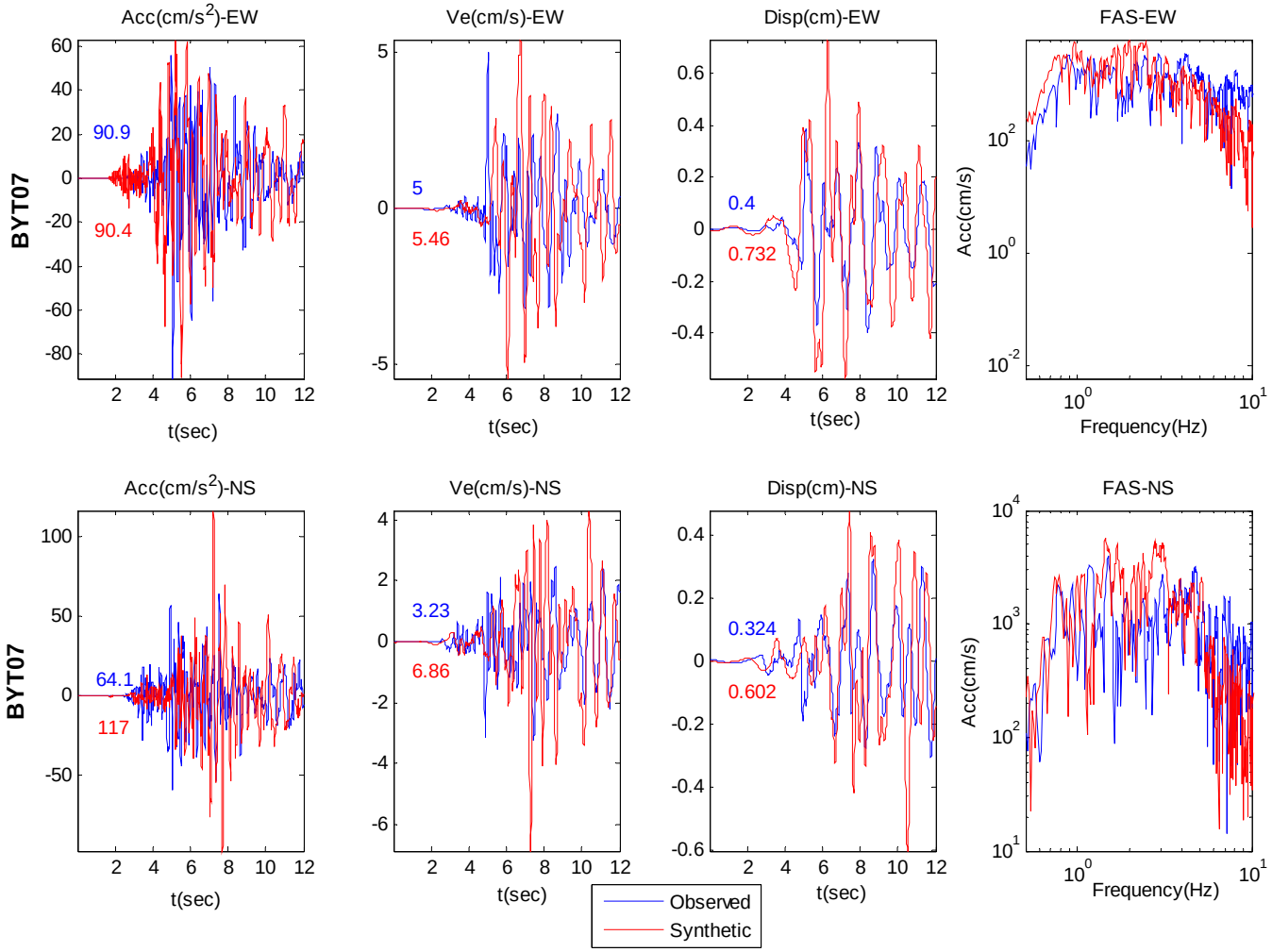

Figure 4.20. Comparison of observed and synthetic waveforms of acceleration, velocity, displacement and acceleration spectra for the 2006 Gemlik earthquake, October, at the BYT07 station according to the focal mechanism determined by Kocaeli University geophysicists

4.3. EGF Program Template

README FILE used in test simulation so as to run EGF program was presented in Appendix B. Input parameters given in the README FILE are the actual input parameters used in the test simulation computations according to the focal mechanism determined by KOERI. One has to make note of how some of these parameters are obtained.

As far as README FILE is concerned, Line 4 is related with the frequency interval being worked on. Focal mechanisms of target and element event are considered to be identical (6^{th} and 8^{th} lines). The rise of the element event on line 9 was evaluated via Equation 4.22 and its value was taken from the Table 4.5.

Shear wave velocity on line 11 was taken as 3.5 km/s. Rupture velocity was taken as the 0.8 multiple of the shear wave velocity. Epicentral distace and azimuth value for each station on line 14 were provided. KSM, KEM, KSA, KEA values of the 15^{th} line were found using trial errors technique by looking at the general trends of synthetic and observed graphs.

5. SCENARIO SIMULATION

As mentioned before, the concerned area being capable of producing the second highest hazard rate in the Marmara Region is more likely to produce a magnitude 7.2+ event with 1000 year recurrence time. As a result, when the future risk mitigation strategies are taken into account, this situation necessitates preparing scenario earthquakes.

The first step in this section of presented study is to simulate middle and large earthquakes (scenario earthquakes) with the small earthquake (Gemlik Earthquake M_w= 4.8) which will be taken to be the Green's function. That is to say, strong ground motion caused by the Gemlik Gulf Earthquake was used to simulate M_w=5.8 and M_w=6.8 scenario earthquakes.

The moment magnitude difference between element event (M_w=4.8) and target event referring to the scenario earthquake can not be high on the grounds of being used in EGF method. Most successful simulations with the empirical Green's function method have been made using not so small events as compared to the target events. For this reason, when the moment magnitude of scenario earthquake will be selected, this rule should be taken into account. The source process of the Gemlik Earthquake in frequency range 0.5 to 10.0 Hz (broadband frequency) was applied by the method of EGF (Irikura, 1986) to image the strong motion generation area assumed to be asperities. For simplification, asperity area of each scenario earthquake was specified according to the assumption based on the equality of the stress drop of small and large events $(C = 1)$. General assumptions are that source of each scenario earthquake contains only single asperity; scenario earthquakes will start at the same location and depth and same focal mechanism of Gemlik Earthquake. S25 and S41 faults were assumed as only one continuous fault. The asperity parameters for each scenario were determined from empirical scaling. Each scenario case was analyzed according to different rupture starting point alternatives in the asperity. Rupture initiation points were selected in the asperity area not fault area due to the fact that hypocenter locations in finite-source models which

indicate that hypocenters are often located close to regions of large slip (asperity) (Manighetti *et al.,* 2005; Mai *et al*., 2005).

Calculation was made for two earthquake scenarios (M_w=5.8, 6.8) and three different rupture starting points in the asperity of each scenario earthquake, which in turn, led the total number of earthquake scenarios to six. Acceleration, velocity and displacement time series were plotted so as to assess near-field directivity effect stemming from different rupture initiation in the asperity. Maximum values obtained from scenario earthquake calculations were placed in the PGA and PGV curves with empirical attenuation relationships. Five per cent damped simulated acceleration response spectra were compared with the current Turkish Seismic Design Code (TSDC 2007) and effects of near-field ground motion due to different rupture nucleation points were evaluated.

5.1. Frequency Range Determination

Firstly, frequency range of the small event is necessary when strong ground motion simulation of a scenario earthquake will be performed. S/N (signal-to-noise) ratio method was applied to investigate frequency range of small event. This frequency range is usable data bandwidth to generate scenario earthquakes.

Signal-to-noise ratio was selected as three. There are nine BYT-Net stations for the M_w: 4.8 earthquake (BYT01, BYT02, BYT04, BYT05, BYT06, BYT07, BYT08, BYT11 and BYT12). The S/N ratio result graphs for M_w: 4.8 earthquake with nine BYT-Net stations were illustrated in Figure 5.1 and 5.2. S/N ratio graphs illustrated that the signal FFT generally intersected with the noise FFT (Fast Fourier Transform) before 0.1 Hz and after 10 Hz (for horizontal components of M_w: 4.8 earthquake at nine BYT stations). Then, appropriate data bandwidth for horizontal components of M_w: 4.8 earthquake is acceptable as (0.1-10) Hz. For the purpose of enhancing the appearance quality of the displacement-time series, the interval between 0.5 to 10 Hz was selected as frequency range in this study.

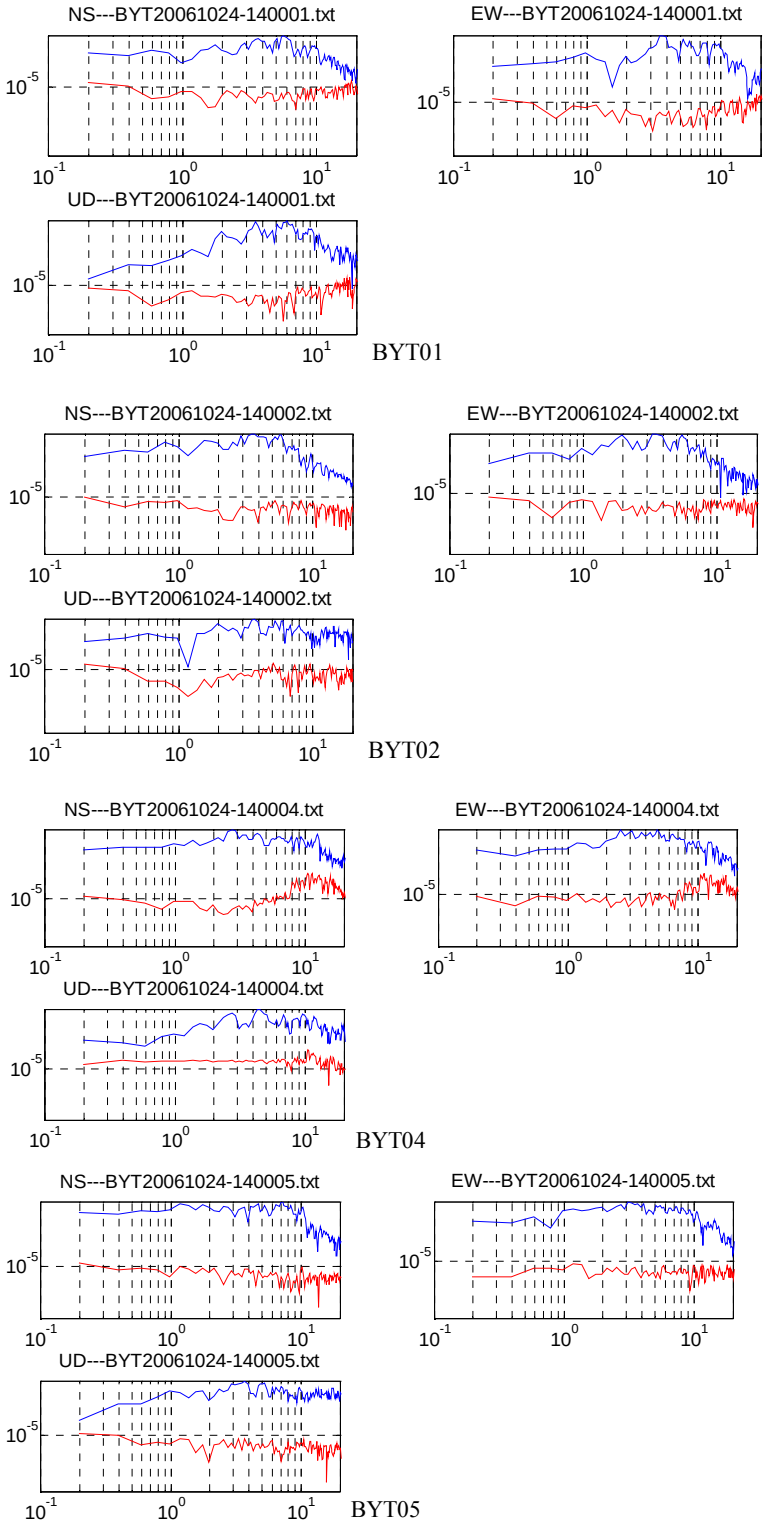

Figure 5.1. Comparison between the FAS of acceleration and noise for Gemlik Gulf Earthquake of October 2006 at BYT01, BYT02, BYT04 and BYT05 stations

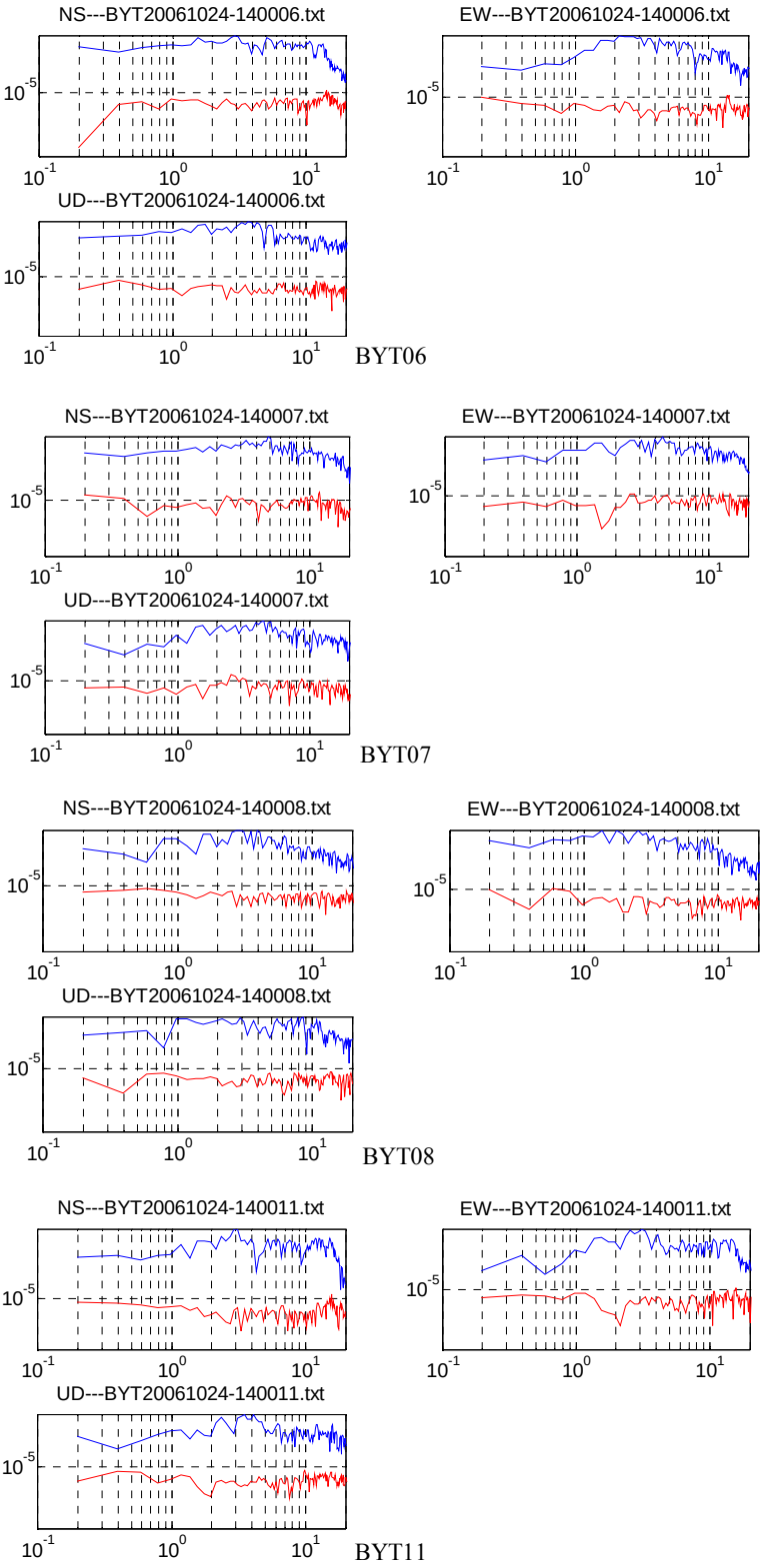

Figure 5.2. Comparison between the FAS of acceleration and noise for Gemlik Gulf Earthquake of October 2006 at BYT06, BYT07, BYT08 and BYT11 stations

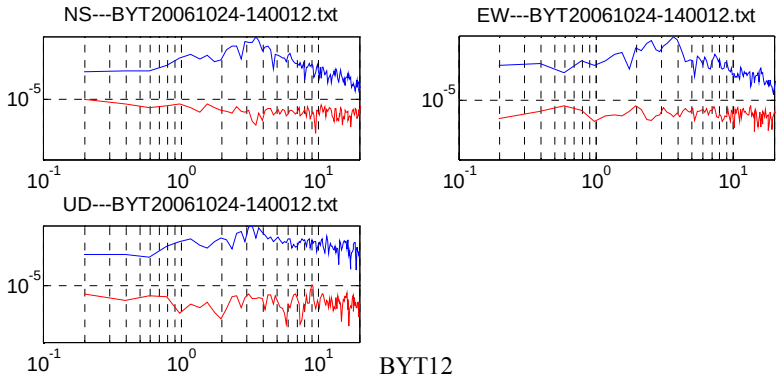

Figure 5.3. Comparison between the FAS of acceleration and noise for Gemlik Gulf Earthquake of October 2006 at BYT12 station

5.2. Source Parameters

The source consisting of single asperity is divided into identical subfaults corresponding to rupture area of small event. In chapter four, rupture area of small event was found to be 0.49 km^2. The seismic moment of each scenario was estimated with the help of Equation 4.23 and located in Table 5.1. Calculation is simplified via taking the value of the stress drop ratio between small and large event as $1\,(C=1)$. By scaling of source parameters between large and small events (Kanamori and Anderson, 1975), N values for each scenario case can be calculated according to Equation 4.16. The value of rupture velocity V_r equals 2.8 km/sec corresponding to 0.8 times the shear wave velocity of 3.5 km/sec (Hartzell and Helmberger, 1982).

In most slip model inversions, the faults with rectangular dimensions are chosen to be at least large enough to accommodate the entire fault rupture, and so they generally overestimate the actual dimensions of the rupture area (Somerville *et al*., 1999), in this study a rectangular-shaped strike-slip fault was considered for each scenario case and rectangular shape with two to one asperity dimension ratio was used in the computations in conformity to the study by Sørensen *et al*. (2007). A rupture was assumed to initiate at the beginning, middle and end point of the asperity and propagate circularly at given velocity.

In section four, rise time of Gemlik Earthquake was found according to the Equation 4.22 evaluated by Hanks and McGuire (1981). Rise time belonging to each scenario corresponds to N times source duration of Gemlik Earthquake.

5.2.1. Estimation of Source Parameters and Calculation

The most important asperity parameters are its area, location, stress drop, seismic moment, rise time and rupture velocity. The total asperity area S_a for every fault segment of fault rupture area S_f was calculated using the empirical ratio (Somerville *et al*., 1999):

$$S_a / S_f = 0.22 \tag{5.1}$$

Results from a dynamic model for rupture of a circular fault (with radius R_f) with an asperity (with radius r_a) at its center Das and Kostrov (1986) suggest that the ratio between the asperity stress drop and the fault average stress drop is approximately equal to r_a / R_f. This combined with Equation (5.1) yields a value for this ratio of 0.47. The total seismic moment for an asperity model can be calculated as:

$$M_0 = (16/7)\Delta\sigma_{ave} r_a R_f^{\,2} (24/7\pi)^2 \tag{5.2}$$

According to Das and Kostrov (1986), substituting Equation (5.1) into Equation (5.2), the following equation is obtained:

$$M_0 = 0.229\Delta\sigma_{ave} S_f^{\,3/2} \tag{5.3}$$

Equation (5.3) gives the total seismic moment of the asperity model (in Nm) in terms of the average stress drop $\Delta\sigma_{ave}$, and the total rupture area $S_f\,(\mathrm{m}^2)$. It is assumed that value of average stress drop is equal to the background region stress drop of scenario earthquakes. This assumption is justified because the asperity area is specified as only 20 per cent of the total area so a weighted average of the stress drop across the fault plane will be close to the background stress drop value. The asperity stress drop is about twice

the average stress drop. With Equation 5.3, asperity stress drop was obtained via multiplying the value of $\Delta\sigma_{ave}$ by two (Pulido *et al.*, 2004).

The locations of the asperities in each fault plane are defined by considering the seismicity. Concerned area lacks of detailed seismicity studies, so the location of the asperity is changed by means of starting rupture at the beginning, middle and end of the asperity (latitude and longitude of R.S.P for each scenario case are fixed).

Near-fault ground motion recordings in the strike-normal and strike-parallel components were archived in order to observe rupture directivity effects special to near field ground motion (Somerville, 2002). Accordingly, near-fault ground motion recordings should be divided in the strike-normal and strike-parallel components. The rotation of the two recorded components North (N) and East (E) into strike-parallel and strike-normal components SP and SN is accomplished using the following transformations:

$$SP = N \cos Ø + E \sin Ø \tag{5.4}$$

$$SN = -N \sin Ø + E \cos Ø \tag{5.5}$$

where Ø is the strike of the fault measured clockwise from North.

Scenario simulations were started taking the focal mechanism proposed by KOERI (strike-slip, strike 316.83, dip 86.55 and rake 156.91) as basis.

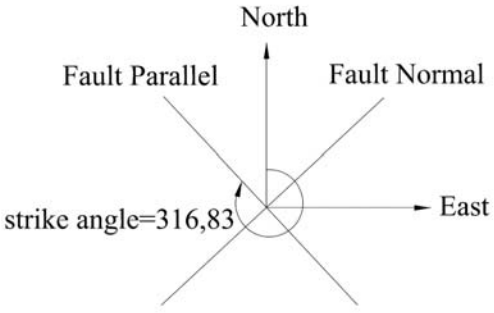

Figure 5.4. Illustration of fault location according to strike angle

It was assumed that the rupture was initiated at a deep level in the asperity for each of the scenario earthquakes. Displacement, velocity, acceleration and acceleration spectra waveforms belonging to target events were plotted when the rupture started at the beginning, midpoint and endpoint of the asperity.

Table 5.1. Mainshock and scenarios used in the EGF simulation

	Date Yr/Mo/Hr:Min(GMT)	Lat (deg)	Long (deg)	Depth (km)	M_w	M_0 (Nm)
Gemlik Earthquake	24/10/2006(14:00)	40.422	28.993	20	4.8	$10^{16.25}$
Scenario 5.8	———	40.422	28.993	20	5.8	$10^{17.75}$
Scenario 6.8	———	40.422	28.993	20	6.8	$10^{19.25}$

Table 5.2. Source parameters for scenario earthquakes generation areas

	N	*C*	Size(km) (length x width)	Rupture Vel.(km/sec)	Rise Time(sec)	Stress Drop (Mpa)
Scenario 5.8	4x2	1	2.8 x 1.4	2.8	0.93	65.2
Scenario 6.8	13x7	1	9.1 x 4.9	2.8	3.1	53.08

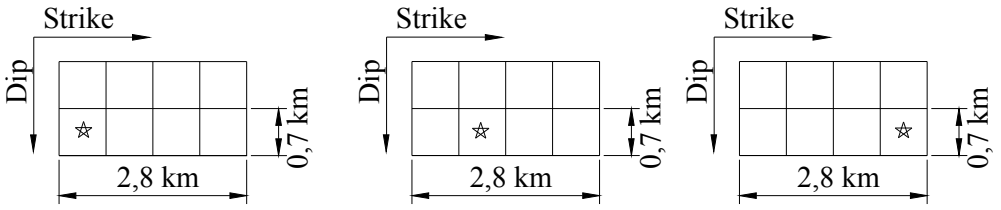

(a) (b) (c)

Figure 5.5. RSP at the beginning (a), middle (b) and end (c) of asperity for 5.8 scenario earthquake

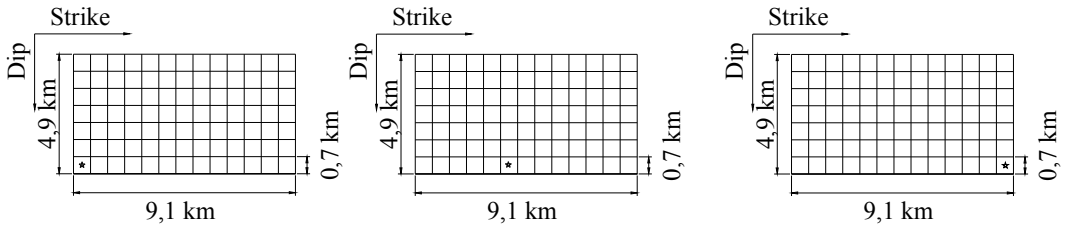

(a) (b) (c)

Figure 5.6. RSP at the beginning (a), middle (b) and end (c) of asperity for 6.8 scenario earthquake

Given in Appendix C are the figures generated with the data of scenario earthquakes which are obtained by repeating the EGF simulation with different rupture starting points in the asperity.

Figures from 5.7 to 5.18 compare the attenuation with distance of simulated PGA and PGV with various empirical attenuation relationships that are Akkar and Bommer (2007), Campbell and Bozorgnia (2006) NGA, Boore and Atkinson (2007) NGA empirical attenuation relationship for peak ground velocity and Boore *et al*. (1997), Campbell and Bozorgnia (2003), Campbell and Bozorgnia (2006) NGA, Boore and Atkinson (2007) NGA empirical attenuation relationship for peak ground acceleration. In these figures, written curve names as Boore 1997, Campbell (2003), Boore NGA, Campbell NGA and Bommer in legend actually respresent Boore *et al*. (1997), Campbell and Bozorgnia (2003), Boore and Atkinson (2007) NGA, Campbell and Bozorgnia (2006) NGA, Akkar and Bommer (2007) attenuation curves.

In this study, fault type is strike-slip and site classes used in scenario simulations are NEHRP site class C (for BYT01, BYT02, BYT08, BYT11, BYT12) and NEHRP site class D (for BYT02, BYT04, BYT05, BYT06, BYT07 and BYT11). Since V_{S30} value of the BYT02 and BYT11 stations is not known, there is no information about which site class they conform to according to NEHRP. For this reason, BYT02 and BYT11 stations were classified in both NEHRP site class C and NEHRP site class D.

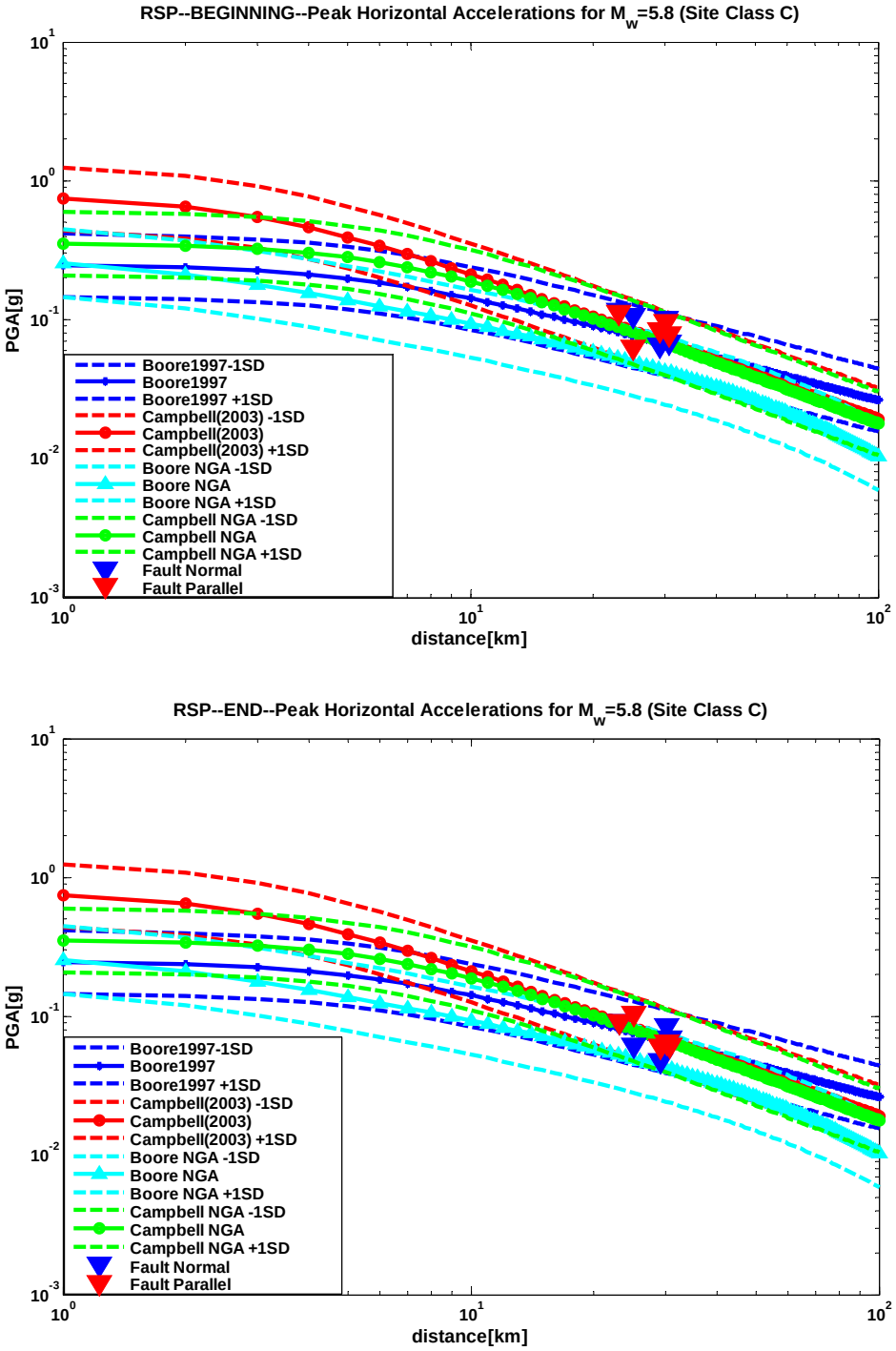

Figure 5.7. Comparison of PGA due to FN and FP components of $M_w = 5.8$ earthquake at BYT01, BYT02, BYT08, BYT11 and BYT12 stations with empirical attenuation relations according to NEHRP site class C for different R.S.P alternatives (RSP at the beginning and end of asperity)

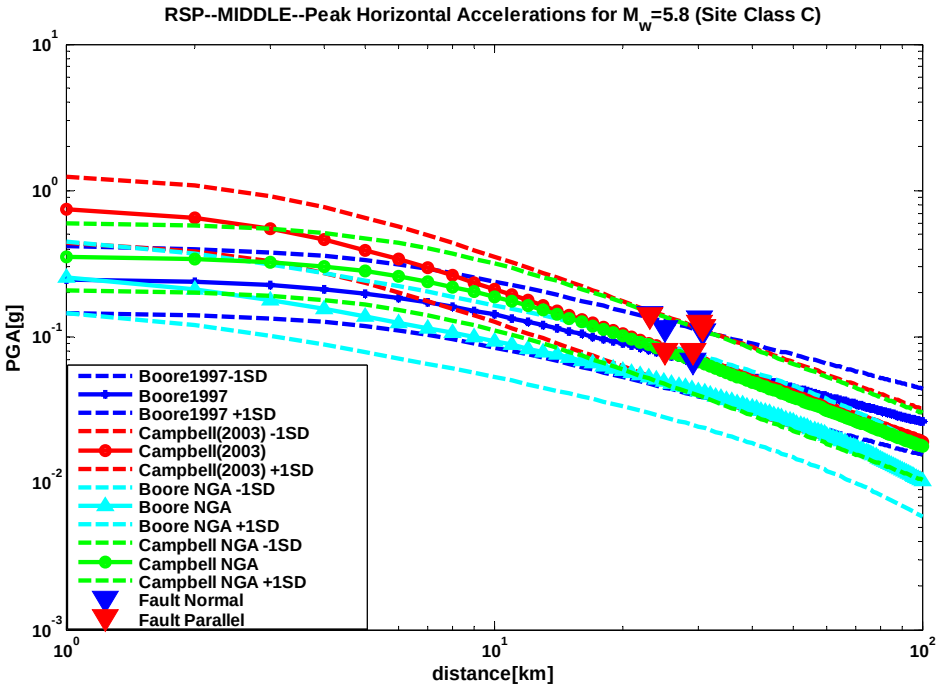

Figure 5.8. Comparison of PGA due to FN and FP components of $M_w = 5.8$ earthquake at BYT01, BYT02, BYT08, BYT11 and BYT12 stations with empirical attenuation relations according to NEHRP site class C for different R.S.P alternatives (RSP at the middle of asperity)

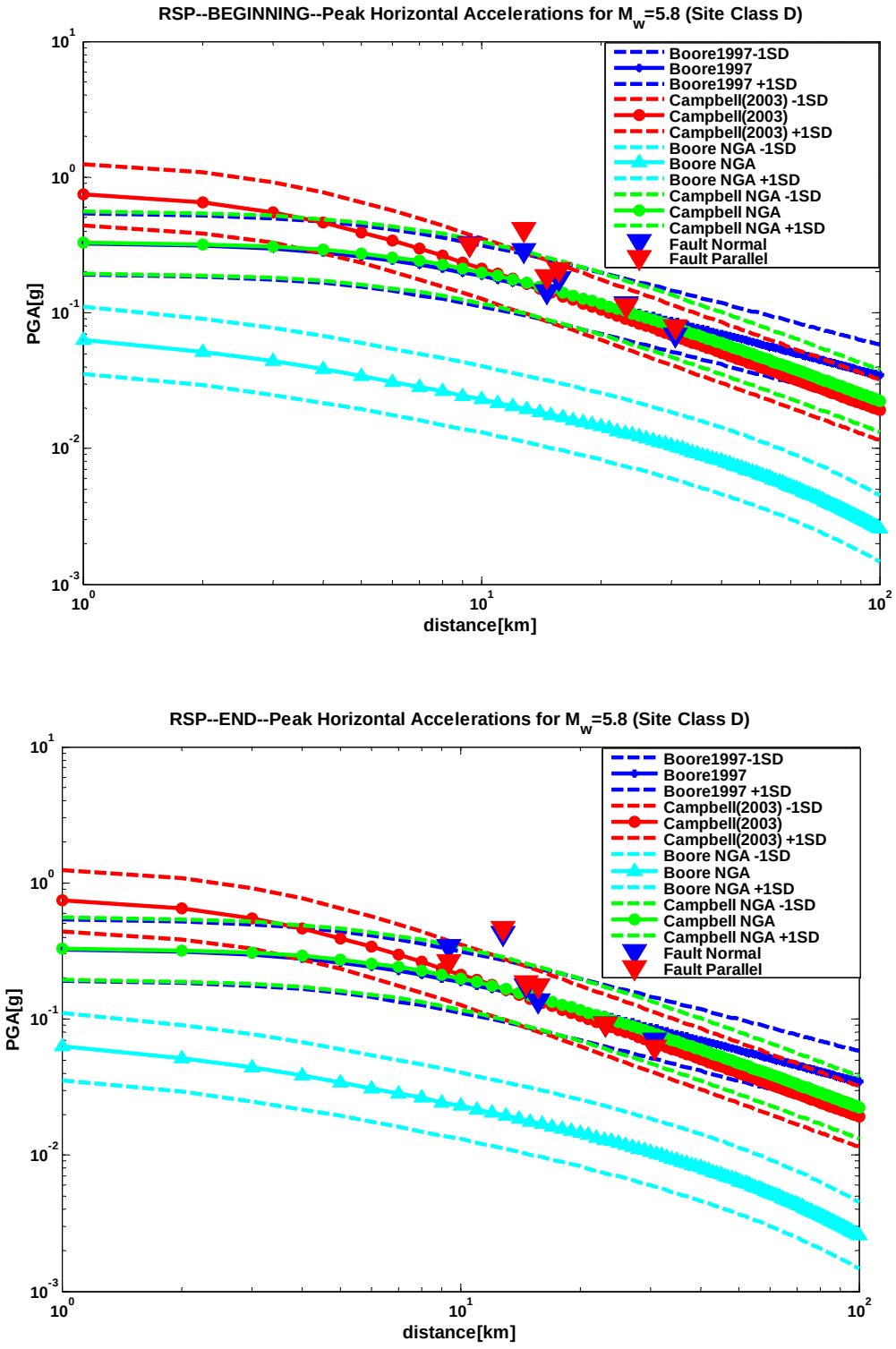

Figure 5.9. Comparison of PGA due to FN and FP components of $M_w = 5.8$ earthquake at BYT02, BYT04, BYT05, BYT06, BYT07 and BYT11 stations with empirical attenuation relations according to NEHRP site class D for different R.S.P alternatives (RSP at the beginning and end of asperity)

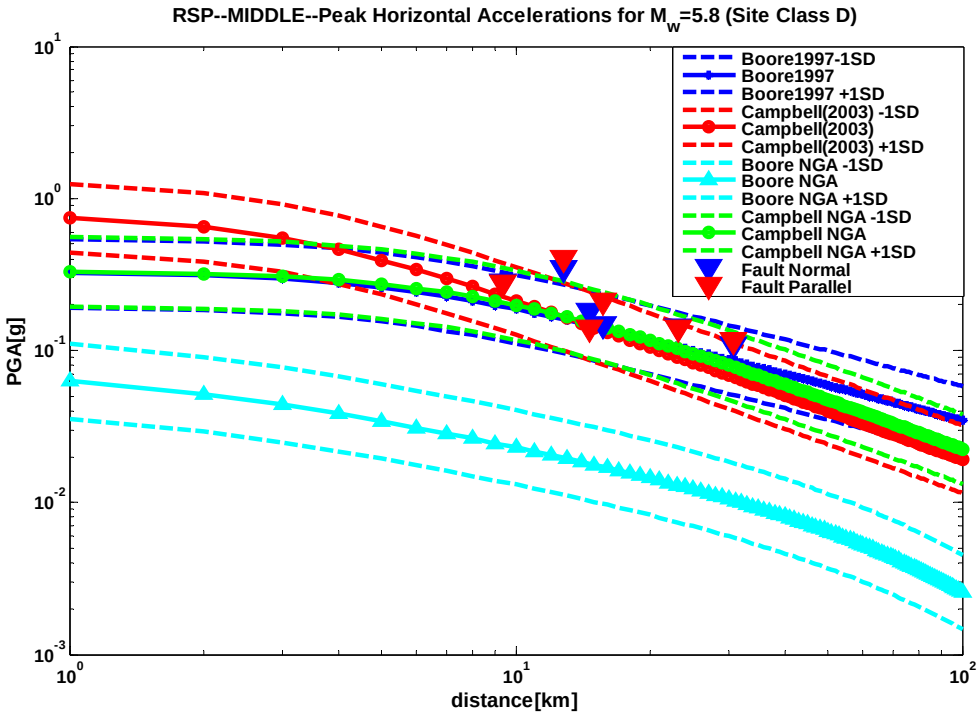

Figure 5.10. Comparison of PGA due to FN and FP components of $M_w = 5.8$ earthquake at BYT02, BYT04, BYT05, BYT06, BYT07 and BYT11 stations with empirical attenuation relations according to NEHRP site class D for different R.S.P alternatives (RSP at the middle of asperity)

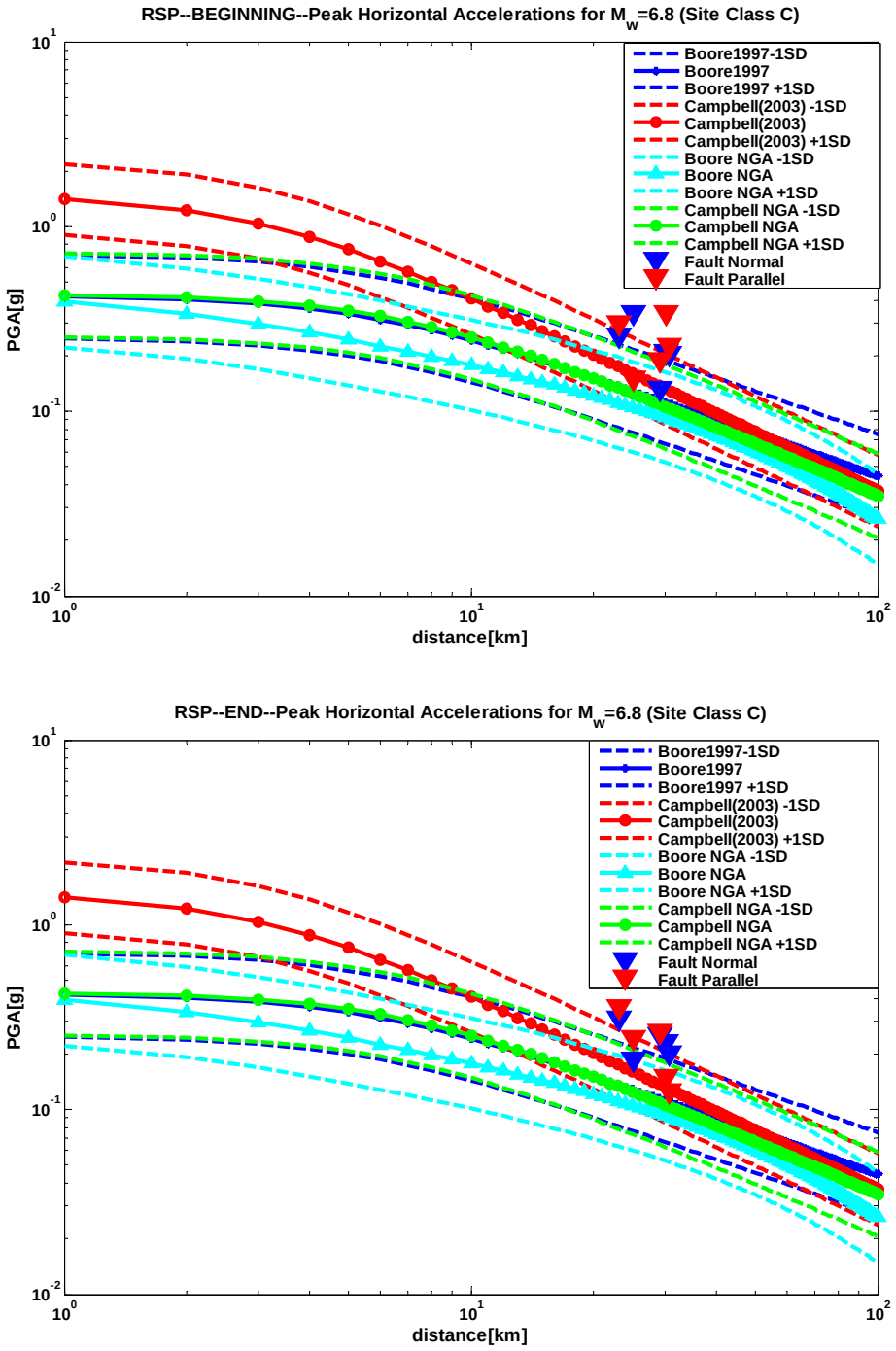

Figure 5.11. Comparison of PGA due to FN and FP components of $M_w = 6.8$ earthquake at BYT01, BYT02, BYT08, BYT11 and BYT12 stations with empirical attenuation relations according to NEHRP site class C for different R.S.P alternatives (RSP at the beginning and end of asperity)

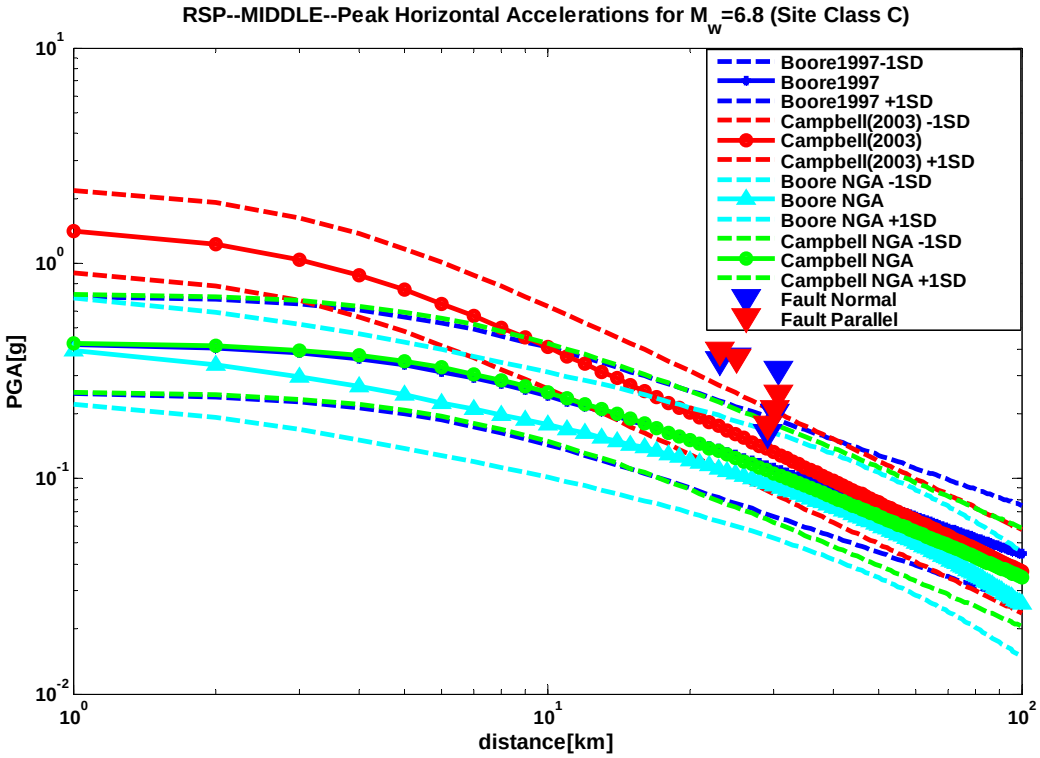

Figure 5.12. Comparison of PGA due to FN and FP components of $M_w = 6.8$ earthquake at BYT01, BYT02, BYT08, BYT11 and BYT12 stations with empirical attenuation relations according to NEHRP site class C for different R.S.P alternatives (RSP at the middle of asperity)

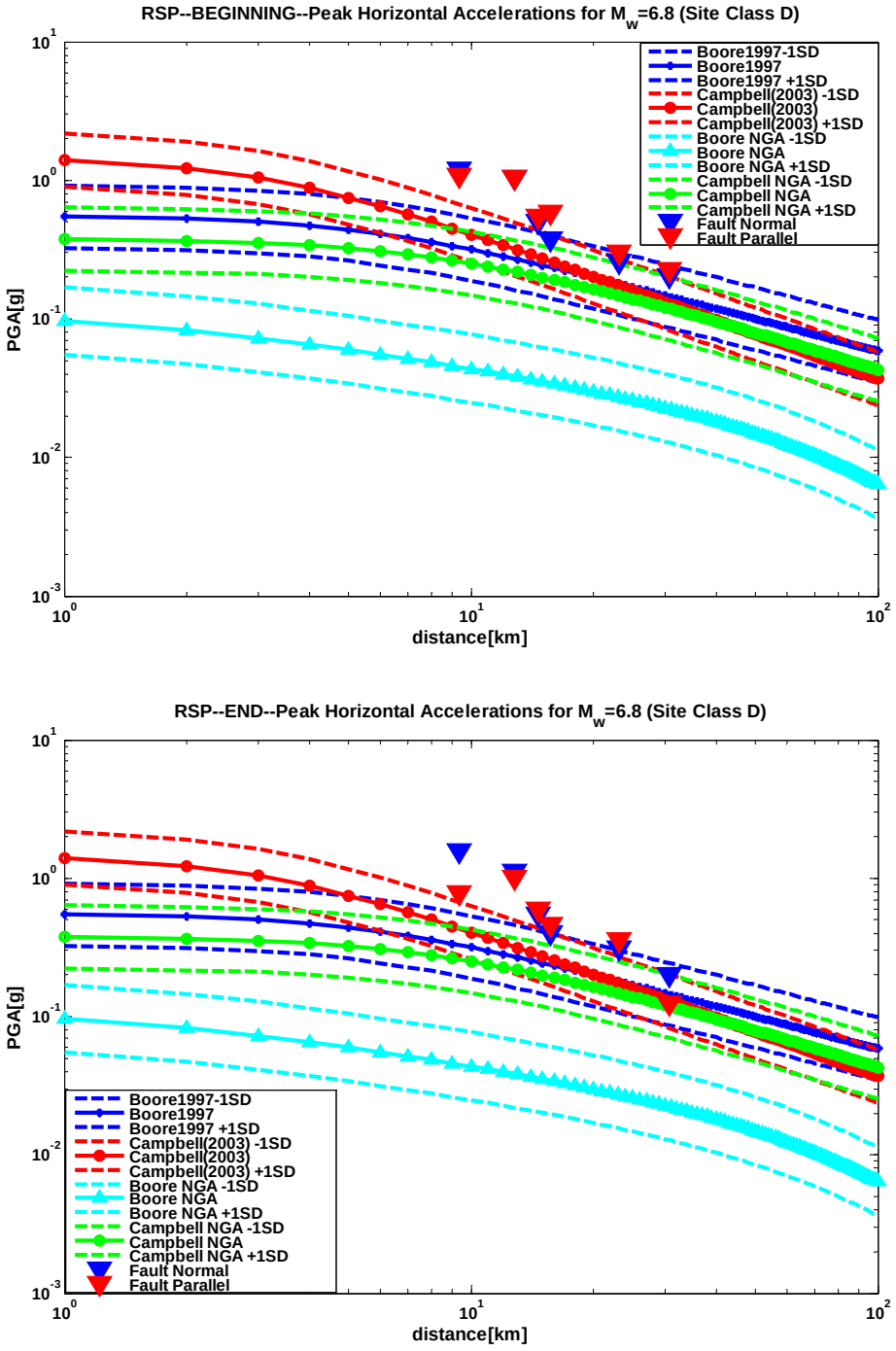

Figure 5.13. Comparison of PGA due to FN and FP components of $M_w = 6.8$ earthquake at BYT02, BYT04, BYT05, BYT06, BYT07 and BYT11 stations with empirical attenuation relations according to NEHRP site class D for different R.S.P alternatives (RSP at the beginning and end of asperity)

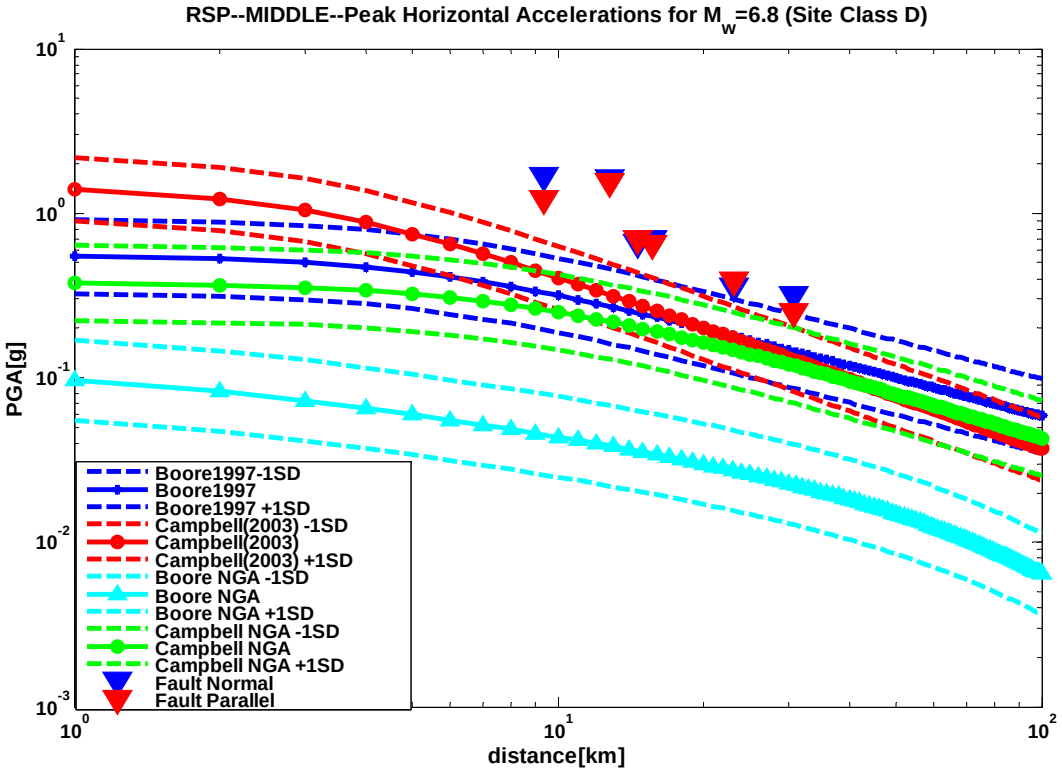

Figure 5.14. Comparison of PGA due to FN and FP components of $M_w = 6.8$ earthquake at BYT02, BYT04, BYT05, BYT06, BYT07 and BYT11 stations with empirical attenuation relations according to NEHRP site class D for different R.S.P alternatives (RSP at the middle of asperity)

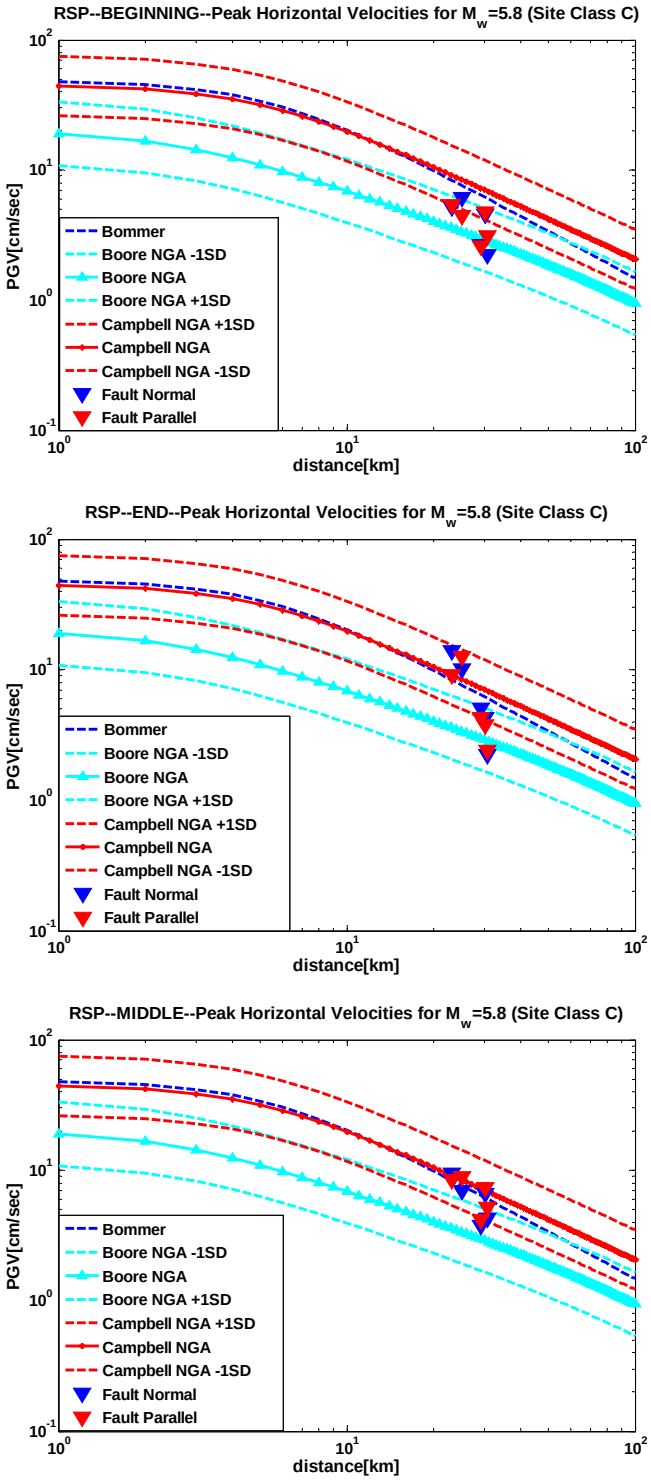

Figure 5.15. Comparison of PGV due to FN and FP components of $M_w = 5.8$ earthquake at BYT01, BYT02, BYT08, BYT11 and BYT12 stations with empirical attenuation relations according to NEHRP site class C for different R.S.P alternatives

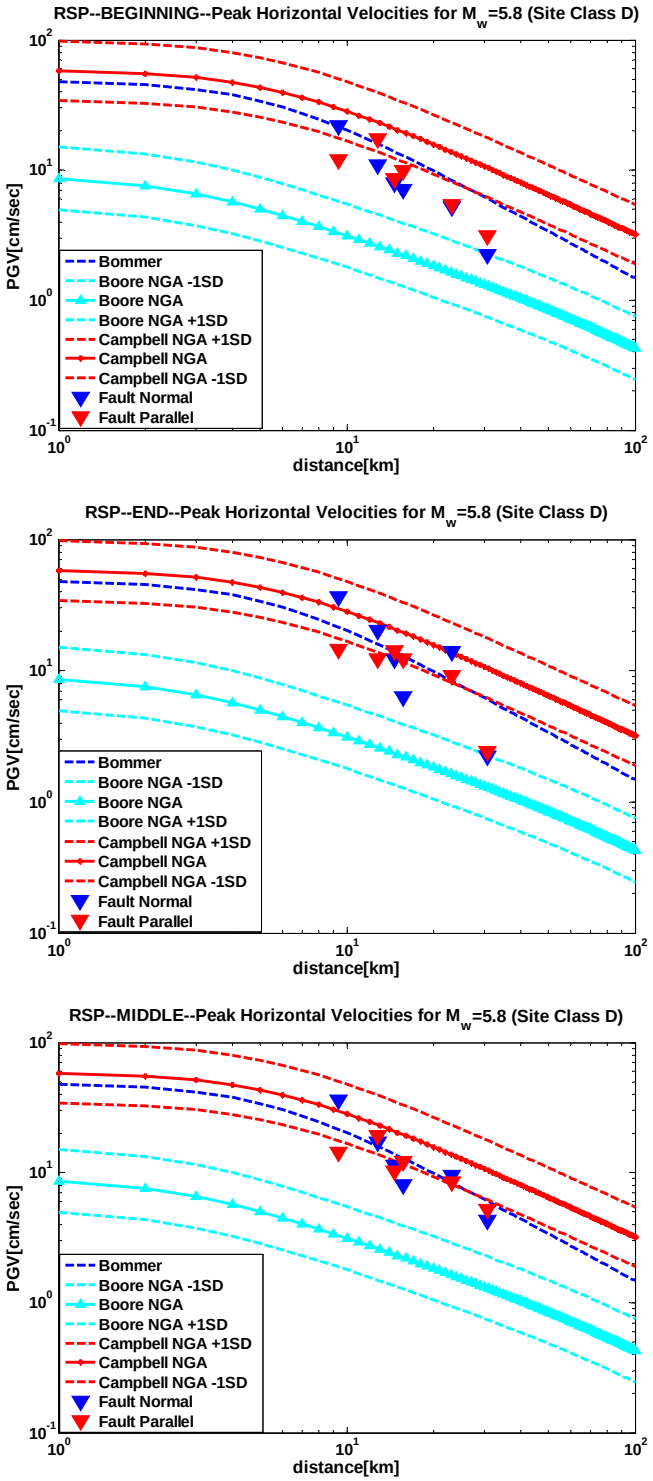

Figure 5.16. Comparison of PGV due to FN and FP components of $M_w = 5.8$ earthquake at BYT02, BYT04, BYT05, BYT06, BYT07 and BYT11 stations with empirical attenuation relations according to NEHRP site class D for different R.S.P alternatives

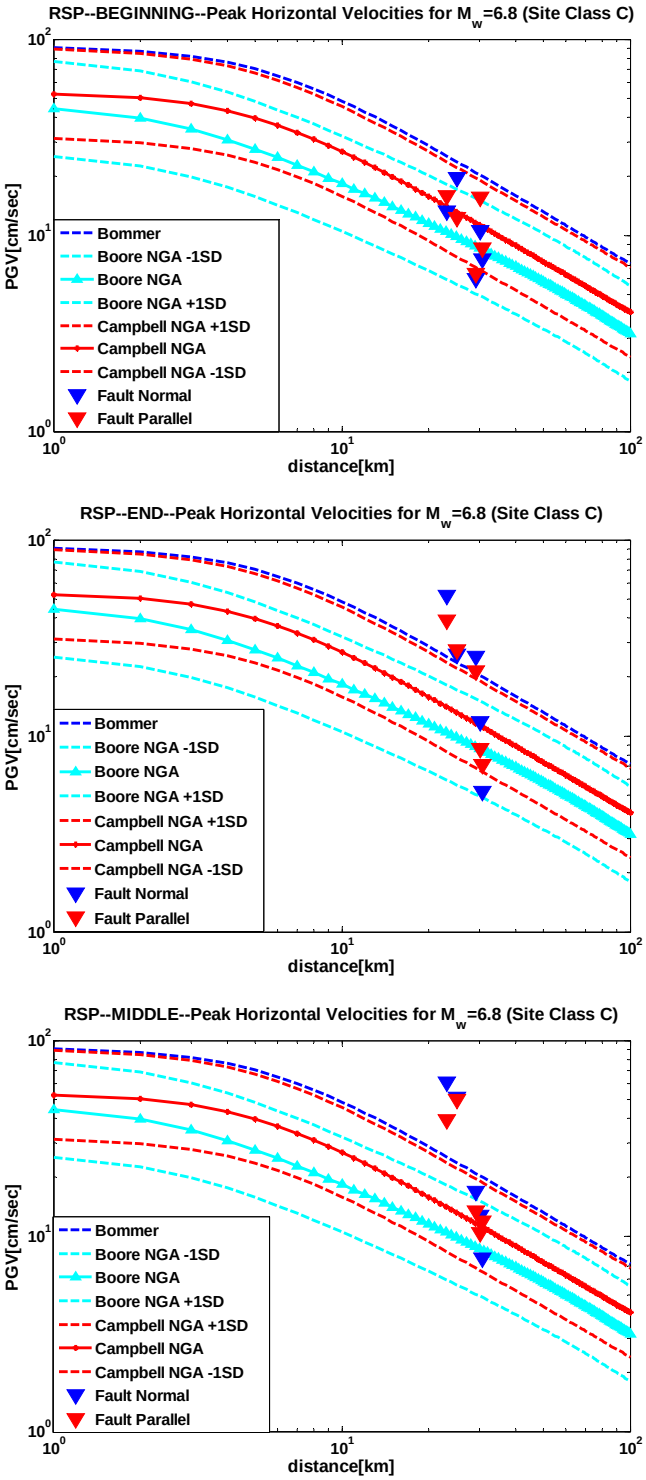

Figure 5.17. Comparison of PGV due to FN and FP components of $M_w = 6.8$ earthquake at BYT01, BYT02, BYT08, BYT11 and BYT12 stations with empirical attenuation relations according to NEHRP site class C for different R.S.P alternatives

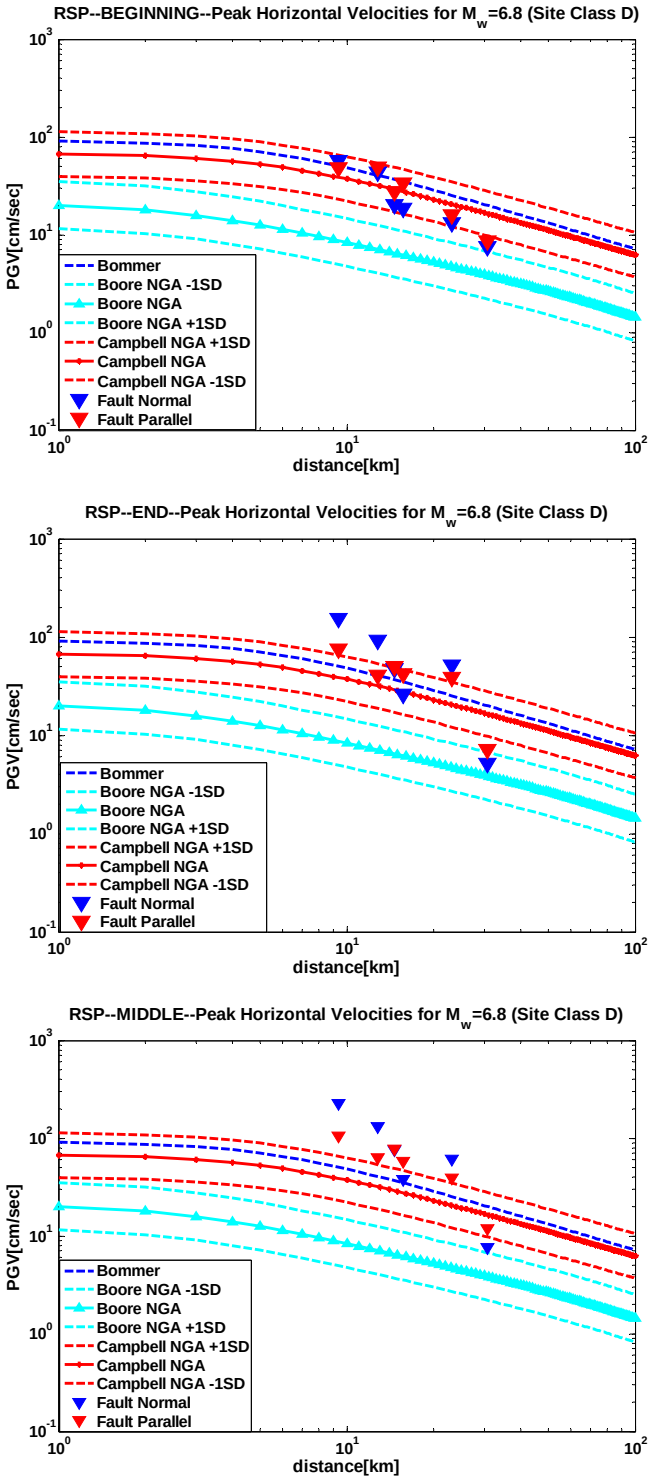

Figure 5.18. Comparison of PGV due to FN and FP components of $M_w = 6.8$ earthquake at BYT02, BYT04, BYT05, BYT06, BYT07 and BYT11 stations with empirical attenuation relations according to NEHRP site class D for different R.S.P alternatives

Simulated acceleration spectra formed on the basis of piece-wise exact method were compared with the current Turkish Seismic Design Code (TSDC 2007) at different rupture starting points (Aydinoğlu, 1998).

Table 5.3. Comparison of the classification schemes in NEHRP-2000 and 2007 Turkish Code

2007 TURKISH CODE	2000 NEHRP REGULATIONS
Z1	B
Z2	C
Z3	D
Z4	E-F

The Spectral Acceleration Coefficient, $A(T)$, corresponding to five per cent damped elastic design acceleration spectrum normalised by the acceleration of gravity, g, is given by Eq. (5.6) (Aydinoğlu, 1998).

$$A(T)=A_o I\, S(T) \tag{5.6}$$

where ;

A_o : The effective ground acceleration coefficient

I : Building importance factor

$S(T)$: Spectrum coefficient

$$S(T)=1+1.5\, T / T_A \qquad (0 \le T \le T_A) \tag{5.7a}$$

$$S(T)=2.5 \qquad (T_A < T \le T_B) \tag{5.7b}$$

$$S(T)=2.5\, (T_B / T)^{0.8} \qquad (T > T_B) \tag{5.7c}$$

Spectrum characteristic periods, T_A and T_B, appearing in Equations 5.7a, b and c are specified in Table 5.4.

Table 5.4. Spectrum characteristic periods (T_A , T_B)

Local Site Class	T_A (second)	T_B (second)
Z1	0.10	0.30
Z2	0.15	0.40
Z3	0.15	0.60
Z4	0.20	0.90

In this calculation, the effective ground acceleration coefficient equals the value of 0.40 because concerned area is found in seismic zone one. Building importance factor was accepted to be one. NEHRP site classes C and D refer to Turkish Code site classes Z2 and Z3, respectively.

Figures from 5.19 to 5.22 compare simulated acceleration spectra drawn according to piece-wise exact method that is used in order to obtain acceleration versus time for different stations with different periods for FN, FP components and different RSP alternatives with the current Turkish Seismic Design Code (TSDC) for C and D site classes (In Turkish Code Z2 and Z3 site classes).

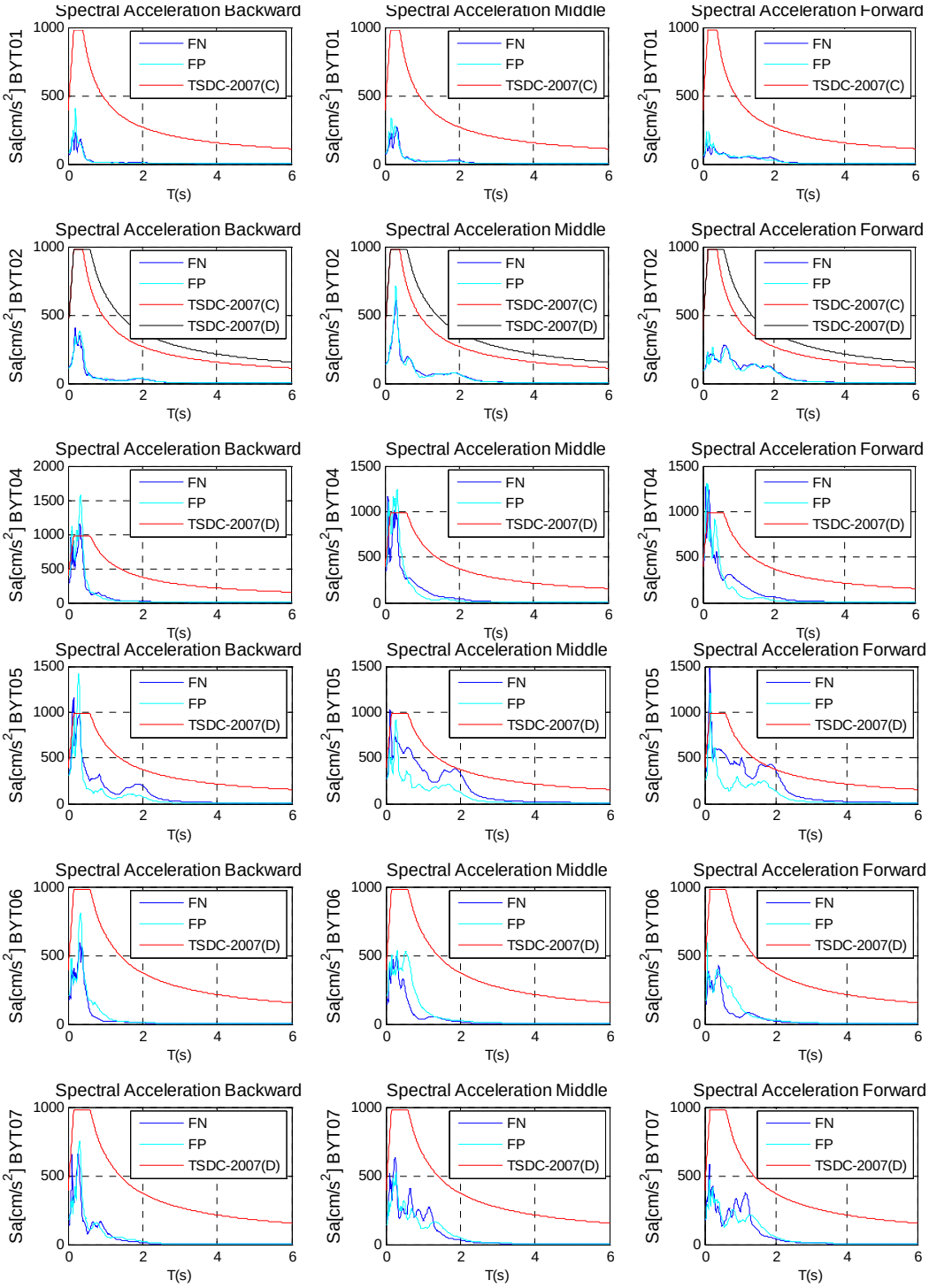

Figure 5.19. Comparison between simulated acceleration response spectra and the current Turkish Seismic Design Code (TSDC) at BYT01, BYT02, BYT04, BYT05, BYT06 and BYT07 stations for scenario 5.8

(RSP at the beginning, middle and end of the asperity)

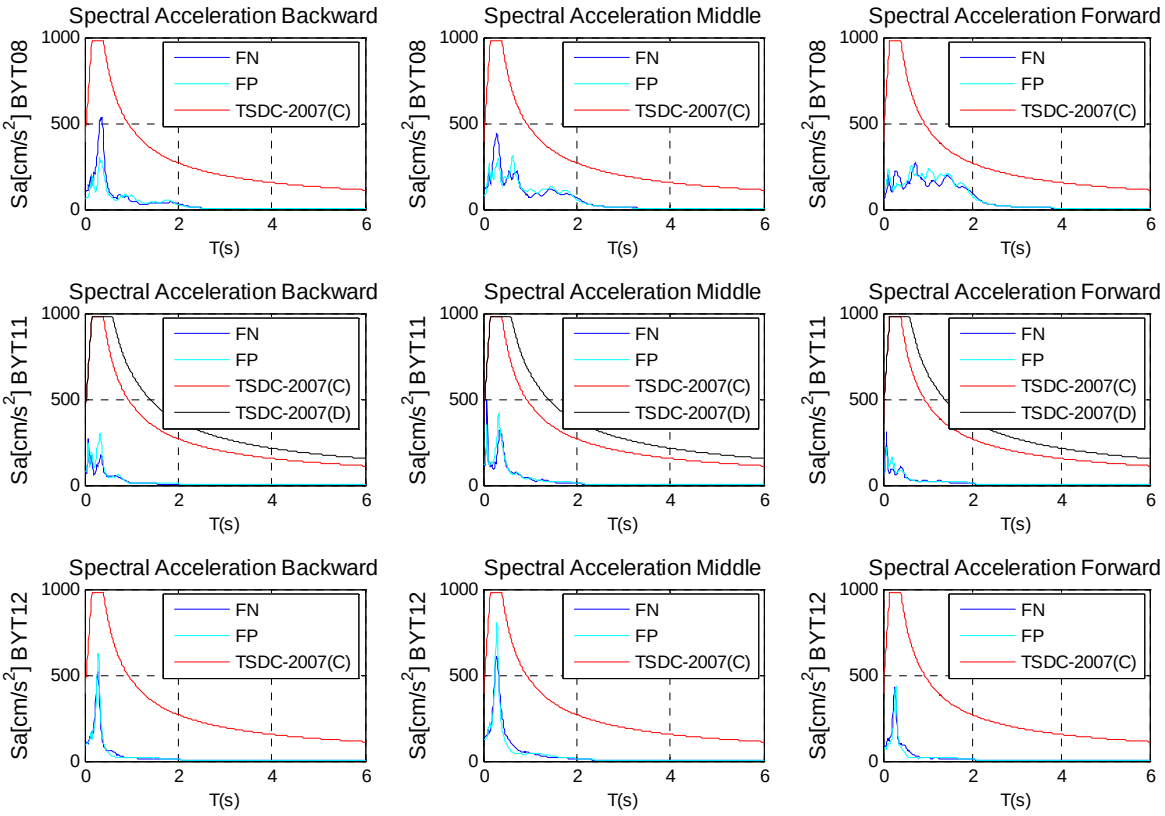

Figure 5.20. Comparison between simulated acceleration response spectra and the current Turkish Seismic Design Code (TSDC) at BYT08, BYT11 and BYT12 stations for scenario 5.8 (RSP at the beginning, middle and end of the asperity)

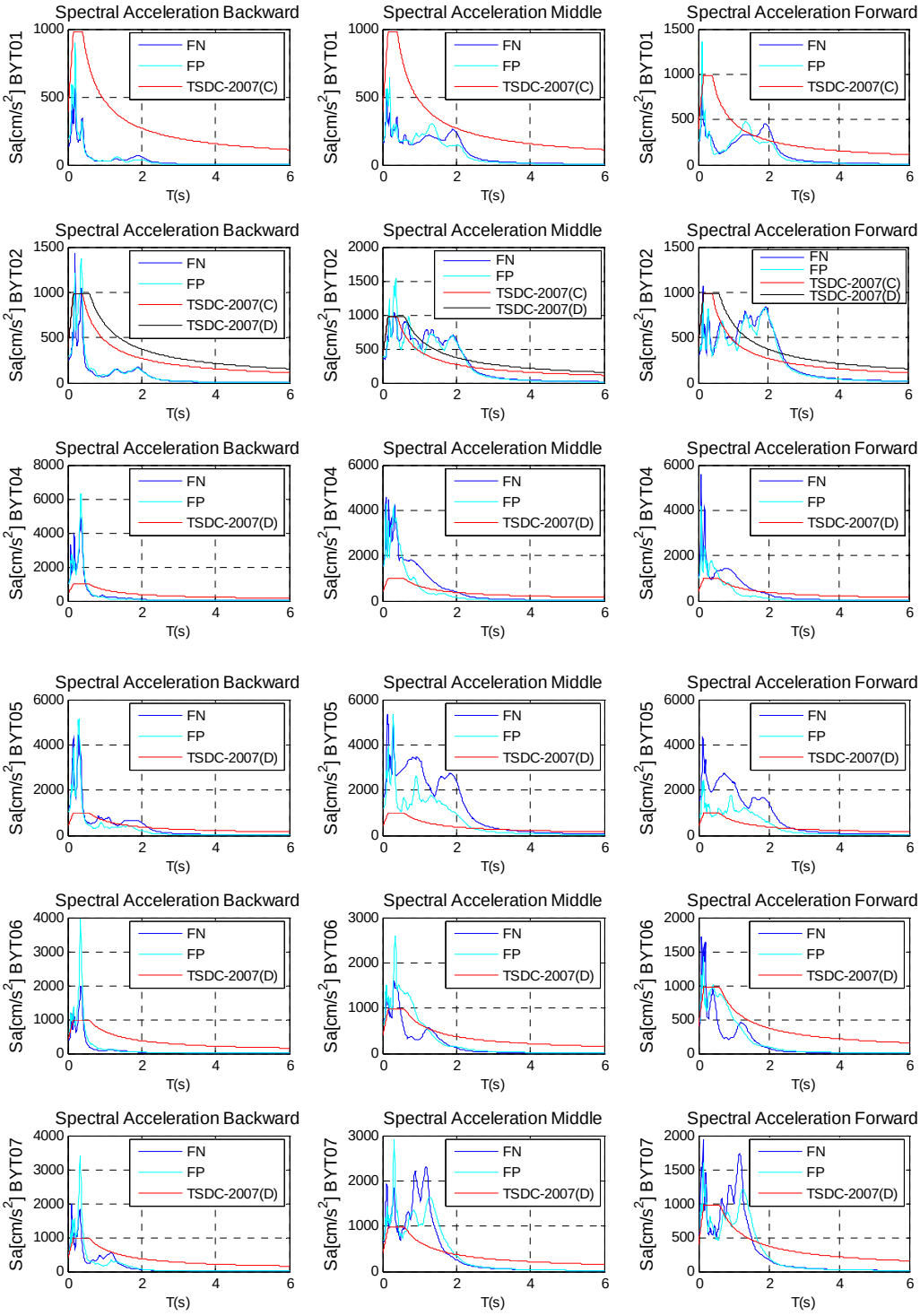

Figure 5.21. Comparison between simulated acceleration response spectra and the current Turkish Seismic Design Code (TSDC) at BYT01, BYT02, BYT04, BYT05, BYT06 and BYT07 stations for scenario 6.8
(RSP at the beginning, middle and end of the asperity)

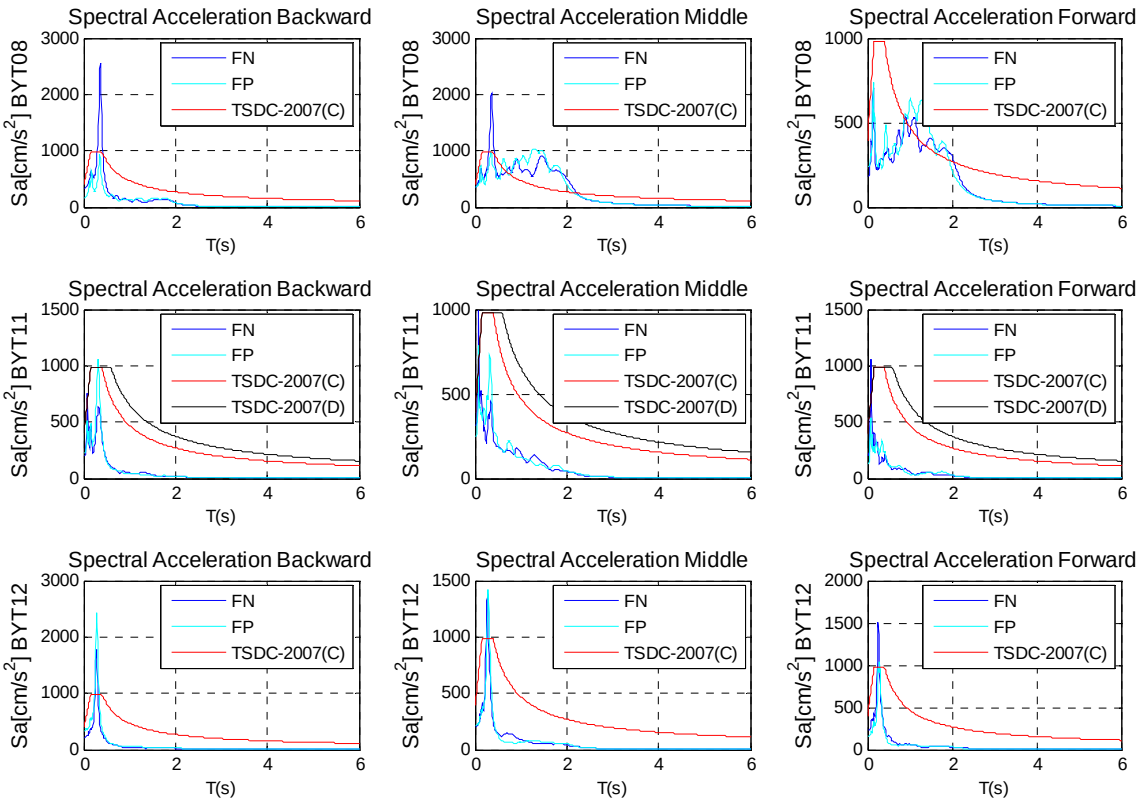

Figure 5.22. Comparison between simulated acceleration response spectra and the current Turkish Seismic Design Code (TSDC) at BYT08, BYT11 and BYT12 stations for scenario 6.8 (RSP at the beginning, middle and end of the asperity)

5.2.2. The Impacts of Various Source Parameters on PGA and PGV

In the prospect of the studies performed for Istanbul by Sørensen *et al*. (2007), a general knowledge about how the variability in source parameters affects PGA and PGV will be obtained.

5.2.2.1. Variability in Rise Time

The effect of the rise time on PGV is clear. Increasing the rise time decreases the PGV and vice versa. The effect on the PGAs is more scattered and diffuse. The general trend is a scattered reduction in PGA for both reduced and increased rise time with the largest impact in regions adjacent to the asperities. Letting the rise time vary randomly also causes a reduction in PGA.

5.2.2.2. Variability in Rupture Velocity

The simulation results show that the rupture velocity has a strong effect on the PGVs, especially in the forward directivity direction. Increasing the rupture velocity also increases the PGV, whereas a reduction in rupture velocity causes reduced PGVs. A similar effect is seen for the PGAs. Reduction of rupture velocity reduces the PGAs, whereas increased rupture velocity causes increased PGA.

5.2.2.3. Variability in Stress Drop

The effect of varying the stress drop is most significant on the PGA levels, which is reasonable because stress drop is only included directly in the high-frequency part of the calculations. Both PGV and PGA decrease when decreasing the absolute level of stress drop and increase for an increased stress drop, affecting a larger area around the rupturing fault for PGA. Reducing the stress drop ratio leads to a very strong increase in the ground motion near the asperities.

5.2.2.4. Summary and Conclusion concerning Variability in Some Source Parameters

The most important parameters for the ground-motion modeling, in terms of ground-shaking levels, are the location of the rupture initiation, stress drop, rise time, rupture velocity, and the anelastic attenuation for the studied region. The impact of these parameters in frequency bands of engineering interest varies, however. From an engineering perspective, the most important parameters are the stress drop and the location of rupture initiation. Also rupture velocity and rise time will play an important role because of their strong effect on PGV. Unfortunately, these parameters are difficult to predict for future earthquakes, but detailed studies should be made ahead of ground-motion modeling, and in case of large uncertainties, extreme values should be considered in the input to the models to set bounds on the predicted ground motions.

The effect of rise time is mainly observed in regions adjacent to the asperities where most of the slip occurs, but also tends to distribute in the direction of rupture propagation.

The rupture velocity, on the other hand, has an important effect along the whole rupture and the largest variations are seen along the forward directivity direction. In both cases the effect on PGA is scattered and, in general, distributed over larger regions than the PGVs.

Based on analysis of the effect of input parameters on ground-motion simulation results following conclusions can be drawn:

- Rise time, rupture velocity, rupture initiation point, and stress drop are the most significant parameters in terms of variations in ground-shaking levels. However, these parameters have their effect in different frequency bands and their engineering significance therefore varies.
- High-frequency ground motion is mainly controlled by the stress drop that has a strong effect on PGA and PGA attenuation.
- Rupture velocity and rise time have a strong effect on the PGV values controlled by the coherent low-frequency ground motion.

Future efforts should focus on improving ability to accurately estimate the most critical parameters influencing the ground motion, namely the rise time, rupture velocity, rupture initiation point, the stress drop, and the potential asperity locations for future earthquakes.

5.3. Empirical Near-Source Attenuation Relationships for Horizontal Components of PGA and PGV

The attenuation relationships are considered to be appropriate for predicting free-field amplitudes of horizontal and vertical components. The scope of this study is associated with horizontal components. Some empirical attenuation relationships are presented for predicting near-field horizontal components of peak ground acceleration (PGA) and peak ground velocity (PGV). Methodology of some empirical attenuation relationships utilized in this study is investigated and presented as follows.

5.3.1. Boore *et.al.* (1997) Attenuation Relationship

The Boore *et al*. (1997) PGA and Spectral Acceleration attenuation relationship are given by the following expressions. The equations predict the random horizontal component peak acceleration and five per cent damped pseudo acceleration response spectra in terms of moment magnitude, distance and site conditions for strike-slip, reverse slip or unspecified faulting mechanism. Site conditions are represented by the shear wave velocity averaged over 30 m, and recommended values of average shear wave velocity are given for typical rock and soil sites and for site categories used in the NEHRP (National Earthquake Hazard Reduction Program) seismic code provisions.

Table 5.5. Recommended values of average shear wave velocity (Boore *et al.*, 1997)

NEHRP Site Class B	1070 m/s
NEHRP Site Class C	520 m/s
NEHRP Site Class D	250 m/s
Rock	620 m/s
Soil	310 m/s

The earthquake mechanism is expressed with the help of a coefficient, namely b_1.

The ground motion estimation equation is:

$$\ln(\overline{Y}) = b_1 + b_2(\mathrm{M}-6) + b_3(\mathrm{M}-6)^2 + b_5 \ln r_{rs} + b_V \ln(V_S / V_A) \tag{5.8}$$

where;

$$r_{rs} = (r_{jb}{}^2 + h^2)^{1/2} \tag{5.9}$$

In Equation 5.8;

$\overline{Y}$ = peak horizontal accelerations in g

M = moment magnitude $\mathrm{M} \geq 5.00$

r_{rs} = closest distance from rupture to the station in km $r_{rs} \geq 20$ km

r_{jb} = closest horizontal distance from the station to a point in km

V_S = average shear-wave velocity to the depth of 30 m (m/s) (Table 5.5)

b_1 = b_{1SS} for strike-slip earthquakes

b_1 = b_{1RS} for reverse-slip earthquakes

b_1 = b_{1ALL} if mechanism is not specified

b_{1SS}, b_{1RS}, b_{1ALL}, b_2, b_3, b_5, b_V, V_A and h = Coefficients presented in Table 5.6.

The standard deviation of the natural logarithm of the ground motion is represented by $\sigma_{\ln \overline{Y}}$.

Table 5.6. The standard deviation PGA and coefficients for PGA (Boore *et al.*, 1997)

Period	b_{1SS}	b_{1RS}	b_{1AAL}	b_2	b_3	b_5	b_V	V_A	h	$\sigma_{\ln \overline{Y}}$
PGA	-0.313	-0.117	-0.242	0.527	0.000	-0.778	-0.371	1396	5.57	0.520

5.3.2. Updated Near-Source Ground-Motion (Attenuation) Relations for the Horizontal and Vertical Components of Peak Ground Acceleration and Acceleration Response Spectra by Campbell and Bozorgnia (2003)

The ground-motion relations (Campbell and Bozorgnia, 2003) for both the average horizontal and vertical components of PGA and PSA are given by

$$\ln \overline{Y} = c_1 + f_1(\mathrm{M_W}) + c_4 \ln \sqrt{f_2(\mathrm{M_W}, r_{seis}, S)} + f_3(F) + f_4(S) + f_5(HW, F, \mathrm{M_W}, r_{seis}) + \varepsilon \tag{5.10}$$

where the magnitude scaling characteristics are given by

$$f_1(\mathrm{M_W}) = c_2 + \mathrm{M_W} + c_3(8.5 - \mathrm{M_W})^2 \tag{5.11}$$

the distance scaling characteristics are given by

$$f_2(\mathrm{M_W}, r_{seis}, S) = r^2{}_{seis} + g(S)^2(\exp[c_8 \mathrm{M_W} + c_9(8.5 - \mathrm{M_W})^2])^2 \tag{5.12}$$

in which the near-source effect of local site conditions is given by

$$g(S) = c_5 + c_6(S_{VFS} + S_{SR}) + c_7 S_{FR} \tag{5.13}$$

the effect of faulting mechanism is given by

$$f_3(F) = c_{10} F_{RV} + c_{11} F_{TH} \tag{5.14}$$

the far-source effect of local site conditions is given by

$$f_4(S) = c_{12} S_{VFS} + c_{13} S_{SR} + c_{14} S_{FR} \tag{5.15}$$

and the effect of the hanging wall (HW) is given by

$$f_5(HW, F, \mathrm{M_W}, r_{seis}) = HW \; f_3(F) \, f_{HW}(\mathrm{M_W}) \, f_{HW}(r_{seis}) \tag{5.16}$$

where

$$HW = (S_{VFS} + S_{SR} + S_{FR}) \begin{cases} 0 & \text{for} \quad r_{jb} \geq 5 \text{ km} \quad \delta > 70^0 \\ (5 - r_{jb})/5 & \text{for} \quad r_{jb} < 5 \text{ km} \end{cases} \tag{5.17}$$

$$f_{HW}(\mathrm{M_W}) = \begin{cases} 0 & \text{for} \quad \mathrm{M_W} < 5.5 \\ \mathrm{M_W} - 5.5 & \text{for} \quad 5.5 \leq \mathrm{M_W} \leq 6.5 \\ 1 & \text{for} \quad \mathrm{M_W} > 6.5 \end{cases} \tag{5.18}$$

and

$$f_{HW}(r_{seis}) = \begin{cases} c_{15}(r_{seis}/8) & \text{for} \quad r_{seis} < 8 \text{ km} \\ c_{15} & \text{for} \quad r_{seis} \geq 8 \text{ km} \end{cases} \tag{5.19}$$

In the previous equations, $\overline{Y}$ is either the vertical component, $\overline{Y}_V$, or the average horizontal component, $\overline{Y}_H$, of PGA or five per cent damped PSA in g (g = 981 cm/sec^2); $\mathrm{M_W}$ is moment magnitude; r_{seis} is the closest distance to seismogenic rupture in kilometers; r_{jb} is the closest distance to the surface projection of fault rupture in kilometers (Boore *et al.*, 1997); δ is fault dip in degrees; $S_{VFS} = 1$ for very firm soil,

$S_{SR} = 1$ for soft rock, $S_{FR} = 1$ for firm rock, and $S_{VFS} = S_{SR} = S_{FR} = 0$ for firm soil; $F_{RV} = 1$ for reverse faulting, $F_{TH} = 1$ for thrust faulting, and $F_{RV} = F_{TH} = 0$ for strike-slip and normal faulting; and ε is a random error term with zero mean and standard deviation equal to $\sigma_{\ln \overline{Y}}$.

The standard deviation, $\sigma_{\ln \overline{Y}}$, is defined either as a function of magnitude,

$$\sigma_{\ln \overline{Y}} = \begin{cases} c_{16} - 0.07\mathrm{M_W} & \text{for } \mathrm{M_W} < 7.4 \\ c_{16} - 0.518 & \text{for } \mathrm{M_W} \geq 7.4 \end{cases} \tag{5.20}$$

Local site conditions at each recording site were classified into one of four categories defined as firm soil, very firm soil, soft rock, or firm rock. In this study, Campbell and Bozorgnia (2003) attenuation curve was drawn for firm soil. In addition, fault type is strike-slip, δ is 86.55^0 (deep angle) and the closest distance to seismogenic rupture is acceptable as

$$r_{seis} = \sqrt{r_{jb}^2 + 3^2} \tag{5.21}$$

This assumption is based on that the depth to seismogenic ruptures is three km (Abrahamson and Shedlock, 1997; Campbell, 2002, 2003).

Furthermore, the hanging wall is defined as a five-km margin around the surface projection of the rupture surface, which can be represented by the distance measure r_{jb} defined by Boore *et al.* (1997). The hanging-wall effect dies out for $r_{seis} < 8$ km, or sooner if $r_{jb} \geq 5$ km or $\delta \geq 70^0$. Due to $r_{jb} \geq 5$ km and $\delta \geq 70^0$, the hanging-wall effect was ignored.

Table 5.7. Guidance on evaluating ground-motion relations for local site conditions (Campbell and Bozorgnia, 2003)

Site Category	Site Parameter			Approximate V_{S30} (m/sec)*	Approximate Site Class*
	S_{VFS}	S_{SR}	S_{FR}		
Firm soil	0.00	0.00	0.00	210-390	D
Very firm soil	1.00	0.00	0.00	290-490	CD
Soft rock	0.00	1.00	0.00	310-530	CD
Firm rock	0.00	0.00	1.00	490-1170	BC
Generic soil	0.25	0.00	0.00	≈310	D
Generic rock	0.00	0.50	0.50	≈620	C
BC boundary	0.00	0.50	0.50	760	BC

Table 5.8. Coefficients and statistical parameters from the regression analysis of PGA for average horizontal component

Average Horizontal Component	c_1	c_2	c_3	c_4	c_5	c_6	c_7	c_8	c_9
Corrected PGA	-4.033	0.812	0.036	-1.061	0.041	-0.005	-0.018	0.766	0.034
Average Horizontal Component	c_{10}	c_{11}	c_{12}	c_{13}	c_{14}	c_{15}	c_{16}	c_{17}	
Corrected PGA	0.343	0.351	-0.123	-0.138	-0.289	0.370	0.920	0.219	

5.3.3. Akkar and Bommer (2007) Empirical Prediction Equations for PGV (Peak Ground Velocity)

Peak ground velocity (PGV) has many applications in engineering seismology and earthquake engineering. Newmark *et al.* (1973) used PGV, together with peak ground acceleration (PGA) and displacement (PGD), to construct elastic response spectra for design. The same concept has been adopted in some seismic design codes, notably the 1985 Canadian code, which used maps of both PGV and PGA for the construction of the elastic spectrum (Basham *et al.*, 1985).

PGV has also been found to correlate well with earthquake damage to buried pipelines (e.g., O'Rourke and Ayala, 1993; Eidinger *et al.*, 1995; Davis and Bardet, 2000; Isoyama *et al.*, 2000; O'Rourke *et al.*, 2001).

For the smaller earthquake, the predicted PGV values are almost identical. For the larger event, there are appreciable differences in the predicted values at short distances (<15 km).

The general form of the equation is:

$$\log(PGV_{xx}) = p_1 + p_2\mathrm{M} + p_3\mathrm{M}^2 + (p_4 + p_5\mathrm{M})\log\sqrt{r_{jb}{}^2 + p_6^2} + p_7 S_S + p_8 S_A + p_9 F_N + p_{10} F_R \quad (5.22)$$

where M is moment magnitude; S_A and S_S are dummy variables representing the influence of site class, taking values of one for stiff and soft soil sites, respectively, and zero otherwise; F_N and F_R are dummy variables for the influence of style-of-faulting, taking values of 1 for normal and reverse ruptures, respectively, and zero otherwise. The unit of PGV_{xx} is cm/sec. The logarithmic expressions in the functional form are logarithm of base 10 (Akkar and Bommer, 2007).

In this study, fault type is strike-slip and site can be classified as soft soil (according to calculated V_S values for each BYT stations and NEHRP-2000 site classification regulations).

Table 5.9. Regression coefficients and magnitude-dependent intra-event and inter-event standard deviations for the prediction equations

MAX	p_1	p_2	p_3	p_4	p_5	p_6
	-1.26	1.103	-0.085	-3.103	0.327	5.504
	p_7	p_8	p_9	p_{10}	σ_1	σ_2
	0.226	0.079	-0.083	0.0116	0.88-0.102M	0.344-0.040M

5.3.4. Campbell and Bozorgnia (2006) NGA Empirical Ground Motion Model for the Average Horizontal Component of PGA, PGV and SA at Selected Spectral Periods Ranging from 0.01–10.0 Seconds

The functional form of the Campbell and Bozorgnia (2006) Next Generation Attenuation EGMM is given by

$$\ln \overline{Y} = f_{mag} + f_{dis} + f_{flt} + f_{hng} + f_{site} + f_{sed} + \varepsilon \tag{5.23}$$

where

f_{mag} (modeling dependence on magnitude) is given by

$$f_{mag} = \begin{cases} c_{0c} + c_{1c}\,\mathrm{M} & \text{for} \quad \mathrm{M} \le 5.5 \\ c_{0c} + c_{1c}\,\mathrm{M} + c_{2c}(\mathrm{M} - 5.5) & \text{for} \quad 5.5 < \mathrm{M} \le 6.5 \\ c_{0c} + c_{1c}\,\mathrm{M} + c_{2c}(\mathrm{M} - 5.5) + c_{3c}(\mathrm{M} - 6.5) & \text{for} \quad \mathrm{M} > 6.5 \end{cases} \tag{5.24}$$

f_{dis} (modeling dependence on source-to-site distance) is given by

$$f_{dis} = (c_{4c} + c_{5c}\,\mathrm{M}) \ln\left(\sqrt{r_{rup}^2 + c_{6c}^2}\right) \tag{5.25}$$

f_{flt} (modeling dependence on style of faulting) is given by

$$f_{flt} = c_{7c} F_{RV} f_{flt,Z} + c_{8c} F_{NM} \tag{5.26}$$

$$f_{flt,Z} = \begin{cases} Z_{TOR} & \text{for} \quad Z_{TOR} < 1 \\ 1 & \text{for} \quad Z_{TOR} \ge 1 \end{cases} \tag{5.27}$$

f_{hng} (modeling dependence on hanging-wall effects) is given by

$$f_{hng} = c_{9c} f_{hng,R} f_{hng,M} f_{hng,Z} f_{hng,\delta} \tag{5.28}$$

$$f_{hng,R} = \begin{cases} 1 & \text{for} \quad r_{jb} = 0 \\ \left[\max\left(r_{rup}, \sqrt{r_{jb}^2 + 1}\right) - r_{jb} \right] \Big/ \max\left(r_{rup}, \sqrt{r_{jb}^2 + 1}\right) & \text{for} \quad r_{jb} > 0 \text{ and } Z_{TOR} < 1 \\ (r_{rup} - r_{jb}) / r_{rup} & \text{for} \quad r_{jb} > 0 \text{ and } Z_{TOR} \geq 1 \end{cases} \tag{5.29}$$

$$f_{hng,M} = \begin{cases} 0 & \text{for} \quad \mathrm{M} \leq 6 \\ 2(\mathrm{M} - 6.0) & \text{for} \quad 6.0 < \mathrm{M} < 6.5 \\ 1 & \text{for} \quad \mathrm{M} \geq 6.5 \end{cases} \tag{5.30}$$

$$f_{hng,Z} = \begin{cases} 0 & \text{for} \quad Z_{TOR} \geq 20 \\ (20 - Z_{TOR}) / 20 & \text{for} \quad Z_{TOR} < 20 \end{cases} \tag{5.31}$$

$$f_{hng,\delta} = \begin{cases} 1 & \text{for} \quad \delta \leq 70 \\ (90 - \delta) / 20 & \text{for} \quad \delta > 70 \end{cases} \tag{5.32}$$

f_{site} (modeling dependence on linear and nonlinear shallow site conditions) is given by

$$f_{site} = \begin{cases} c_{10c} \ln\left(\dfrac{V_{S30}}{k_1}\right) + k_2 \left\{ \ln\left[A_{1100} + \overline{cc}\left(\dfrac{V_{S30}}{k_1}\right)^{\overline{nn}} \right] - \ln[A_{1100} + \overline{cc}] \right\} & \text{for} \quad V_{S30} < k_1 \\ (c_{10c} + k_2 \overline{nn}) \ln\left(\dfrac{V_{S30}}{k_1}\right) & \text{for} \quad V_{S30} \geq k_1 \end{cases} \tag{5.33}$$

and f_{sed} (modeling dependence on shallow sediment effects and 3-D basin effects) is given by

$$f_{sed} = \begin{cases} c_{11c}(Z_{2.5} - 1) & \text{for} \quad Z_{2.5} < 1 \\ 0 & \text{for} \quad 1 \leq Z_{2.5} \leq 3 \\ c_{12c} k_3 e^{-0.75} [1 - e^{-0.25(Z_{2.5} - 3)}] & \text{for} \quad Z_{2.5} > 3 \end{cases} \tag{5.34}$$

In the above equations, $\overline{Y}$ is the geometric mean of the two horizontal components of peak ground acceleration (PGA) in g or five per cent damped pseudo-absolute response

spectral acceleration (SA) in g, peak ground velocity (PGV) in cm/s; M is moment magnitude; r_{rup} is closest distance to coseismic rupture in kilometers; r_{jb} is closest distance to surface projection of coseismic rupture (so-called Joyner-Boore distance) in kilometers; F_{RV} is an indicator variable representing reverse and reverse-oblique faulting, where $F_{RV} = 1$ for $30^0 < \lambda < 150^0$ and $F_{RV} = 0$ otherwise and where λ is rake angle, defined as the average angle of slip in degrees measured in the plane of rupture between the strike direction and the slip vector (e.g., Lay and Wallace, 1995); F_{NM} is an indicator variable representing normal and normal-oblique faulting, where $F_{NM} = 1$ for $-150^0 < \lambda < -30^0$ and $F_{NM} = 0$ otherwise; Z_{TOR} is depth to the top of coseismic rupture in kilometers; δ is the average dip of the rupture plane in degrees; V_{S30} is average shear-wave velocity in the top 30 m of the site profile in meters per second; A_{1100} is the value of PGA on rock with $V_{S30} = 1100$ m/sec $Z_{2.5}$ is depth to the 2.5 km/s shear-wave velocity horizon (sediment depth) in kilometers; ε is a random error term with a mean of zero and a standard deviation equal to σ_T; $\overline{nn}$ and $\overline{cc}$ are period-independent, theoretically constrained model coefficients; k_i are period-dependent, theoretically constrained model coefficients; and c_{ic} are empirically derived model coefficients. The value of $\overline{cc}$ and $\overline{nn}$ equals 1.88 and 1.18 for all spectral periods, respectively.

In this study, V_{S30} values for C and D site classes were evaluated as 520 and 250 m/s respectively with the help of Table 5.5.

The total aleatory standard deviation of $\ln \overline{Y}$ is given by

$$\sigma_T = \sqrt{\sigma^2 + \tau^2} \tag{5.35}$$

5.3.4.1. Limits of Applicability

Generally speaking, the Campbell and Bozorgnia (2006) NGA empirical ground motion model is valid for shallow continental earthquakes in worldwide active tectonic regimes for which the following conditions apply:

- M = 4.0–8.5 (strike-slip faulting)
- M = 4.0–8.0 (reverse faulting)
- M = 4.0–7.5 (normal faulting)
- r_{rup} = 0-200 km
- V_{S30} = 180-1500 m/sec (NEHRP B,C and D)
- $Z_{2.5}$ = 0-6 km
- Z_{TOR} = 0-20 km
- $\delta = 15\text{-}90^0$

$Z_{2.5}$ can be set to a default value of two km (actually any value between one and three km).

Table 5.10. Model coefficients for the Campbell and Bozorgnia (2006) NGA empirical ground motion model

PGA	c_{0c}	c_{1c}	c_{2c}	c_{3c}	c_{4c}	c_{5c}	c_{6c}	c_{7c}	c_{8c}
	-1.715	0.500	-0.530	-0.262	-2.118	0.170	5.60	0.280	-0.120
	c_{9c}	c_{10c}	c_{11c}	c_{12c}	k_1	k_2	k_3	σ_T	
	0.490	1.058	0.040	0.610	865	-1.186	1.839	0.526	
PGV	c_{0c}	c_{1c}	c_{2c}	c_{3c}	c_{4c}	c_{5c}	c_{6c}	c_{7c}	c_{8c}
	0.954	0.696	-0.309	-0.019	-2.016	0.170	4.00	0.245	0.000
	c_{9c}	c_{10c}	c_{11c}	c_{12c}	k_1	k_2	k_3	σ_T	
	0.358	1.694	0.092	1.000	401	-1.955	1.929	0.525	

5.3.5. Boore and Atkinson (2007) NGA

The equation for predicting ground motions is:

$$\ln \overline{Y} = F_M(\mathrm{M}) + F_D(r_{jb}, \mathrm{M}) + F_S(V_{S30}, r_{jb}, \mathrm{M}) + \varepsilon\sigma_T \tag{5.36}$$

In this equation, F_M, F_D and F_S represent the magnitude scaling, distance function, and site amplification, respectively. M is moment magnitude, r_{jb} is the Joyner-Boore distance (defined as the closest distance to the surface projection of the fault, which is approximately equal to the epicentral distance for events of M < 6), and the velocity V_{S30} is the inverse of the average shear-wave slowness from the surface to a depth of 30 m. The predictive variables are M, r_{jb}, and V_{S30}; the fault type is an optional predictive variable that enters into the magnitude scaling term as shown in Equation (5.38). ε is the fractional number of standard deviations of a single predicted value of $\ln \overline{Y}$ away from the mean value of $\ln \overline{Y}$. All terms, including the coefficient σ_T, are period dependent. σ_T is computed using the Equation 5.35.

In Equation 5.35, σ is the intra-event aleatory uncertainty and τ is the inter-event aleatory uncertainty.

5.3.5.1. The Distance and Magnitude Functions

The distance function is given by:

$$F_D(r_{jb}, \mathrm{M}) = [c_{1b} + c_{2b}(\mathrm{M} - M_{ref})]\ln(r / r_{ref}) + c_{3b}(r - r_{ref}) \tag{5.37}$$

Closest distance from rupture to the station can be calculated with the help of Equation 5.9.

c_{1b}, c_{2b}, c_{3b}, M_{ref}, r_{ref} and h are the coefficients to be determined in the analysis.

The magnitude scaling is given by:

a) $\mathrm{M} \le M_h$

$$F_M(\mathrm{M}) = e_{1b}U + e_{2b}SS + e_{3b}NS + e_{4b}RS + e_{5b}(\mathrm{M} - M_h) + e_{6b}(\mathrm{M} - M_h)^2 \qquad (5.38a)$$

b) $\mathrm{M} > M_h$

$$F_M(\mathrm{M}) = e_{1b}U + e_{2b}SS + e_{3b}NS + e_{4b}RS + e_{7b}(\mathrm{M} - M_h) \qquad (5.38b)$$

where U, SS, NS, and RS are dummy variables used to denote unspecified, strike-slip, normal- slip, and reverse-slip fault type, respectively, as given by the values in Table 5.11, and M_h, the "hinge magnitude" for the shape of the magnitude scaling, is a coefficient to be set during the analysis.

5.3.5.2. Site Amplification Function

The site amplification equation is given by:

$$F_s = F_{LIN} + F_{NL} \qquad (5.39)$$

where F_{LIN} and F_{NL} are the linear and nonlinear terms, respectively.

The linear term is given by:

$$F_{LIN} = b_{lin} \ln(V_{S30} / V_{ref}) \qquad (5.40)$$

where b_{lin} is a period-dependent coefficient, and V_{ref} is the specified reference velocity (=760 m/s), corresponding to NEHRP B/C boundary site conditions.

The nonlinear terms is given by:

a) $pga4nl \le a_{1b}$:

$$F_{NL} = b_{nl} \ln(pga\_low / 0.1) \tag{5.41a}$$

b) $a_{1b} < pga4nl \le a_{2b}$:

$$F_{NL} = b_{nl} \ln(pga\_low / 0.1) + \bar{c}[\ln(pga4nl / a_{1b})]^2 + \bar{d}[\ln(pga4nl / a_{1b})]^3 \tag{5.41b}$$

c) $a_{2b} < pga4nl$:

$$F_{NL} = b_{nl} \ln(pga4nl / 0.1) \tag{5.41c}$$

where a_{1b} (=0.03g) and a_{2b} (=0.09g) are assigned threshold levels for linear and nonlinear amplification, respectively, pga_low (=0.06 g) is a variable assigned to transition between linear and nonlinear behaviors, and $pga4nl$ is an initial estimate of the predicted PGA in g for $V_{ref} = 760$ m/s, as given by Equation (5.36) with $F_S = 0$ and $\varepsilon = 0$. The three Equations for the nonlinear portion of the soil response (Equation (5.41)) are required for two reasons: 1) to prevent the nonlinear amplification from increasing indefinitely as $pga4nl$ decreases and 2) to smooth the transition from linear to non-linear behavior. The coefficients $\bar{c}$ and $\bar{d}$ in Equation (5.41) are given by

$$\bar{c} = (3\Delta y - b_{nl}\Delta x) / \Delta x^2 \tag{5.42}$$

and

$$\bar{d} = -(2\Delta y - b_{nl}\Delta x) / \Delta x^3 \tag{5.43}$$

where

$$\Delta x = \ln(a_{2b} / a_{1b}) \tag{5.44}$$

and

$$\Delta y = b_{nl} \ln(a_{2b} / pga\_low) \tag{5.45}$$

The nonlinear slope b_{nl} is a function of both period and V_{S30} as given by:

a) $V_{S30} \le V_1$:

$$b_{nl} = b_{1b} \tag{5.46a}$$

b) $V_1 < V_{S30} \le V_2$:

$$b_{nl} = (b_{1b} - b_{2b}) \ln(V_{S30} / V_2) / \ln(V_1 / V_2) + b_{2b} \tag{5.46b}$$

c) $V_2 < V_{S30} < V_{ref}$:

$$b_{nl} = b_{2b} \ln(V_{S30} / V_{ref}) / \ln(V_2 / V_{ref}) \tag{5.46c}$$

d) $V_{ref} \le V_{S30}$:

$$b_{nl} = 0.0 \tag{5.46d}$$

where $V_1 = 180$ m/s, $V_2 = 300$ m/s, and b_{1b} and b_{2b} are period-dependent coefficients (and consequently, b_{nl} is a function of period as well as V_{S30}).

5.3.5.3. Coefficients of the Equations

The coefficients for the GMPEs (ground motion prediction Equations) are given in Tables 5.12, 5.13, 5.14, 5.15 and 5.16. The coefficients are for $\ln \overline{Y}$, where $\overline{Y}$ has a unit of g for PSA and PGA and cm/s for PGV. The units of distance and velocity are km and m/s, respectively.

Table 5.11. Values of dummy variables for different fault types

Fault Type	*U*	*SS*	*NS*	*RS*
Unspecified	1	0	0	0
Strikeslip	0	1	0	0
Normal	0	0	1	0
Thrust/reverse	0	0	0	1

Table 5.12. Period-dependent site-amplification coefficients

Period	b_{lin}	b_{1b}	b_{2b}
PGV	-0.600	-0.500	-0.06
PGA	-0.360	-0.640	-0.14

Table 5.13. Period-independent site-amplification coefficients

Coefficient	a_{1b}	pga_low	a_{2b}	V_1	V_2	V_{ref}
Value	0.03g	0.06g	0.09g	180 m/s	300 m/s	760 m/s

Table 5.14. Distance-scaling coefficients (M_{ref} =4.5 and $r_{ref} = 1.0$ km for all periods)

Period	c_{1b}	c_{2b}	c_{3b}	h
pga4nl	-0.55000	0.00000	-0.01151	3.00
PGV	-0.87370	0.10060	-0.00334	2.54
PGA	-0.66050	0.11970	-0.1151	1.35

Table 5.15. Magnitude-scaling coefficients

Period	e_{1b}	e_{2b}	e_{3b}	e_{4b}	e_{5b}	e_{6b}	e_{7b}	M_h
pga4nl	-0.03279	-0.03279	-0.03279	-0.03279	0.29795	-0.20341	0.00000	7.00
PGV	5.00121	5.04727	4.63188	5.08210	0.18322	-0.12736	0.00000	8.50
PGA	-0.53804	-0.50350	-0.75472	-0.50970	0.28805	-0.10164	0.00000	6.75

Table 5.16. Aleatory uncertainities (σ : intra-event uncertainty; τ : inter-event uncertainty; σ_T :combined uncertainty ($\sqrt{\sigma^2 + \tau^2}$); subscripts $\overline{U}$, $\overline{M}$ for fault type unspecified and specified, respectively)

Period	σ	$\tau_{\overline{U}}$	$\sigma_{T\overline{U}}$	$\tau_{\overline{M}}$	$\sigma_{T\overline{M}}$
PGV	0.500	0.286	0.576	0.256	0.560
PGA	0.502	0.265	0.566	0.260	0.564

5.3.5.4. Limits on Predictor Variables

The equations should be used only for predictor variables in these ranges:

- M = 5–8
- $r_{jb} < 200\,\text{km}$
- $V_{S30} = 180 - 1300$ m/s

These limits are subjective estimates based on the distributions of the recordings used to develop the equations.

5.4. Discussion and Conclusion

When rupture starting point was accepted at the middle and end of the asperity for this study case, the rupture front propagates toward the site (toward the BYTNet stations), which in turn, is an omen of the forward rupture directivity causing large pulse of motion to be oriented in the direction perpendicular to the fault plane, causing the strike-normal component of ground motion to be larger than the strike-parallel component at periods longer than about 0.5 seconds. Strike-normal component of ground motion is more effective than strike-parallel component of ground motion. There is forward directivity effect on the ground motions, which is especially evident in the PGV distribution (see Figure 5.18). Forward directivity effects are manifested in the time histories as large velocity pulses on the strike normal component of ground motion. As indicated through some figures the maximum acceleration and velocity values placed on the attenuation curves are increasing at some BYT stations on account of forward directivity effect. Especially the stations BYT04 and BYT05 that are subjected to strike-normal component of ground motion went through this effect. Along the strike normal direction when the rupture is initiated at the middle of the asperity, velocity pulse is observed due to forward directivity at the stations BYT04 and BYT05 as seen in the Figure B.16 for scenario earthquake with 6.8 magnitude. In the case of scenario earthquake with 5.8 magnitude, forward directivity effect was not observed at all BYT stations clearly in Figures from 5.7 to 5.10 which are comparison graphs generated according to NEHRP site class C and D.

The reason for this is that most peak horizontal acceleration values lie in between the limits of the empirical attenuation curves. As it can be seen on the D site class PGV graphs of the same earthquake (see Figure 5.16), although PGVs at BYT02, BYT04 and BYT05 stations being in the limits of the empirical attenuation curve, fault normal components are higher in value than the fault parallel components especially when rupture is initiated at the end of the asperity. The comparison graphs obtained for the 6.8 magnitude earthquake when the rupture is nucleated at the beginning and end of the asperity, especially at D site class BYT04 and BYT05 stations, show that fault normal components exceed the limits of the attenuation curve due to forward directivity effect. As it can be observed at the site class C PGV graphs of 6.8 magnitude earthquake at BYT01 and BYT02 stations (see Figure 5.17), although the hypocenter of the earthquake is close to the BYTNET stations when rupture is at the beginning of the asperity, PGV values are lower. In addition, the hypocenter of the earthquake is far away from the BYTNET stations when rupture is at the middle and end of the asperity, PGV values on the strike normal component of ground motion are higher. This result shows how effective is the forward directivity. On the other hand PGV graphs of the same earthquake for the D site class, in Figure 5.18 it is shown that forward directivity effect is influential since PVG values on the fault normal components are higher than those on the fault parallel components at BYT02, BYT04 and BYT05 stations. As illustrated via response spectra graphs, strike-normal component of ground motion affects structures in terms of vulnerability to high damage at long periods. As it can be seen in the simulated acceleration response spectra Figures 5.19 and 5.20 of the 5.8 magnitude earthquake at the stations BYT01, BYT02, BYT04, BYT06, BYT08, BYT11, BYT12 that Turkish Seismic Design Code overestimates the spectral accelerations along the fault parallel and normal directions. Besides, at the station BYT05 fault normal spectral accelerations exceed fault parallel spectral accelerations when the period is higher than 0.5 seconds. In conclusion Turkish Design Code meets the expectations for the 5.8 magnitude earthquake.

In this study, backward directivity effect is observed when the rupture is initiated at the begining of the asperity, which in turn, occurs when the rupture propagates away from the site, gives rise to the opposite effect from forward directivity effect (see the first column of Figure 5.21) : Motions have low amplitudes at long periods. For the 6.8 magnitude earthquake, in the first column of Figures 5.21 and 5.22 backward directivity

effect is apparent when the rupture starting point is at the beginning of the asperity and in the second and third column of Figures 5.21 and 5.22 forward directivity effect is apparent when the rupture starting point is at the middle and end of the asperity. It can be seen from the Figures 5.21 and 5.22 that Turkish Design Code is insufficient especially at high periods except the stations BYT01 and BYT11.

6. CONCLUSIONS

The EGF method is very powerful as long as appropriate small event records are available from target source areas. There are total 14 BYTNet stations founded around Bursa – Yalova region in 2001. Due to the reason that these stations were newly founded and due to presence of reliably and accurately recorded small earthquake data, it was found suitable to make simulation using EGF method.

After confirming the focal mechanism determined by KOERI, near source ground motion simulation based on Empirical Green's function method in the frequency range 0.5-10 Hz was carried out for two scenario earthquakes (scenario M_w=5.8 and M_w=6.8) synthesized by summing the records of M_w=4.8 Gemlik Earthquake, under the assumption that ground motions were generated only from asperities.The scenario simulation of ground motion was performed at nine BYTNET stations for different rupture starting point alternatives.

As known,the locations of the asperities in each fault plane are defined by considering the historical seismicity. Since there are no detailed studies as regards historical seismicity and large slip regions for Armutlu Peninsula, large slip regions corresponding to asperity in the zone could not be exactly determined. Hence, asperity area selected in the computations relies on assumptions. Results of the graphs determined according to asperity area based on assumptions like taking stress drop ratio between target and element event as one are open to discussion.

For each of the scenario earthquakes it was assumed that the rupture existing in the asperity area occurs at a deep level and after obtaining asperity values of each of these earthquake scenarios, displacement, velocity and acceleration wave forms were plotted when rupture was initiated at the beginning, midpoint and endpoints of the asperity. Maximum values of the time series graphs drawn for the diverse RSP alternatives at each of these stations at the beginning, midpoint and endpoints were compared with the empirical ground-motion-attenuation-relations. As it is seen from the graphs, when rupture starts at the end and midpoint of the asperity, forward directivity effect as an

expected result of near-field-ground-motion is observed especially at the stations BYT04 and BYT05. The effect of forward rupture directivity on the response spectrum is to increase the level of the response spectrum of the horizontal component normal to the fault strike at periods longer than 0.5 seconds. As illustrated in acceleration response spectra graphs, at short periods FN and FP components of ground motion are overlapping but at long periods, structures subjected to fault normal component of ground motion are vulnerable to high damage as depicted acceleration response spectra graphs. As far as middle earthquakes are concerned, Turkish Seismic Design Code meets the expectations by means of overestimating spectral acceleration response but as far as big earthquakes are concerned, Turkish Seismic Design Code cannot meet the expectations due to the fact that appropriate approximation as regards spectral acceleration response cannot provided especially at high periods. Compatibility or incompatibility between obtained maximum values after scenario simulation and empirical attenuation curves can be attributed to assumptions associated with selection of the asperity, rupture velocity and so forth. Near fault effects cannot be adequately described by uniform scaling of a fixed response spectral shape; instead the shape of the spectrum becomes richer in long periods as the level of the spectrum increases. This means the combination of fling and directivity peculiar to near-field ground motion can have destructive effects on long-period structures, such as bridges, high-rise and base-isolated buildings. So, the efforts should focus on archiving near-fault ground motion recordings in the strike-normal and strike-parallel components in order to observe rupture directivity effects.

The results of this study reveal that even there are reliable ground-motion estimation methodologies, the prediction of ground motions from future earthquakes is restricted with limited knowledge of the source and attenuation parameters. This uncertainty is important and should always be kept in mind when interpreting ground-motion simulation results. However, being aware of the uncertainties, ground-motion simulations still provide a strong tool in determining seismic-hazard levels in places with a high probability of exceedence.

APPENDIX A: BAND-PASS FILTERING FOR GEMLIK EARTHQUAKE

This section includes the figures generated with the data of Gemlik earthquake which were band-pass filtered for [0.5-2] Hz. and [1-5] Hz. intervals.

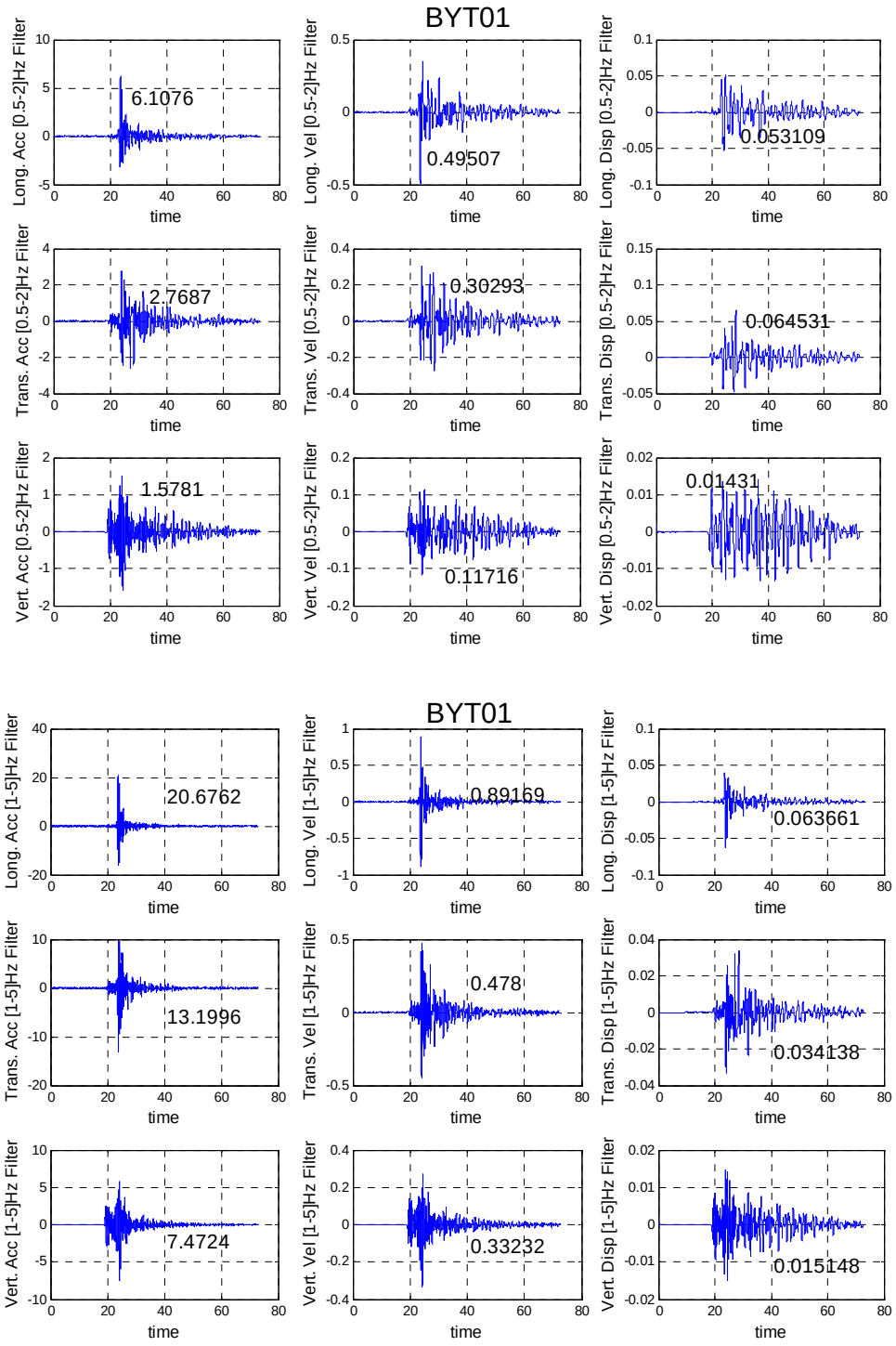

Figure A.1. [0.5-2] Hz. and [1-5] Hz. Band-Pass Filtering for BYTNet01 Station

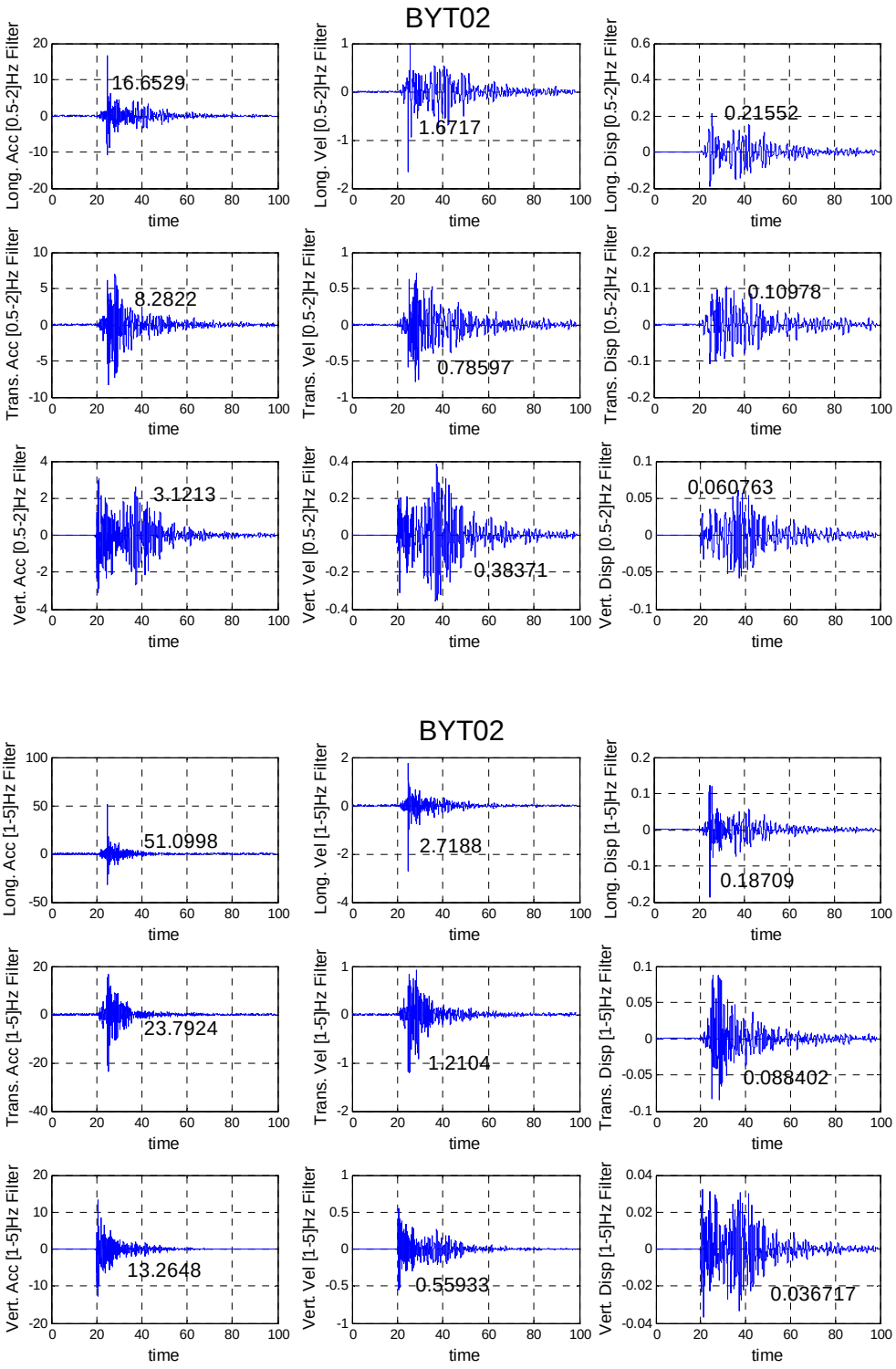

Figure A.2. [0.5-2] Hz. and [1-5] Hz. Band-Pass Filtering for BYTNet02 Station

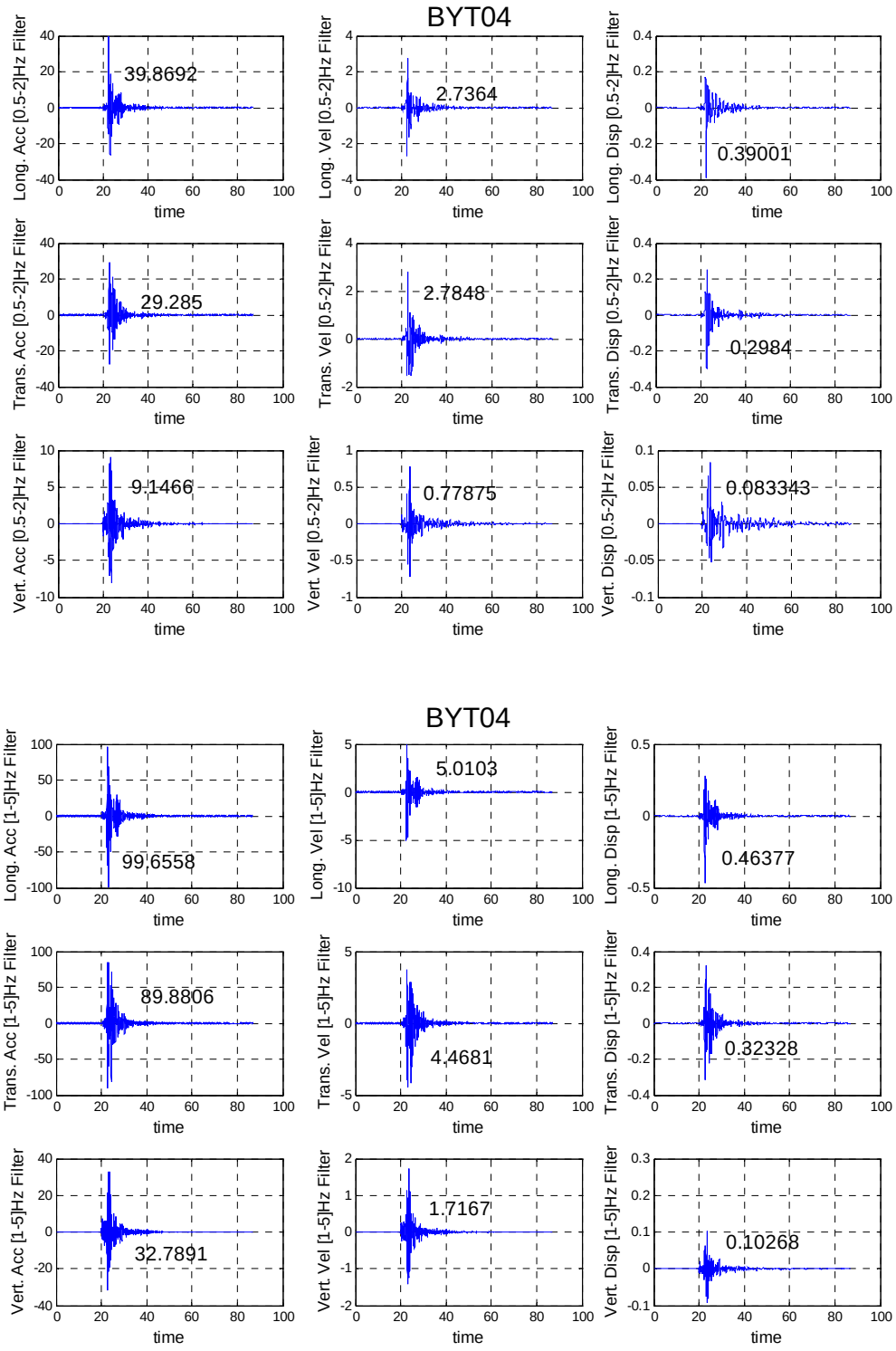

Figure A.3. [0.5-2] Hz. and [1-5] Hz. Band-Pass Filtering for BYTNet04 Station

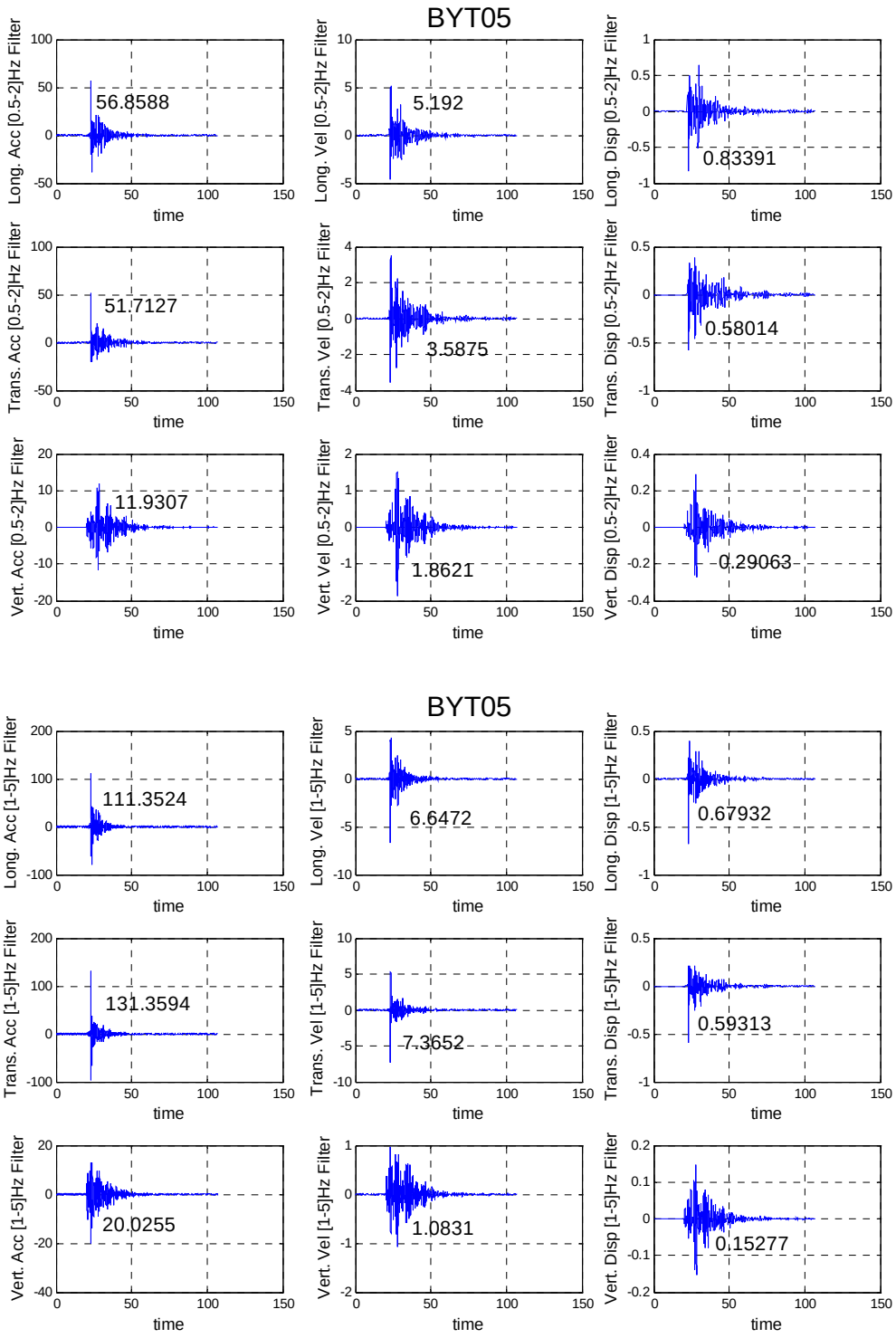

Figure A.4. [0.5-2] Hz. and [1-5] Hz. Band-Pass Filtering for BYTNet05 Station

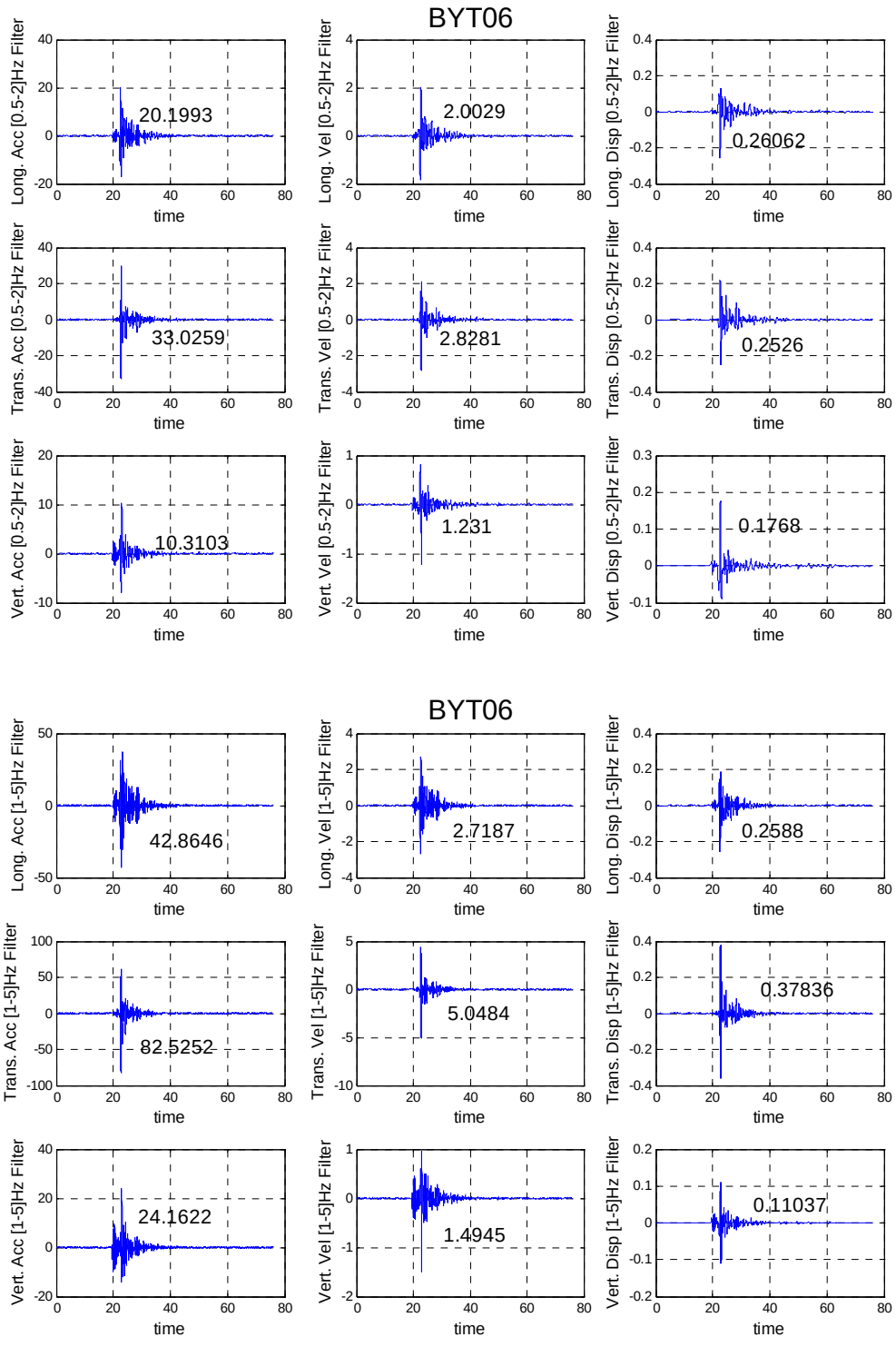

Figure A.5. [0.5-2] Hz. and [1-5] Hz. Band-Pass Filtering for BYTNet06 Station

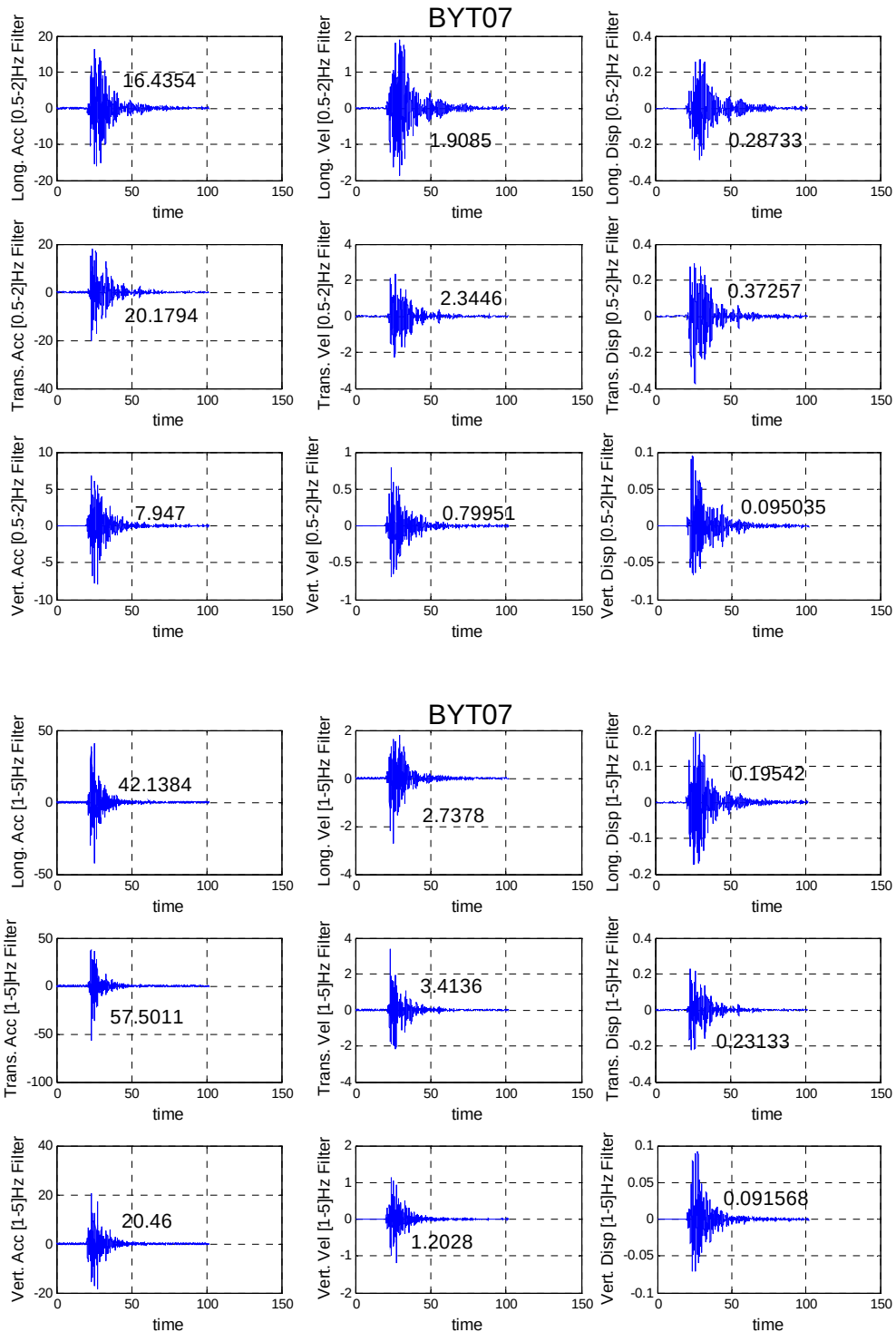

Figure A.6. [0.5-2] Hz. and [1-5] Hz. Band-Pass Filtering for BYTNet07 Station

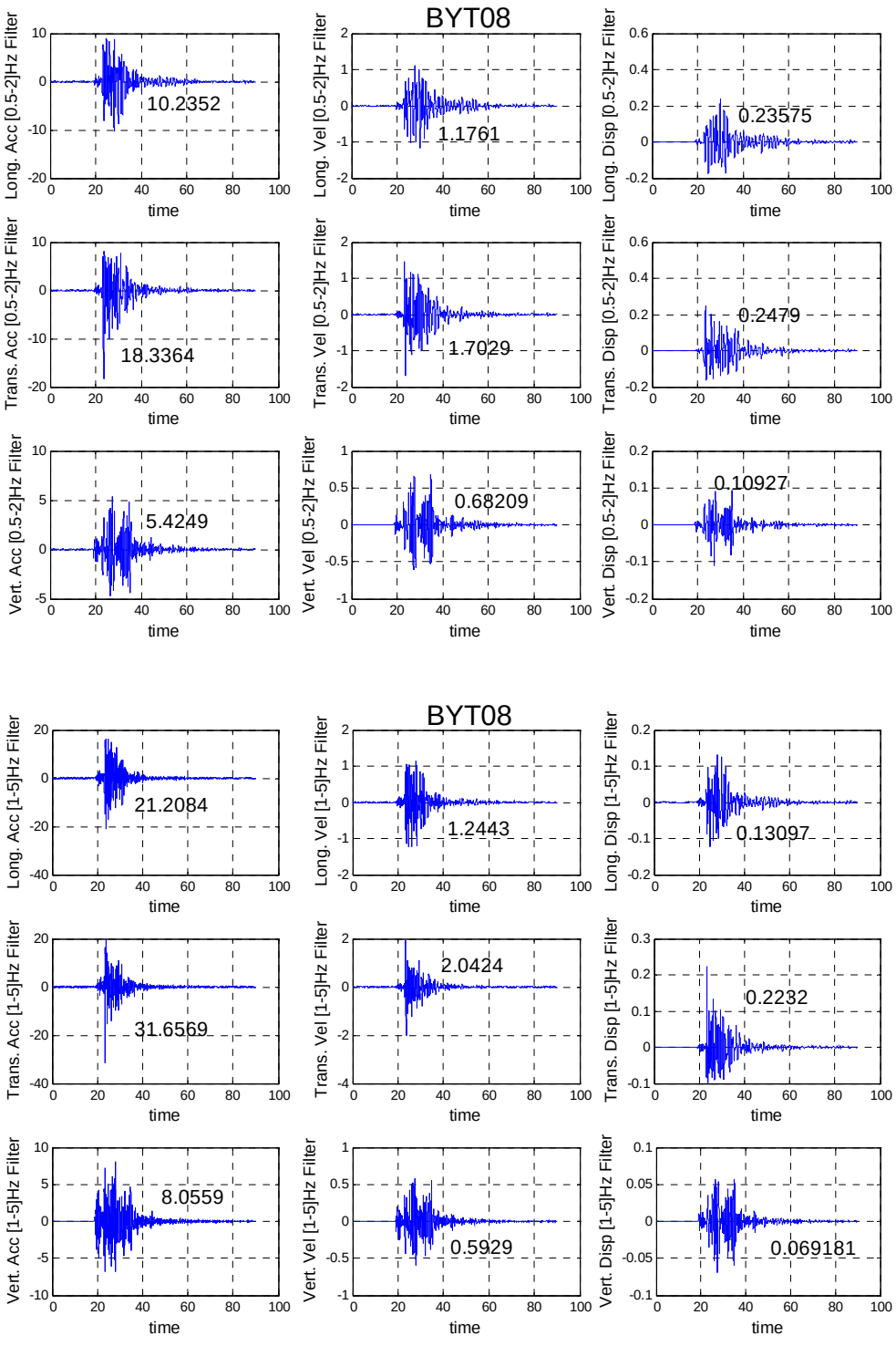

Figure A.7. [0.5-2] Hz. and [1-5] Hz. Band-Pass Filtering for BYTNet08 Station

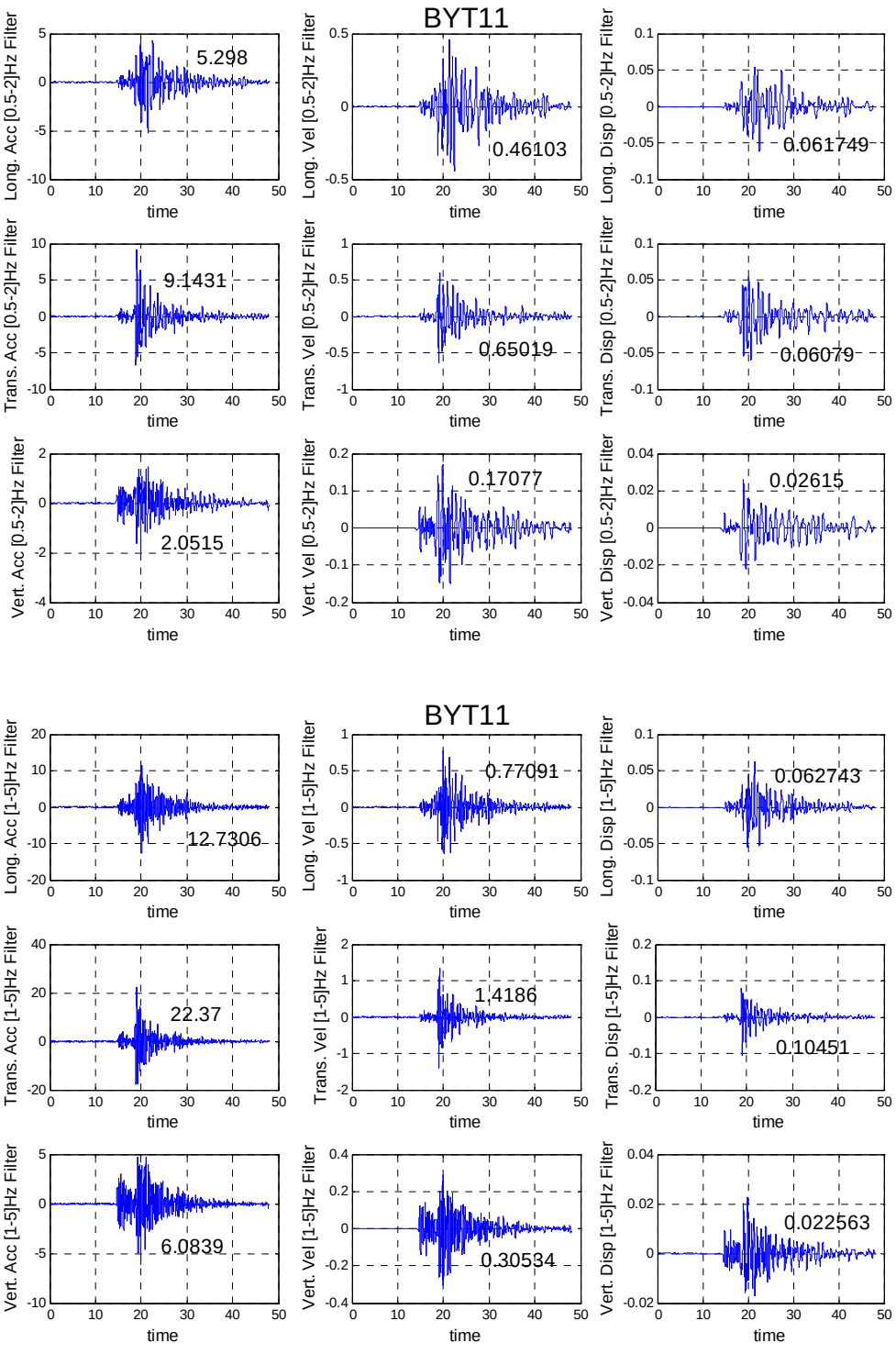

Figure A.8. [0.5-2] Hz. and [1-5] Hz. Band-Pass Filtering for BYTNet11 Station

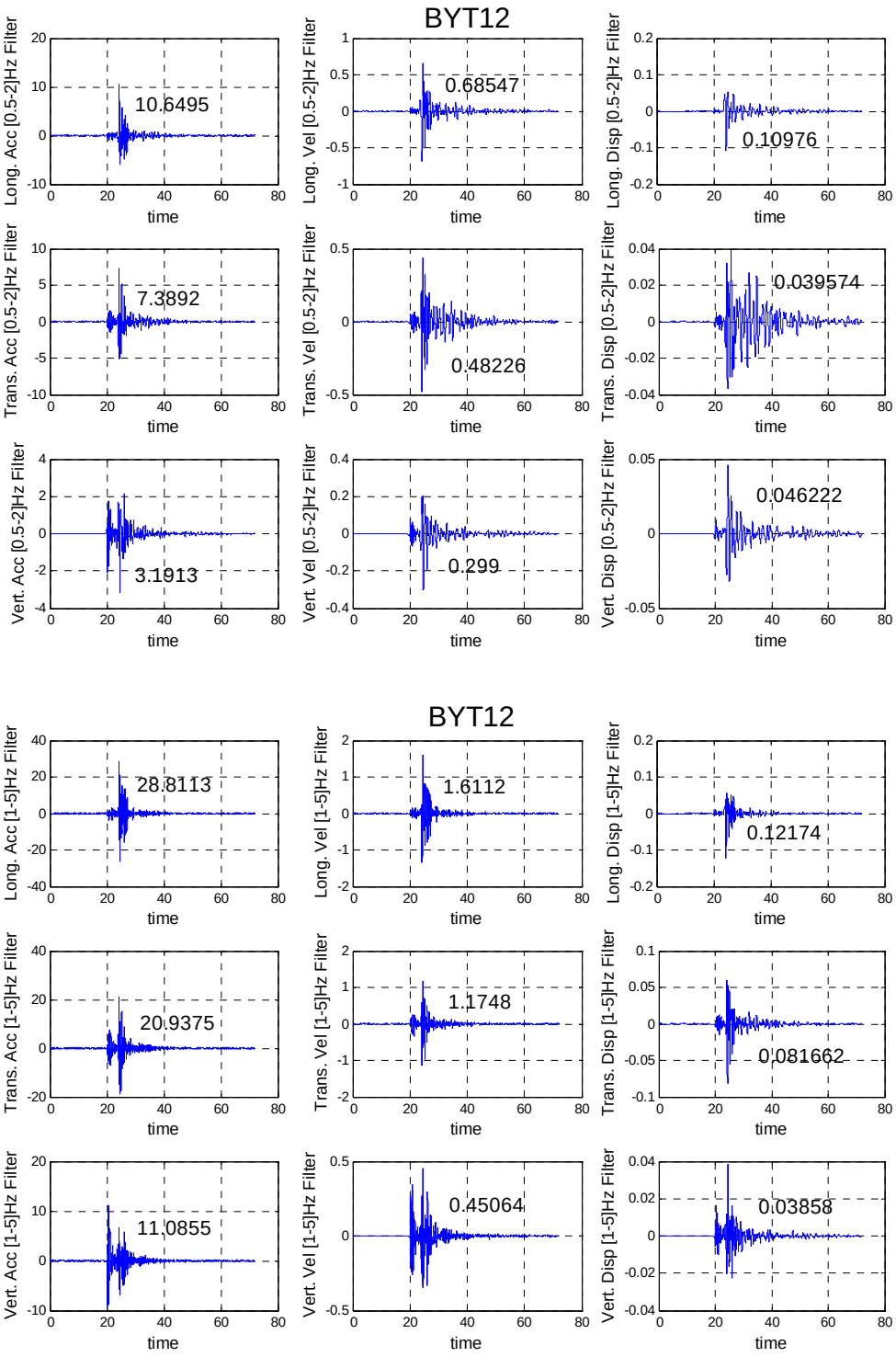

Figure A.9. [0.5-2] Hz. and [1-5] Hz. Band-Pass Filtering for BYTNet12 Station

APPENDIX B: README FILE IN ORDER TO RUN EGF PROGRAM

This section encompasses README FILE so as to run EGF program in test simulation and input parameters presented in the README FILE.

B.1. README FILE of EGF Program

<< README FILE of How to run EGF? >>

Last modification 2007/06/04 by Gulum Tanircan

Example "egfm_zoo1.in"

3)	1	IFILT: 1-USE FILTER 2-NO FILTER
4)	0.5 20.0 25.0 0.1 30.0	PARAM. OF FILTER: FL, FH, FS, AP, AS
5)	5.0 0.0 -3.0 16.0 -1.0 -2.0 4.0	PARAM. FOR GRAPHIC: UT, Q (1) -Q (6)
6)	316.83 86.55 156.91 20	STRIKE, DIP, RAKE and DEPTH OF TARGET
7)	1	NO. OF COMPONENT
8)	316.83 86.55 156.91 10	STRIKE, DIP, RAKE and DEPTH OF ELEMENT
9)	0.175 0.233 0.23 0 0 0	DX, DW, TRA, DX0, DW0, TR0
10)	4 3 3 20 2 1 0 12	NX, NW, NT, NTT, NSX, NSW, NS, C FACTOR
11)	3.5 2.8 2 0	VS, VR, IRAD, IPFM
14)	23.06 162.78 21.21 168.14 00.0 3	EP. DIST. and AZIMUTH, CMP, IMDL
15)	1900 5000 1600 5000	KSM KEM KSA KEA
16)	BYT02	STATION
17)	4.8/3.3	RATIO OF MAGNITUDE
18)	1000 5000 100	IS, IE, IWIND

B.1.1. Explanation of Input Parameters

3) IFILT is the option for filter: 1-use filter, 2-no filter.
4) FL, FH, FS, AP, AS are the parameters for filter. See the Figure B.1.

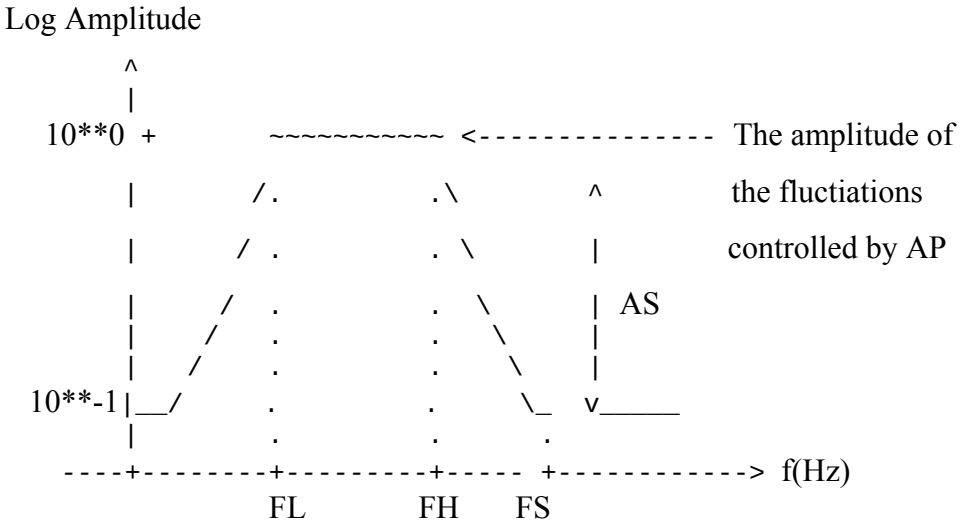

Figure B.1. Filter paramer graph

5) PARAM. FOR GRAPHIC <NOT USE>
6) STR, DIP, and RAK are the strike, dip and rake angles of the target event (degree). Definitions of these angles follow "Quantitative Seismology", by Aki and Richards.
7) NCMPT is the number of the components you treat. The procedure 8-18 is repeated NCMPT times. <NOT USE>
8) STRA, DIPA, and RAKA are the strike, dip and rake angles of the element event.
9) DX and DW are the length of the fault (km) along the strike direction and along the dip direction, respectively.
   TRA is the rise of the element event (sec).
   DX0, DW0, and TR0 are used in case of a multiple shock.
10) NX and NW are the number of the subfaults along the strike direction and along the dip direction, respectively.
   NT is the number of the element event summed up at each subfault.
   NTT is used in order to avoid the artificial periodicity that appears when NTT element events are summed up with the interval TRA (sec).
   NSX and NSW is the location of the rupture starting point.
   NS is used in case of a multiple shock.
   CFACTOR is a parameter used to correct the difference in stress drop between the element event and the mainshock.
   CFACTOR = (stress drop large event) / (stress drop small event)
11) VS is the S-wave velocity (km/s) of the medium between the source and the station.

VR is the rupture velocity (km/s).

IRD is an option for style of rupture propagation:

1 - Lateral propagation

2 - Radial propagation.

IPFM is an option for radiation pattern correction:

0 - No correction

1 - Correct

2 - Correct only sign.

14) RM and PM are the epicentral distance (km) and the azimuth (degree) of the target event (Azimuth is the angle between the north and the vector from the source to the station, and is measured clockwise from the north).

RA and PA are the epicentral distance and the azimuth of the element event.

CMP is the angle indicating the component of the data.

CMP is measured clockwise from the north. For example:

In case of NS component ....CMP = 0 degree.

EW	90
SN	180
WE	270

Vertical components are special cases:

In case of UD component ...CMP = 1000

DU	-1000

IMDL is an option for the style of summation on the time axis

It means the shape of slip time function:

[Omega-cube model]

IMDL=1 --> boxcar (low frequency model)

[Omega-square model]

IMDL=2 --> delta+boxcar (high frequency model)

IMDL=3 --> delta+exponential (improve model)

IMDL=4 --> root t (dynamic model)

15) For the target event, data from KSM to KEM is used for the synthesis.

For the element event, data from KSA to KEA.

16) STATION is the name of the station

17) MAGNITUDE is ratio of mainshock/aftershock

18) IS is the starting data point for the spectra.
IE is the ending data point for the spectra.
IWIND is window length for calculating the spectra.

APPENDIX C: GRAPHS BELONGINIG TO SIMULATED EARTHQUAKES FOR DIFFERENT RSP

This section includes the figures generated with the data of scenario earthquakes which were obtained by repeating the EGF simulation with different rupture starting points in the asperity.

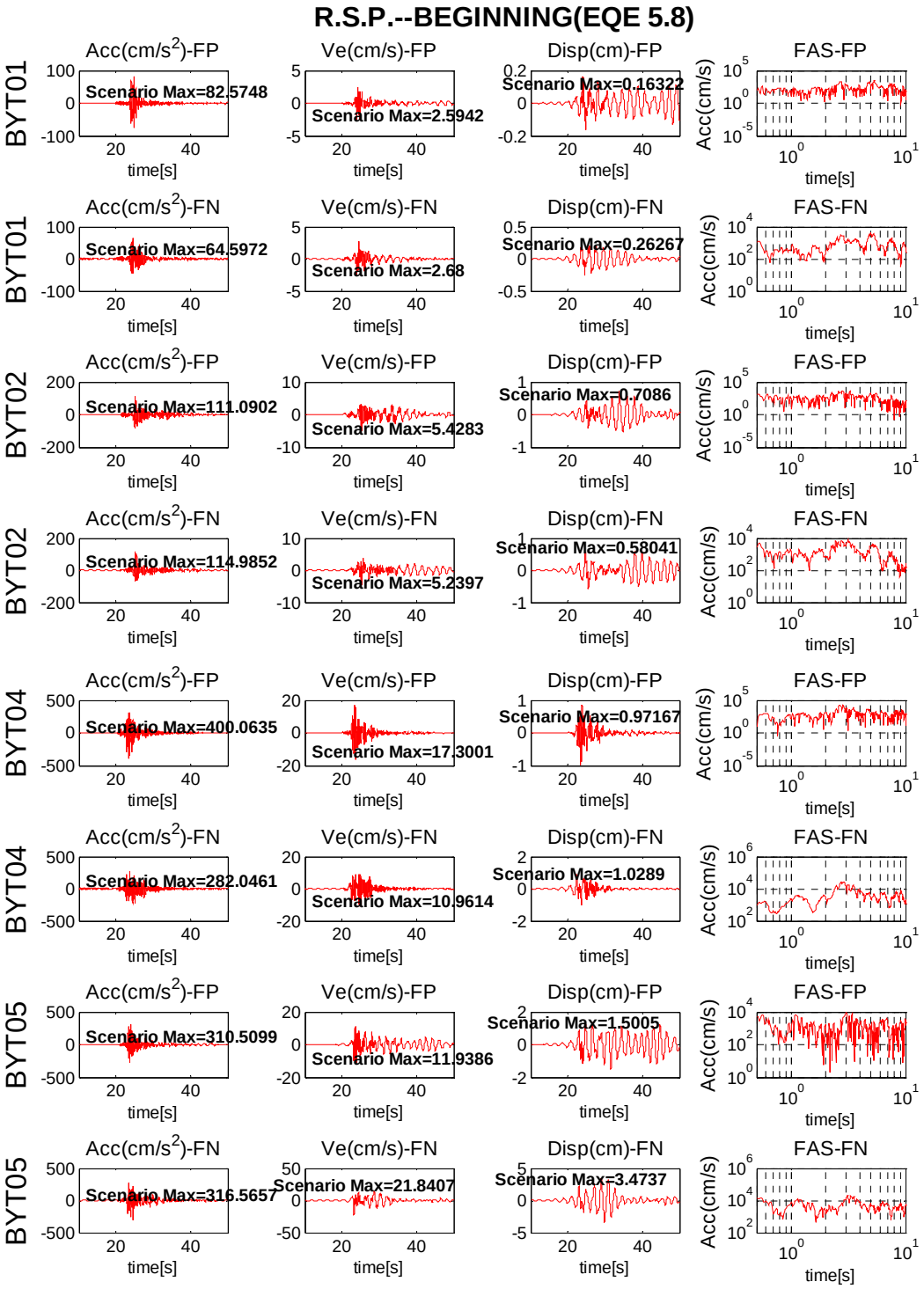

Figure C.1. Scenario earthquake 5.8, rupture starting at the beginning of the asperity for BYT01, BYT02, BYT04 and BYT05 stations

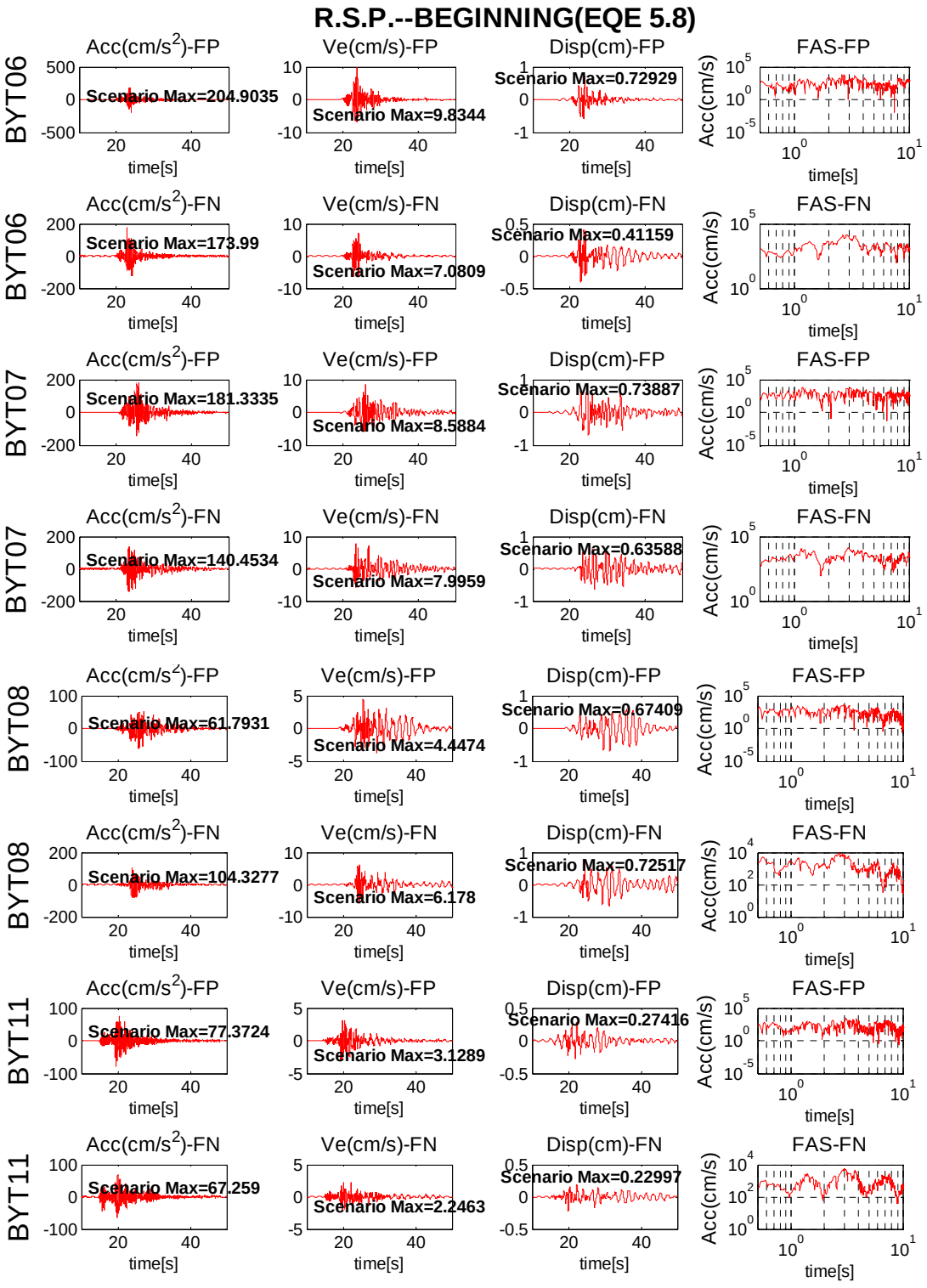

Figure C.2. Scenario earthquake 5.8, rupture starting at the beginning of the asperity for BYT06, BYT07, BYT08 and BYT11 stations

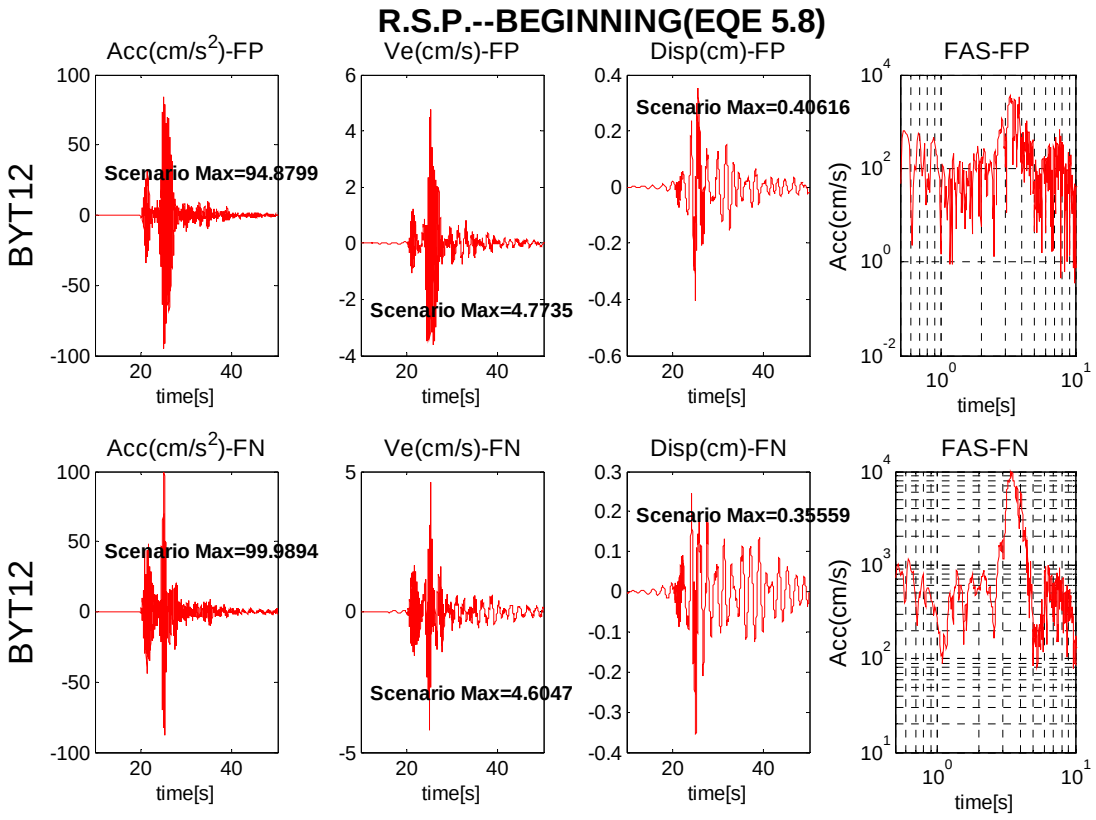

Figure C.3. Scenario earthquake 5.8, rupture starting at the beginning of the asperity for BYT12 station

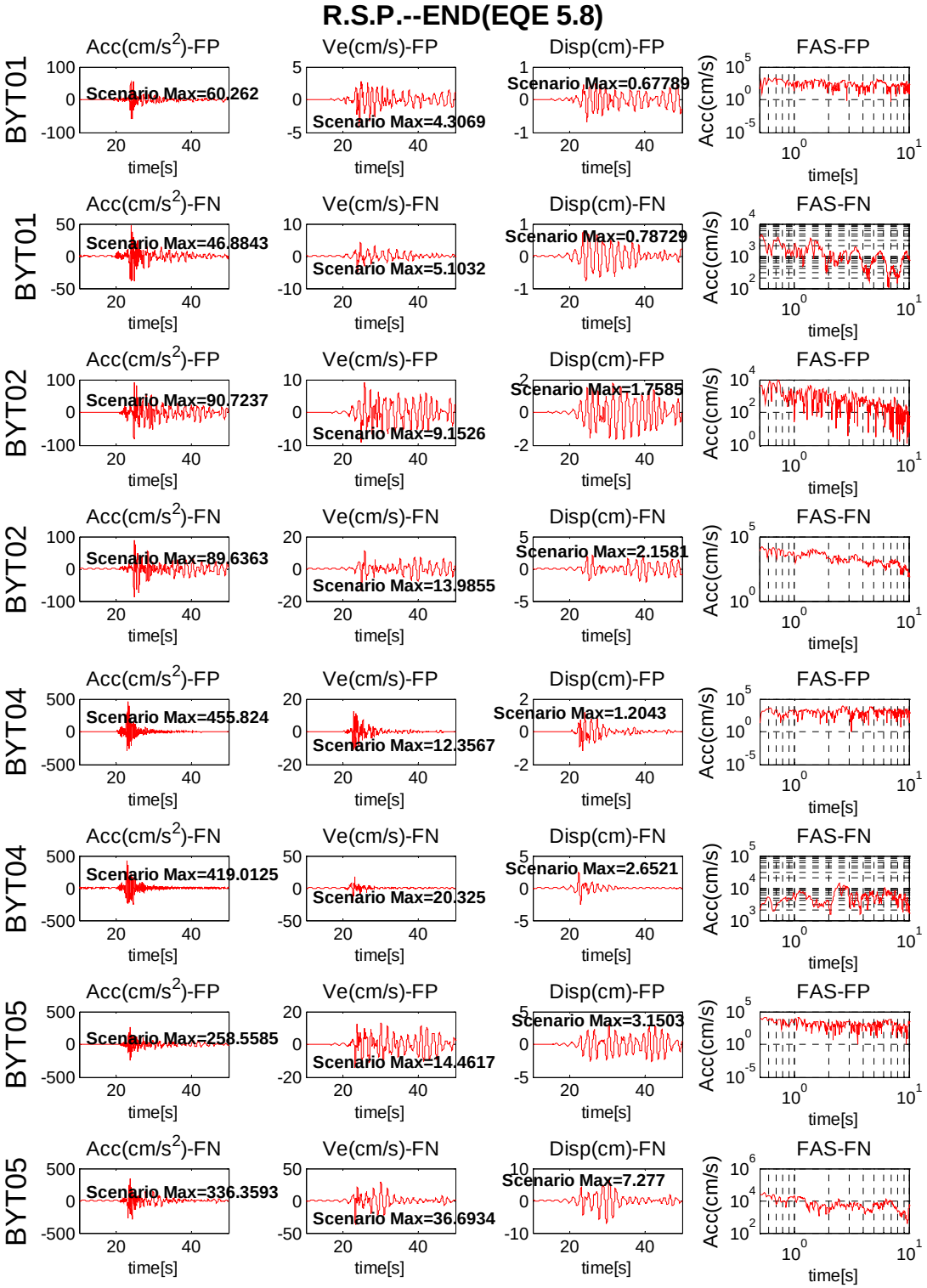

Figure C.4. Scenario earthquake 5.8, rupture starting at the end of the asperity for BYT01, BYT02, BYT04 and BYT05 stations

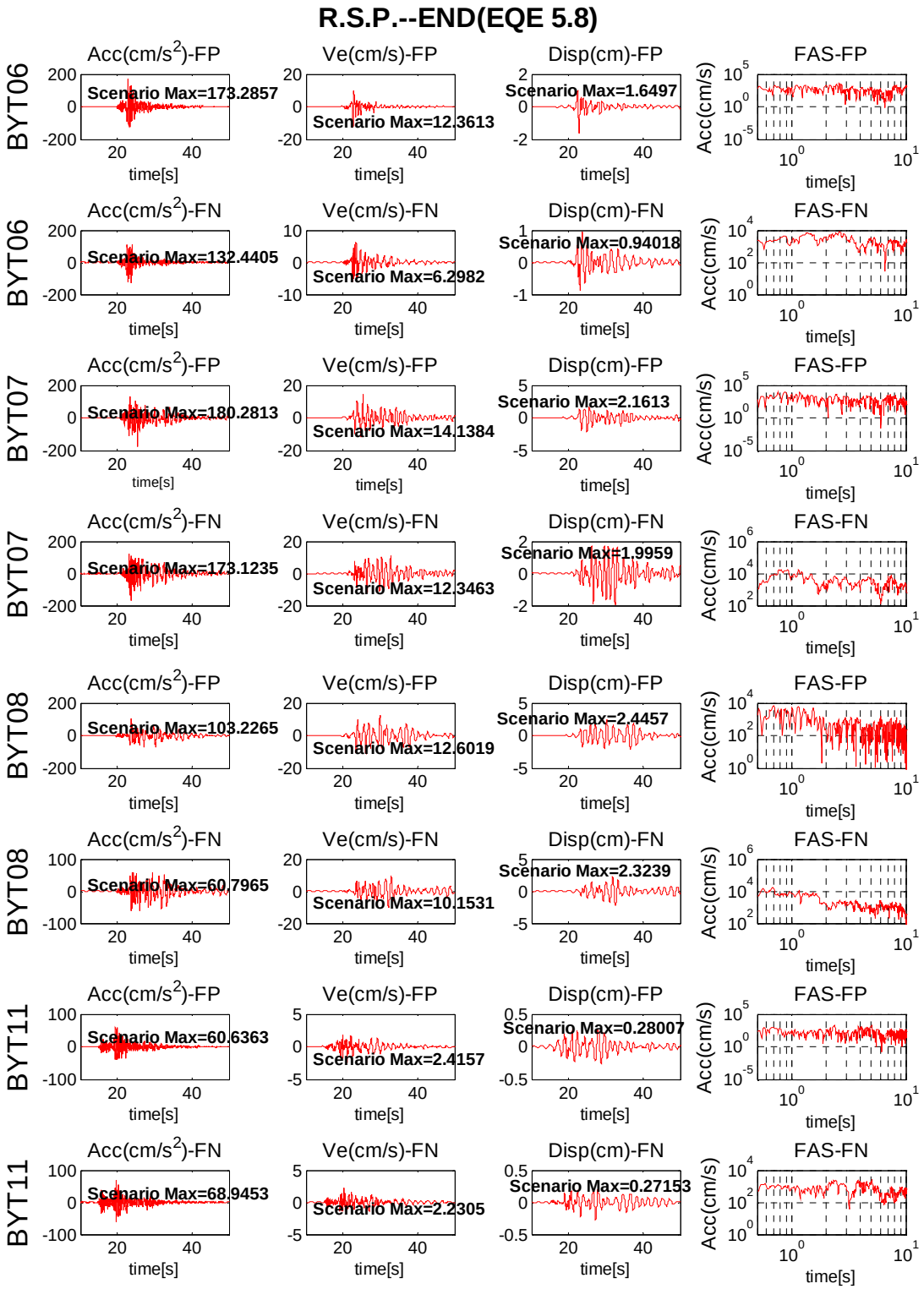

Figure C.5. Scenario earthquake 5.8, rupture starting at the end of the asperity for BYT06, BYT07, BYT08 and BYT11 stations

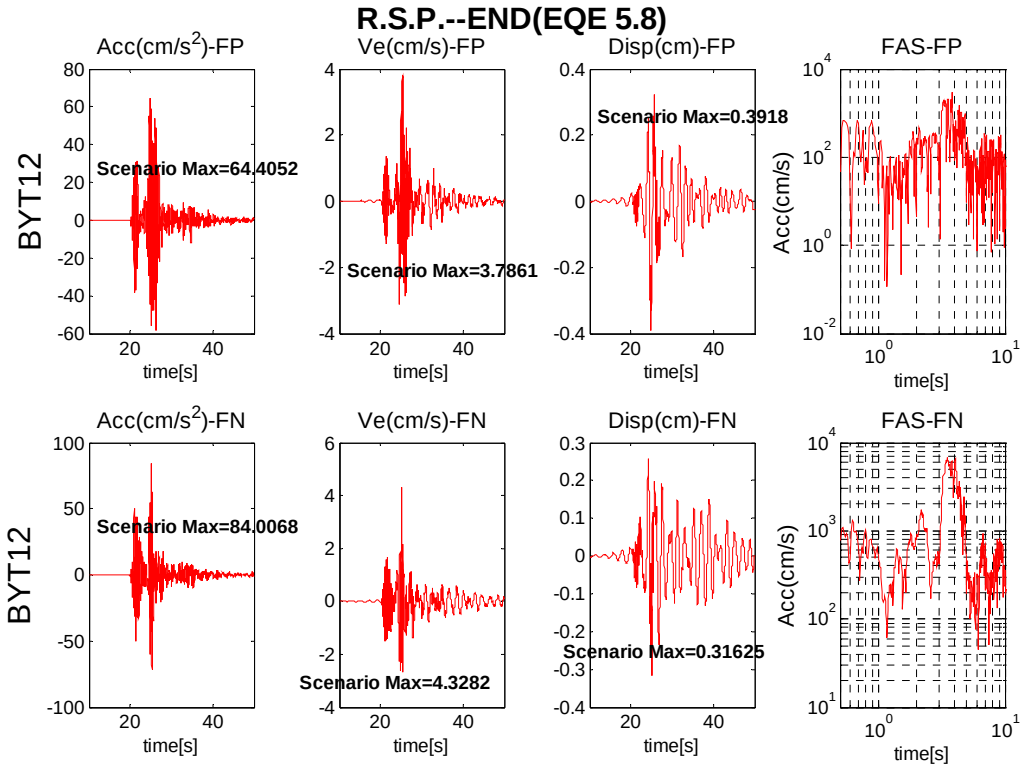

Figure C.6. Scenario earthquake 5.8, rupture starting at the end of the asperity for BYT12 station

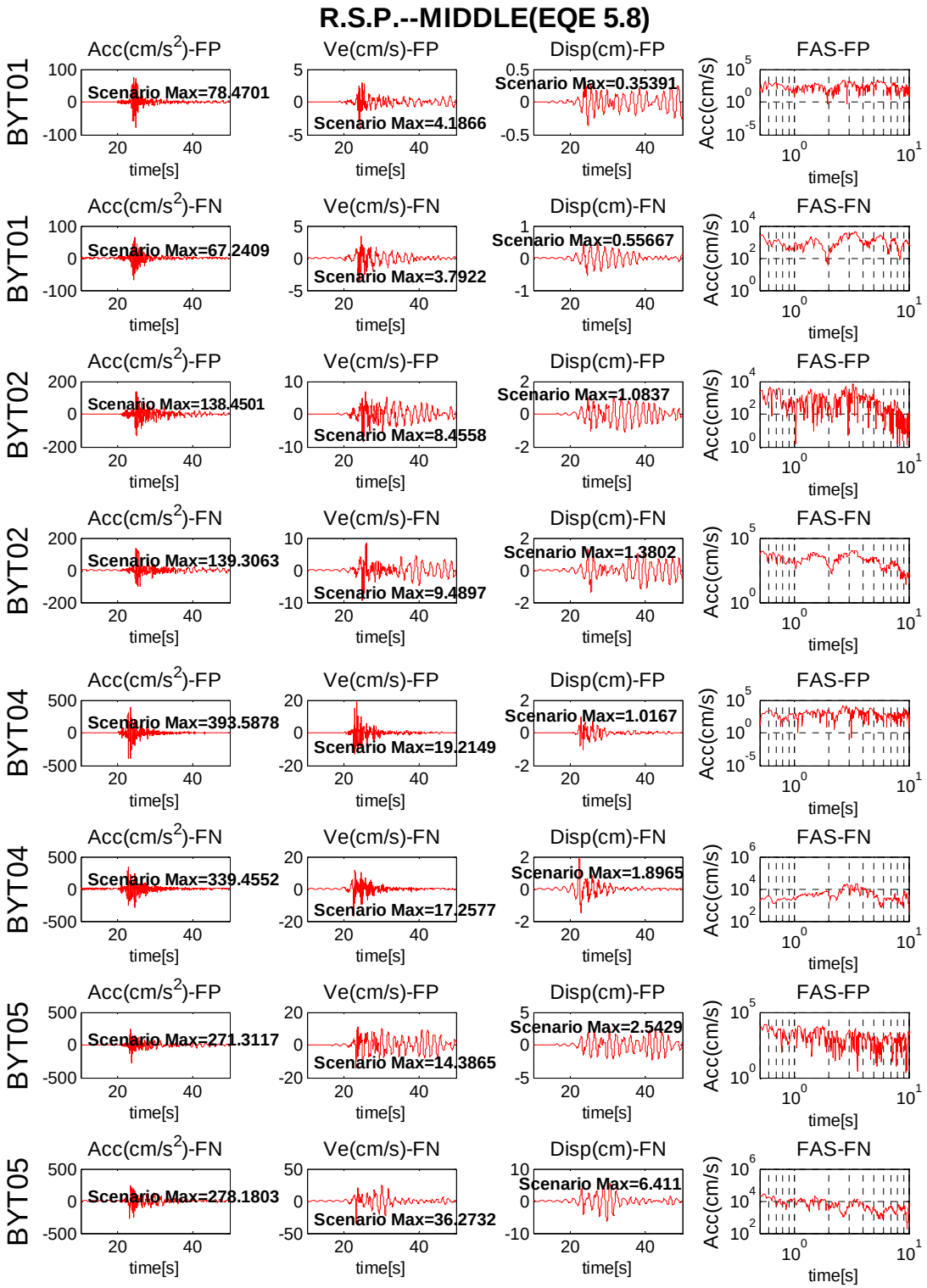

Figure C.7. Scenario earthquake 5.8, rupture starting at the middle of the asperity for BYT01, BYT02, BYT04 and BYT05 stations

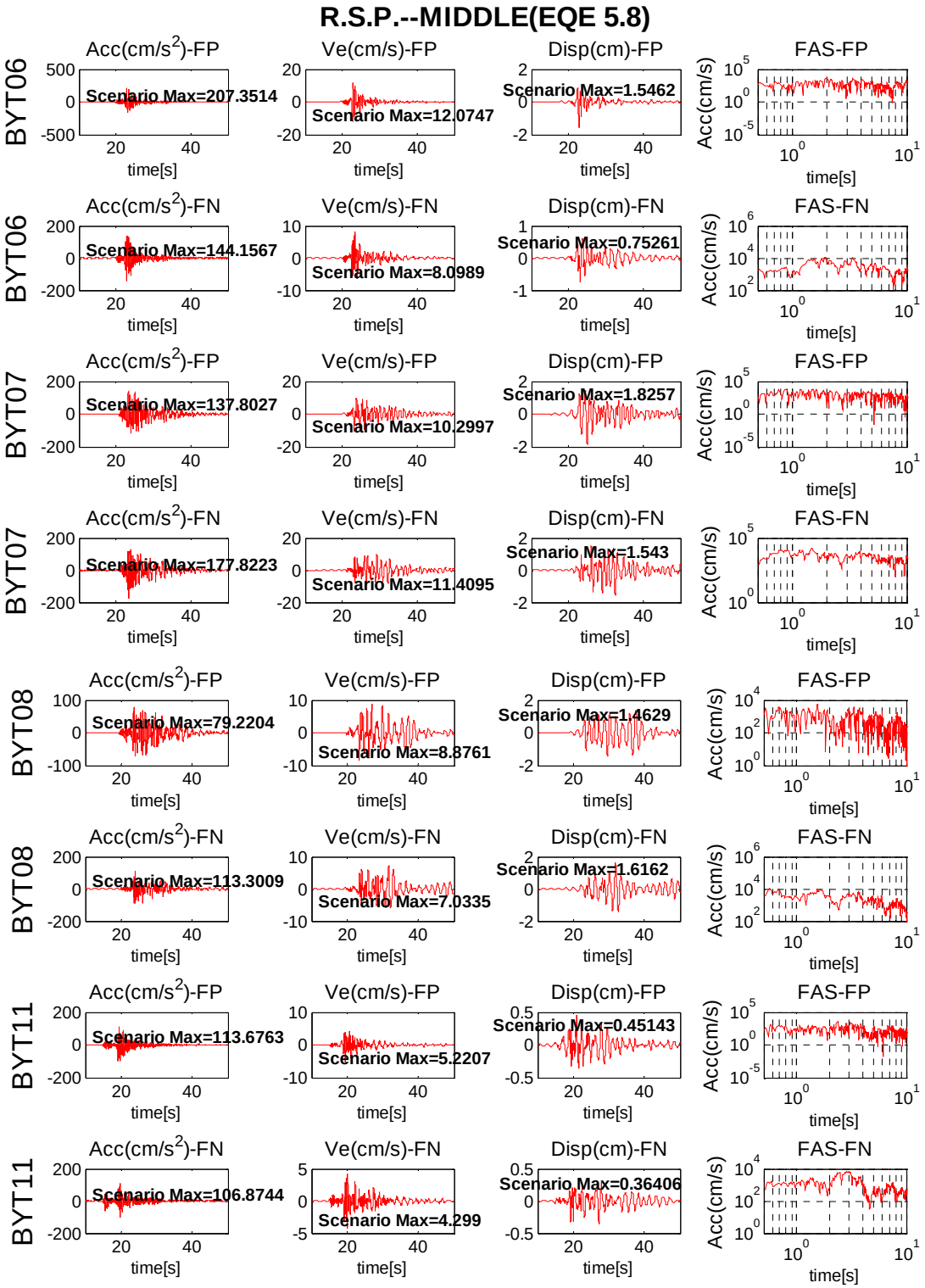

Figure C.8. Scenario earthquake 5.8, rupture starting at the middle of the asperity for BYT06, BYT07, BYT08 and BYT11 stations

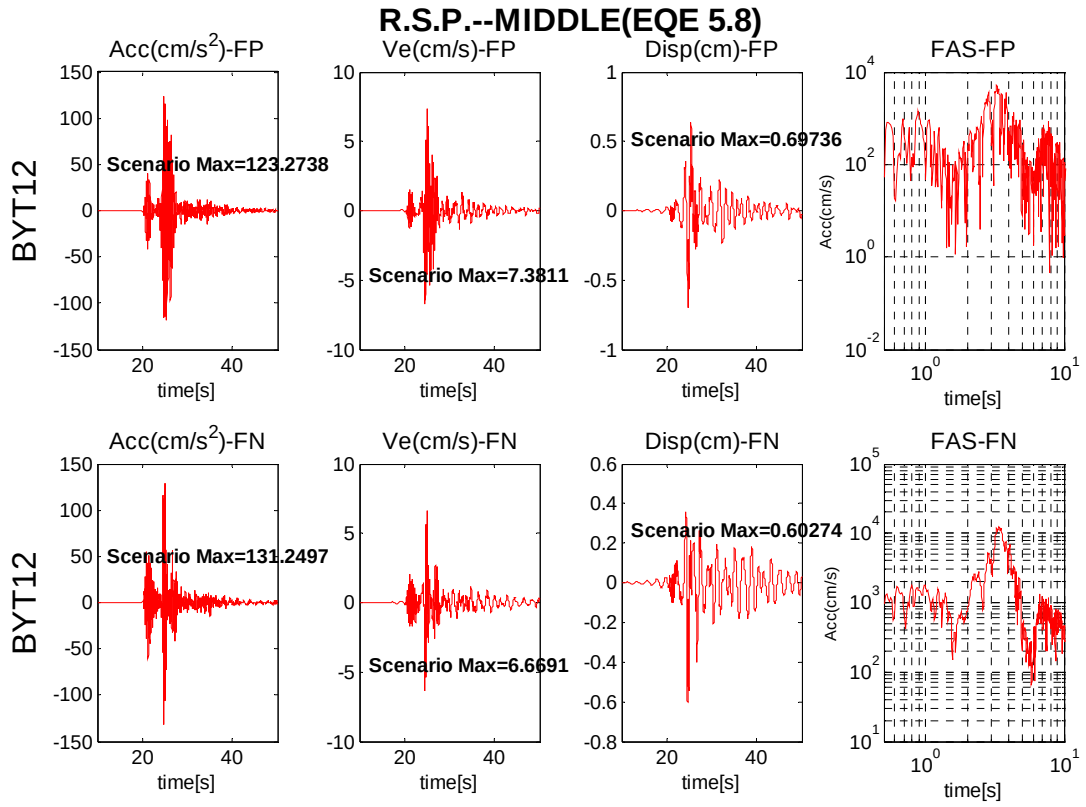

Figure C.9. Scenario earthquake 5.8, rupture starting at the middle of the asperity for BYT12 station

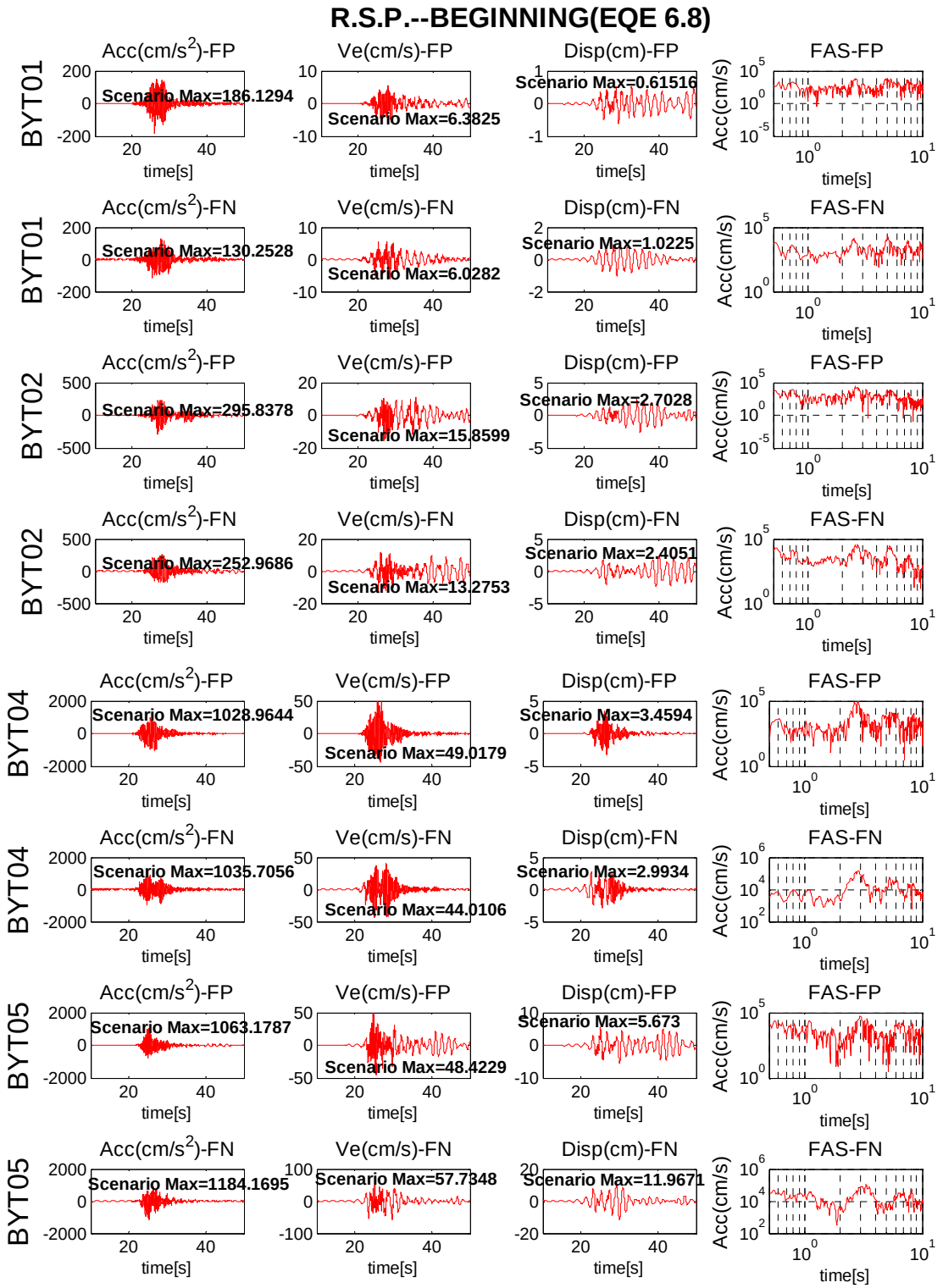

Figure C.10. Scenario earthquake 6.8, rupture starting at the beginning of the asperity for BYT01, BYT02, BYT04 and BYT05 stations

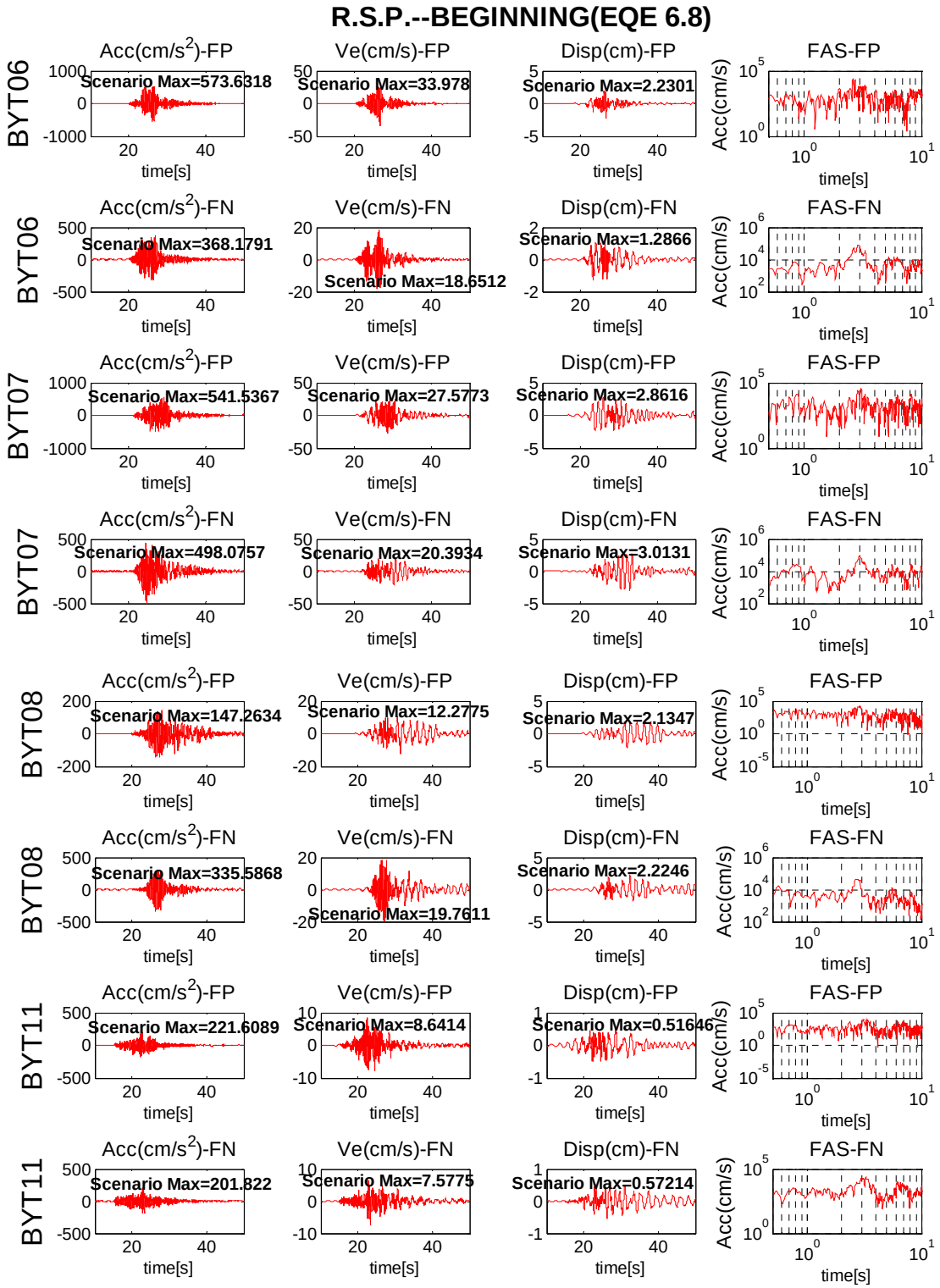

Figure C.11. Scenario earthquake 6.8, rupture starting at the beginning of the asperity for BYT06, BYT07, BYT08 and BYT11 stations

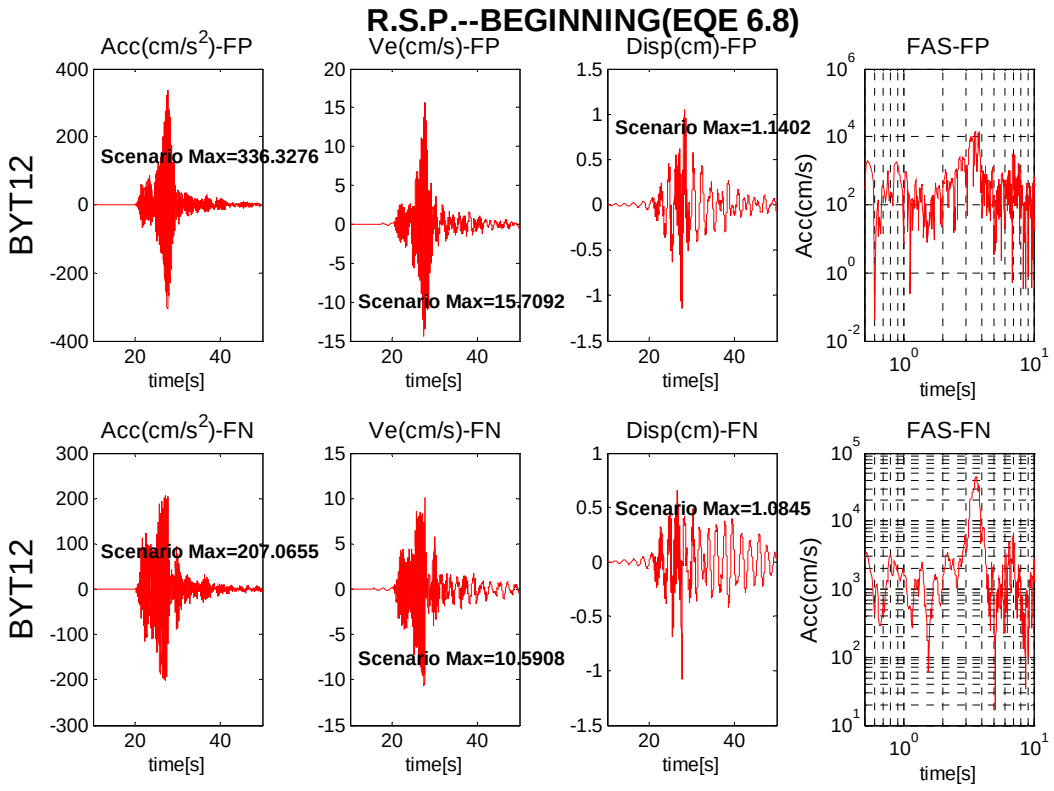

Figure C.12. Scenario earthquake 6.8, rupture starting at the beginning of the asperity for BYT12 station

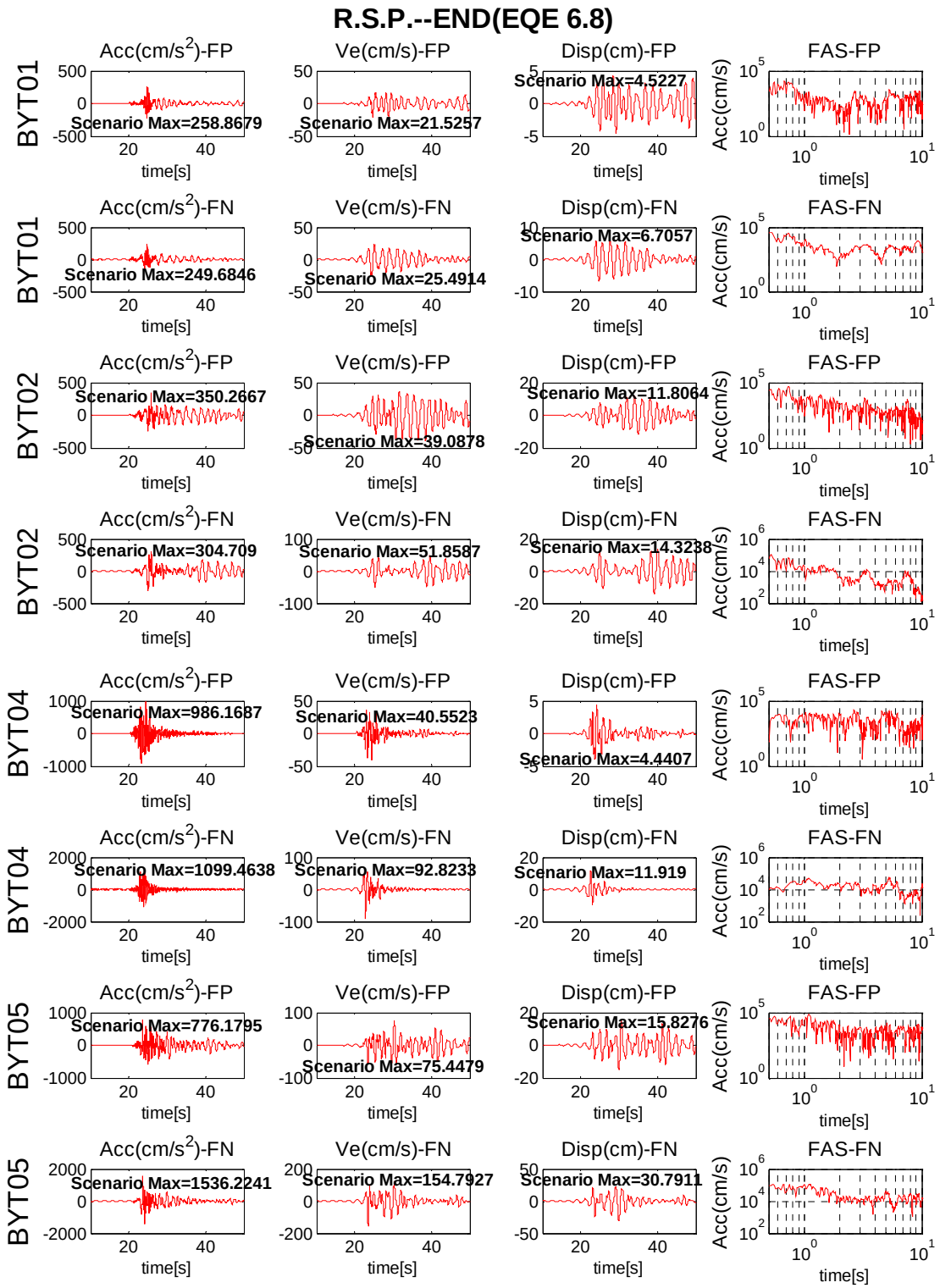

Figure C.13. Scenario earthquake 6.8, rupture starting at the end of the asperity for BYT01, BYT02, BYT04 and BYT05 stations

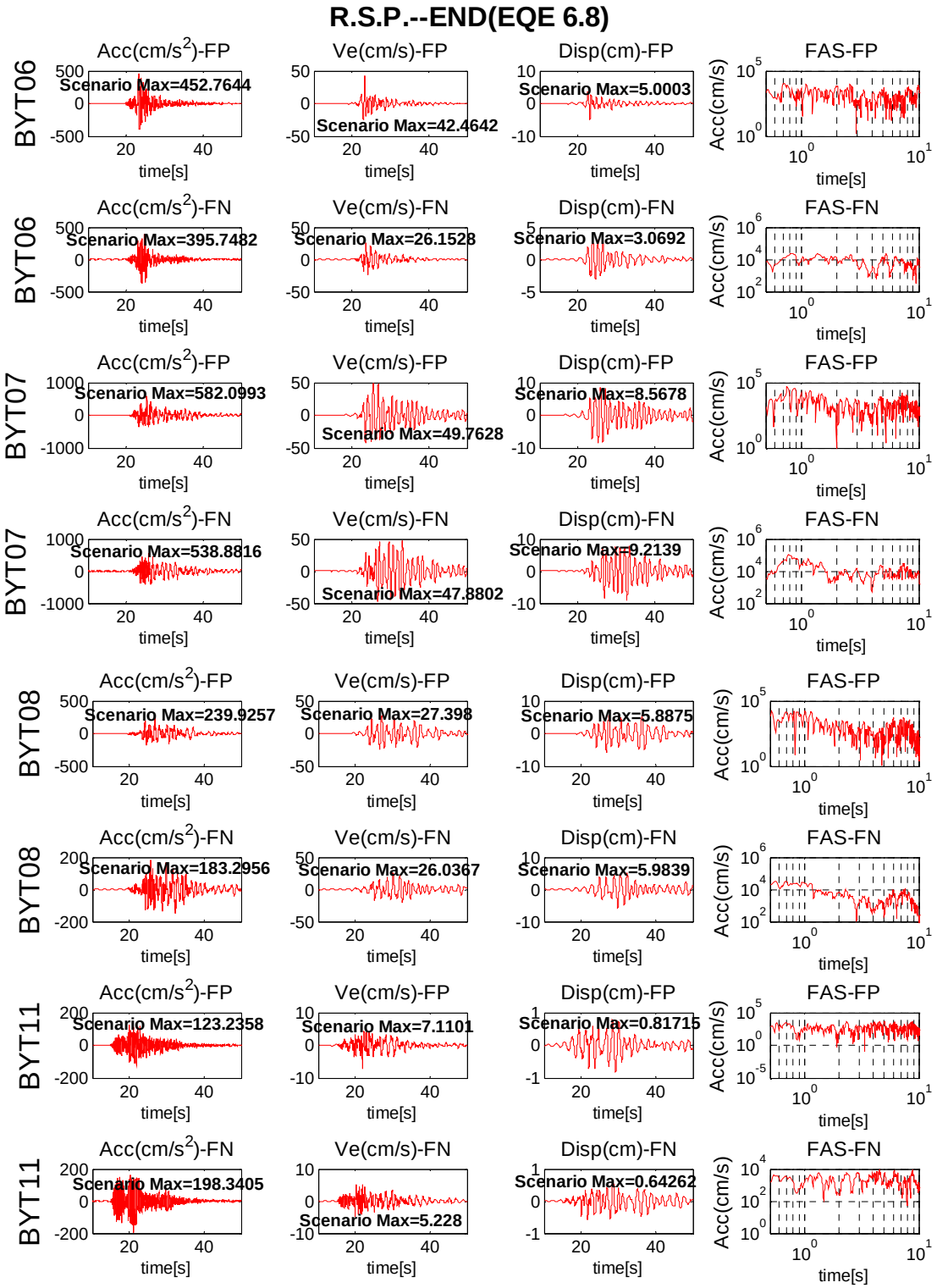

Figure C.14. Scenario earthquake 6.8, rupture starting at the end of the asperity for BYT06, BYT07, BYT08 and BYT11 stations

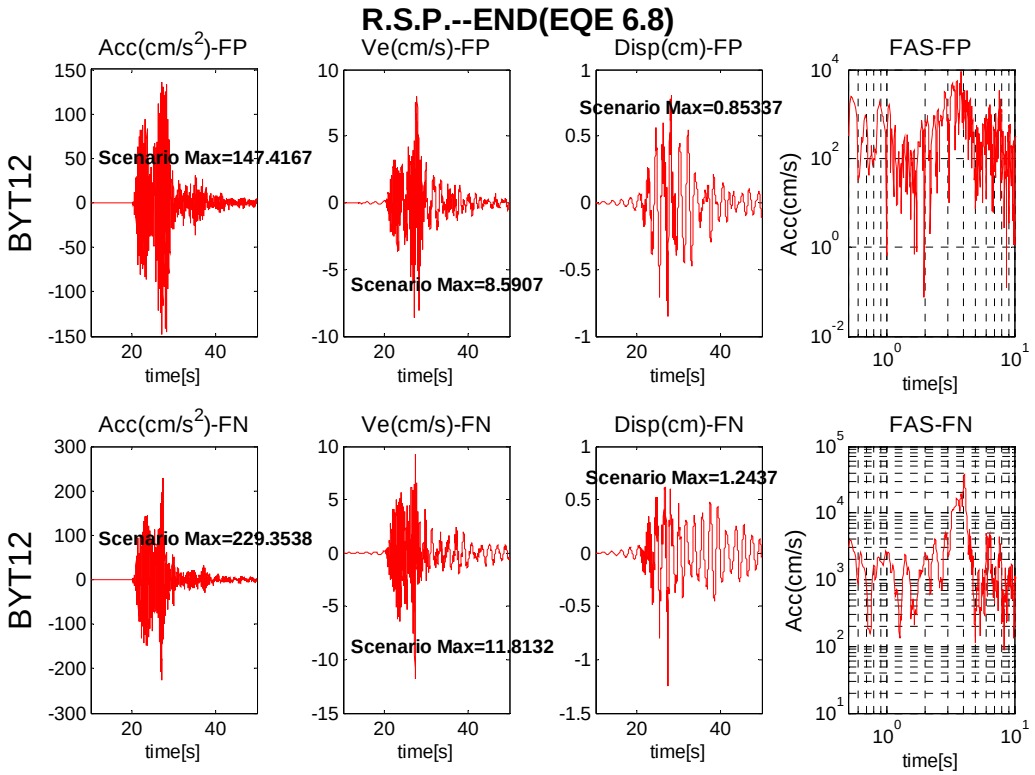

Figure C.15. Scenario earthquake 6.8, rupture starting at the end of the asperity for BYT12 station

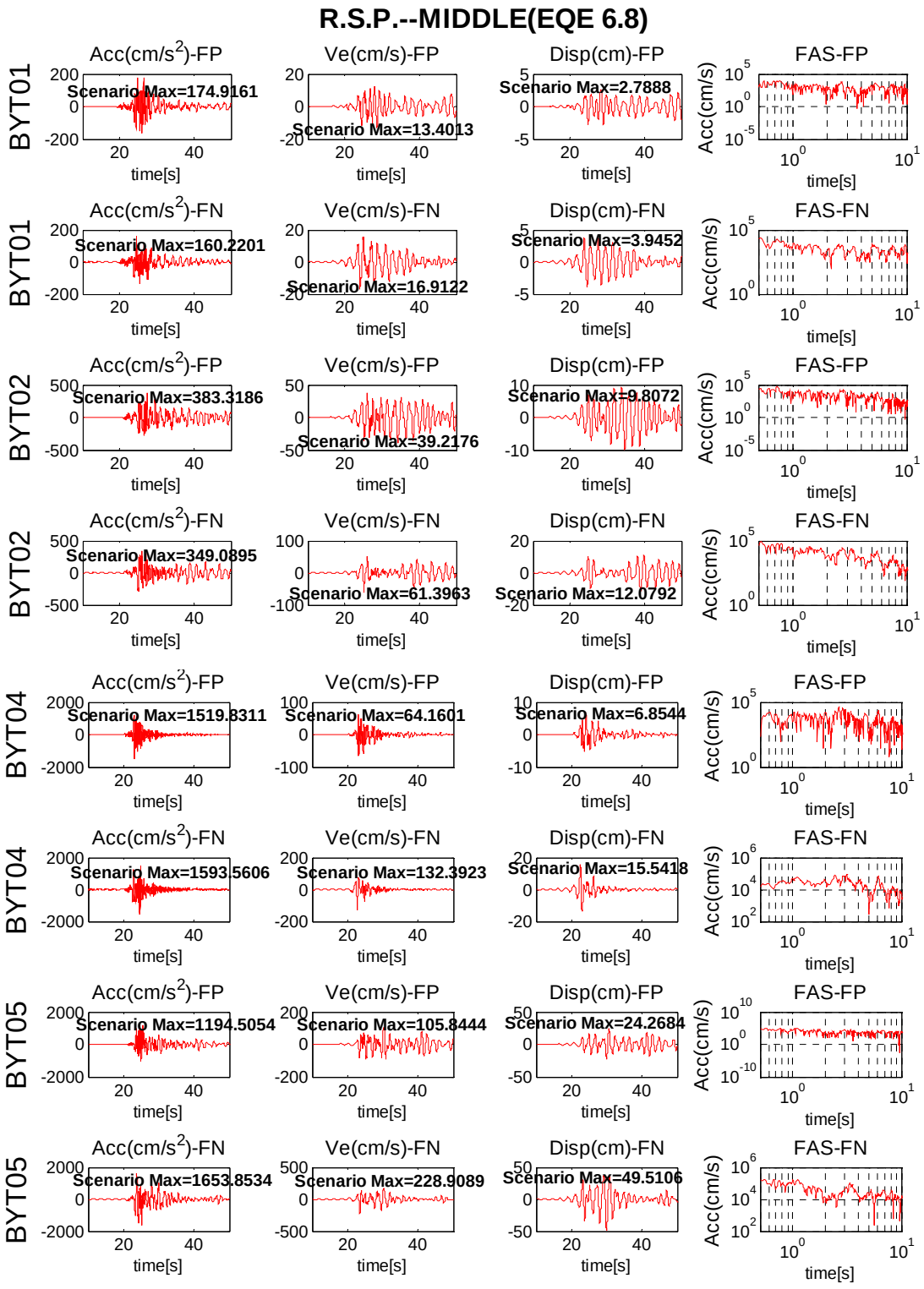

Figure C.16. Scenario earthquake 6.8, rupture starting at the middle of the asperity for BYT01, BYT02, BYT04 and BYT05 stations

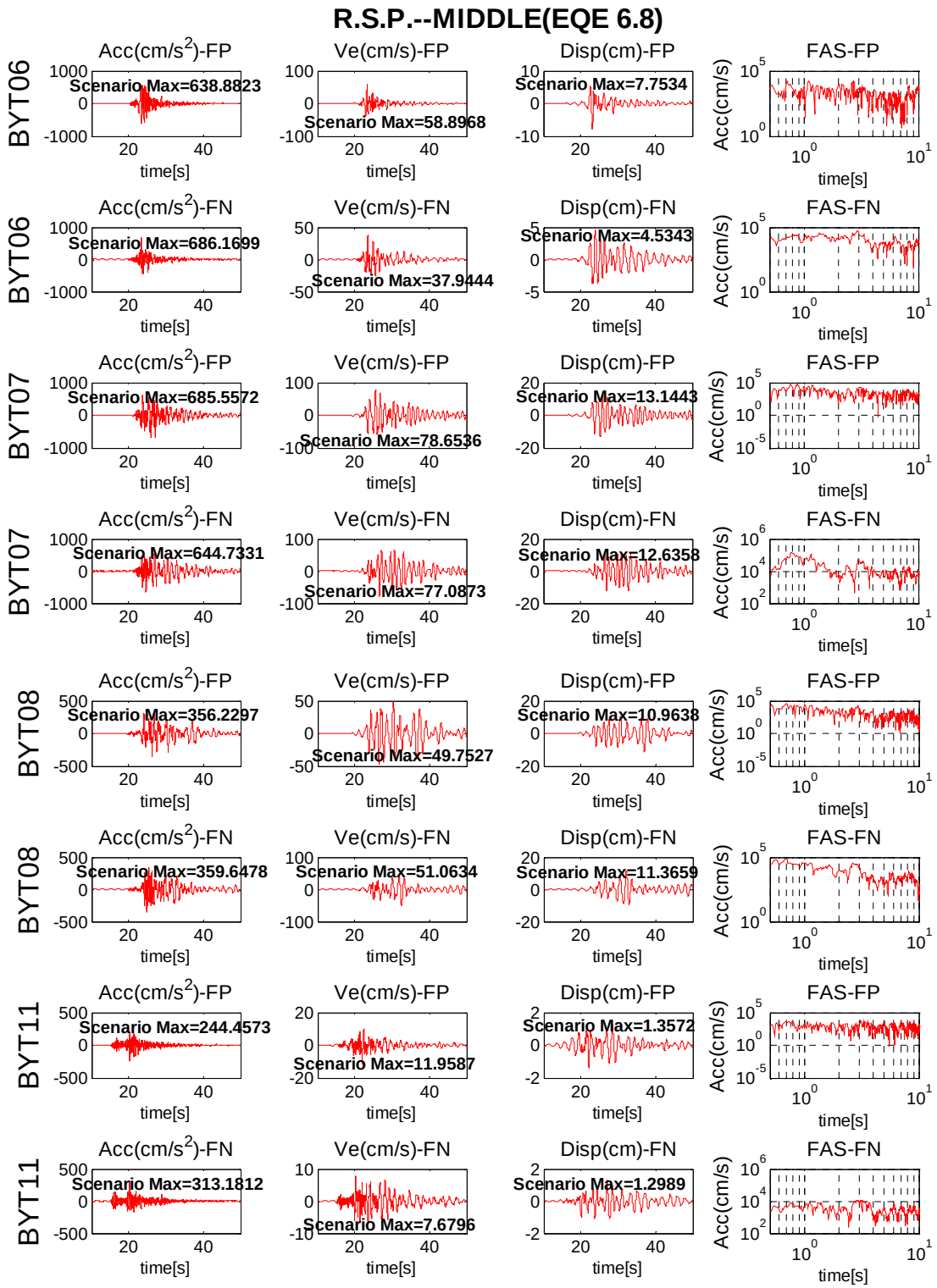

Figure C.17. Scenario earthquake 6.8, rupture starting at the middle of the asperity for BYT06, BYT07, BYT08 and BYT11 stations

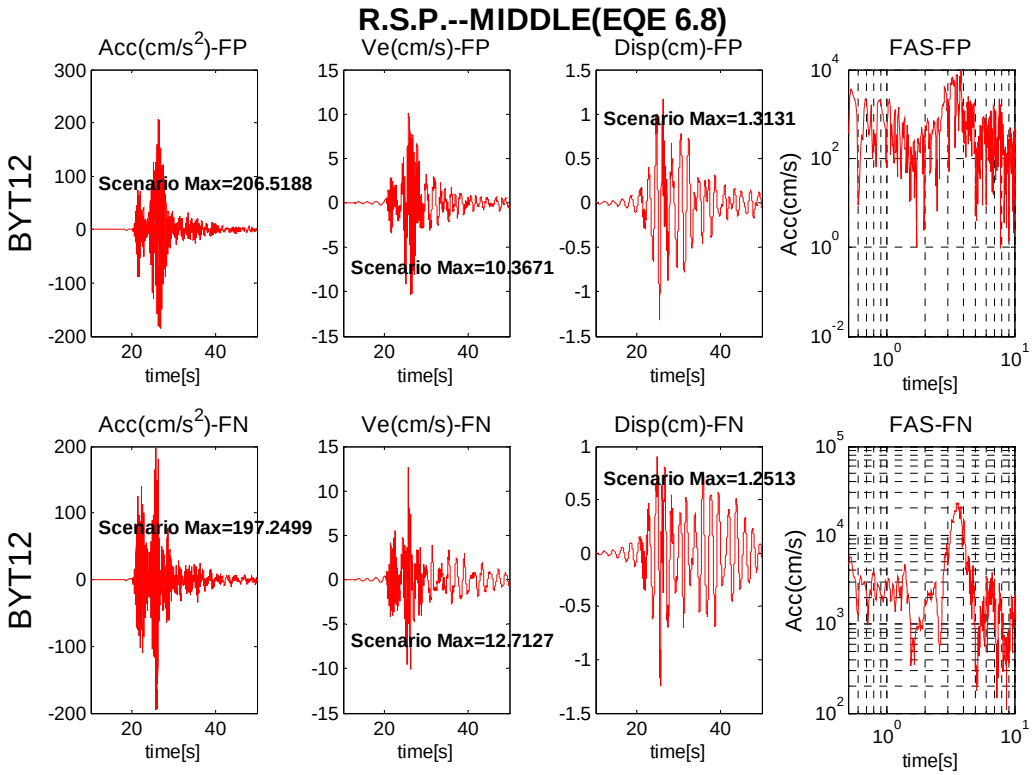

Figure C.18. Scenario earthquake 6.8, rupture starting at the middle of the asperity for BYT12 station

REFERENCES

Abrahamson, N. A. and K. M. Shedlock, 1997, "Overview", *Seismological Research Letters,* Vol. 68, pp. 9-23.

Aki, K., 1967, "Scaling Law of Seismic Spectrum", *Journal of Geophysical Research*, Vol. 72, pp. 1217-1231.

Akkar, S. and J. J. Bommer, 2007, "Empirical Prediction Equations for Peak Ground Velocity Derived from Strong-Motion Records from Europe and the Middle East", *Bulletin of the Seismological Society of America*, Vol. 97, No. 2, pp. 511–530, April.

Ambraseys, N. N. and J. A. Jackson, 2000, "Seismicity of the Sea of Marmara (Turkey) Since 1500", *Geophysical Journal International,* Vol. 141, No. 3, pp. F1–F6.

Ambraseys, N. N., 2002, "The Seismic Activity of the Marmara Sea Region Over the Last 2000 years", *Bulletin of the Seismological Society of America*, Vol. 92, No. 1, pp. 1–18.

Archuleta, R. J. and S. H. Hartzell, 1981, "Effects of Fault Finiteness on Near-Source Ground Motion", *Bulletin of the Seismological Society of America*, Vol. 71, pp. 939-957.

Aydinoğlu, N., 1998, *Specifications for Structures to be Built in Disaster Areas*, Turkish Seismic Design Code (English Translation), Official Gazette Nos. 23098 and 23390, Ministry of Public Works and Settlement, Government of Republic of Turkey.

Bard, P. Y., 1994, "Effects of Surface Geology on Ground Motion: Recent Results and Remaining Issues", *Proceedings of the 10th European Conference on Earthquake Engineering*, 28 August-2 September 1994, G. Duma (Editor), Vienna, Austria, Vol. 1, pp. 305-325.

Barka, A. A. and K. Kadinsky-Cade, 1988, "Strike-Slip Fault Geometry in Turkey and its Influence on Earthquake Activity", *Tectonics Journal*, Vol. 7, No. 3, pp. 663-684, June.

Basham, P. W., D. H. Weichert, F. M. Anglin and M. J. Berry, 1985, "New Probabilistic Strong Ground Motion Maps of Canada", *Bulletin of the Seismological Society of America*, Vol. 75, pp. 563–595.

Birgören, G. and K. Irikura, 2004, "Stochastic Green's Function Technique with Phase Dependent Site Response: Case of the Düzce Basin, Turkey", http://www.icce.ac.cn/shr_iaspei/docs/iugg_special_volume/iugg_p016_Birgoren.pdf

Boatwright, J., 1988, "The Seismic Radiation from Computer Models of Faulting", *Bulletin of the Seismological Society of America*, Vol. 78, pp. 489-508.

Bolt, B., P. G. Somerville, N. A. Abrahamson and A. Zerva, 2004, *Workshop Proceedings: Effects of Earthquake-Induced Transient Ground Surface Deformations on at-grade Improvements, Earthquake Damage Assessment and Repair Project*, Curee Publications, April.

Bonilla, L. F., J. H. Steidl, G. T. Lindley, A. G. Tumarkin and R. J. Archuleta, 1997, "Site Amplification in the San Fernando Valley, California: Variability of Site-effect Estimation Using the S-Wave, Coda and H/V Methods", *Bulletin of the Seismological Society of America*, Vol. 87, pp. 710-730.

Boore, D. M., 1983, "Stochastic Simulation of High-frequency Ground Motions based on Seismological Models of the Radiated Spectra", *Bulletin of the Seismological Society of America*, Vol. 73, No. 6, pp. 1865-1894, December.

Boore, D. M., W. B. Joyner and T. E. Fumal, 1997, "Equations for Estimating Horizontal Response Spectra and Peak Acceleration from Western North American Earthquakes: A summary of Recent Work", *Seismological Research Letters,* Vol. 68, No 1, pp. 128-153, January/February.

Boore, D. M. and M. G. Atkinson, 2007, "Ground-Motion Prediction Equations for the Average Horizontal Component of PGA, PGV and 5 per cent damped PSA at Spectral Periods between 0.01 s and 10.0 s", *NGA Special Volume of Earthquake Spectra*.

Borcherdt, R. D., 1970, "Effects of Local Geology on Ground Motion Near San Francisco Bay", *Bulletin of the Seismological Society of America*, Vol. 60, pp. 29-61.

Borcherdt, R. D. and J. F. Gibbs, 1976, "Effects of Local Geological Conditions in the San Francisco Bay Region on Ground Motions and the Intensities of the 1906 Earthquake", *Bulletin of the Seismological Society of America*, Vol. 66, pp. 467-500.

Bouchon, M., 1979, "Discrete Wave Number Representation of Elastic Wave Fields in Three-Space Dimensions, *Journal of Geophysical Research*, Vol. 84, pp. 3609-3614.

Bouckovalas, G. and I. Krikeli, 1991, "Effect of Local Soil Stratigraphy on Microtremor Measurements", *Proceedings of the Second International Conference on Recent Advances in Geotechnical Earthquake Engineering and Soil Dynamics*, Missouri, Paper No. 8.21, pp. 1245-1251.

Bray, J. B., R. B. Seed, L. S. Cluff and H. B. Seed, 1994, "Earthquake Fault Rupture Propagation through Soil", *Journal of Geotechnical Engineering*, *ASCE*, Vol. 120, No. 3, pp. 543-561.

Brune, J. N., 1970, "Tectonic Stress and the Spectra of Seismic Shear Waves from Earthquakes", *Journal of Geophysical Research*, Vol. 75, pp. 4997-5009.

Brune, J. N., 1971, "Tectonic Stress and the Spectra of Seismic Shear Waves from Earthquakes", *Journal of Geophysical Research*, Vol. 76, p. 5002.

Byerly, P. and J. DeNoyer, 1958, "Energy in Earthquakes as Computed from Geodetic Observations", *Contributions in Geophysics: In Honor of Beno Gutenberg*, Pergamon Press, NY.

Campbell, K. W., 2002, *Engineering Models of Strong Ground Motion*, *Earthquake Engineering Handbook*, W. F. Chen and C. Scawthorn (Editors), CRC Press, Boca Rotan, Florida, Chapter 5-1–5-76.

Campbell, K. W., 2003, *Strong Motion Attenuation Relationships*, *International Handbook of Earthquake and Engineering Seismology*, W. H. K. Lee, H. Kanamori, P. C. Jennings and C. Kisslinger (Editors), Academic Press, London, Vol. 2, Chapter 60.

Campbell, K. W. and Y. Bozorgnia, 2003, "Updated Near-Source Ground-Motion (Attenuation) Relations for the Horizontal and Vertical Components of Peak Ground Acceleration and Acceleration Response Spectra", *Bulletin of the Seismological Society of America*, Vol. 93, No. 1, pp. 314–331, February.

Campbell, K. W. and Y. Bozorgnia, 2006, "Campbell-Bozorgnia NGA Empirical Ground Motion Model for the Average Horizontal Component of PGA, PGV and SA at Selected Spectral Periods ranging from 0.01–10.0 seconds", *Interim Report for USGS Review*.

Catalyurekli, Y., 2004, *S-Wave Spectral Analysis of 1999 Kocaeli and Duzce Earthquake Sequences*, M.S. Thesis, Boğaziçi University.

Crampin, S. and R. Evans, 1986, "Neotectonics of the Marmara Sea Region of Turkey", *Journal of Geology Society,* Vol. 143, No. 2, pp. 343–346, London.

Das, S. and B. V. Kostrov, 1986, "Fracture of a Single Asperity on a Finite Fault: A Model for Weak Earthquakes?", S. Das, J. Boatwright and C. Scholz (Editors), *Earthquake Source Mechanism. American Geophysical Union*, Washington, pp. 91–96.

Davis, C. A. and J. P. Bardet, 2000, "Responses of Buried Corrugated Metal Pipes to Earthquakes", *Journal of Geotechnical and Geoenvironmental Engineering*, *ASCE*, Vol. 126, No. 1, pp. 28-39.

Delouis, B., D. Giardini, P. Lundgren and J. Salichon, 2002, "Joint Inversion of InSAR, GPS, Teleseismic and Strong-motion Data for Spatial and Temporal Distribution of Earthquake Slip", *Bulletin of the Seismological Society of America*, Vol. 92, No. 1, pp. 278–299.

Durgesh, C. R., 2000, "Future Trends in Earthquake-Resistant Design of Structures", *Indian Institute of Science Seismology Journal,* November.

Eidinger, J., B. Maison, D. Lee and B. Lau, 1995, "East Bay Municipal District Water Distribution Damage in 1989 Loma Prieta Earthquake", *Proceedings of the Fourth US Conference on Lifeline Earthquake Engineering*, *ASCE*, Technology Council on Lifeline Earthquake Engineering, Monograph 6, pp. 240–247.

Erdik, M. and E. Durukal, 2002, *Simulation Modeling of Strong Ground Motion , Earthquake Engineering Handbook*, CRC Press.

Erdik, M., M. Demircioglu, K. Sesetyan, E. Durukal and B. Siyahi, 2004, "Earthquake Hazard in Marmara Region, Turkey", *Soil Dynamics and Earthquake Engineering*; Vol. 24, Issiue 8, pp. 605-631.

Field, E. H. and K. H. Jacob, 1993, "The Theoretical Response of Sedimentary Layers to Ambient Seismic Noise", *Geophys. Res. Lett*., Vol. 20, pp. 2925-2928

Field, E. H. and K. H. Jacob, 1995, "A Comparison and Test of Various Site Response Estimation Techniques, Including Three that are not Reference–Site Dependent", *Bulletin of the Seismological Society of America*, Vol. 85, pp. 1127-1143.

Field, E. H., 1996, “Spectral Amplification in a Sediment-Filled Valley Exhibiting Clear Basin-Edge-Induced Waves”, *Bulletin of the Seismological Society of America*, Vol. 86, pp. 991-1005.

Finn, W. D. L., 1991, “Geotechnical Engineering Aspects of Microzonation”, *Fourth International Conference on Seismic Zonation*, Stanford, California, pp. 236-253.

Gurbuz, C., M. Aktar, H. Eyidogan, A. Cisternas, H. Haessler, A. Barka, M. Ergin, N. Turkelli, O. Polat, B. Ucer, S. Kuleli, S. Baris, B. Kaypak, T. Bekler, E. Zor, F. Bicmen and A. Yoruk, 2000, “The Seismotectonics of the Marmara region (Turkey): Results from a microseismic experiment”, *Tectonophysics*, No. 316, pp. 1–17.

Hanks, T. C. and H. Kanamori, 1979, “A Moment Magnitude Scale”, *Journal of Geophysical Research*, Vol. 84, No. 2, pp. 2348-2350.

Hanks, T. C. and R. K. McGuire, 1981, “The Character of High-frequency Strong Ground Motion”, *Bulletin of the Seismological Society of America*, Vol. 71, pp. 2071-2095.

Hartzell, S. H., 1978, “Earthquake Aftershocks as Green’s Functions” *Geophysical Research Letters*, Vol. 5, pp. 1-4.

Hartzell, S. and D. V. Helmberger, 1982, “Strong-Motion Modeling of the Imperial Valley Earthquake of 1979”, *Bulletin of the Seismological Society of America*, Vol. 72, pp. 571-596.

Hartzell, S.H. and T.H. Heaton, 1983, “Inversion of Strong Ground Motion and Teleseismic Waveform Data for the Fault Rupture History of the 1979 Imperial Valley, California Earthquake”, *Bulletin of the Seismological Society of America*, Vol. 73, pp. 1553-1583.

Hartzell, S. H. and T. H. Heaton, 1988, "Failure of Self-Similarity for Large ($M_w > 8^{1/4}$) Earthquakes", *Bulletin of the Seismological Society of America*, Vol. 78, pp. 478-488.

Hays, W. W., 1986, "Site Amplification of Earthquake Ground Motion", *Proceedings of the 3rd United States National Earthquake Engineering Conference*, 24-28 August 1986, Earthquake Engineering Research Institute, Charleston, North Carolina, Vol. 1, pp. 357-368.

Houston, H. and H. Kanamori, 1986, "Source Spectra of Great Earthquakes: Teleseismic Constraints on Rupture Process and Strong Motion", *Bulletin of the Seismological Society of America*, Vol. 76, pp. 19-42.

Hutchings, L., S. Jarpe, P. Kasameyer and W. Foxall, 1997, "Validation of a Ground Motion Synthesis and Prediction Methodology for the 1988, M=6.0, Saguenay Earthquake", *NCEER Workshop on Ground Motion Methodologies for the Eastern United States*, October.

Irikura, K., 1983, "Semi-Empirical Estimation of Strong Ground Motions during Large Earthquakes", *Bull. Disas. Prev. Res. Inst., Kyoto Univ*., Vol. 33, pp. 63-104.

Irikura, K., 1986, "Prediction of Strong Acceleration Motion Using Empirical Green's Function", *Proceedings 7th Japan Earthquake Engineering Symposium*, Tokyo, pp. 151-156.

Irikura, K., 1988, "Estimation of Near-Field Ground Motion Using Empirical Green's Function", *Proceedings 9th World Conference Earthquake Engineering*, Vol. VII, pp. 37-42.

Irikura, K. and K. Katsuhiro, 1994, "Estimation of Strong Ground Motion in Broad-frequency Band Based on a Seismic Source Scaling Model and an Empirical Green's Function Technique", *Annali Di Geofisica,* Vol. 37, No. 6, pp. 1721-1743, December.

Irikura, K. and K. Kamae, 1996, *Estimation of Strong Ground Motion Using Hybrid Green's Function*, Fundamental Research for the Mitigation of Urban Disasters by Near-Field Earthquakes, p. 5.

Irikura, K., T. Kagawa and H. Sekiguchi, 1997, "Revision of the Empirical Green's Function Method by Irikura (1986)", *Programme and Abstracts*, *Seismol. Soc. Jpn.*, Vol. 2, p. B25.

Irikura, K. and H. Miyake, 2003, "Lecture Notes on Strong Motion Seismology", http://www.kojiro-irikura.jp/english.html.

Irikura, K. and H. Miyake, 2006, "Recipe for Predicting Strong Ground Motions: The State of the Art and Future Prospects", *Proceedings of the 8th U.S. National Conference on Earthquake Engineering, San Francisco, California, USA,* Paper No. 744, April.

Irmak, T. S., H. Grosser, M. F. Özer, H. Woith and S. Baris, 2007, "The 24 October 2006 Gemlik Earthquake (M=5.2)", *Geophysical Research Abstracts*, Vol. 9, p. 10212.

Isoyama, R., E. Ishida, K. Yune and T. Shirozu, 2000, "Seismic Damage Estimation Procedure for Water Supply Pipelines", *Proceedings of the Twelfth World Conference on Earthquake Engineering*, Auckland, New Zealand, 1–4 January, p. 1762.

Joshi, A. and S. Midorikawa, 2004, "A Simplified Method for Simulation of Strong Ground Motion using Finite Rupture Model of the Earthquake Source", *Journal of Seismology*, No. 8, pp. 467-484.

Joyner, W. B. and D. M. Boore, 1986, "On Simulating Large Earthquakes by Green's Function Addition of Smaller Earthquakes", *Earthquake Source Mechanics*, Edited by S. Das and J. Boatwright, Vol. 6, pp. 269-274.

Kamae, K. and K. Irikura, 1998, "Source Model of 1995 Hyogo-ken Nanbu Earthquake and Simulation of Near-Source Ground Motion", *Bulletin of the Seismological Society of America*, Vol. 88, No. 2, pp. 400-412, April.

Kanamori, H. and D. L. Anderson, 1975, "Theoretical Basis of Some Empirical Relations in Seismology", *Bulletin of the Seismological Society of America*, Vol.65, pp. 1073-1095.

Kanamori, H., 1979, "A Semi Empirical Approach to Prediction of Long Period Ground Motions from Great Earthquakes", *Bulletin of the Seismological Society of America*, Vol. 69, pp. 1645-1670.

Kennett, B. L. N., 1983, *Seismic Wave Propagation in Stratified Media*, Cambridge University Press, Cambridge.

Konno, K. and T. Ohmachi, 1995, "A Smoothing Function Suitable for Estimation of Amplification Factor of the Surface Ground from Microtremor and Its Application", *Journal of JSCE*, Vol. 525, pp. 247-259 (in Japanese).

Konno, K. and T. Ohmachi, 1998, "Ground-Motion Characteristics Estimated from Spectral Ratio between Horizontal and Vertical Components of Microtremor", *Bulletin of the Seismological Society of America*, Vol. 88, No. 1, pp. 228-241.

Krawinkler, H. and B. Alavi, 1998, "Development of Improved Design Procedures for Near-Fault Ground Motions," *SMIP98, Seminar on Utilization of Strong Motion Data*, Oakland, California.

Lachet, C. and P. Y. Bard, 1994, "Numerical and Theoretical Investigations on the Possibilities and Limitations of Nakamura's Technique", *Journal of Physics and Earth*, Vol. 42, No. 5, pp. 377-397.

Lachet, C., D. Hatzfeld, P. Y. Bard, C. P. Theodulidis and A. Savvaidis, 1996, "Site Effects and Microzonation in the City of Thessaloniki (Greece): Comparison of Different Approaches", *Bulletin of the Seismological Society of America*, Vol. 86, pp. 1692-1703.

Langston, C. A., 1979, "Structure under Mount Rainier, Washington, Inferred from Teleseismic P Waves", *Journal of Geophysical Research*, Vol. 84, pp. 4749-4762.

Lay, T. and T. C. Wallace, 1995, *Modern Global Seismology*, Academic Press, San Diego.

Lazarte, C. A., J. D. Bray, A. M. Johnson and R. E. Lemmer, 1994, "Surface Breakage of the 1992 Landers Earthquake and its Effects on Structures", *Bulletin of the Seismological Society of America*, Vol. 84, pp. 547-561.

Le Pichon, X., T. Taymaz, A. M. C. Sengör, M. Karaca and D. N. Ural, 1999, "The Marmara Fault and the Future Istanbul Earthquake", *International Conference on the Kocaeli Earthquake, 17 August 1999, Istanbul Proceedings*, pp. 41–54, Istanbul Technical University Press House, Istanbul.

Le Pichon, X., A. M. C. Sengör, E. Demirbag, C. Rangin, C. Imren, R. Armijo, N. Görür, N. Çagatay, B. Mercier de Lepinay, B. Meyer, R. Saatçılar and B. Tok, 2001, "The Active Main Marmara Fault", *Earth Planet Science. Letters,* Vol. 192, No. 4, pp. 595–616.

Lermo, J. and F. J. Chavez-Garcia, 1993, "Site Effect Evaluation Using Spectral Ratios with Only One Station", *Bulletin of the Seismological Society of America*, Vol. 83, pp.1574-1594.

Lermo, J. and F. J. Chavez-Garcia, 1994, "Are Microtremors Useful in Site Response Evaluation?", *Bulletin of the Seismological Society of America*, Vol. 84, pp. 1350-1364.

Mai, P. M., P. Spudich and J. Boatwright, 2005, "Hypocenter Locations in Finite-Source Rupture Models", *Bulletin of the Seismological Society of America*, Vol. 95, No. 3, pp. 965-980.

Manighetti, I., M. Campillo, C. Sammis, P. M. Mai and G. King, 2005, "Evidence for Self-similar, Triangular Slip Distributions on Earthquakes: Implications for Earthquakes and Fault Mechanics", *Journal of Geophysical Research*, Vol. 110, p. 5302.

Miyake, H., T. Iwata and K. Irikura, 1999, "Strong Ground Motion Simulation and Source Modeling of the Kagoshima-Ken Hokuseibu Earthquakes of March 26 (M_{JMA}6.5) and May 13 (M_{JMA}6.3), 1997, Using Empirical Green's Function Method", *Zisin*, Vol. 51, pp. 431-442.

Molnar, S., J. F. Cassidy and S. E. Dosso, 2004, "Site Response in Victoria, British Columbia, from Spectral Ratios and 1D Modeling", *Bulletin of the Seismological Society of America*, Vol. 94, No. 3, pp. 1109-1124, June.

Nakamura, Y., 1989, "A Method for Dynamic Characteristics Estimation of Subsurface Using Microtremor on the Ground Surface", *QR of RTRI*, Vol. 30, No. 1, pp. 25-33.

Newmark, N. M., J. A. Blume and K. K. Kapur, 1973, "Seismic Design Spectra for Nuclear Power Plants", *Journal of the Power Division*, *ASCE*, Vol. 99, No. 2, pp. 287–303.

Nogoshi, M. and T. Igarashi, 1970, "On the Propagation Characteristics of Microtremors", *Journal of Seismological Society of Japan*, Vol. 23, pp. 264-280 (in Japanese).

Nogoshi, M. and T. Igarashi, 1971, "On the Amplitude Characteristics of Microtremors", *Journal of Seismological Society of Japan*, Vol. 24, pp. 24-40 (in Japanese).

Ohmachi, T., Y. Nakamura and T. Toshinawa, 1991, "Ground Motion Characteristics of the San Francisco Bay Area Detected by Microtremor Measurements", *Proceedings of the Second International Conference on Recent Advances in Geotechnical Earthquake Engineering and Soil Dynamics*, Missouri, Paper No. LP08, pp. 1643-1648.

Ohmachi, T., K. Konno, T. Endoh and T. Toshinawa, 1994, "Refinement and Application of an Estimation Procedure for Site Natural Periods Using Microtremor", *Japan Society of Civil Engineers*, Vol. 489, pp. 251-261 (in Japanese).

O'Rourke, M. J. and G. Ayala, 1993, "Pipeline Damage Due to Wave Propagation", *Journal of Geotechnical Engineering, ASCE*, Vol. 119, No. 9, pp. 1490–1498.

O'Rourke, M. J., H. E. Stewart and S. S. Jeon, 2001, "Geotechnical Aspects of Lifeline Engineering", *Proceedings of the Institution of Civil Engineers: Geotechnical Engineering*, Vol. 149, No. 1, pp. 13-26.

Papageorgiou, A.S., B. Zhang and G. Dong, 1997, "Estimation of Strong Ground Motion from the Great 1964 Prince William Sound Earthquake", *Seismological Research Letters*, Vol. 68, p. 325.

Pinar, N., 1943, *Marmara Denizi Havzasinin Sismik Jeolojisi ve Meteorolojisi*, *Science Faculty Monographies*, A7, Ph.D. Thesis, İstanbul Üniversitesi.

Pitarka A., Somerville, P. G., Y. Fukushima, T. Uetake and K. Irıkura, 2000, **"**Simulation of Near-Fault Strong-Ground Motion Using Hybrid Green's Functions**",** *Bulletin of the Seismological Society of America*, Vol. 90, No. 3, pp. 566-586.

Polat, O., H. Haessler, A. Cisternas, H. Philip, H. Eyidogan, M. Aktar, M. Frogneux, D. Comte and C. Gürbüz, 2002, "The Izmit (Kocaeli) Turkey Earthquake of 17 August 1999: Previous Seismicity, Aftershocks and Seismotectionics", *Bulletin of the Seismological Society of America*, Vol. 92, No.1, pp. 361–375.

Pulido, N., A. Ojeda, K. Atakan and T. Kubo, 2004, "Strong Ground Motion Estimation in the Sea of Marmara Region (Turkey) based on a Scenario Earthquake", *Tectonophysics,* No. 391, pp. 357– 374, June.

Reid, H. F., 1911, "The Elastic-Rebound Theory of Earthquake", *University of California Publications in the Geological Sciences*, Vol. 6, pp. 413-444.

Somerville, P. G., R. W. Graves and C. K. Saikia, 1995, "Characterization of Ground Motions during the Northridge Earthquake of January 17, 1994", *Program to Reduce the Earthquake Hazards of Steel Moment Frame Buildings*, SAC Report.

Somerville, P. G., 1996, "Strong Ground Motions of the Kobe, Japan Earthquake of Jan. 17, 1995 and Development of a Model of Forward Rupture Directivity Effects Applicable in California, *Proceedings of the Western Regional Technical Seminar on Earthquake Engineering for Dams*, Association of State Dam Safety Officials, Sacramento, April 11-12.

Somerville, P. G., N. F. Smith, R. W Graves and N. A. Abrahamson, 1997, "Modification of Empirical Strong Ground Motion Attenuation Relations to Include the Amplitude and Duration Effects of Rupture Directivity", *Seismological Research Letters*, Vol. 68, No. 1, pp. 180-222, January/February.

Somerville, P. G., 1998, "Development of An Improved Representation of Near-Fault Ground Motions", *Proceedings of the SMIP98 Seminar on Utilization of Strong-Motion Data*, California Strong Motion Instrumentation Program.

Somerville, P. G., K. Irıkura, R. Graves, S. Sawada, D. Wald, N. A. Abrahamson, Y. Iwasaki, T. Kagawa, N. Smith and A. Kowada, 1999, "Characterizing Crustal Earthquake Slip Models for the Prediction of Strong Ground Motion", *Seismological Research Letters*, Vol. 70, No. 1, pp. 59-80.

Somerville, P. G., 2002, *Characterizing Near Fault Ground Motion for the Design and Evaluation of Bridges*, URS Corp., February.

Somerville, P. G., 2003, "Magnitude Scaling of the Forward Rupture Directivity Pulse ", *Physics of the Earth and Planetary Interiors*, Vol. 137, No 1, pp. 201-212.

Sørensen, M. B., N. Pulido and K. Atakan, 2007, "Sensitivity of Ground-Motion Simulations to Earthquake Source Parameters: A Case Study for Istanbul, Turkey", *Bulletin of the Seismological Society of America*, Vol. 97, No. 3, pp. 881–900, June.

Stewart, J. P., S. Chiou, J. D. Bray, R. W. Graves, P. G. Somerville and N. A. Abrahamson, 2001, *Ground Motion Evaluation Procedures for Performance-Based Design,* Peer Report, September.

Triantafyllidis, P., P. M. Hatzidimitriou, N. Theodulidis, P. Suhadolc, C. Papazachos, D. Raptakis and K. Lontzetidis, 1999, "Site Effects in the City of Thessaloniki (Greece) Estimated from Acceleration Data and 1D Local Soil Profiles", *Bulletin of the Seismological Society of America*, Vol. 89, pp. 521-537.

Wald, D. J. and T. H. Heaton, 1994, "Spatial and Temporal Distribution of Slip for the 1992 Landers, California earthquake", *Bulletin of the Seismological Society of America*, Vol. 84, pp. 668-691.

Wald, D. J., T. H. Heaton and K. W. Hudnut, 1997, "Estimation of Uniformly Spaced, Near-Source, Broadband Ground Motions for the 1994 Northridge Earthquake from Forward and Inverse Modelling", *CURE Proceedings*, Los Angles.

Wells, D. L. and K. J. Coppersmith, 1994, "New Empirical Relationships among Magnitude, Rupture Length, Rupture Width, Rupture Area and Surface Displacement", *Bulletin of the Seismological Society of America*, Vol. 84, pp. 974-1002.

Yaltırak, C., 2002, "Tectonic Evoluation of Marmara Sea and its Surroundings", *Marine Geology*, Vol. 3175, pp. 1-37.